

University of Nottingham

UK | CHINA | MALAYSIA

Thermal Properties of Lattice Structures by Laser Powder Bed Fusion for Aerospace Systems

Richard Roger Joachim SÉLO

Supervised by Prof. Christopher TUCK, Prof. Ian ASHCROFT,

and Dr. Ian MASKERY

Thesis submitted to the University of Nottingham

for the degree of Doctor of Philosophy

June 2021

“The man who works recognizes his own product in the World that has actually been transformed by his work. He recognizes himself in it, he sees his own human reality in it he discovers and reveals to others the objective reality of his humanity of the originally abstract and purely subjective idea he has of himself” – Alexandre Kojève

Declaration

This dissertation is the result of my own work and includes nothing, which is the outcome of work done in collaboration except where specifically indicated in the text. It has not been previously submitted, in part or whole, to any university or institution for any degree, diploma, or other qualification.

Signed: 

Date: 30/06/2021

Richard Roger Joachim SÉLO

Abstract

In the aerospace industry, thermal management concerns numerous components but is bounded to the limitations of traditional manufacturing processes which results in inefficient and inadequately large equipment. Consequently, a change in how heat exchangers are manufactured and designed is needed. Additive manufacturing (AM) techniques such as laser powder bed fusion (LPBF) are capable of alleviating conventional design drawbacks. Among new complex structures, triply periodic minimal surface (TPMS) lattice structures are of particular interest with their high surface area to volume ratios that are ideal to increase surface-based interactions such as heat transfer. However, the adoption of LPBF for thermal applications is impeded by the lack of available material for LPBF and insufficient knowledge on how AM material thermal properties are affected by the LPBF process and of the thermal properties of lattice structures.

The first part of this thesis focused on the characterisation of the thermal conductivity of materials and lattice structures manufactured by LPBF using an in-house developed testing apparatus based on the guarded comparative longitudinal heat flow technique. AlSi10Mg is the most applied aluminium alloy in LPBF, however, there is an incomplete body of knowledge surrounding its thermal conductivity. In this thesis, AlSi10Mg specimens were manufactured by LPBF and tested to characterise the effect of the unique LPBF microstructure and heat treatments on the thermal conductivity. In addition, the effect of lattice parameters on their apparent thermal conductivity was investigated by manufacturing and testing lattice structures made by LPBF in several alloys of interest for aerospace (Ti6Al4V, AlSi10Mg, and Hastelloy-X). Models were proposed to predict the thermal conductivity of lattices and specimens with tailored conductivity were manufactured.

Forced convection heat transfer of AlSi10Mg lattice structures manufactured by LPBF was evaluated by measuring pressure drop and heat transfer of the structures using an in-house developed testing apparatus. A metric based on the maximum variation of the cross-sectional area was proposed as a quick estimate of the lattice structures pressure drop. It was demonstrated that the thermal performance of lattice structures can be up to 6 times higher than that of pin-fin geometry.

The last part of this thesis focused on the extension of LPBF material library with the high-strength aluminium alloy EN AW 2618. Despite a wide range of parameter optimisation and high relative density (>99 %), crack-free EN AW 2618 has not been manufactured due to its crack sensitivity and high cooling rates in LPBF. Subsequently, A20X, a newly developed high-strength aluminium alloy specifically designed for LPBF was investigated. Crack-free material with high relative density (>99 %) was achieved. It was demonstrated that its thermal and mechanical properties can compete with those of conventional EN AW 2618.

The results from this thesis presented lattice structures made by LPBF as a route through which enhanced heat exchangers could be designed. Through these improvements, heat exchangers can potentially become more efficient and compact with possible multifunctional properties that could be generated as part of the design process.

Publications

Included in this thesis:

Sélo, R.R.J., Catchpole-Smith, S., Maskery, I., Ashcroft, I., Tuck, C., (2020) 'On the thermal conductivity of AlSi10Mg and lattice structures made by laser powder bed fusion', *Additive Manufacturing*, 34, p. 101214. DOI: 10.1016/j.addma.2020.101214.

Catchpole-Smith, S., **Sélo, R.R.J.**, Davis, A.W., Ashcroft, I.A., Tuck, C.J., Clare, A., (2019) 'Thermal Conductivity of TPMS Lattice Structures Manufactured via Laser Powder Bed Fusion', *Additive Manufacturing*, 30, p. 100846. DOI: 10.1016/j.addma.2019.100846.

Journal articles not included in this thesis:

Speidel, A., **Sélo, R.R.J.**, Bisterov, I., Mitchell-Smith, J., Clare, A., (2021), 'Post processing of additively manufactured parts using electrochemical jet machining', *Materials Letters*, p129671. DOI: 10.1016/j.matlet.2021.129671

Conferences

- Engineering Research Showcase, University of Nottingham, 2019, Nottingham, United Kingdom

Poster presentation ‘Forced convective apparatus for thermal performance of lattice structures’

- American Society of Mechanical Engineers (ASME) Turbomachinery Technical Conference and Exposition (TurboExpo) 2019, Phoenix, Arizona, United States of America

Poster presentation ‘Convective Heat Transfer Performance of Lattice Structures’

- Additive Manufacturing with Powder Metallurgy (AMPM) 2019, Phoenix, Arizona, United States of America.
- 149th Annual Meeting and Exhibition of The Minerals, Metals & Materials Society (TMS2020), San Diego, California, United States of America

Talk ‘A20X and AlSi10Mg Aluminium Alloys: A Comparison’

Acknowledgements

This journey was only possible thanks to many people who helped me closely, from far and far far away, directly or indirectly. I, therefore, must acknowledge you all first.

I would like to thank Professor Adam Clare, who allowed me to be part of the research community, and James Murray who showed me how addictive research could be. Both of you and your guidance ultimately led to my pursuit of a Ph.D. degree at the University of Nottingham.

I am thankful to Professors Christopher Tuck and Ian Ashcroft who supervised me during these four years and for all their feedback and insight which have helped me to grow. In addition, special thanks go to Dr. Ian Maskery who supervised me and helped me with data analysis, writing of this thesis, and more.

No part of this project would have been possible without my sponsor company, Leonardo, with special thanks to Sam, Marek, Luke, and Robert. I am also very grateful for all the help received from Alexander Jackson-Cripps, Mark Hardy, and Jason Greaves.

Sam Catchpole-Smith, I am very grateful to have met and work with you during my Ph.D. I learnt a lot! I do not think all this work would have been possible if we did not have teamed up and became friends.

Yazid Lakhdar, my French copain, thank you for the much-needed coffee breaks, talking and teaching me so many things. I will not forget to invest!

I would like to thank Cassidy Silbernagel and Leonidas Gargalis, the SLM corner guys, for their good mood, especially when nothing was working as it was supposed to, for their conversations and laboratory assistance. Guys, I’m glad to have met and work with you. I hope we will work together again soon.

I am glad to have met you, Alistair Speidel, work with you, and exchange cooking side projects during lunchtimes.

Vincent, Pierre, Mathieu, and Adrien, “Top 1 ou rien”, thanks for helping me to relax in stressful times.

Alice, thank you for being by my side, supporting me, and helping me to develop all along this journey, I would not have finished this work without you.

At last but not least I am infinitely grateful to my parents who never put any pressure and only wanted me to do something I enjoy. Merci Maman, merci Papa!

Contents

Abstract ..... **iii**

Publications ..... **v**

Included in this thesis: v

Journal articles not included in this thesis: v

Conferences ..... **vi**

Acknowledgements ..... **vii**

Contents ..... **ix**

List of Tables ..... **xii**

List of Figures ..... **xiv**

Abbreviations ..... **xviii**

Nomenclature ..... **xx**

1 Introduction **1**

1.1 Aim, objectives, and methodology 1

1.2 Heat exchangers 2

1.3 Additive manufacturing and laser powder bed fusion 5

1.4 Design for additive manufacturing 8

1.5 Challenges addressed in this research 10

1.6 Thesis outline 11

2 Literature Review **12**

2.1 Introduction 12

2.2 Laser Powder Bed Fusion 12

2.3 Lattice Structures 30

2.4 Summary of research gaps 49

3 Materials and Methods 51

3.1 Introduction 51

3.2 Design model preparation before manufacturing 51

3.3 Laser Powder Bed Fusion equipment 56

3.4 Metal powders 61

3.5 Parameter optimisation and process validation 68

3.6 Summary 75

4 Original Method 76

4.1 Introduction 76

4.2 Thermal conductivity of LPBF components 76

4.3 Apparatus for forced convection heat transfer characterisation 89

4.4 Summary 99

5 Thermal conductivity of LPBF components 101

5.1 Introduction 101

5.2 Thermal conductivity and heat treatment of LPBF specimens 102

5.3 Thermal conductivity of lattice structures 109

5.4 Discussion 121

5.5 Design models for thermal conductivity of lattices 128

5.6 Summary 129

6 Forced Convection Heat Transfer 132

6.1 Introduction 132

6.2 Pin fin benchmark 133

6.3 TPMS lattice structures 136

6.4 Summary 154

7 High-strength aluminium alloy for LPBF 157

7.1 Introduction 157

7.2 EN AW 2618 LPBF parameter optimisation 159

7.3 A20X LPBF parameter optimisation 169

7.4 Discussion 183

7.5 Summary 189

8 Conclusion and future work 192

8.1 Conclusions 193

8.2 Future work 196

9 References 200

List of Tables

Table 2.1: Thermal conductivities and densities of different metals at atmospheric pressure and room temperature (25 °C). 17

Table 3.1: Process parameters used to manufacture Ti6Al4V bulk and lattice specimens on Realizer "SLM50" LPBF machine. 57

Table 3.2: Process parameters used to manufacture AlSi10Mg bulk and lattice specimens on Renishaw "AM250" LPBF machine. 59

Table 3.3: Ti6Al4V chemical composition supplied by LPW Technology Ltd (UK). ... 63

Table 3.4: AlSi10Mg chemical composition supplied by LPW Technology Ltd (UK). 64

Table 3.5: AA2618 chemical composition supplied by TLS Technik GmH. 65

Table 3.6: A20X powder chemical composition supplied by the manufacturers. 67

Table 3.7: Powder size distribution of the materials studied in this thesis. 67

Table 3.8: Grinding and polishing procedure for LPBF AlSi10Mg. 70

Table 3.9: Grinding and polishing procedure for LPBF EN AW AA2618. 70

Table 3.10: Grinding and polishing procedure for LPBF A20X. 70

Table 4.1: Review of the main methods to measure the thermal conductivity of solids. 81

Table 5.1: Relative densities of test specimens in various heat treatment conditions. . 104

Table 5.2: Curve fitting parameters for the linear and power-law fits relating apparent thermal conductivity to the actual volume fraction with degree of freedom ν, and goodness of fit indicators: χ_{min}^2 and reduced-χ^2. Fitting parameters are given within one standard deviation. 114

Table 5.3: Fitting parameters with one standard deviation for a linear model linking apparent thermal conductivity to actual volume fraction for each of the tested unit cell designs. Fitting parameters are given within one standard deviation..... 119

Table 5.4: Design parameters and experimental data for the Ti6Al4V target thermal conductivity lattice specimens. 120

Table 5.5: Surface area, volume, and the minimum wall thickness of each lattice structure CAD model. 126

Table 6.1: Pin-fin benchmark dimensions. 133

Table 6.2: Lattice structures CAD vs. measured volume fractions..... 139

Table 7.1: EN AW 2618 LPBF variables for initial parameter optimisation..... 160

Table 7.2: 1st parameter set tested to produce crack-free EN AW 2618 by LPBF. 165

Table 7.3: Porosity range for the tested scan parameters. 166

Table 7.4: 2nd set of parameters tested to produce crack-free EN AW 2618 by LPBF. 167

Table 7.5: Tensile properties of heated aluminium alloys: LPBF AlSi10Mg, conventional EN AW 2618, and A20X. 169

Table 7.6: A20X LPBF process parameters for Renishaw AM400 using a meander scan strategy. 171

Table 7.7: Averaged tensile properties of LPBF A20X in as-built and after a T7 heat treatment developed in this thesis. 180

Table 7.8: Minimum and maximum yield strength and yield elongation of as-built A20X. 181

Table 7.9: Thermal conductivity of LPBF A20X and AlSi10Mg in as-built and heat-treated state measured in this thesis. 182

Table 7.10: Comparative of A20X, EN AW 2618, and AlSi10Mg thermo-mechanical properties. 191

List of Figures

Figure 1.1: Heat exchangers: (a) shell and tube, (b) plates, (c) heatsink. 3

Figure 1.2: Illustration of design freedom offered by additive manufacturing processes: (a) rocket chamber by laser powder bed fusion (LPBF) [7], (b) bracket by fused deposition modelling (FDM) [8], (c) vases by stereolithography (SLA) [9], (d) turbine wheel by binder jet [10]. 5

Figure 1.3: Laser Powder Bed Fusion machine schematic. 6

Figure 1.4: (a) Satellite component from Thales Alenia Space [22], (b) Collaboration between Betatype and Amaero for a rocket chamber [23]. 9

Figure 2.1: Most prominent parameters on LPBF builds based on Aboulkhair *et al.* (2014) [31]. 13

Figure 2.2: Illustration of LPBF scan parameters with a meander scan strategy. 15

Figure 2.3: Examples of scan strategy used in LPBF with a 90° rotation between each layer. The fractal is illustrated by a 2nd order Hilbert curve. 15

Figure 2.4: Melt pool formation mechanisms (a) conduction mode, (b) keyhole mode, (c) keyhole with porosity formation taken from Balbaa *et al.* (2020) [38]. 16

Figure 2.5: Typical temperature history of specimen manufactured by LPBF taken from Luo *et al* (2020) [57]. 21

Figure 2.6: SE SEM images of AlSi10Mg microstructure manufactured by (a) LPBF as-built condition, (b) die-casting. Red dashes on (a) shows the coarser microstructure at the boundary of the melt pool. On (b), A represents the Al-Si needle-shaped eutectic, B denotes Si dispersed in Al matrix, and C points to Fe-rich intermetallic phases. The orange arrow denotes a porosity due to lack of fusion. Image taken from Uzan *et al.* (2018) [62]. 23

Figure 2.7: Optical micrographs of AlSi10Mg microstructure (a) as-built condition, (b) heat-treated. SEM observation of the as-built microstructure in (c) build direction, and (d) transverse direction. (e) Si spheroids in the α-Al matrix after T6 heat treatment. Image taken from Aboulkhair *et al.* (2016) [71]. 24

Figure 2.8: Al-Cu binary phase diagram 29

Figure 2.9: Classification of cellular solids. 31

Figure 2.10: Comparison of reported experimental (a) compressive strength and (b) modulus with predictions of the Gibson-Ashby model taken from Maconachie et al. [20]. 34

Figure 2.11: Illustration of Fourier's law 35

Figure 2.12: Heat transfer mechanisms contributing to the apparent thermal conductivity 37

Figure 2.13: Illustration of fin geometries: (a) rectangular, (b) trapezoidal, (d) offset strip, (e) louvred, (f) pin. Image based on Dewatwal *et al.* (2009) [132]. 42

Figure 2.14: Compilation of results of cellular material (a) friction factor and (b) Nusselt number, against Reynolds number taken from Gao and Sun (2014) [144]. 47

Figure 3.1: Illustration of the gyroid matrix and network phase definition and the effect of volume fraction. 53

Figure 3.2: Representation of lattice structures used in this thesis and their associated surface equations. 54

Figure 3.3: Realizer SLM50 LPBF machine, (a) outside (b) Inside chamber. 57

Figure 3.4: (a) Renishaw AM250; (b) inside chamber of Renishaw AM250 and AM400 LPBF machine chamber. 59

Figure 3.5: Renishaw AM400 reduced build volume environment. 61

Figure 3.6: Ti6Al4V powder (a) SE SEM image at X500 magnification, (b) Powder size distribution. 63

Figure 3.7: SE SEM images (×500) of the powder used in this thesis. 67

Figure 3.8: Build axis and orientation, represented in black the cross-sections examined for porosity and microstructure analysis. 69

Figure 3.9: (a) Tensile test specimen dimensions (in mm); (b) Machined tensile bars spray-painted with a speckle pattern for strain measurement. 74

Figure 4.1: (a) Schematic of the apparatus used to measure the thermal conductivity of LPBF specimens. (b) Close view of the test stack with the position of the temperature measurements. Z_i and T_i denote the blocks' height and the position of the thermocouples. 84

Figure 4.2: Thermal conductivity of brass reference block for apparatus validation. Error bars represent the measurement uncertainty according to 4.2.4. 86

Figure 4.3: Cubic specimen used for thermal conduction tests; gyroid matrix 5 mm cell size (a) 0.20 volume fraction, (b) 0.50 volume fraction, (c) 1.0 volume fraction... 87

Figure 4.4: Unit cell designs and illustration of a variation of number cell at a constant 0.2 volume fraction. 89

Figure 4.5: Specimen dimensions for forced convection heat transfer testing apparatus. 90

Figure 4.6: Schematic of the forced convection heat transfer apparatus (a) overall apparatus, (b) close view of the test chamber with the position of the pressure sensors P_i and thermocouples T_i, (c) Close view of the test stack with the position of the temperature measurements. 93

Figure 4.7: Part orientation and support structure for LPBF manufacture of (left) the lattice structures and (right) pin-fin specimens. 98

Figure 4.8: (a) CAD geometry for the pin-fin benchmark coupon with spanwise spacing S_S = 5.00 mm and streamwise spacing S_T = 3.90 mm, pin diameter D = 2.27 mm, and pin height H = 10 mm. (b) Pin-fin layout can be seen in isometric view (top and bottom skin removed for clarity). 99

Figure 5.1: (a)-(j): Optical micrographs of polished specimens after etching. Al-rich areas have lighter contrast and Si-rich regions have dark contrast. Black arrows show LPBF melt pool boundaries; (k)-(t): SE SEM images showing the microstructure of LPBF AlSi10Mg after different heat treatments. Si-rich areas are light grey features and Al-rich regions are darker regions. 105

Figure 5.2: Microstructure of LPBF gyroid lattice structure in: as-built condition (a), (b), (e) and (f); annealed condition, (c), (d), (g) and (h). Si-rich regions are light grey features and Al-rich areas have darker contrast. 106

Figure 5.3: Evolution of micro-hardness of AlSi10Mg after different heat treatments. 107

Figure 5.4: Thermal conductivity of AlSi10Mg after different heat treatments. Error bars represent measurement uncertainty as described in section 4.2.4. 108

Figure 5.5: Apparent thermal conductivity of AlSi10Mg gyroid lattice structures before and after annealing heat treatment. Error bars represent the measurement uncertainty. 109

Figure 5.6: Influence of the volume fraction of a gyroid matrix lattice structure on the apparent thermal conductivity normalised from bulk material properties. 113

Figure 5.7: Normalised apparent thermal conductivity against lattice cell size at 0.2 designed volume fraction for Ti6Al4V lattice specimens. Error bars are calculated from the measurements as described in 4.2.4. 116

Figure 5.8: Normalised apparent thermal conductivity against lattice cell size at 0.5 designed volume fraction for Ti6Al4V lattice specimens. Error bars are calculated from the measurements as described in 4.2.4. 117

Figure 5.9: Relative apparent thermal conductivity against actual volume fraction of lattice structures. Error bars are calculated from the measurements as described in section 4.2.4. 119

Figure 5.10: Cross-sectional representation of changes in wall thicknesses and internal free space across different unit cell sizes at a constant 0.2 volume fraction for the gyroid, diamond, and primitive matrix lattices. 125

Figure 6.1: Friction factor of pin-fin benchmark coupon against Reynolds number based on the pin diameter D and U_{max} compared to the existing literature for similar geometries. Error bars represent the measurement uncertainty. 135

Figure 6.2: Nusselt number of pin-fin benchmark coupon against Reynolds number based on the pin diameter and U_{max} along with existing literature for similar geometries. Error bars represent the measurement uncertainty. 136

Figure 6.3: View of 10 × 10 × 10 mm section with 5 mm unit cell size cut of unit cell under investigation in this chapter in ISOmetric and in FLOW Direction. Lattice specific surface area per unit volume S_v are reported along with the minimal cross-sectional area of the fluid domain in the flow direction for each lattice. 137

Figure 6.4: Pressure drop against mass flow rate (a) matrix and (b) network TPMS lattice structures along with the pin-fin benchmark coupon. Error bars represent the measurement uncertainty. Note the larger error bars for matrix 2.5 mm cell size for mass flow rate > 0.03 $kg \cdot s^{-1}$ are due to the use of a higher pressure sensor than for the rest of the measurements. 142

Figure 6.5: Pressure drop of TPMS lattice structures against mass flow rate and S_v 143

Figure 6.6: (a) Cross-sectional slices of the tested lattices for one unit cell, (b) change in flow area through the flow direction for one unit cell. 145

Figure 6.7: Pressure drop of TPMS lattice structures against the mass flow rate and A_{range}/C_s. 146

Figure 6.8: Modified heat transfer coefficient against mass flow rate at minimal cross-sectional area for (a) matrix and (b) network TPMS lattices along with the pin-fin benchmark coupon. Error bars represent measurement uncertainty. 149

Figure 6.9: Modified heat transfer coefficient of TPMS lattice structures against mass flow rate and S_v. 150

Figure 6.10: Modified heat transfer coefficient of TPMS lattice structures against mass flow rate and A_{range}/C_s. 150

Figure 6.11:Thermal performance of (a)-(b) matrix and (c)-(d) network phase lattice structures along with the pin-fin benchmark coupon. Error bars correspond to the measurement uncertainty. 153

Figure 7.1: Thin wall specimen schematic 160

Figure 7.2: Wall thicknesses for the tested process parameters. 161

Figure 7.3: Porosity of EN AW 2618 initial build based on AlSi10Mg parameters. 162

Figure 7.4: Illustration of the tested scan strategies. 163

Figure 7.5: Example of (a) macro-cracks indicated with solid black arrows for specimen with 2.5 $m \cdot s^{-1}$ laser scan speed, (b) micro-cracks indicated with dashed black arrows for 1.5 $m \cdot s^{-1}$ laser scan speed. 165

Figure 7.6: EN AW 2618 microstructure in (a) as-built condition, (b) after stress-relief heat treatment. 168

Figure 7.7: A20X LPBF parameters and relative densities achieved for initial parameter optimisation. 170

Figure 7.8: Optical micrograph of A20X porosity in initial parameter optimisation (a) P1, (b) E1. 171

Figure 7.9: XRD patterns of A20X powder feedstock and as-built LPBF specimen. The Miller indices represent α-Al. 173

Figure 7.10: Optical micrographs of A20X cross-sections in the *xy*-plane showing (a) the scan tracks, (b) the ultrafine microstructure at high magnification. 173

Figure 7.11: SE SEM images of etched A20X in as-built condition for (a) *xy*-plane and (b) *yz*-plane. 175

Figure 7.12: SE SEM image with EDS elemental mapping 175

Figure 7.13: XRD patterns of A20X after SHT at 520 °C for various soaking time. 176

Figure 7.14: SE SEM images of LPBF A20X microstructure in the *xy*-plane: (a) as-built condition, after SHT at 520 °Cfor (c) 0.5 h, (e) 1 h, (g) 2 h, and (i) after T7 treatment; and in the *yz*-plane (b) as-built condition, after SHT for (d) 0.5 h, (f) 1 h, (h) 2 h, and (j) after T7 heat treatment. 177

Figure 7.15: Hardness and relative density of LPBFed A20X in as-built, annealed at 300 °C for 2 h, solutionised at 520 °C with varying soaking time and after a 2 h SHT followed by varying ageing duration. The error bars represent the standard deviation. 179

Figure 7.16: Example of A20X tensile behaviour of as-built and T7 states in build and transverse directions. 181

Abbreviations

1D, 2D, 3D	One, two, three dimensional
AA	Artificial ageing (artificially aged)
AM	Additive manufacturing
ASTM	American society for testing materials
BSE	Backscatter electron
CAD	Computer-aided design
CFD	Computer fluid dynamics
CHX	Compact heat exchangers
DAQ	Data acquisition
DED	Directed energy deposition
DfAM	Design for additive manufacturing
EDM	Electrical discharge machine (machining)
EDS	Energy dispersive x-ray spectroscopy
FLAC	Functional lattices for automotive components
GP	Guinier-Preston
HDHC	High drawn high conductivity
HV	Vickers hardness
ICDD	International Centre for Diffraction Data
ISO	International organisation for standardisation
LALLS	Low angle laser light scattering
LFM	Lattice-frame material
LPBF	Laser powder bed fusion
PBF	Powder bed fusion

PCB	Printed circuit board
PID	Proportional-integral-derivative
PLC	Portevin-Le Chatelier
PTC	Positive temperature controller
RAM	Reactive additive manufacturing
RMSE	Root mean squared error
SAED	Selected area electron diffraction
SE	Secondary electron
SEM	Scanning electron microscope (microscopy)
SHT	Solution heat treatment (treated)
SLM	Selective laser melting
SLS	Selective laser sintering
SSE	Sum of squared error
SSSS	Supersaturated solid solution
STL	Standard tessellation language file format
TEM	Transmission electron microscopy
TPMS	Triply periodic minimal surface
UTS	Ultimate tensile strength
XRD	X-ray diffraction
YPE	Yield-point elongation

Nomenclature

α	Thermal diffusivity
ΔP	Pressure drop
ΔT	Temperature difference
ε	Pore fraction
κ	Electrical conductivity
λ	Thermal conductivity
λ_{air}	Air thermal conductivity
λ_M	Thermal conductivity of reference block
$\lambda_{specimen}$	Thermal conductivity of the measured specimen
λ_s	Thermal conductivity of bulk material
λ_p	Thermal conductivity of pore material
λ^*	Apparent thermal conductivity of lattice structure
λ_c^*	Conduction within the cells of the lattice structure
λ_g^*	Convection though the gas within the lattice structure
λ_r^*	Radiation through the cell walls and across the cell voids of the lattice
λ_s^*	Conduction through the solid of lattice structure
λ^*/λ_s	Relative apparent thermal conductivity of lattice structure
μ_{air}	Air dynamic viscosity
ν_{air}	Air kinematic viscosity
υ	Degree of freedom
ρ_{air}	Air density
ρ_s	Density of bulk material
ρ^*	Density of lattice structure

ρ^*/ρ_s	Volume fraction of lattice structure
σ_s	Strength of bulk material
σ^*	Strength of lattice structure
σ^*/σ_s	Relative strength
χ^2	Chi-square statistic
A	Heat transfer surface area
A_{base}	Area of the base specimen
A_{min}	Minimal cross-sectional area
A_{max}	Maximal cross-sectional area
A_{range}	Difference between minimal and maximal cross-sectional area
c_p	Specific heat capacity
C_s	Cell size
D	Pin diameter
D_h	Hydraulic diameter
f	Darcy friction factor
f_D	Darcy friction factor based on the pin diameter
h	Heat transfer coefficient
L	Specimen length
L_c	Characteristic length
L_N	Lorenz number
$\dot{m}$	Mass flow rate
Nu	Nusselt number
Nu_D	Nusselt number based on the pin diameter
P	Laser power
$\bar{P}$	Mean air pressure across the specimen

q	Heat flux
R	Specific gas constant
Re	Reynolds number
$Re_{D,Umax}$	Reynolds based on the pin diameter and air maximum velocity U_{max}
$Rp_{0.2\%}$	0.2 % offset yield strength
s_v	Scanning speed
S_S	Pin spanwise spacing
S_T	Pin streamwise spacing
S_v	Specific surface area per unit volume
T	Temperature
T_∞	Temperature of the oncoming fluid
$\bar{T}$	Mean air temperature across the specimen
T_{base}	Temperature at the base of the specimen
T_{body}	Surface temperature of the body
T_{in}	Temperature of the air before passing through the test specimen
T_{out}	Temperature of the air after passing through the test specimen
U	Air velocity
U_{flow}	Mean air velocity
U_{max}	Maximum air velocity calculated at A_{min}
$wt.\%$	Weight percent
$\bar{x}$	Arithmetic mean average
$\%diff$	Percentage difference

1 Introduction

The aerospace industry is constantly trying to improve component efficiency, in addition to reducing the weight and enhancing quality. In such high-value industries, heat transfer devices can challenge this due to large packaging or by limiting the maximal working temperature, thus reducing the efficiency.

They have numerous applications from cooling printed circuit boards (PCB) to dissipating the heat of turbine blades inside the engine. Heat exchanger designs and geometries are limited by constraints from conventional manufacturing techniques. These techniques can also have a negative effect on their lifespan with the appearance of premature cracks and leaks due to, for instance, bad joining.

In this thesis, an additive manufacturing (AM) technique, laser powder bed fusion (LPBF), is presented as a novel technique to alleviate conventional design drawbacks. For example, LPBF allows designs with high surface area to volume ratios to be manufactured, which would have been challenging, if not impossible, with traditional techniques such as casting, extrusion, etc. However, the narrow list of suitable materials for LPBF limits its acceptance. This thesis will also investigate the development of a high-strength aluminium alloy to address this issue. These could result in lighter and better heat transfer and efficiency, which can allow the development of more compact heat exchangers (CHX) and reduce the amount of material waste and greenhouse gases.

1.1 Aim, objectives, and methodology

The overall aim of this thesis is to demonstrate how more efficient and lightweight heat exchangers can be made by AM , increasing fuel efficiency and reducing CO_2 emissions within an aerospace context. This will take advantage of the design freedom that AM enables; lattice structures with their high surface area to volume ratio and their easily

controllable properties are investigated to achieve this aim. This research also aims to address the lack of measured thermal properties of parts manufactured by LPBF. The materials studied are lightweight aerospace alloys: Ti6Al4V titanium alloy, EN AW 2618 and A20X and AlSi10Mg aluminium alloys.

This research has four objectives:

- To determine the thermal conductivity of LPBF AlSi10Mg alloy to understand the effect of post-processing heat treatments and to improve this property and thermal exchange.
- To understand how lattice structures may be used to control the thermal conductivity of components made by LPBF to enable tailored and more efficient components.
- To determine the thermal performance of lattice structures under forced convective heat transfer and compare them to conventional design. This will help designers to build analytical models and take full advantage of lattice structures for thermal management.
- To determine the process parameters for high-strength aluminium alloy with good thermal conductivity for the LPBF process to address the shortcomings of AlSi10Mg such as its low mechanical strength.

1.2 Heat exchangers

Heat exchangers transfer heat from one medium to another. They do so by directly or indirectly exposing a warmer medium to a cooler medium. These media may be solid, liquid, gas or a combination of them. They can be used either for cooling or heating, however, they are dominantly used to prevent temperature-sensitive components and

equipment from overheating. They can adopt various shapes (see **Figure 1.1**) and use different fluids but are usually grouped in the following categories:

- Shell and Tubes
- Air Cooled
- Plate and Frame
- Others

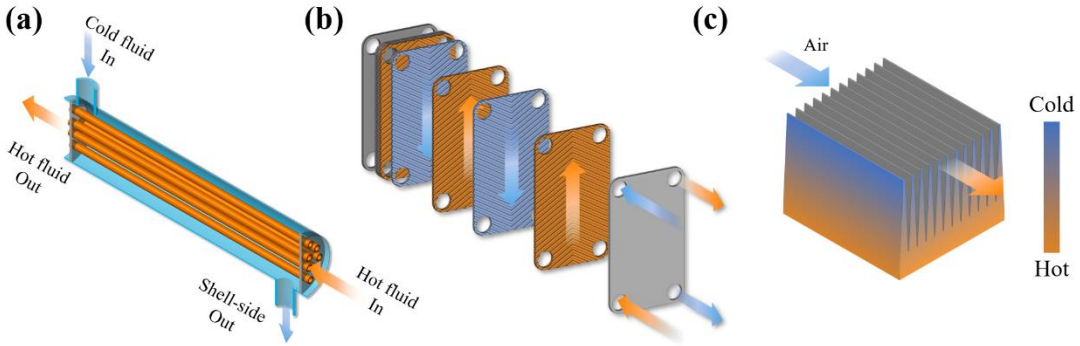


Figure 1.1: Heat exchangers: (a) shell and tube, (b) plates, (c) heatsink.

The technology used today in designing and manufacturing tube heat exchangers comes from the research and development of the 1960s, such as the work of Kays and London [1]. Since then, improvements in design, materials, manufacturing techniques and performance metrics have been limited [2]. New brazing techniques have been introduced, allowing the development of smaller and more compact heat exchangers [3]. More recently, AM has disrupted the manufacturing industry by overcoming historical limitations to allow the fabrication of new structures. However, AM is a relatively new area where two main challenges need to be overcome before wide adoption for heat transfer applications. Firstly, the development of a wider variety of materials with good thermal properties for AM needs to be undertaken. These have generally been proven to be difficult to manufacture with laser-based AM processes [4]. For instance, aluminium and its alloys have high reflectivity at commercial laser wavelengths (e.g. 1064 nm), high

thermal conductivity and high thermal expansion coefficients, which leads to high residual stresses and therefore cracking. Some researchers have successfully manufactured high strength aluminium alloys, but usually by altering the chemical composition, thus reducing its strength compared to the initial alloy. High thermal conductivity alloys are necessary for heat exchangers since this property intrinsically determines their efficacy at dissipating heat. This research aims to manufacture high strength aluminium alloys with good thermal conductivity for multifunctional heat exchangers by adjusting AM process parameters and not the composition. Properties of AM parts can be significantly different compared to those made by conventional methods. Therefore, these properties need to be determined precisely for each new material processed by AM. There are relatively few published works on the thermal conductivity of alloys processed by LPBF. Some machine manufacturers published measured thermal conductivities of printed parts [5], however, no details were given on the method used, the specimen sizes and microstructures. This is an area this thesis aims to address.

Secondly, most heat exchanger designs are based on 2D profiles extruded into a 3D shape. The performance of these heat exchangers can be easily predicted because general analytical solutions exist. They can also be manufactured easily by conventional processes. Oppositely, lattice (or cellular) structures, 3D geometries with complex shapes and interpenetrating channels pose significant challenges for design, manufacture and performance prediction. The progress of computer-aided design (CAD) and the development of computational fluid dynamics (CFD) have helped to design and analyse new geometries. However, CFD is highly computationally demanding and relies on initial experimental data to validate numerical solutions. This means experimental data is necessary before being able to effectively model and simulate these structures. This will also be a focus of this research. Some researchers are already investigating AM and laser powder bed fusion (LPBF) processes to fabricate lattice structures for use in heat

exchangers [6], but those are usually limited to strut-based lattice structures, which are not fully optimised for AM and LPBF. Before progressing, a portrait of additive manufacturing, how it works and how it affects the properties of manufactured parts needs to be depicted.

1.3 Additive manufacturing and laser powder bed fusion

Additive Manufacturing (AM) or often called '3D printing' refers to a group of processes in which, instead of removing material from an initial stock item with various tooling techniques (subtractive manufacturing), the material is 'added', layer by layer according to a 3D computer model. As a result, additive manufacturing processes allow manufacturing parts that could not be otherwise made using subtractive techniques or forming techniques such as casting. It is often said to have total freedom of design, but there are still some limitations, which are very distinct from conventional manufacturing. An illustration of parts made by AM techniques is shown in **Figure 1.2**.

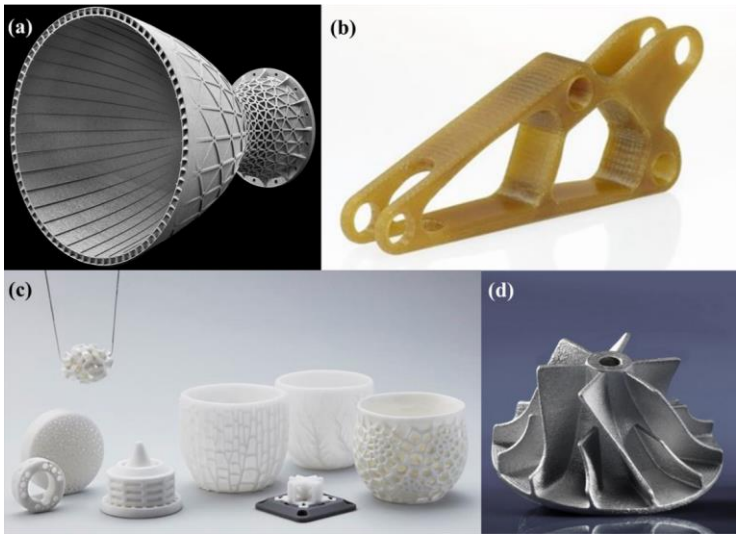


Figure 1.2: Illustration of design freedom offered by additive manufacturing processes: (a) rocket chamber by laser powder bed fusion (LPBF) [7], (b) bracket by fused deposition modelling (FDM) [8], (c) vases by stereolithography (SLA) [9], (d) turbine wheel by binder jet [10].

The American Society for Testing and Materials (ASTM) and the International Organisation for Standardisation (ISO) distinguishes seven different processes in the standard 52900:2015(E) [11]. These are:

- Binder jetting
- Directed energy deposition (DED)
- Material extrusion
- Material jetting
- Powder bed fusion (PBF)
- Sheet lamination
- Vat photopolymerisation

These seven processes can be subdivided into a myriad of techniques and produce polymers, metal, ceramics and composites materials. Most metal AM parts are produced by DED and PBF processes. PBF groups two processes that differ by the energy source they use to melt the powder, either a focused electron beam or laser source. The work conducted for this thesis focuses on laser powder bed fusion (LPBF).

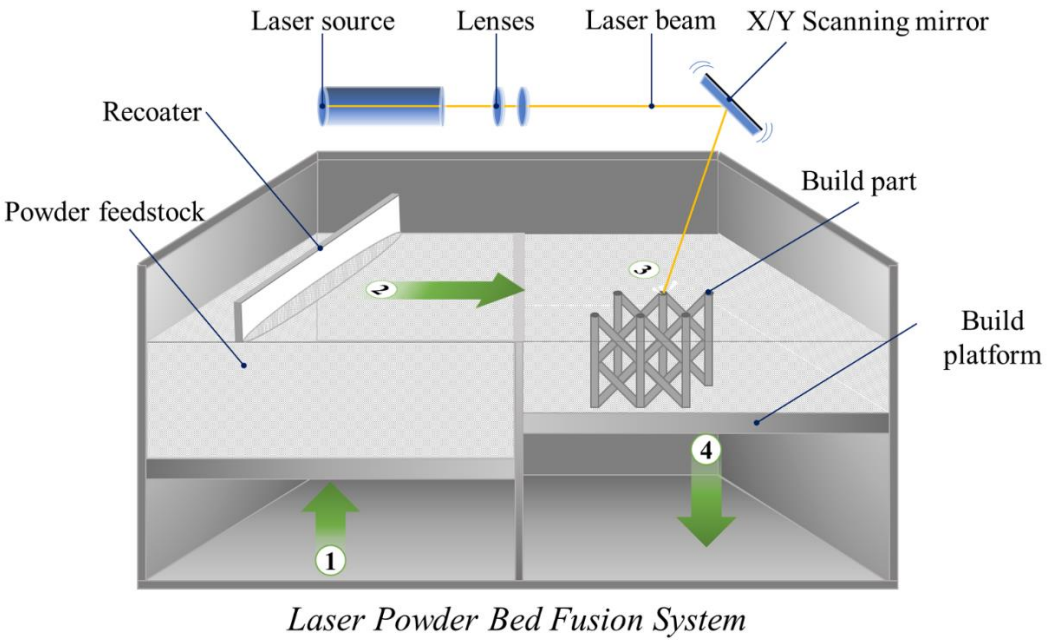


Figure 1.3: Laser Powder Bed Fusion machine schematic.

An illustration of LPBF process is shown in **Figure 1.3**. A thin layer of metal powder, typically between 15 μm and 100 μm, is spread flat across a build platform that is usually made of similar material to the powder. The spread layer of powder is then selectively irradiated by a focused laser beam (with a spot size diameter generally between 10 μm and 200 μm) until melting occurs at the focused points and in the previously solidified layers. The build platform is then lowered, a new layer of powder is spread, and the process is repeated, layer by layer, until the full height of the part is achieved. The build chamber is kept in an inert environment (nearly oxygen-free), by filling it with nitrogen or argon gas, to prevent any hazard by melting the powder, and to minimise oxygen pickup and oxide formation in the melt-pool.

The build platform is often maintained at high temperature to reduce stresses resulting from the rapid solidification of the melt area. Despite having a heated build platform, large thermal gradients during the LPBF process, from melting and re-melting layers, can promote the building up of significant residual stresses, depending on material properties, geometry and laser parameters [12–14]. Support structures are used to prevent distortion during the manufacturing process, anchoring firmly the component(s) to the build platform. However, high residual stresses can exceed the material strength and induce cracking in the supports or within the part, leading to a potential failure.

LPBF technology can produce near net shape fully dense parts and has attracted several industries with high-value components and low production volumes such as aerospace, healthcare and more recently high-end automotive. One of the many potential benefits of LPBF is the ability to increase component complexity through new design rules without incurring significant time or cost penalties [15]. Traditionally, complexity is very expensive whether in manufacturing time, material usage or waste. Despite leveraging new complexity freedom, the limited understanding of how the LPBF process affects the component properties have restrained its adoption. Industries are mainly focused on

copying pre-existing designs from their catalogue with AM, despite, newly complex features uniquely possible with AM such as lattice structures.

1.4 Design for additive manufacturing

AM provides a range of processes with new possibilities and constraints for designers to create, adapt, and tailored components where the forms follow the function. Principles and design practices have been developed and represent a maturing discipline called design for additive manufacturing (DfAM). These design practices include performance improvement by creating complex internal geometry, reduction of part assembly counts by the consolidation of multiple parts into one, or weight reduction by removing excess material with the help of topology optimisation software. DfAM implementation can follow four levels of approaches: (1) recreate an existing design with no modification and manufacture it using the AM process of choice; (2) redesign a part to reduce weight and/or improve part performance; (3) create a multifunctional part by combining multiple parts; (4) redesign the assembly based on design requirements and first principles. Each level has its pros and cons and requires more resources as it progresses to a higher level.

Among the tools of DfAM, topology optimisation and latticing have emerged as the two major lightweight strategies [16–19], best exploiting the AM design freedom. Lattice structures, a form of cellular material, are three-dimensional and spatially ordered open-cell structures comprising a repeating unit cell. They extend the single-value properties of solids, widening the field of possibilities in terms of stiffness, strength, thermal conductivity or thermal isolation, gas permeability as well as acoustic absorption. Thus, they exhibit low density, and therefore low mass, making them good candidates for lightweight structures with high stiffness-to-weight ratios, both desirable qualities for the aerospace industry as illustrated in **Figure 1.4**. They have been used mostly for space-filling but they have more potential owing to their tailorable properties through several

features of their design (e.g. cell size, volume fraction, unit cell design). For these reasons, lattice structures are often depicted as the next step change in enhancing component performance [20] and multifunctional components [21]; however, little research on these structures has been done.

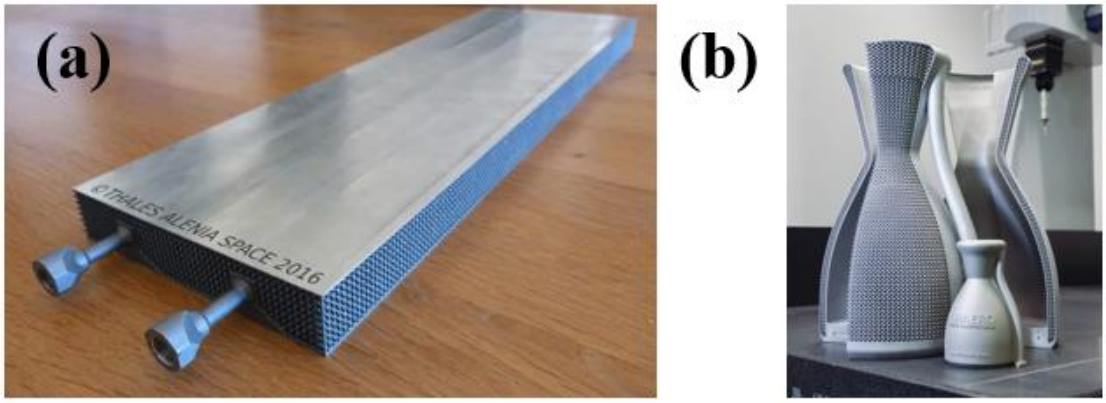


Figure 1.4: (a) Satellite component from Thales Alenia Space [22], (b) Collaboration between Betatype and Amaero for a rocket chamber [23].

The combination of DfAM with lattice structures, LPBF, and characterised AM materials could potentially transform how heat exchangers and thermal management are designed. Generation of heat transfer devices incorporating lattice structures would be impossible to manufacture using conventional methods. Studies have been performed to investigate the thermal properties of LPBF structures [24], but no studies have been performed to establish the dependency of lattice parameters on thermal performance. This thesis helps to establish a baseline and encourages the development and adoption of LPBF lattice structures for thermal components.

1.5 Challenges addressed in this research

Before heat transfer components (with or without lattice structures) made by LPBF will be broadly adopted, two research challenges need to be tackled.

First, highly thermally conductive materials for LPBF need to be developed. The intrinsic nature of the LPBF process limits the use of conventionally employed Al and Cu alloys, so bespoke alloys need to be designed to address this issue. This research investigates the processability of a high strength and highly conductive conventional aluminium alloy, EN AW 2618, and a bespoke aluminium alloy for AM, A20X, developed by Aeromet International Ltd. Only a limited number of high-strength aluminium alloys have been reported in the AM literature and this thesis contributes to broadening the material selection. Materials made with LPBF exhibit a distinctive microstructure giving unique properties. Despite extensive studies on AlSi10Mg aluminium alloy processed by LPBF, no characterisation of the thermal properties of this alloy have been accomplished. Effects of the unique microstructure on the thermal conductivity of LPBF material with respect to the build orientation and post-processing heat treatments are reported in this work.

Secondly, the research community focuses mainly on understanding the mechanical properties of lattice structures. However, how lattice structures affect thermal properties has received little to no attention. This work fills this gap of knowledge, by first investigating the thermal conductivity of triply periodic minimal surfaces (TPMS) lattice structures manufactured by LPBF. Forced convection heat transfer performance of TPMS lattice structures has not been reported in the literature, and only a small amount of data is available for strut-based lattices which are not made by AM process. This thesis examines lattice structures in terms of pressure drop, heat transfer, and overall thermal performance comparing them to conventional pin-fin geometry and proposes guidelines to use lattice structures in heat transfer applications.

1.6 Thesis outline

Chapter 1: Aims and objectives of this thesis. Also, an overview of heat exchangers, additive manufacturing, laser powder bed fusion, lattice structures and design for additive manufacturing.

Chapter 2: A literature review on the LPBF process state of the art, AlSi10Mg and high strength aluminium alloys processed by LPBF, lattice structures, their thermal conductivity, and their use in forced convection heat transfer.

Chapter 3: A comprehensive description of all the general experimental methods and materials characterisation processes used in this thesis.

Chapter 4: A description of the apparatuses and methods developed in this thesis for the thermal characterisation of LPBF components.

Chapter 7: High-strength aluminium alloy development for laser powder bed fusion.

Chapter 5: Thermal conductivity of materials and lattice structures manufactured by LPBF.

Chapter 6: Forced convection heat transfer of lattices structures produced by LPBF.

Chapter 7: A general conclusion on the previous chapters' results and their implications, demonstrating how this research achieved its aims and objectives including the contribution to the research community and recommendations for future work.

2 Literature Review

2.1 Introduction

This chapter defines the scope of the work presented in this thesis by identifying research challenges and gaps. A description of LPBF and the processing of aluminium alloys along with a description of the unique microstructures produced by LPBF will be given. Thermal conductivity and forced convection heat transfer characterisation of LPBF parts and lattice structures will be reviewed along with a description of heat transfer mechanisms.

2.2 Laser Powder Bed Fusion

LPBF creates layer by layer parts from a powder bed using a laser as an external energy source to sinter or melt the powder particles together according to CAD design. LPBF can be classified into two categories based on the amount of energy brought to melt the powder feedstock partially or fully. In the former, the term selective laser sintering (SLS) is usually preferred. For metals, materials considered weldable are considered manufacturable with LPBF since it is essentially a powder-based micro-laser welding process. Melting the powder allows achievement of greater mechanical properties than sinter-based processes [25] and the resulting parts exhibit properties close to or superior to that of wrought or cast material [26,27].

The LPBF process offers design freedom where component complexity does not incur significant time or cost penalties [15]. Machines have a wide range of build dimensions but are typically in a cubic volume of 250 mm^3. Bigger machines exist but have been tailored fit for specific applications and are not commercially available. This limits the manufacturable size of heat exchangers. However, LPBF can manufacture finely detailed

structures whose size mainly depends on the laser spot size and layer thickness [28,29]. The real manufacturing resolution is often higher than the theoretical value due to excessive power concentration over a small area leading to powder sintering [29] and usually require fine-tuning of parameters [30]. Also, powder removal from parts with very thin cavities can be complicated and could necessitate exit hole incorporation to allow the powder to be removed effectively. However, these exit holes will require extra post-processing work to close them after the de-powdering process is completed.

2.2.1 Process parameters overview

Despite the seeming simplicity of LPBF, it is a complex process involving numerous parameters that need to be characterised and controlled to achieve good quality, defect-free, and repeatable parts. Some of the most influential parameters affecting the quality of LPBF builds are illustrated in **Figure 2.1**.

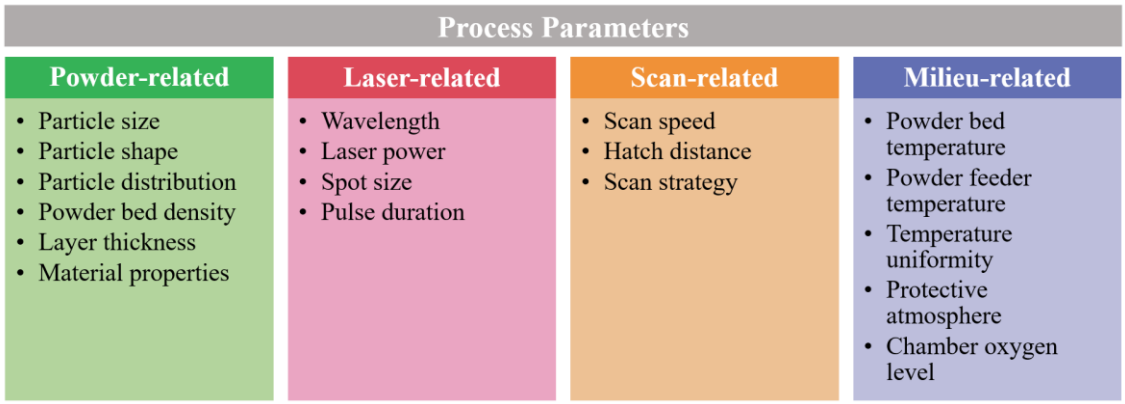


Figure 2.1: Most prominent parameters on LPBF builds based on Aboulkhair *et al.* (2014) [31].

Most studies focus on laser and scan related properties to achieve the manufacture of high quality parts such as laser power, layer thickness, hatch distance, scan speed, and scan strategy. These parameters are illustrated in **Figure 2.2** and **Figure 2.3**. The laser power controls the size of the melt pool and the continuity of the scan track, insufficient power

will lead to partial melting and incomplete filling of the melt pool during solidification, creating defects [32]. Also, excessive laser power can change the welding mode from conduction mode to keyhole [33]. Keyhole formations occur by the vaporisation of the surface material, promoting the formation of gas bubbles that can remain trapped inside the melt pool and creating defects in the solidified material as illustrated in **Figure 2.4**. Increasing the laser energy also promotes the Marangoni effect, therefore increasing the probability of dragging gases towards the bottom of the melt pool [34]. Excessive laser energy can also vaporise elements with low boiling points, leading to defects and changes in chemical composition [35].

Laser scan speed is defined by the product of exposure time and point distance, the lower the speed, the more energy is delivered to the powder bed per unit time and the larger the scan track. Slower speed also hold the material in a molten state for longer, slowing the solidification rate, affecting the microstructure. The hatch distance defines the distance between each scan track and is set to provide some overlap with the previous track to assure good metallurgical bonding. However, excessive overlap results in significant remelting of the same volume, thus a longer manufacturing time. The layer thickness is set based on the melt pool depth for good interlayer bonding. The layer thickness controls the precision and minimal feature size manufacturable in the build direction but it should be large enough to reduce the manufacturing time. The powder size distribution also affects the choice of layer thickness to achieve good layer compaction. It was shown by Liu *et al.* [36] that powder distribution can also impact the porosity, mechanical properties and surface finish of LPBF parts. Typical layer thicknesses used for LPBF are between 25 μm and 60 μm. The scan strategy describes the laser path to irradiate the powder according to the object to manufacture. Some of the most used scan strategies are reported in **Figure 2.3**. Additional interlayer parameters, such as rotation between each layer is used to limit the alignment of defects during the manufacture. Scan strategies are

used to minimise defects but can also be used to control the microstructure. Thijs et *al.* [37] demonstrate this possibility by tailoring the crystallographic texture in LPBF AlSi10Mg. Scan strategy plays also an important role in the formation of residual stress and will be detailed in **section 2.2.4**.

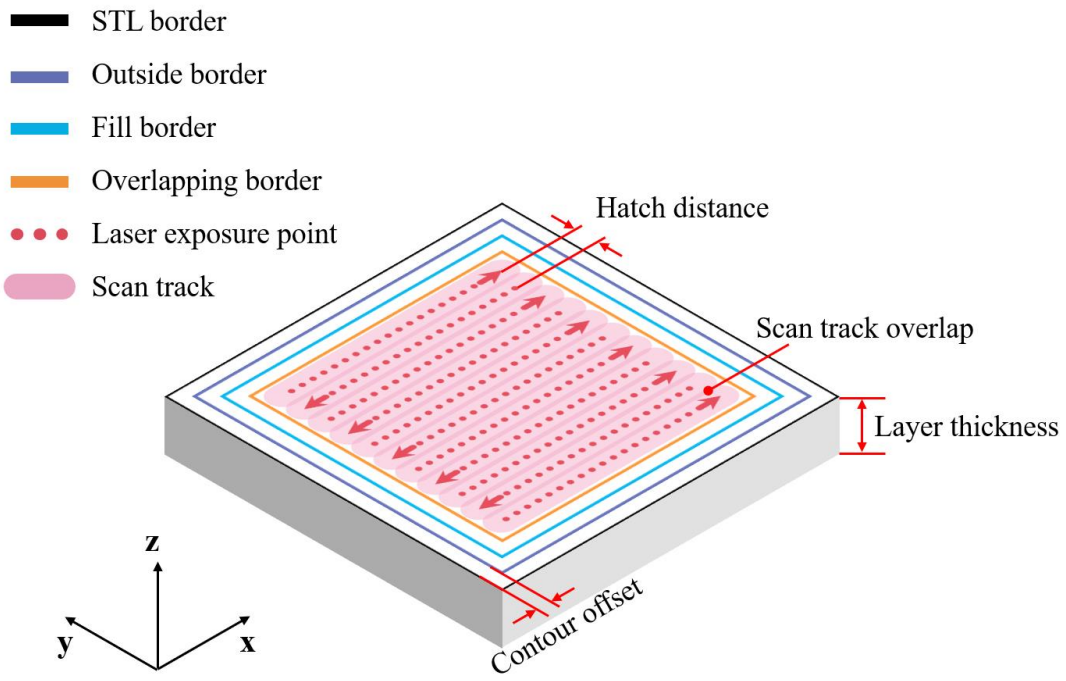


Figure 2.2: Illustration of LPBF scan parameters with a meander scan strategy.

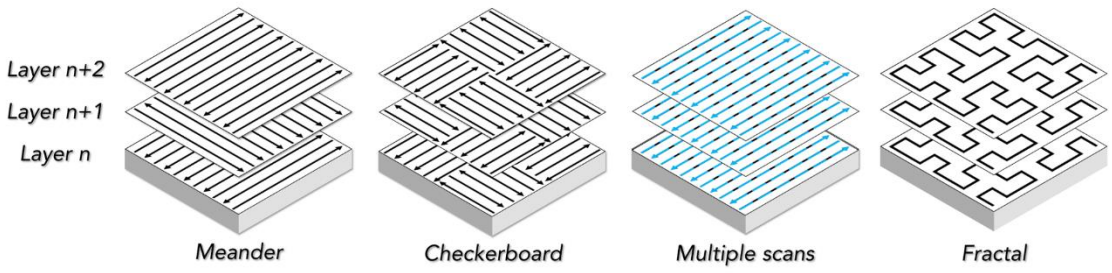


Figure 2.3: Examples of scan strategy used in LPBF with a 90° rotation between each layer. The fractal is illustrated by a 2nd order Hilbert curve.

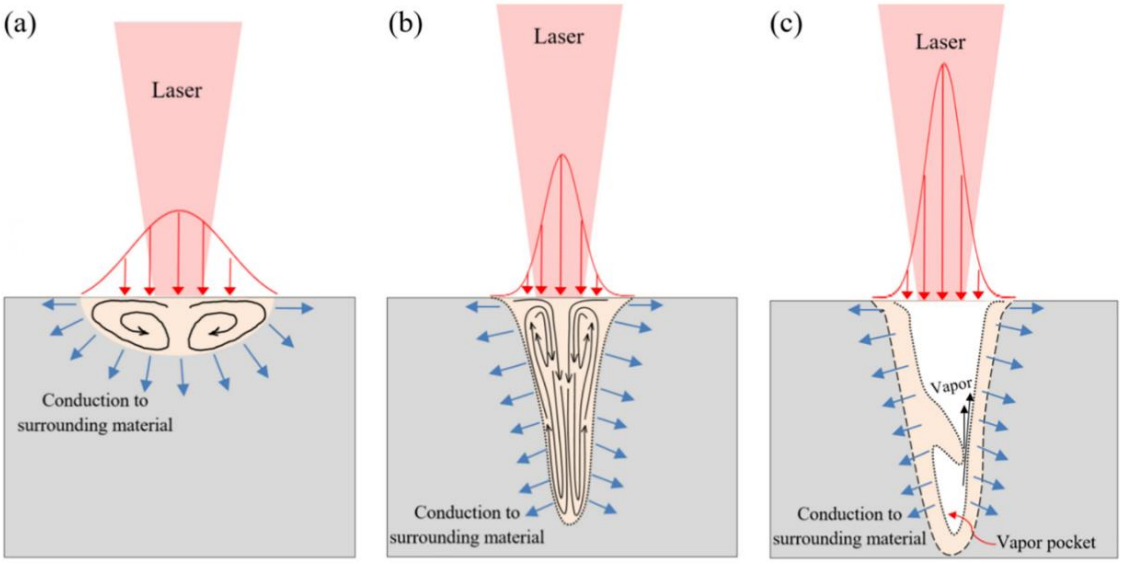


Figure 2.4: Melt pool formation mechanisms (a) conduction mode, (b) keyhole mode, (c) keyhole with porosity formation taken from Balbaa *et al.* (2020) [38].

2.2.2 Thermal conductivity of LPBF materials

The thermal conductivity of pure metals and alloys used of interest for LPBF along with their densities are reported in **Table 2.1**. In thermal applications, a high thermal conductivity is desired to maximise the heat transfer for passive cooling (i.e. heatsinks). However, the mass of flying components plays usually a more important role in materials selection. Based on thermal conductivity as listed in **Table 2.1**, those with the highest thermal conductivity are silver and copper-based materials. However, silver's high costs make it prohibitive to use in thermal components and copper alloys with their high densities have usually limited usage. Furthermore, copper has been proven to be very difficult to manufacture with commercial LPBF machines equipped with the standard 1064 nm wavelength laser [39]. The third column in the table consists of the ratio of thermal conductivity to density, where a higher ratio is more beneficial for lightweight applications which is an important design requirement for aerospace and automotive. This ratio highlights the advantage of aluminium over pure copper and silver, as it is over 70 % lighter than those materials. Furthermore, copper has a significantly higher cost than

aluminium. These reasons explain why aluminium alloys are widely used in thermal applications for aerospace.

Table 2.1: Thermal conductivities and densities of different metals at atmospheric pressure and room temperature (25 °C).

Material	λ **(W·m^{-1}·K^{-1})**	ρ **(g·cm^{-3})**	**λ/ρ**
Pure copper [40]	398	8.96	44
Pure silver [40]	428	10.5	41
Pure aluminium [40]	247	2.70	101
AlSi10Mg cast [41]	140 – 170	2.67	52 – 64
EN AW AA2618 (T61) [42]	147	2.6 – 2.8	52 – 56
Stainless steel 304 [43]	16.2	8	2
Ti6Al4V [42]	6.6 – 6.8	4.43	≈2

2.2.3 Aluminium alloys

Aluminium and its alloys have been proven to be challenging to be manufactured with LPBF. Firstly, its high thermal conductivity causes rapid heat transfer away from the melt pool through the previously solidified material. Also, its high reflectivity [44] at the laser wavelength commonly used in LPBF machines (1064 nm) can lead to insufficient melting, resulting in incomplete filling of the melt pool during solidification and porosity in the final component. Recent developments from machine manufacturers have seen laser power increase from 200 W to more than 1 kW. With higher laser power, the energy absorption of Al drastically increases as demonstrated by Trapp *et al.* [44] with discs made of aluminium alloy 1100. The higher available power has allowed the manufacture of high density parts made of pure aluminium as reported by Kimura and Nakamoto using

an EOS M280 equipped with a 400 W Yb laser [45]. Secondly, the formation of oxide films on previously melted layers disrupts the melt pool and reduces wettability. These oxides can create regions of weakness within the manufactured component [46] and lead to premature rupture.

LPBF of aluminium alloys is of interest to the aerospace industry with a major emphasis on high-strength aluminium alloys with good ductility such as Al-Cu (2xxx series), Al-Mg (5xxx series), Al-Mg-Si (6xxx series), and Al-Zn-Mg (7xxx series). These alloys can exhibit strengths exceeding 400 MPa with an elongation at break over 10 %. The development of these alloys is key for wider adoption of LPBF in aerospace where, for instance, aluminium alloys represent up to 81% of materials used in a Boeing 747 [47]. However, these alloys suffer from solidification cracking during the LPBF manufacturing process [35,48–51]. This arises when the liquid in the melt pool cannot accommodate the solidification shrinkage. Characteristics such as the cooling rate, solidification range between the liquidus and solidus temperatures, shrinkage factor, thermal expansion coefficient, and the fluidity of the melt play an important role in the hot cracking susceptibility [48]. Furthermore, the low vaporisation temperature of some alloying elements (e.g. Mg, Zn) and the high energy of the laser can modify the chemical composition in the alloy which can also increase the hot cracking susceptibility [35].

Casting aluminium alloys are less prone to solidification cracking, and therefore have been more studied, with AlSi10Mg receiving most of the attention due to its excellent processability with LPBF. This cast alloy presents a high content of Si, reducing the melting point, increasing the fluidity of the melt [52–54], and most importantly, decreases shrinkage during solidification preventing cracks to occur [35]. Large additions of Si in Al also increase the tensile strength but at the cost of a drastic reduction in the elongation at break [53]. A wide range of properties for the Al-Si binary system have been reported with a yield strength around 200 MPa and low elongation at break, typically around

4 % [51]. These low values limit the use of Al-Si alloys for mechanical applications. The presence of Mg in AlSi10Mg induces age-hardening through Mg-Si precipitation, thus improving its mechanical properties [55]. This is achieved by solution heat treatment followed by artificial ageing to finely control the size and distribution of precipitates. Despite the wide investigation of AlSi10Mg, there has not been any focus on the thermal conductivity and how this is affected by the microstructure generated by LPBF. The focus has generally involved reporting the parameter optimisation process, the microstructure, mechanical properties, and how heat treatment affects both. Kimura *et al*. [53] reported the effect of varying content of Si in Al-xSi binary alloy on mechanical properties and thermal conductivity. It was the highest for pure Al then decreases gradually as Si content increases. They determined the thermal conductivity, by a laser flash method, in both build and transverse direction, using small LPBF manufactured discs (10 ×3.5 mm). However, they did not report the effect of the build orientation and the microstructure on the measured thermal conductivity. The thermal conductivity of other materials made by LPBF has not been investigated which can be attributed to the main factor driving their use, which is the fabrication of lightweight components. Indeed, materials often processed by LPBF like Ti and Steel, have low thermal conductivity and are mainly used for mechanical applications.

2.2.3.1 LPBF microstructure

AlSi10Mg was among the first alloys used in LPBF, therefore it has been widely investigated and numerous studies have used this material to understand the physical processes occurring in LPBF. AlSi10Mg is one of the materials used in this thesis and will be used to present the main mechanisms affecting the material microstructure produced by LPBF.

The thermal history during the LPBF process controls the microstructure of the manufactured part and leads to thermal gradients along the build direction. This is due to the higher thermal conductivity of the melted material over the unmelted powder which acts as a thermal insulator [56]. The layer-by-layer nature of the process means the material is also re-melted several times due to the penetration of the laser beam to ensure good metallurgical bonding between layers and to avoid delamination. An illustration of the thermal history of a manufactured region from Luo *et al.* [57] is reported in **Figure 2.5**. The initial peak in the zoomed part corresponds to the laser approaching the point where the temperature is measured. It is then followed by a much steeper peak that corresponds to the laser scanning the measurement point. The subsequent diminishing peaks correspond to the conducted heat from the laser source scanning the neighbouring tracks. It should be noted that the double-curved dash lines correspond to the y-axis break to improve the readability of the figure. The measured point experiences similar heating and cooling cycles with the successive printed layer with decreasing peak intensity. Consequently, the temperature oscillates around the melting point of the material due to the successive melting and solidification of the successive layer and oscillates toward an intermediate temperature, usually the build plate temperature, until the end of the manufacturing process. This hold in temperature can promote the formation of secondary and tertiary phases. Aversa *et al.* [58] demonstrated the possibility to use it as in-situ ageing heat treatment.

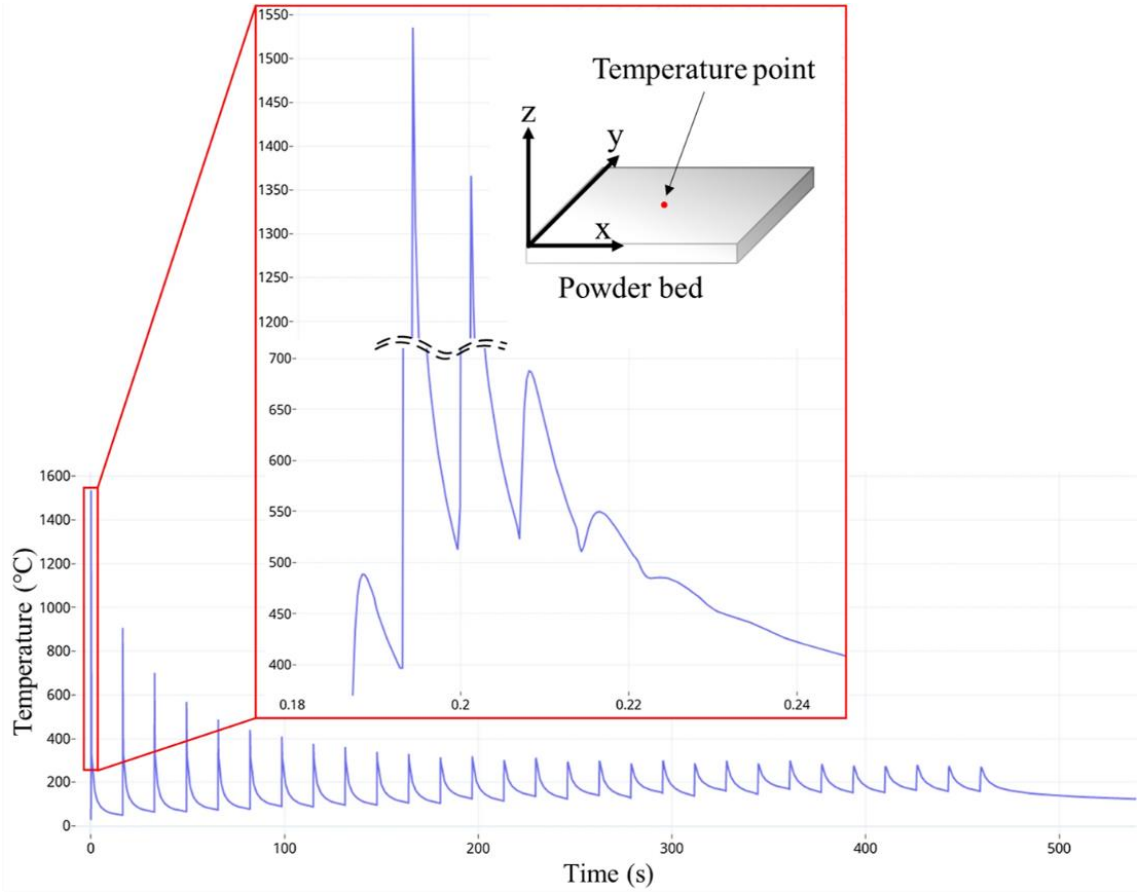


Figure 2.5: Typical temperature history of specimen manufactured by LPBF taken from Luo *et al* (2020) [57].

Melt pool cooling occurs at very high rates (10^6 K·s^{-1} [56]), which increases with laser power and scan speed [59] and produces ultrafine microstructures [60] with possible metastable phases [61]. Rapid solidification has been intensively investigated due to several advantages such as a refined microstructure, extended solid solubility, increased chemical homogeneity, and the formation of non-equilibrium phases [61]. The difference between the casting microstructure and LPBF microstructure of AlSi10Mg has been reported in the work of Uzan *et al.* [62] and can be appreciated in **Figure 2.6**. The cellular microstructure of LPBF AlSi10Mg comprised of small aluminium nodules surrounded by Si-rich area contrasts heavily with the large cast grains and the presence of large Al-Si needle-shaped eutectic phases. The finer microstructure of LPBF AlSi10Mg compared with the cast material can give higher mechanical properties [27]. The as-built

microstructure of AlSi10Mg manufactured by LPBF in both build and transverse directions is shown in **Figure 2.7**. In the optical micrographs (**Figure 2.7(a)-(b)**), the elongated ellipse shapes that can be clearly seen in the transverse direction are the scan tracks. The melt pools can be observed as concave shapes in the build direction. Higher magnifications (**Figure 2.7(c)-(d)**) reveal three distinct regions within the melt pool: (1) a fine microstructure in the melt pool core, (2) a coarser microstructure with more elongated grains around the melt pool core, and (3) a disordered microstructure at the melt pool boundaries due to the successive reheating during the manufacturing process [60]. The high-velocity solidification front and the constitutional supercooling happening in the LPBF stimulated a cellular type of solidification, as reported by Prashanth *et al.* in AlSi12 [63]. During the solidification of the melt pool, α-Al solidifies first because of the high cooling rates, rejecting Si in the liquid and increasing its concentration. Consequently, Si is segregated at the grain boundaries. The solubility of Si in Al decreases with the temperature under conventional cooling rates (e.g. casting). However, the high cooling rates of LPBF greatly extend the solubility of Si in Al to ~7 wt.% from 1.6 wt.%, as reported by Li *et al.* [64]. Takata *et al.* [65] observed changes in the microstructure depending on the specimen size printed. Smaller specimens had Si particles inside the Al columnar grains, indicating the precipitation of Si during the manufacturing process, where larger specimens did not show Si particles in the Al columnar grains. This could be explained by the difference in cooling rates. Hooper [56] reports a reduction in cooling rates for overhangs caused by the surrounding unmelted powder, which has lower thermal conductivity compared to melted material, thus limiting the heat flow and the cooling rates. The extended periods at elevated temperature allow the precipitation of Si in the Al columnar grains.

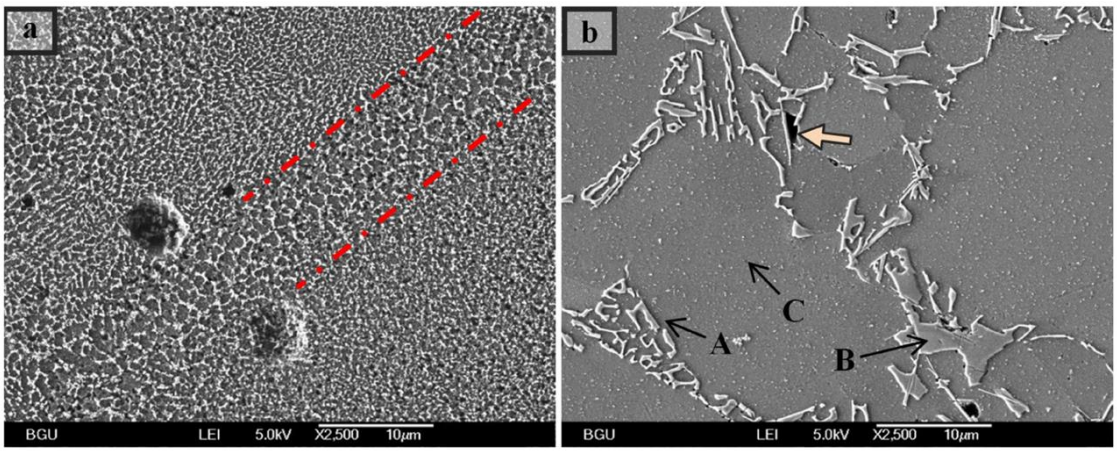


Figure 2.6: SE SEM images of AlSi10Mg microstructure manufactured by (a) LPBF as-built condition, (b) die-casting. Red dashes on (a) shows the coarser microstructure at the boundary of the melt pool. On (b), A represents the Al-Si needle-shaped eutectic, B denotes Si dispersed in Al matrix, and C points to Fe-rich intermetallic phases. The orange arrow denotes a porosity due to lack of fusion. Image taken from Uzan *et al.* (2018) [62].

The thermal gradient generated by the laser source leads to the formation of columnar or elongated α-Al grains in the microstructure [66] that can be observed along the build direction (**Figure 2.7(c)**). These grains can be observed as equiaxed in the transverse direction where α-Al nodules are surrounded by Si cellular network (**Figure 2.7(d)**). Similar metallurgy has been observed in high-strength aluminium alloys EN AW 2618, 6061, and 7075 [67–69]. Columnar grain growth promotes the formation of cracks during the solidification in those alloys. High-strength aluminium alloys will be discussed in more detail in **section 2.2.4**. This anisotropic microstructure with elongated grains leads to anisotropic mechanical properties, with better elongation at break in the transverse direction [27,70].

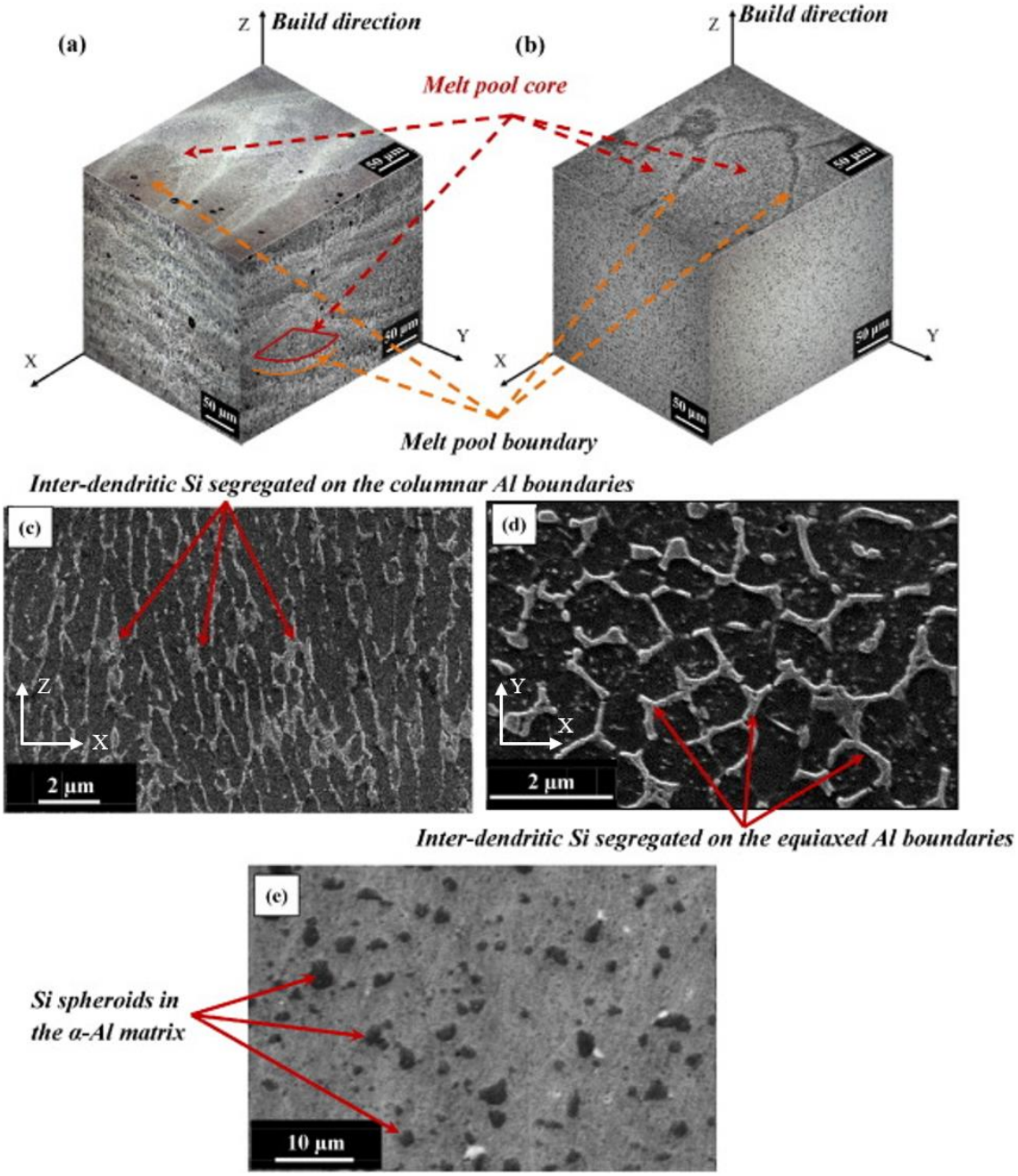


Figure 2.7: Optical micrographs of AlSi10Mg microstructure (a) as-built condition, (b) heat-treated. SEM observation of the as-built microstructure in (c) build direction, and (d) transverse direction. (e) Si spheroids in the α-Al matrix after T6 heat treatment. Image taken from Aboulkhair *et al.* (2016) [71].

2.2.3.2 Effect of heat treatment on the microstructure

Heat treatments aim to modify the microstructure of an alloy to change its physical properties, which are, in most cases, mechanical properties. Heat treatments are necessary for LPBF parts since as-built parts exhibit generally high levels of internal stresses [72], low ductility [73], and anisotropic microstructures [37].

Specific heat treatments have been developed for AlSi10Mg [66] due to the significantly different LPBF microstructure compared to conventionally manufactured parts. Consequently, conventional heat treatments do not lead to the most improvement in the targeted properties in LPBF manufactured material. Also, studies on heat treatments generally focus on the maximisation of mechanical properties. No studies in the literature report the effect of these heat treatments on the thermal conductivity of LPBF parts. However, such studies have been conducted for die cast AlSi10Mg and other die-cast aluminium alloys. Cingi *et al.* [74] tested the thermal conductivity of die-cast AlSi10Mg after heat treatment at temperatures up to 450 °C with a soaking time of 3 hours and furnace cooled. They reported that the thermal conductivity of AlSi10Mg increased considerably as the heat treatment temperature increased. They stated that the reduction of Si in solid solution by its precipitation causes an increase in thermal conductivity. They also stated that the thermal conductivity is further enhanced by the dissolution of grain boundaries and could be further enhanced with higher heat treatment temperature and slower cooling rates. Since the effect of heat treatment on thermal conductivity has not been investigated for LPBF, designers cannot take full advantage of heat treatments to enhance the thermal performance of LPBF components, thus impeding the application of LPBF process. Annealing heat treatment has been reported for AlSi10Mg consisting of holding the manufactured part at 300 °C for 2 hours. This heat treatment is often used as a stress relief to remove internal stresses in parts before being separated from the build plate. However, the microstructure is affected as the Si segregates at the α-Al grain

boundaries and dissolved in the α-Al grain forms spheroids of Si. A reduction in strength and improvement of ductility has been observed by Takata *et al.* [75]. Solution heat treatment (SHT) leads to a reduction in Si in solid solution by allowing it to diffuse out of the α-Al matrix, Si spheroids coarsen with the solution heat treatment duration [75,76]. SHT is usually followed by an ageing step to achieve a fine distribution of precipitates in the material and improve mechanical performance. An example of SHT followed by an artificial ageing step is reported in **Figure 2.7(e)** from Aboulkhair *et al.* (2016) [71]. It can be observed that the Si has precipitated into spheroids and it was reported by Aboulkhair *et al.* that the heat treatment led to microstructure coarsening. Such changes in the microstructure could increase the thermal conductivity of LPBF AlSi10Mg similarly to what was reported by Cingi *et al.* [74] for die cast AlSi10Mg.

2.2.4 Overcoming cracking and high-strength aluminium alloys

As LPBF is analogous to a welding process, unweldable aluminium alloys are therefore not suitable for this process due to steep cooling curves. Conventional high-strength aluminium alloys (which are part of unweldable alloys) processed by LPBF result in printed material exhibiting cracks spanning many printed layers [69]. This cracking issue arises during the solidification melt pool owing to the large solidification range of high-strength aluminium alloys, the high solidification shrinkage and the poor fluidity of the molten phase [67]. Large solidification range is illustrated with the binary Al-Cu phase diagram in **Figure 2.8**. The impossibility of printing ‘unweldable’ aluminium alloys has impeded wider adoption of LPBF process for applications requiring high specific strength, fracture toughness, and fatigue life.

To overcome the cracking issue of high-strength aluminium, various options have been explored. Firstly, the scan strategy can promote the growth of columnar grains in the direction of the thermal gradient, leaving interdendritic liquid at the liquid-solid interface

[51] which when coupled with shrinkage and high residual stresses [51] leads to the formation and propagation of cracks along the grain boundaries. Consequently, the scan strategy can be optimised to control the thermal gradient to limit the columnar grain growth and reduce the level of thermal stress induced by the high cooling rates of LPBF [13,56]. Typically, meander scan strategies are used to manufacture parts but this usually leads to large thermal gradients across the part during manufacturing, resulting in high residual stresses post-manufacture. Scan strategies limiting large thermal gradients, such as the checkerboard or island scan strategy illustrated in **Figure 2.3**, have shown a reduction in residual stress [13,49]. Multiple scan passes have also been proposed to mitigate residual stresses and improve relative density [31]. These scan strategies can consist of a first scan to pre-sinter the powder with a reduced power followed by a full-power scan to effectively melt the material. Koutny et al. [49] reported the influence of several scanning strategies on the processability of aluminium alloy EN AW 2618, however, none of the tested scan strategies resulted in a crack-free specimen. Fractal scan strategies have been proposed and successfully tried on unweldable Ni-superalloy, Hastelloy-X [77] which suffers from similar cracking issues as high-strength Al alloys. However, fractal scan strategies have not been applied to Al alloys. Thermal gradients between the unmelted and melted powder can be reduced by using a higher powder bed temperature than the typical 100 – 200 °C. A few recent commercial LPBF machines such as the TruPrint 5000 from TRUMPF GmH + Co. KG (Germany) can maintain bed temperatures up to 500 °C [78].

Another route studied is the addition of alloying elements to reduce cracking. Additions of Si to conventional aluminium alloy 6061 and 7075 have been reported [79,80] to solve cracking issues. However, the resulting alloys exhibit lower mechanical properties compared to the base alloy. Additions of Zr to Al-Cu-Mg alloys [81,82] have been shown to eliminate cracking and further enhance the mechanical properties of the base alloy.

Moreover, the addition of Zr has removed the typical anisotropy found in LPBF microstructure. The absence of cracks and improvement in the mechanical properties was due to the precipitation of Al_3Zr, which acts as a grain refiner by increasing the number of nucleation sites in the melt. It also prevents the formation and propagation of cracks during solidification. Similarly, the addition of Sc has been a focus on the development of Scalmalloy by EADS Innovation Works (Airbus SE) [83]. Its ultimate tensile strength of 530 MPa is one of the highest among LPBF aluminium alloys. However, the scarcity and high costs of Sc (134 USD per gram in 2019 [84]) have limited its adoption to critical applications and replacement alloys using less Sc or Sc-free are actively investigated [85]. Along with Zr and Sc, the use of grain refiners to create high-strength aluminium alloys in LPBF has gathered interest in recent years [86–91]. The objective behind the development of tailored alloys for LPBF is to create materials with properties similar to or superseding the conventionally manufactured versions while taking advantage of LPBF design freedom. This has led to the development of a new class of aluminium alloys such as the RAM (reactive additive manufacturing) series developed by Elementum 3D, which uses a proprietary blend of ceramic grain refiners [92]. Another example of this new class of aluminium alloy is A205, commercially designated as A20X, developed by Aeromet. It is based on high strength A201 casting alloy which had been modified to incorporate 2 to 4 % of TiB_2 by volume [93] and a small fraction (typically 0.1 to 0.6 %) of Ag for corrosion resistance and to control the precipitation mechanisms [42,94]. According to the manufacturer, it also exhibits better high-temperature performance compared to Al-Si-Mg alloys. For these reasons, A20X will be studied in this thesis as a potential replacement to AlSi10Mg for high-strength applications. Lattice structures manufactured with this alloy could allow the development of lightweight thermo-mechanical heat transfer devices.

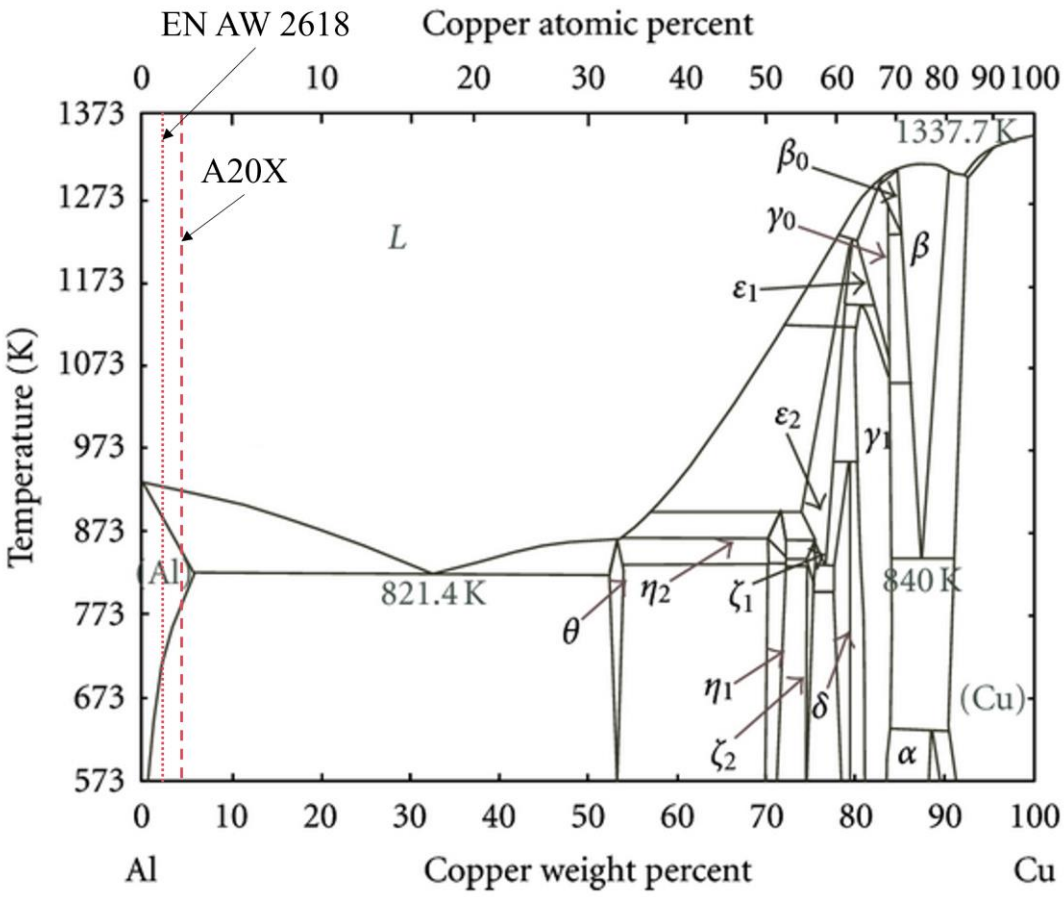


Figure 2.8: Al-Cu binary phase diagram

Key findings from this section:

- The LPBF process has numerous parameters that need to be controlled to achieve fully dense and crack-free parts.
- High-strength aluminium alloys are difficult to manufacture by LPBF. AlSi10Mg is the go-to Al alloy but has low mechanical properties limiting applications.
- Thermal conductivity of LPBF parts has not fully been investigated even in the most studied alloy, AlSi10Mg. No studies compared the build orientation, microstructure, and heat treatments to the thermal conductivity of LPBF parts.

2.3 Lattice Structures

2.3.1 Introduction to cellular materials

Cellular materials or cellular solids represent a wide category of structures of which lattice structures are a subcategory. Gibson and Ashby in Cellular Solids: Structure and Properties [95] described them:

> *"A cellular solid is one made up of an interconnected network of solid struts or plates which form the edges and faces of cells".*

They are categorised following the type of porosity, open (open-cell) or closed (closed-cell), and the porosity distribution, stochastic or periodic as illustrated in **Figure 2.9**. Stochastic open-cell porosity occurs, for example, in sponges, while open periodic cellular solids refer to lattice and honeycombs. However, honeycombs are usually used in sandwich panels, and so can be considered as pseudo-closed cells. Nature makes extensive use of cellular structures to suit various functions within the constraints imposed by its environment and have evolved these structures for more than 3.8 billion years [96]. Consequently, nature has found some of the most efficient solutions to engineering problems using cellular solids, such as transporting fluids from the roots to the top of the plant while using a minimal amount of material and retaining strength in its branches.

Fluid flow and heat transfer through cellular materials are of interest for use in heat exchangers and heat sinks [21,97–100]. The fabrication of stochastic porous structures has been widely investigated using conventional methods and has been reviewed by Banhart [101]. However, stochastic porous structures suffer from limited control on the distribution of material that can be achieved, leading to inconsistent responses that demand more conservative design rules [102]. AM techniques such as LPBF enable the manufacture of cellular materials, disregarding their periodicity or cell connectivity and

without requiring tooling [103]. Open-cell structures ease the removal of the powder after manufacture. Conversely, closed-cell structures will retain powder within the cells. This will increase part weight and therefore LPBF is not used to produce such structures.

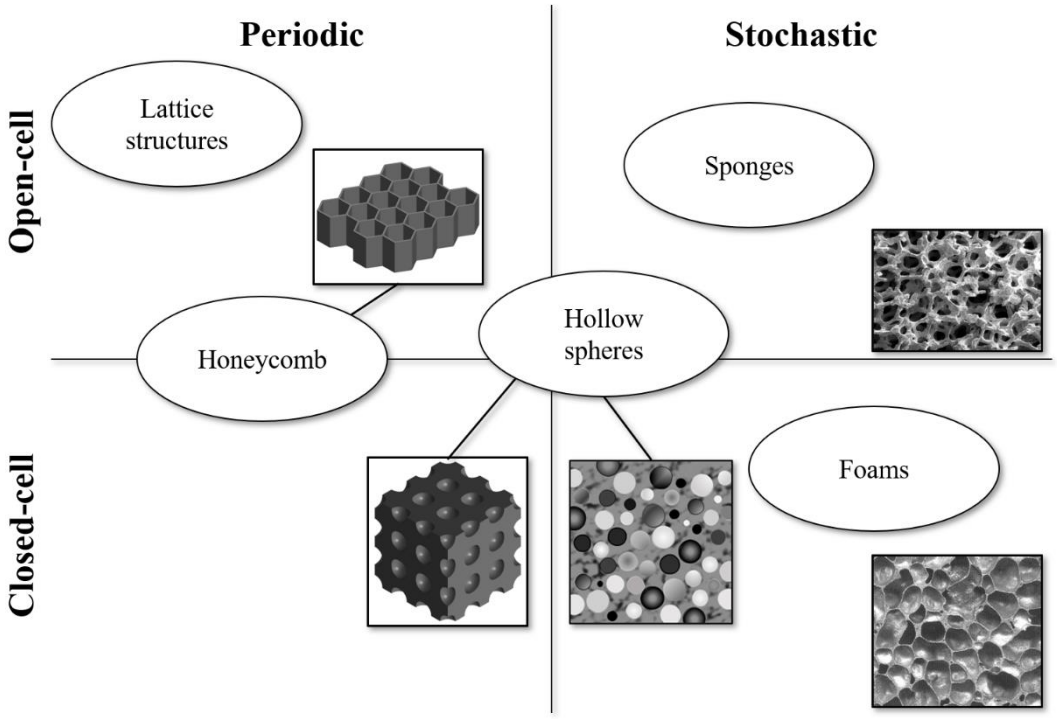


Figure 2.9: Classification of cellular solids.

2.3.2 Lattice structures

Lattice structures are spatially ordered open-cell structures made of a unit cell repeated in the three dimensions. At the unit cell scale, lattice structures can be seen as structures with specific features and properties, but at the overall structural level, lattice structures behave like a homogeneous metamaterial [104]. Lattice structures offer complete control over the distribution of material (connectivity, volume fraction, cell size, overall dimensions). An important parameter for lattice structure is its relative density ρ^*/ρ_s which represents the density of the lattice structure ρ^* divided by that of the solid material from which the cells are made ρ_s. Similarly, lattice physical properties such as mechanical strength are expressed as fractions of the property of the solid material.

Lattice structures are usually divided into two categories. The first and most studied category is strut-based lattice structures where unit the unit cell consists of connected beams and is tessellated across a spatial domain. These structures have received the most attention in the lattice-related literature. They can exhibit high surface area to volume ratios, relatively high stiffness, and energy absorption [105,106]. Despite these promising properties, their main disadvantage for mechanical applications lies in the stress concentration at the nodes where the beams connect due to small fillet radii [107]. They also have anisotropic properties and perform less optimally or poorly when loads are not aligned with their struts [108]. A few strut-based lattice structures have been manufactured, with some difficulty, by non-AM processes such as investment casting or deformation forming techniques [109]. In most cases, the high cost for performance enhancement has not been enough to justify switching from conventional geometries. Strut-based lattice structures are not ideal to be manufactured by LPBF due to overhangs, which require support structures, especially for large cell size [108].

The second category of lattice structures are those based on triply periodic minimal surfaces (TPMS). These were described by Schwarz [110] in 1865 and his student Neovius [111] in 1883 and were reintroduced, in 1970, by A. Shoen in his work for NASA [112]. A minimal surface has a mean curvature of zero at any point which means they are equally convex and concave at any point and without self-intersection. TPMS lattices are mathematically defined, their equations and generation will be discussed in the next chapter (see **section 3.2.1**). These structures have shown promising properties compared to strut-based lattices in terms of energy absorption [113]. Also, their continuous curvatures improve the manufacturability by creating self-supporting structures (i.e. subsequent layers are supported by a previously melted layer). The continuous curvature has also been reported to be beneficial for bio-applications by promoting cell attachment [114].

The mechanical properties of LPBF lattice structures have been recently reviewed by Maconachie *et al.* [20] and are reported in **Figure 2.10**. They compared the relative compressive strength and relative modulus of different types of lattice structures with various volume fractions to the Gibson and Ashby model. This model correlates the relative mechanical property (such as relative compressive strength σ^*/σ_s) of the structure to its volume fraction ρ^*/ρ_s in the form of a positive power-law with a coefficient C and exponent n as reported in **Equation 2.1**. Maconachie *et al.* [20] concluded that mechanical properties, such as the relative compressive strength and relative modulus of lattice structures can be predicted by the Gibson and Ashby model. Similar findings have been reported by Maskery *et al.* [115] for different TPMS lattice structures. These findings show lattice structure mechanical properties can be controlled by designers and allow the development of specifically tailored components. Furthermore, the mathematical definition of the TPMS lattice structures gives complete control of the material distribution and allows designers to spatially vary properties for further performance gains. Analogously, establishing general relationships between thermal properties and intrinsic lattice properties (such as unit cell design, volume fraction, surface area, etc.) would unlock the development of advanced lattice components for thermal applications.

$$\frac{\sigma^*}{\sigma_s} = C\left(\frac{\rho^*}{\rho_s}\right)^n \qquad \textbf{Equation 2.1}$$

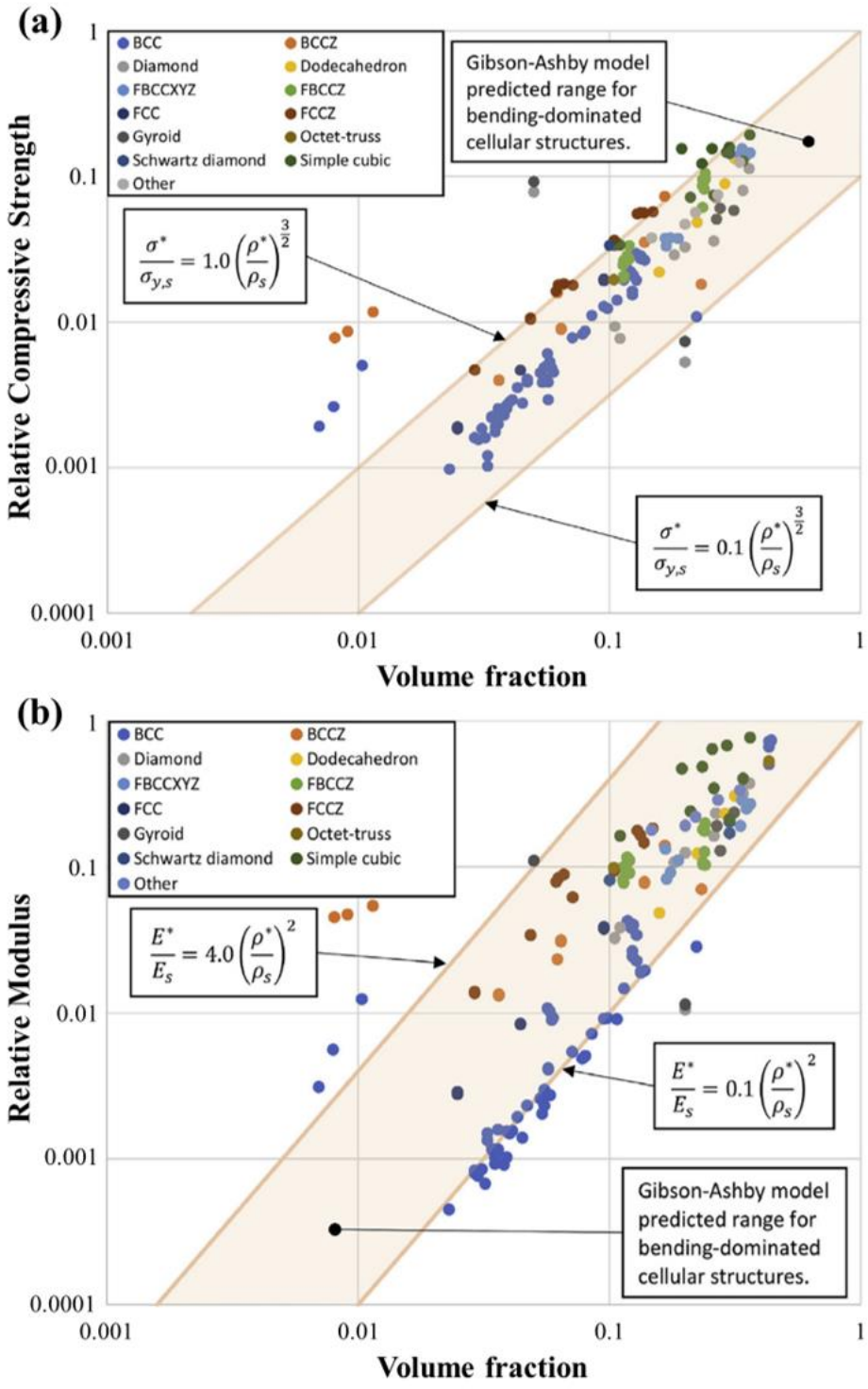


Figure 2.10: Comparison of reported experimental (a) compressive strength and (b) modulus with predictions of the Gibson-Ashby model taken from Maconachie et al. [20]**.**

2.3.3 Thermal conductivity of lattice structures

Thermal conduction is the transfer of internal energy by vibrations and collisions at the atomic scale within a body, without any motion of the material as a whole. In the case of a temperature gradient within a homogeneous body, the energy transfer rate, q, is calculated by Fourier's law (**Equation 2.2**) where $\partial T/\partial x$ is the temperature gradient in the direction normal to the area A as illustrated in **Figure 2.11**. The thermal conductivity λ is an intrinsic property of the material. The minus sign in Fourier's law is required by the second law of thermodynamics; thermal energy transfer initiated by a thermal gradient must be from a hotter to a colder region.

$$q_{conduction} = -\lambda A \frac{\partial T}{\partial x} \qquad \textbf{Equation 2.2}$$

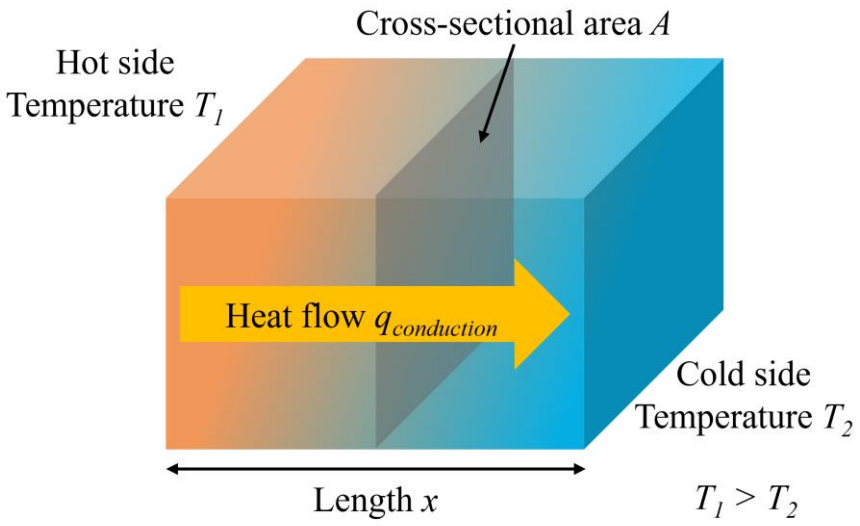


Figure 2.11: Illustration of Fourier's law

Thermal conductivity of solids is influenced by the temperature at which the measurement takes place. For typical metals, it increases with temperature to a maximum and plateaus, then sharply decreases as the temperature continues to increase, and reaches a minimum close to the material melting point. Chemical composition and the distribution of alloying elements play an important role in thermal conductivity. Rauta *et al.* [116] investigated

the factors affecting the thermal conductivity of aluminium alloys. They reported that the reduction of solutes in the α-Al phase leads to a significant increase in thermal conductivity. They also studied the effect of the grain boundaries on the thermal conductivity of AlSi10Mg. Grain boundaries in microstructure act as obstacles to heat flow, therefore smaller grain size decreases the thermal conductivity [117]. Rauta *et al.* [116] showed that the grain boundary has a negligible impact on the thermal conductivity of AlSi10Mg. Macro or microstructural anisotropy in the specimen can act as barriers or conductive pathways to heat flow, therefore changing the conductivity and make the measurement dependent on the heat flow direction [117]. This is of major importance for materials produced by LPBF which often present anisotropic microstructures. The presence of porosity within the material lowers the thermal conductivity due to the lower conductivity of gas and voids to those of solids. Consequently, the characterisation of microstructure and porosity of material produced by LPBF is of major importance before the measurement of thermal conductivity.

Similarly to the definition of the thermal conductivity of solids λ (see **Equation 2.2**), the apparent thermal conductivity of cellular solids λ^* can be defined by **Equation 2.3** where q is the uniform heat flux, ΔT is the temperature difference and t is the thickness of the cellular solid.

$$\lambda^* = \frac{q}{\Delta T/t} \qquad \textbf{Equation 2.3}$$

The apparent thermal conductivity of cellular solids can be seen as the sum of contributions of four distinct heat transfer mechanisms (see **Equation 2.4** and **Figure 2.12**): (1) conduction through the solid λ_s^*, (2) conduction through the gas λ_g^*, (3) convection within the cells λ_c^*, and (4) radiation through the cell walls and across the cell voids λ_r^*. Each mechanism has complex relationships that compete against each other [95].

$$\lambda^* = \lambda_s^* + \lambda_g^* + \lambda_c^* + \lambda_r^* \qquad \textbf{Equation 2.4}$$

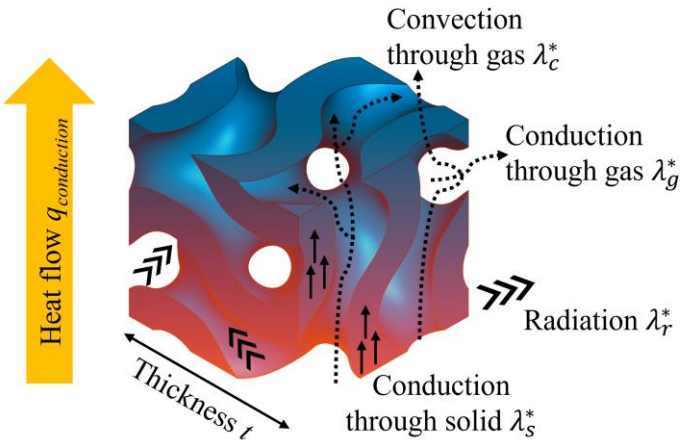


Figure 2.12: Heat transfer mechanisms contributing to the apparent thermal conductivity

In the literature, there are a significant number of studies investigating the prediction of the apparent thermal conductivity of cellular solids (foams, packed beds etc.). Bianchi et al. [118] organised the existing work into three categories: (1) asymptotic solutions which incorporate the theoretical correlations (upper and lower apparent conductivity bounds); (2) empirical correlations which are deduced from fitting the experimental data; (3) unit cell approaches with theoretical models based on simplified descriptions of the cellular solid geometry. The most commonly used asymptotic solution to predict the apparent thermal conductivity (λ^*) simply accounts for the volume fraction of each substance using a mixing law:

$$\lambda^* = \varepsilon\lambda_p + (1-\varepsilon)\lambda_s \qquad \textbf{Equation 2.5}$$

where ε is the pore fraction, λ_s and λ_p are the conductivity of the solid and the pore materials, respectively. This model does not account for the distribution of material but is still widely used to estimate the thermal conductivity of composite structures due to its simplicity. However, considerable errors can arise in the prediction of λ^*, when the solid

conductivity differs significantly from the pore conductivity [119]. Various modifications to that model have been developed to better predict the thermal conductivity of cellular solids. Ranut [120] have reviewed analytical models and empirical data of the apparent conductivity of aluminium metal foams with porosity higher than 0.89. Ranut reported most models in the literature are solely based on the porosity level, but good predicting capability can be achieved by tuning empirical or fitting constants. More surprisingly, Ranut reported that models using a more complex theoretical approach by accounting for the foam geometry does not always produce more accurate results. This was reported to be caused by excessive simplifications introduced in the foam geometry.

Conventional manufacturing of cellular solids only allows a limited volume fraction range. On the other hand, AM enables graduation from low volume fraction [121] to fully dense within the same part [122], which conventional models do not accommodate, therefore preventing their generalisation to AM lattice structures. Furthermore, the geometry and periodicity of lattice structures allow simplifications of models compared to stochastic foams.

Strut-based lattice structures have been studied due to their simplicity and manufacturability without AM techniques [123]. Studies have mainly focused on the thermal performance in forced-convection mode and on the overall geometry and fluid flow pattern without studying the conductivity of the lattice structure itself [98,124–126]. Determining the thermal conductivity of a lattice structure and its relation to the different lattice parameters (unit cell design, volume fraction, cell size, etc.) is necessary to provide design guidelines and develop predictive models for broader adoption of lattice structures for thermal application and will be investigated in this thesis. Secondly, increasing the thermal conductivity, by selecting highly conductive materials or heat treatments, can improve the thermal performance for convective applications [126]. The apparent thermal conductivity of strut-based lattice structures has been numerically investigated by

Bianchi *et al.* [127]. They reported behaviour similar to other cellular foams, the apparent thermal conductivity increases non-linearly with the pore fraction from 0.75 to 0.95. They further reported that previous models designed for cellular solids do not predict the thermal conductivity of strut-based lattice structure accurately. They proposed a new correlation to predict the apparent thermal conductivity of strut-based lattice with a pore fraction ranging from 0.75 to 1 using a best-fitting second-order polynomial regression and is reported in **Equation 2.6**. This correlation is based on the work of Maxwell for electrical conductivity [128] and considering the thermal conductivity of strut material predominant over that of the pore phase. They also imposed the following constraints $\lambda^* \to 0$ for $\varepsilon \to 1$ and $\lambda^* \to 1$ for $\varepsilon \to 0$. They also reported that the shape or strut cross-section does not significantly influence the thermal conductivity. However, this study was for pure thermal conduction with no experimental comparison.

$$\lambda^* = \frac{(1-\varepsilon)}{[0.36 + 0.64(1-\varepsilon)]^{-1}} \qquad \textbf{Equation 2.6}$$

Abu Al-Rub *et al.* [129] numerically investigated the apparent thermal conductivity of interpenetrating phase composites with TPMS lattice structure reinforcement. This study mainly focuses on the thermal conductivity mismatch between the reinforcement material (TPMS structure) and the interpenetrating phase (matrix) and compared the calculated conductivity to analytical bounds such as the Hashrin-Shtrikman model [130]. They found that the material distribution of TPMS lattices impacts their apparent conductivity. However, there are no investigations of the effect of volume fraction and cell size on the thermal conductivity of TPMS structures. To the knowledge of the author, no other studies have been conducted to measure the thermal conductivity of TPMS lattice structures. It is of special importance to determine the thermal conductivity of lattice structure and understand how it is affected by the lattice parameters before using them for heat transfer devices where several heat transfer mechanisms act simultaneously.

2.3.4 Forced convection heat transfer of lattice structures

2.3.4.1 Forced convection heat transfer fundamentals

Thermal convection is the transfer of heat due to the mass movement of molecules within fluids. For instance, when a fluid is exposed to a warmer surface, the fluid molecules are carried away and scattered causing the mass of that fluid to become less dense. The warmed mass will be displaced upward and the colder and denser mass will be displaced downward. Through this process, called natural convection, the molecules of the hot fluid transfer heat continuously toward the volumes of the colder fluid. On the other hand, convection can be forced by the movement of the fluid other than buoyancy forces.

Thermal convection is complex but can be generally estimated using Newton's law of cooling (**Equation 2.7**), where h is the local value of heat transfer coefficient or film coefficient, A is the area of the heat exchange (i.e. solid-fluid interface), T_{body} and T_{∞} are the surface temperature of the body and the temperature of the oncoming fluid. The determination of the thermal heat transfer coefficient h is difficult and dependent on all the parameters that have an effect on the amount of heat transferred by convection: the geometry and surface roughness of the body, the boundary layer form, the fluid and flow properties. Consequently, the determination of the heat transfer coefficient on a specific problem is crucial and very influential to the results.

$$q_{convection} = hA\left(T_{body} - T_{\infty}\right) \qquad \textbf{Equation 2.7}$$

Nusselt number represents the ratio of convective to conductive heat transfer at the boundary in the fluid. It can be calculated using **Equation 2.8** where λ_{fluid} is the thermal conductivity of the fluid and L_c is a characteristic linear dimension. L_c is based on a geometrical feature descriptive of the studied specimen or used more generally is the hydraulic diameter. One definition of the hydraulic diameter is equal to four times the

cross-sectional area of the flow divided by the active heat transfer surface. A Nusselt number of 1 represents heat transfer by pure conduction, values between 1 and 10 are characteristic of a laminar flow, and turbulent flow has a Nusselt number ranging typically between 100 – 1000.

$$Nu = \frac{h \cdot L_c}{\lambda_{fluid}} \qquad \textbf{Equation 2.8}$$

The type of flow is crucial and subsequently affects heat and mass transfer properties. The Reynolds number is a dimensionless number that expressed the flow inertial forces compared to the viscous forces within the studied fluid and is calculated using **Equation 2.9** where ρ_{fluid}, μ_{fluid}, and U are the density, the dynamic viscosity and the velocity of the fluid, and L_c is a characteristic linear dimension as described previously. Reynolds number is used to define the type of flow and the patterns associated with it. They are classified into three categories: (1) laminar (Re < 2000) where the fluid particles follow smooth paths in layers with adjacent layers having little to no mixing; (2) 2000 < Re < 3000 transitions between laminar to turbulent flow condition; (3) turbulent (Re > 3000) where the fluid motion undergoes irregular fluctuations.

$$Re = \frac{\rho_{fluid} \cdot U \cdot L_c}{\mu_{fluid}} \qquad \textbf{Equation 2.9}$$

As a fluid flows through a system (e.g. tubular pipe), resistance to the flow is created due to friction between the flow and the surface and is characterised by a pressure drop. The larger pressure drop, the larger the pumping power or fan power required to maintain that flow, the greater energy losses to the coolant. The friction factor *f* is a dimensionless number often used instead of pressure drop to allow comparison across various systems. It represents the proportion of energy of the fluid flow lost to frictional effect and is calculated using **Equation 2.10**, where ΔP is the pressure drop through the structure; D_h

is the hydraulic diameter, L_c is the flow path length, ρ_{fluid} and U are the fluid density and velocity.

$$f = \Delta P \cdot \frac{2}{\rho_{fluid} \cdot U^2} \cdot \frac{D_h}{L_c} \qquad \textbf{Equation 2.10}$$

2.3.4.2 Convective heat transfer of heat sinks and AM structures

The main parameters to characterise a forced convection heat transfer device are its heat transfer performance and its resistance to fluid flow along with mechanical strength, manufacturing technique, and cost. The larger the pressure drop, the larger the pumping power or fan power, and the greater energy losses to the coolant. In heat exchangers, the aim is to increase the heat transfer while maintaining a low-pressure drop. Conventional manufacturing processes limit the development of more complex and compact geometries. AM alleviates this and allows the manufacture of complex designs, such as cellular materials that are difficult or impossible to manufacture with conventional techniques, thus unlocking higher performance. AM can also accelerate the development of complex and costly to manufacture geometries (such as wavy fins, offset strip fins, and louvred fins, illustrated in **Figure 2.13**) and parameter variations [131].

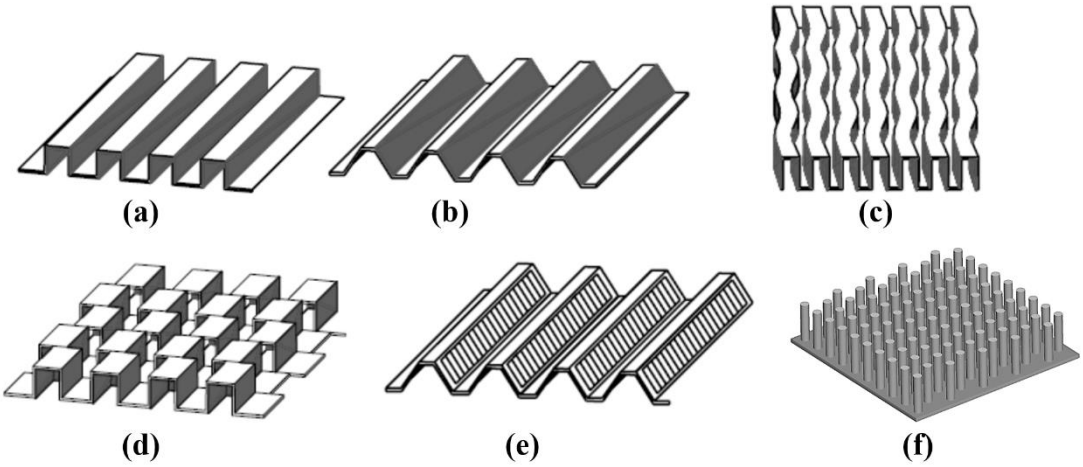


Figure 2.13: Illustration of fin geometries: (a) rectangular, (b) trapezoidal, (d) offset strip, (e) louvred, (f) pin. Image based on Dewatwal *et al.* (2009) [132].

Pin fins have widely replaced continuous fin arrays (e.g. plate, wavy fins) due to the higher attainable heat transfer rates [133]. This is achieved through two mechanisms: first, by the restriction of the thickening of the boundary layer and, second, by the promotion of oscillations in the flow, thus increasing heat transfer by generating vortices that force cooler fluid toward the fin [134]. Pin fins are also preferred due to their simplicity to be modelled and their manufacturability by conventional techniques (machining, die casting, folding, brazing etc.) [135]. The addition of fins on heat transfer surfaces has been shown by Sahiti *et al.* [136] to enhance the heat transfer coefficient, but also increases the pressure drop, while maintaining a low hydraulic diameter. Careful design of the fins considering the geometry, size, number, and distribution of pins must be undertaken and have been the subject of numerous studies and are still investigated to this day [137–139]. Similar to fin geometries, lattice structures exhibit a wide variety of shapes via controllable design parameters that determine the morphology and the surface area of the channels. The high surface area to volume ratio of lattice structures could offer higher heat transfer properties. However, hydraulic diameter, easily defined for simple structures such as straight pipe or pin fin arrays, are much more complicated to define for lattice structures with their complex and interconnected flow paths. Therefore, new metric(s) would need to be developed. Despite significant differences between fin geometries and lattice structures, similar methodology to identify good candidates for heatsinks with fin designs could be reused for lattice structures.

Wong *et al.* [24] compared pin-fins, elliptical, diamond, and v-shaped heatsinks manufactured by LPBF in two different materials. They showed that aluminium 6061 performed better than stainless steel 316L due to its higher thermal conductivity. The best performing geometry was the diamond resulting from forcing the fluid to flow over each fin in such a way as to prevent a thick boundary layer from forming. However, the relative densities of manufactured structures were below 90 %, affecting the conductivity of the

material. Structure geometry affects the relative density in the LPBF process [49,140], consequently, variation in the relative density (i.e. amount of material) would affect thermal properties and change the reported heat transfer enhancement. Whilst Wong *et al.* demonstrated that LPBF manufacture of heatsink devices is possible, the geometrical freedoms of the LPBF process were not heavily exploited. In a second study, Wong *et al.* [141] additional geometries were manufactured including a lattice example. The BCC-Z strut-type lattice specimen resulted in the lowest thermal performance among all tested geometries. They hypothesised this could be due to the thin beams being unable to conduct heat from the base at a sufficient rate to enable effective transfer of the heat into the cooling media flow. The strut thicknesses were more than ten times smaller than the other tested heatsinks. They also reported that the flow through the chosen lattice geometry was poor due to the alignment of the strut in the flow stream, creating large open channels that limited flow mixing. This demonstrates that increasing the structure surface area by using a strut-based lattice structure does not necessarily lead to improvement in the heat transfer coefficient; the fluid path needs to be considered to maximise fluid interaction. Surface area can also be increased by increasing the surface roughness. LPBF surfaces typically exhibit much higher surface roughness than machined counterparts. This is considered detrimental to fatigue life [71] and corrosion resistance [142], however, can benefit surface-based phenomenon such as heat transfer [143]. Kirsch *et al.* [138] used LPBF to manufacture channels with pin-fin heat exchange arrays with a range of spanwise and streamwise spacing. They reported that the high surface roughness inherent to the LPBF process provides a significant improvement in heat transfer especially at high Reynolds numbers and for tighter spacings compared to smooth surfaces due to greater interaction between the coolant flow and the geometry over conventionally manufactured smooth design. They also reported that surface roughness of the pin fin array manufactured by LPBF is intrinsically linked to the pin

spacing in the array and equally influenced the overall thermal performance of the pin fin. In other words, a less dense pin fin array can provide better thermal performance than a densely packed array. Indeed, they observed that an LPBF coupon with six times fewer pins exhibited similar heat transfer performances to that of a conventionally manufactured pin fin array. Such a reduction in the number of pin fins offers a significant weight reduction, which is of particular interest in the aerospace sector to achieve higher fuel efficiency. They also reported that the roughness level and the pin shape are linked to the pin spacing in the LPBF manufactured array. This demonstrates the requirement for greater understanding of advantages and drawbacks of AM processes, such as the surface roughness to allow more efficient heat exchangers.

Lu *et al.* [126] studied the effect of unit cell topology (design, size, and volume fraction) on the fluid flow and heat transfer properties of prismatic strut-based lattices. They reported that at a fixed volume fraction, smaller cell sizes increase heat transfer, but also increases the pressure drop regardless of the unit cell design and an optimum transfer can be calculated. They showed that the volume fraction shows a similar trend to that of cell size where both heat transfer and pressure drop increase with volume fraction. They reported that optimum thermal performance is typically found around a volume fraction of 0.2 and varies around that number depending on the flow regime and the type of fluid. Lu *et al.* also investigated the effect of unit cell design by measuring the airflow and temperature at the scale of the lattice unit cell and compared it to CFD simulations. Similar to the offset strip [134], Lu *et al.* observed that struts create vortices that promote flow mixing and enhance heat transfer. They also compiled and reported the friction factor and Nusselt number for various types of cellular solid geometries (foams, corrugated duct, louvered fins, etc.) across a wide range of Reynolds numbers. This work has been completed by Gao and Sun [144] shown in **Figure 2.14**. Channel height was chosen as the characteristic length for each medium to ensure compatibility with the

results. As shown in **Figure 2.14(a)**, packed bed, wire screens, and metallic foams exhibit a higher Nusselt number (i.e. heat transfer performance). This is due to the high thermal conductivity and complex internal geometry. Metallic foams do not exhibit a large variation in Nusselt number despite different manufacturing processes. For high porosity foams, heat transfer is dominated by forced convection over thermal conduction, depending on the parent material. Sintered packed beds have higher heat transfer performances due to less thermal contact resistance over non-sintered packed beds. **Figure 2.14(b)** compares the overall pressure losses of different heat dissipation media in the form of friction factor. Strut-based lattice structures exhibit an overall low friction factor compared to foams or packed-beds. The low porosity of packed beds limits the flow, increasing the pumping power, thus increasing the friction factor. The stochasticity of foams leads to differences in flow channels and flow patterns and results in a higher-pressure loss compared to periodic structures. This exemplifies the role of topology on the overall pressure loss. Also, **Figure 2.14(a)-(b)** illustrates the countervailing influences of the topology on the friction factor and Nusselt number: an optimum heat exchanger balances the conduction of heat through the structure (by maximising the volume fraction) against the need to create easy flow paths (by minimising the volume fraction).

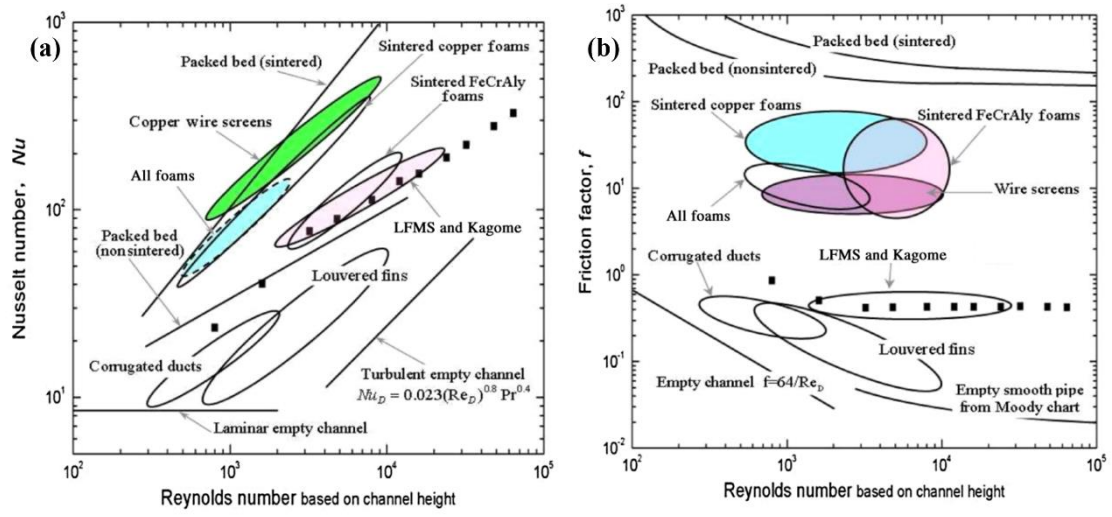


Figure 2.14: Compilation of results of cellular material (a) friction factor and (b) Nusselt number, against Reynolds number taken from Gao and Sun (2014) [144].

No studies have been reported using TPMS lattice structures for forced convection heat transfer. TPMS lattice structures exhibit a wide variety of unit cell designs, cell sizes, and volume fractions, therefore, can cover a large portion of the corrugated duct, fins, foams, and strut-based structures (e.g. LFM (lattice-frame material) and Kagome) and foams displayed in **Figure 2.14**. TPMS lattices are surface-based structures and are consequently expected to have both a higher friction factor and Nusselt number compared to the aforementioned structures due to their high surface area to volume ratios and complex fluid flow paths. However, investigations need to be carried out to confirm these assumptions. This could be achieved via computational fluid dynamics (CFD) where the convective heat is simulated. CFD methods can highlight local mechanisms, but the geometrical complexity of lattice structures makes CFD computationally expensive and the solutions are numerical approximations of real phenomena. Furthermore, the lack of experimental measurements in the literature prevents the validation of CFD results and the development of fluid flow models for lattice structures. On the other hand, experiments allow assessment of performance-related properties such as pressure drop, which is important for heatsink designs. Results from experiments are tied to material properties for which LPBF are not fully apprehended due to their inherent link to process parameters. Therefore, there is a necessity to experimentally characterise the heat transfer properties of lattice structures to create guidelines for designing high-performance heatsinks. Forced convection heat transfer properties of AM components have been reported in the literature, however, there are no standardised test apparatus nor measurement methods. Studies tend to rely on in-house developed apparatus tailored for a specific application. This complicates the direct comparison of results reported in the literature. The development of a test apparatus dedicated to the measurement of heat

transfer properties of lattice structures in forced-convection mode will be necessary and will be covered in **section 4.3**.

Key findings from this section:

- Lattice structures offer complete control over the distribution of material, thus the possibility to tailor properties for a specific application.
- Thermal conductivity of lattice structures has been mainly studied numerically but little to no experimental study was reported.
- Fin-based heat exchangers are conventionally used for numerous applications. We have seen here new designs only manufacturable by AM that can outperform pin fin in heat transfer and pumping power. However, a balance must be made between heat transfer and pressure drop. A larger pressure drop requires higher pumping requirements and is usually the limiting factor to design heat exchangers.
- Increasing the surface area of a structure does not necessarily increase the heat transfer and have usually an adverse effect on the pressure drop.
- Strut-based lattices have been investigated in forced convection heat transfer and show a wide range of heat transfer properties between those of corrugated walls and metallic foams.
- Forced convection heat transfer of TPMS lattice has not been investigated and lack of experimental work in the literature impede the development of CFD simulation due to the impossibility to validate the results.

2.4 Summary of research gaps

AlSi10Mg has been widely studied due to its low cost and its large processing window within LPBF. In this chapter, it has been shown that the build orientation significantly affects the microstructure and the physical properties of the final parts. Anisotropic microstructures lead to anisotropic heat transfer properties, but this has not been assessed with respect to the build orientation. No studies have linked the unique as-built microstructure to the thermal conductivity of LPBF parts. Furthermore, the effect of heat treatment and the possible enhancement of that property has not been studied. The determination of the effect of the microstructure on thermal conductivity is necessary to predict accurately the thermal behaviour of LPBF components.

In this chapter, it has been shown that the manufacture of conventional high-strength aluminium alloys by LPBF is difficult due to their high cracking susceptibility and the high cooling rates during LPBF. The literature reports the successful reduction of porosity and reduction of residual stress using complex scan strategies, however, scan strategies reported in the literature were insufficient to produce crack-free specimens. Fractal scan strategies have been shown as successful to eliminate cracking in Ni superalloys but have not been applied to high-strength aluminium alloys. A second approach was the addition of grain refiners in these alloys and was successfully demonstrated. Recently, high-strength aluminium alloys tailored for AM process conditions have been developed and are commercially available but little to no investigation has been made available in the literature.

Lattice structures offer the possibility to extend the thermal performance of components along with mechanical properties, paving the way for the development of multifunctional components. The thermal conductivity of lattice structures has only been numerically investigated for TPMS lattice and to date, no parametric studies reporting the effect of

volume fraction, cell size, and unit cell design exist. The importance of the thermal conductivity of the base structure dictates that such parametric study needs to be explored.

Forced convection heat transfer of lattice structures has only be carried for strut-based lattices. To date, the heat transfer in forced convection mode of TPMS lattice has not been reported despite the wide investigation of their mechanical properties and their multifunctional applications. Knowledge in this regard would promote wider adoption of lattice structures through the definition of the usable palette of parameters for heatsink applications.

3 Materials and Methods

3.1 Introduction

This chapter details the generation of lattice structures, material selection, LPBF fabrication, material characterisation techniques, as well as data analysis and performance metrics applied throughout the subsequent chapters.

3.2 Design model preparation before manufacturing

AM is a digitally based technology using CAD models to manufacture components. Before manufacturing, several steps using different software programs are required. These programs are employed to design the geometries, prepare the resulting designs and layout for manufacturing and translate the designs to machine-specific formats with the desired processing parameter sets. This is achieved through slicing and hatching the designs to generate the appropriate tool paths for the manufacturing machines.

3.2.1 Generation of TPMS lattice structures

It is desirable to design structures with tailorable volume fractions (ratio between void to solid material) since it is known to influence much of the structural and thermal performance and could allow the design of structures with tailorable properties [95]. Triply periodic minimal surface (TPMS) is a special class of surface that has a zero-mean curvature at every point. These surfaces are defined by an implicit function (i.e. $U(x, y, z)$) [145,146]. The periodicities of the function are defined as:

$$k_i = 2\pi n_i \qquad \textbf{Equation 3.1}$$

where $i = x, y, z$ and n_i correspond to the numbers of cell repetitions in each of those directions. For simplicity, the cosine and sin functions are defined as:

$$C_i = cos\left(k_i \frac{i}{L_i}\right) \quad \textbf{Equation 3.2}$$

$$C_{2i} = cos\left(2k_i \frac{i}{L_i}\right) \quad \textbf{Equation 3.3}$$

$$S_i = sin\left(k_i \frac{i}{L_i}\right) \quad \textbf{Equation 3.4}$$

with $i = x, y, z$ and L_i are the absolute sizes of the lattice structures in those dimensions.

The lattice structures are created by finding the $U(x, y, z) = t$ isosurface of the corresponding TPMS equations. When the level-set equation is plotted at $t = 0$, the resulting surface divides the space into two non-connected sub-domains of equal volume. The volume of these sub-domains can be adjusted by varying *t*, to thicken or thin surfaces. A network phase TPMS lattice can be created by solidifying the volume for $U(x, y, z) > t$ or $U(x, y, z) < t$. On the other hand, a matrix phase TPMS lattice can be created by solidifying the volume for $U(x, y, z) = \pm t$. The difference between TPMS network and matrix phases is illustrated in **Figure 3.1**. These two phases offer different flow paths that could promote differently flow mixing and will be investigated in Chapter 6). The relationship between t and the volume fraction is unique for each TPMS structure and was obtained by curve-fitting with high order polynomials to ensure the lattices have the exact desired volume fraction as reported by Maskery *et al.* [146]. Volume fraction is preferred as a lattice descriptor since it can be used to compare any lattice type. The volume fraction effect on the gyroid matrix geometry is also illustrated in **Figure 3.1**. It is desirable to design structures with tailorable volume fractions because it is known to influence much of the thermal and structure performance.

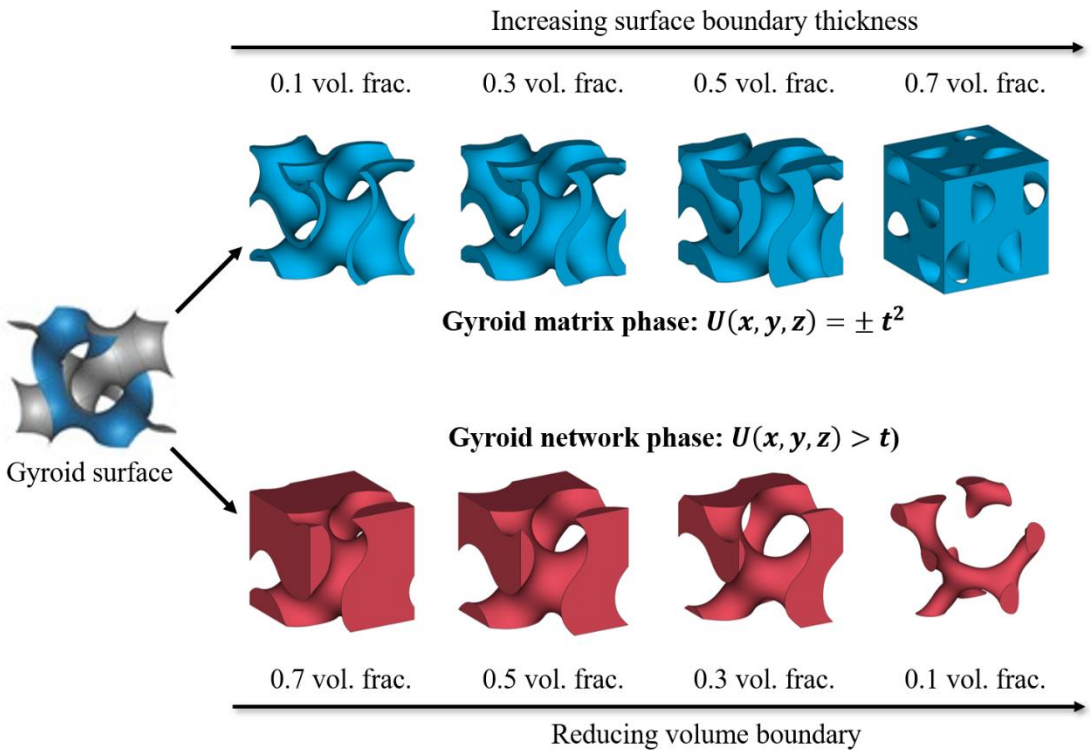
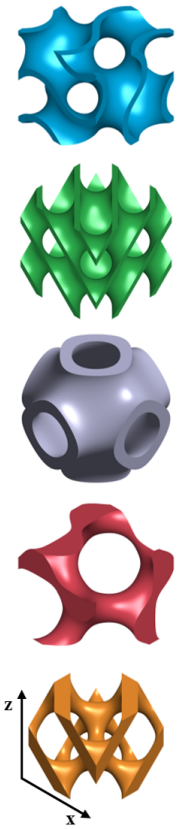


Figure 3.1: Illustration of the gyroid matrix and network phase definition and the effect of volume fraction.

In this thesis, five different lattice unit cell designs have been investigated and are represented in **Figure 3.2** with the TPMS equation (**Equation 3.5 – 3.9**) used for their generation. These structures have been chosen due to their different geometries offering various material distribution and flow paths, thus exhibiting different thermal performance. Furthermore, their mechanical properties have already been studied [20,146], as reported in the literature review (see section **2.3.2**), and their thermal characterisation would enable their application for thermo-mechanical loads.



$$U_{gyroid\ matrix} = \left(C_xS_y + C_yS_z + C_zS_x\right)^2 = \pm t^2 \quad \textbf{Equation 3.5}$$

$$U_{\text{diamond } matrix} = \left(C_xC_yC_z + S_xS_yC_z + S_xC_yS_z + C_xS_yS_z\right)^2 = \pm t^2 \quad \textbf{Equation 3.6}$$

$$U_{primitive\ matrix} = C_x + C_y + C_z = \pm t \quad \textbf{Equation 3.7}$$

$$U_{gyroid\ network} = C_xS_y + C_yS_z + C_zS_x > t \quad \textbf{Equation 3.8}$$

$$U_{diamond\ network} = S_xS_yS_z + S_xC_yC_z + C_xS_yC_z + C_xC_yS_z > t \quad \textbf{Equation 3.9}$$

Figure 3.2: Representation of lattice structures used in this thesis and their associated surface equations.

The lattice structures were generated using in-house developed software called FLatt Pack, based on MATLAB code and developed by Dr. Ian Maskery [113,115,146,147]. FLatt Pack stands for Functional Lattice Package. The program allows the generation of lattice structures within several types of customisable bounding box geometries (cuboid, cylindrical, spheroid, or defined by user input via STL file). Then, the number of cell repetitions in x, y, z direction is inputted, and the lattice unit cell design is chosen before entering the lattice volume fraction profile which is calculated via built-in relationships between t and the volume fraction. The software provides further customisation such as graded volume fraction, shift and/or rotating the unit cell, structure skinning, etc. Finally, the lattice design is generated and are exported as STL files.

3.2.2 CAD software

Designs beyond basic shapes (i.e. cuboids), such as pin fins, were created using Solidworks 2018-2019 by Dassault Systèmes (France). Solidworks is a 3D CAD software package, designed parts were exported to STL file format, using a deviation and angle tolerances below 0.0106 mm and 1°, respectively.

3.2.3 STL files and corrections

Materialise Magics software version 21.1 from Materialise NV (Belgium) was used to load, fix, and adjust .STL files. Structures need to be watertight and error-free to avoid any issues during the subsequent slicing and hatching steps. The files were checked for inverted normals, bad edges, water tightness, noise shells and intersecting or overlapping triangles. Automatic adjustments were performed using Magics software proprietary algorithm with a stitching tolerance of 0.01 mm to remove such imperfections in the models. STL files of lattice structures are made with a high number of triangles (>100,000) and achieving a defect-free part can be non-trivial. Overlapping or intersecting triangles corrections were undertaken to limit them to a low number (<50). However, simpler geometries (i.e. with low number of triangles) were fixed to be defect-free.

3.2.4 Machine pre-processing

Machine pre-processing software was provided by Realizer GmbH and Renishaw plc. RDesigner version 0.93.183 was used for the Realizer SLM50 desktop machine and QuantAM software version 5.1 for the AM250 and AM400 machines from Renishaw plc (UK). RDesigner and QuantAM software can generate support structures, anchoring the overhanging areas of the models to the build plate. The layout and orientation of the parts in the build environment were also completed with these two programs. Each part can be

assigned with a material file that includes parameters such as scan strategies, laser power, scan speeds, and layer thickness, etc. The material files were created in RDesigner and Renishaw Material Editor version 5.1 for the respective system. The final layout assigned with the material files was sliced, hatched, and converted into machine files (RDN files for Realizer and MTT for Renishaw). Visualisation of the scan paths was performed before transferring the file to the machine. The Realizer SLM50 system was controlled using ROperator software version 1.0.2.295.

Advanced scan strategies for the parameter development of high-strength aluminium alloys were not available in QuantAM software. Instead, they were created using a MATLAB script developed in-house by Dr. Luke Parry. This code inputs the specimen geometry from an STL file and the process parameters as well as the number and position of specimen and output an MTT file ready to be transferred to the Renishaw LPBF machine. This was necessary to gain control of the cooling rates and was used to define the custom scan strategy such as multi-scans or 2nd order Hilbert curve fractal used in chapter 7.

3.3 Laser Powder Bed Fusion equipment

3.3.1 Realizer SLM50

Three different LPBF machines were used for the work in this thesis. The machine used to manufacture Ti6Al4V bulk and lattice specimens was a Realizer “SLM50” desktop machine illustrated in **Figure 3.3**. The SLM50 machine uses a continuous ytterbium fibre laser (YLM-100-AC) with a maximum power of 100 W and a powder bed spot size of 20 µm. The laser has a wavelength of 1070 nm. The built envelope of this machine is Ø70 mm by 40 mm high, which is ideal for the manufacture of small specimens and material development.

All Ti6Al4V builds were conducted with a Ti6Al4V substrate heated to 200 °C in a protective Ar atmosphere with an oxygen content kept <0.2 % by volume. A double silicone blade was used to spread the powder and wipe twice the powder bed to ensure good compactness of the layer. Process parameters were derived from previously published work by Simonelli *et al.* [148] and the parameters used to fabricate Ti6Al4V specimens are reported in **Table 3.1**.

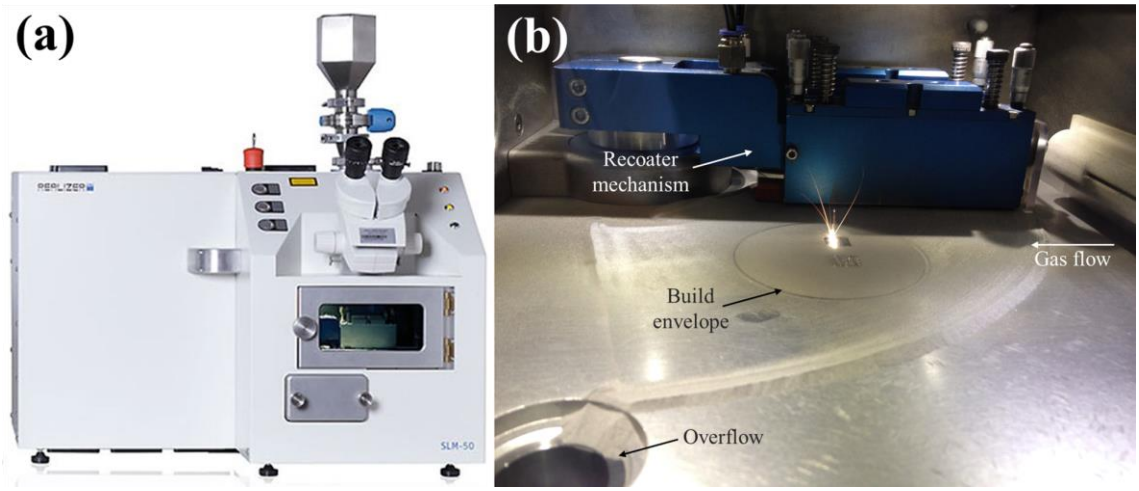


Figure 3.3: Realizer SLM50 LPBF machine, (a) outside (b) Inside chamber.

Table 3.1: Process parameters used to manufacture Ti6Al4V bulk and lattice specimens on Realizer "SLM50" LPBF machine.

	Inner fill	**Border**
Laser power (W)	80	40
Point distance (µm)	30	10
Exposure time (µs)	40	40
Hatch distance (mm)	0.09	
Hatch offset (mm)	0.06	
Layer thickness (µm)	40	
Focus position (mm)	12.5	
Scan strategy	1×X, 1×Y	

3.3.2 Renishaw AM250

AlSi10Mg bulk and lattice specimens have been manufactured with a Renishaw "AM250" laser powder bed fusion system (shown in **Figure 3.4**) from Renishaw plc (UK). It has a ytterbium fibre continuous wavelength laser made by SPI Laser (UK) with a wavelength of 1070 nm ± 10 nm and a spot size of 70 μm ± 5μm. The maximum laser power is 200 W with a maximum laser speed up to 1000 $mm \cdot s^{-1}$. The machine has a build volume of 250 mm × 250 mm × 360 mm. This machine was used for producing all AlSi10Mg lattices onto an aluminium alloy build plate maintained at 80 °C. The build plates, with a minimum thickness of 25 mm, were supplied by Aalco Metals Ltd (UK) and were made from aluminium alloy 5083-O (BS EN 573-3:2009). This alloy is known to retain its strength after welding, making it ideal for LPBF, which can be considered as a powder-based micro-welding process.

Before fabrication, the whole chamber is pumped to near-vacuum before being filled with protective argon gas to minimise oxidation and contamination, and the oxygen content was kept below 500 parts per million during fabrication. A checkerboard scanning strategy (also called island scanning strategy) was used and the process parameters were derived from previously published work by Aboulkhair *et al.* [66] are reported in **Table 3.2**.

The inside chamber of the Renishaw AM250 LPBF system is displayed in **Figure 3.4**. The metal powder is stored, in a hopper, at the top of the machine and is distributed by a gravity-based dosing mechanism. A silicone blade arm controls the opening and closing of the system to dispense a defined volume of powder. The arm then moves forward and spreads the powder onto the build plate, in a single motion, and an overflow located at the end collects any powder excess into a canister. The powder excess can be later sieved and used to top up the hopper during the manufacturing process to maximise powder

usage. All produced specimens had an extra 1.5 mm solid extrusion at their bottom to allow them to be removed from the build plate wire-Electrical Discharge Machining (EDM).

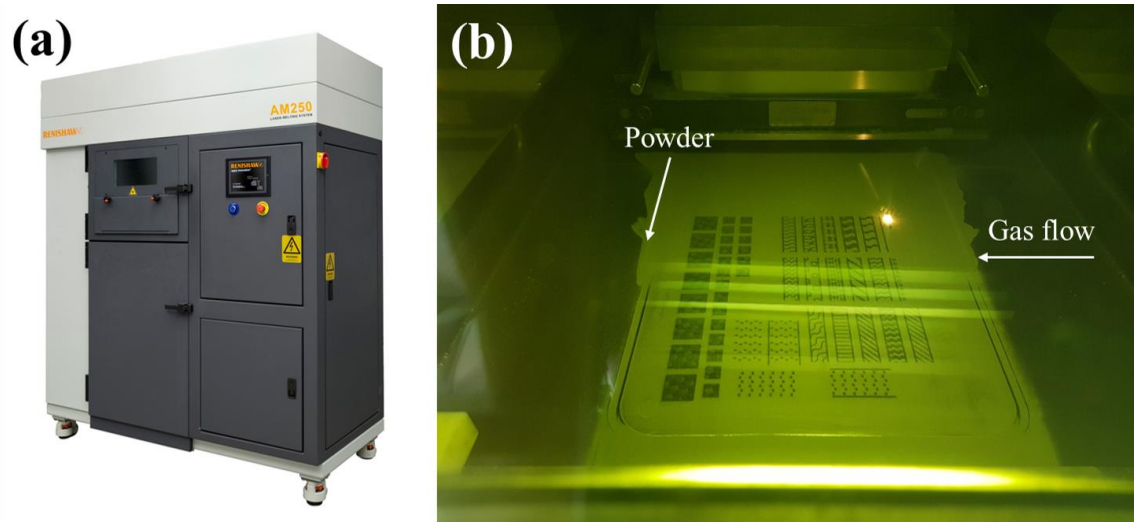


Figure 3.4: (a) Renishaw AM250; (b) inside chamber of Renishaw AM250 and AM400 LPBF machine chamber.

Table 3.2: Process parameters used to manufacture AlSi10Mg bulk and lattice specimens on Renishaw "AM250" LPBF machine.

	Value
Laser power (W)	200
Point distance (µm)	140
Exposure time (µs)	80
Hatch distance (µm)	130
Layer thickness (µm)	25
Hatch scan	5 mm island
Island rotation (°)	67

3.3.3 Renishaw AM400

The development of aluminium alloy EN AW 2618 and A20X has been carried out using an "AM400" from Renishaw plc (UK), which is similar to the AM250 with a maximum laser power of 400 W. The AM400 LPBF machine also offers the possibility to use a reduced build volume (RBV), shown in **Figure 3.5**. The RBV is a retrofit insert that allows to speed up material or process parameter development by using small amounts of material (typically <1 kg compared to >15 kg needed for the normal dosing mechanism). The maximum build envelop is 78 × 78 × 55 mm. Powder is delivered using a dosing piston that moves incrementally upwards before the recoater arm passes over it and spread a thin layer of powder across the build plate. The build platform does not include a heater, thus there is no possibility to pre-heat the build plate and maintain a constant temperature throughout the manufacturing process. The RBV was only used for asserting the A20X suitability with LPBF by building thin walls and initial cubes. Once the process parameters window had been explored and reduced, the machine was reverted to use its full capability.

Unlike Ti6Al4V and AlSi10Mg, there was no optimised set of processing parameters for EN AW 2618 and A20X with the Renishaw AM400 LPBF machine. Consequently, the best combination of parameters in terms of laser power, point distance, and exposure time and scan strategy, whilst keeping the layer thickness and hatch distance constant was determined to achieve fully dense and crack-free material. This will be covered in chapter 7.

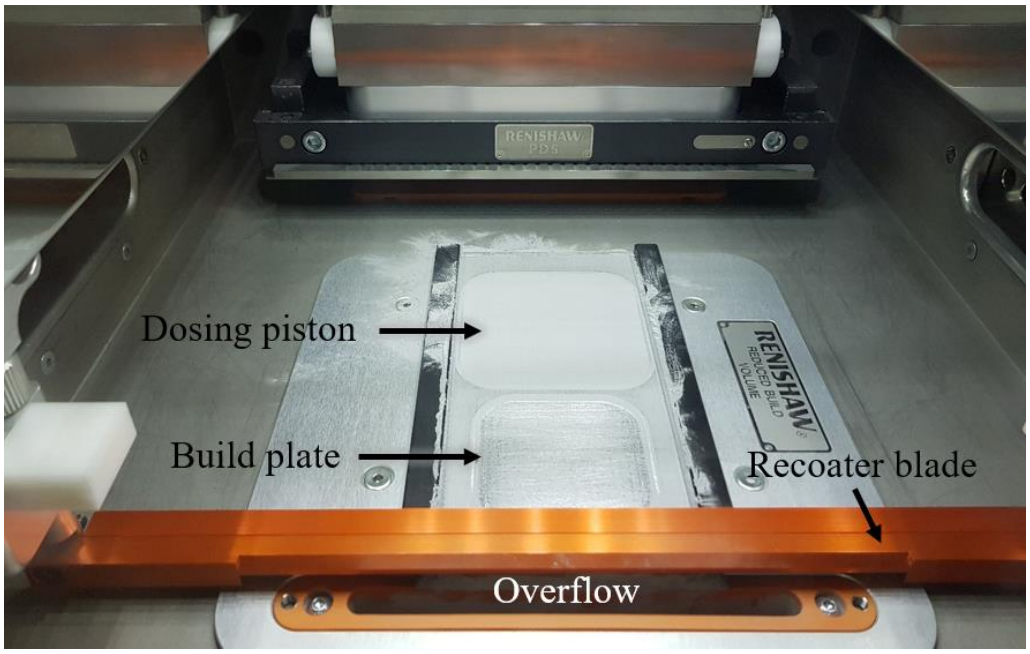


Figure 3.5: Renishaw AM400 reduced build volume environment.

3.4 Metal powders

Characterisation of the powder feedstock for LPBF is an important task since imperfections from the feedstock can lead to possible defects in the final manufactured part. Three main points are examined [149]. Firstly, particle shape influences the overall flowability of the powder, hence the ideal morphology is spherical [150]. Secondly, the particle size affects flowability but also the homogeneity of the spread layer [149]. Large particles (typically > 63 μm) may not receive enough energy from the laser to completely melt, or on the other hand, small particles may be overexposed causing them to ball, spatter or swell [151]. Furthermore, a high number of fine particles are also non-desirable since they have a strong tendency to form aggregates [152]. Thirdly, the chemical composition is examined to verify the absence of contamination and impurities in the powder feedstock. These can lead to porosity or inclusions defects and therefore reduce drastically the mechanical properties.

The shape of the different powders was examined using a “tabletop TM3030” scanning electron microscope (SEM) from Hitachi High-Technologies (Japan) equipped with a secondary electron (SE) detector. Images were taken using an acceleration voltage of 15 kV along with an energy dispersive X-ray (EDS) spectrometer for elemental composition analysis and Quantax 70 software from Bruker.

The powder size distribution was measured using a “Mastersizer 3000” from Malvern Panalytical Ltd (UK). It was equipped with an “Aero S” dry powder disperser which accelerates particles through a venturi using compressed air and pulled them through the measurement cell using a vacuum source with a pressure of 1 bar. The powder size is determined by measuring the intensity of light scattered as a laser beam passes through the dispersed particles. This technique is also known as low angle laser light scattering (LALLS). A minimum of 15 seconds was used as measurement duration to reduce variability as recommended by ISO 13320:2009 [153]. A minimum of three measurements was taken per specimen for each type of powders, taken at different locations in the powder containers. The reported powder distribution results correspond to the average of the measurements. The Dv represents the volume distribution, with Dv10, Dv 50 and Dv90 are the size of particle in microns which respectively lies below 10 %, 50 %, 90 % of the specimen. Powders were stored in air-tight containers between uses with silica gel bags to minimise oxygen contamination, however, the loading of powders into the AM machines and the sieving does introduce a source of oxygen exposure.

3.4.1 Ti6Al4V powder

A plasma atomised Ti6Al4V metal powder alloy was supplied by LPW Technology Ltd (UK) with a centred powder size distribution, reported by the manufacturer, of 5 % below 15 μm and 5 % higher than 45 μm and 90 % between 15 and 45 μm. The powder was

spherically shaped with a few small particles as seen in **Figure 3.6(a)**. The powder size distribution had an average Dv50 of 31.7 µm as reported in **Figure 3.6(b)**. The chemical composition is reported in **Table 3.3** and was found to be within the specifications.

After each build, the powder was recycled by manual sieving with stainless steel sieve with a mesh size of 63 µm purchased from Scientific Laboratory Supplies Ltd (UK). After sieving, the powder was stored back into an air-tight container with silica gel desiccant.

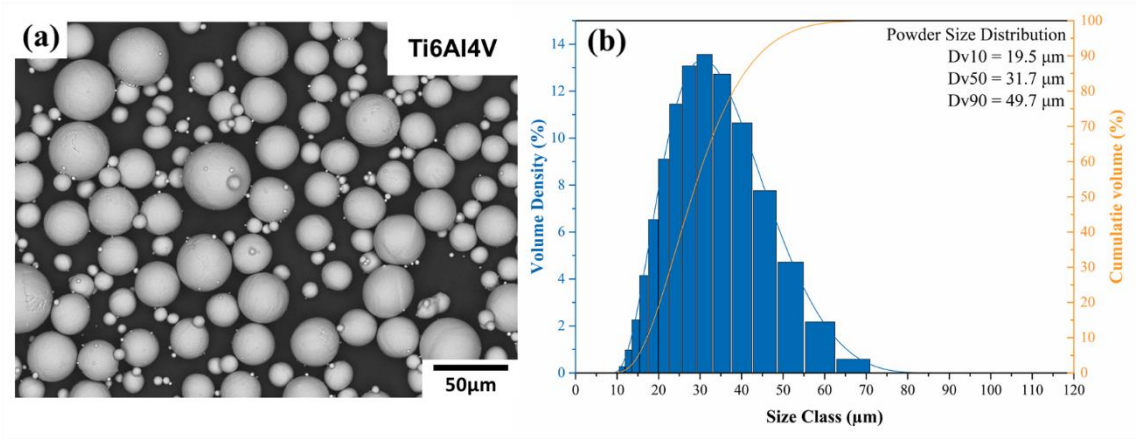


Figure 3.6: Ti6Al4V powder (a) SE SEM image at X500 magnification, (b) Powder size distribution.

Table 3.3: Ti6Al4V chemical composition supplied by LPW Technology Ltd (UK).

	Ti	Al	V	Fe	O	C	N	H
Min	Bal.	5.5	3.5	<0.25	<0.13	<0.08	<0.03	<0.0125
Max		6.5	4.5					
LPW	89.5	6.2	4.1	0.04	0.1	0.01	0.01	0.0033
EDS	89.7	6.1	4.1	<0.1	-	-	-	-

3.4.2 AlSi10Mg powder

AlSi10Mg was argon gas atomised provided by LPW Technology Ltd. The powder was spherical with few satellites and almost no irregular shapes particles as shown in **Figure 3.7(a)**. The manufacturer ensured a centred powder distribution, where 99.5 % of particle size is below 63 μm and 7.89 % is below 20 μm. The measured powder distribution is reported in **Table 3.7**. The entire distribution was slightly shifted to a higher particle mean size compared to the specification, due to many cycles of sieving and reuse as also reported by Ardila *et al.* [154]. The chemical composition provided by LPW is reported in **Table 3.4** and is within the standard for AlSi10Mg alloy. The powder was recycled during the manufacturing process by using an "MS400" high-capacity vibrating stainless steel sieve from Russell Finex Ltd equipped with a 63 μm mesh aperture.

The chemical composition, size distribution, and morphology met the typical requirements of AlSi10Mg and thus the manufactured parts should exhibit similar properties as found in the literature.

Table 3.4: AlSi10Mg chemical composition supplied by LPW Technology Ltd (UK).

	Al	**Si**	**Mg**	**Fe**	**Mn**	**Cu**	**Pb**	**Zn**	**Ti**	**Ni**
Min	Bal.	9	0.2	<0.55	<0.45	<0.05	<0.05	<0.1	<0.15	<0.05
Max		11	0.45							
LPW	89.11	9.71	0.41	0.50	0.06	0.05	0.04	0.04	0.02	0.02
EDS	89.2	9.9	0.4	0.5	-	-	-	-	-	-

3.4.3 EN AW 2618 powder

EN AW Aluminium alloy 2618 (AA2618) was provided by TLS Technik GmH & Co. Spezialpulver KG. The powder had a spherical shape but contains a number of small particles and satellites as reported in **Figure 3.7(b)**. This was seen to affect the flowability of powder during the manufacturing process and in some occurrence has led to clogging in the powder hopper or the overflow system. Good layer compaction was achieved by reducing the recoater speed. The size distribution reported in **Table 3.7** was broad, ranging up to 120 μm, but the measurements could be affected by the large presence of small aggregated particles. It also confirms the high content of fines with a Dv10 of 15 μm. The manufacturer specified a Dv90 of 61.7 μm which is 17 % lower than the value measured. This could be due to aggregated particles. The chemical composition shows a higher amount of Mg than the standard value, however, Mg can be vaporised during the LPBF process due to its low boiling point (1090 °C [155]).

The powder was recycled during the manufacturing process by using an "MS400" high-capacity vibrating sieve equipped with an ultrasonic deblending from Russell Finex Ltd. The screen had a mesh aperture of 63 μm mesh aperture.

Table 3.5: AA2618 chemical composition supplied by TLS Technik GmH.

	Al	**Cu**	**Mg**	**Fe**	**Ni**	**Si**	**Ti**	**Zn**
Min	Bal.	1.80	1.20	0.90	0.80	0.15	<0.20	<0.15
Max		2.70	1.80	1.40	1.40	0.25		
TLS	93.6	2.6	1.55	0.95	1	0.2	0.1	<0.002
EDS	92.9	2.4	2	1.1	1.1	0.2	0.2	0.1

3.4.4 A20X powder

The A20X is cast in ingot by Aeromet International Ltd and is atomised by different atomiser companies. In the first part of this work, the powder used was atomised by ECKA Granules GmbH (Germany). The SEM observation, presented in **Figure 3.7(c)**, shows the powder morphology was spherical and had a high content of fines. This is further confirmed with the powder size distribution reported in **Table 3.7** with a Dv10 of 14.9 μm, an average particle size of 33.4 μm and 90 % of the powder is below 51.4 μm. The large amount of fines is believed to cause the observed clogging issues and uneven layer height during recoating.

After heat treating specimens manufactured by LPBF, spherical pores were observed, concluded to originate from hydrogen contamination in the supplied powder. A new batch was ordered with a different atomiser company, TLS Technik GmH (Germany), and the previous powder batch was discarded.

The powder distribution reported in **Table 3.7** changed significantly between the second and first batch with an average particle size of 44.8 μm compared to 33.4 μm, respectively. The number of fines has been reduced as Dv10 value of 26.4 μm suggests compared to 14.9 μm previously. The distribution is also larger with a Dv90 of 71.6 μm.

Both A20X powder batches were recycled by sieving through a screen with a mesh aperture of 63 μm using the “MS400” high-capacity vibrating sieve from Russell Finex Ltd.

Table 3.6: A20X powder chemical composition supplied by the manufacturers.

	Al	Cu	Mg	Ag	B	Ti	Si	Fe
Min	Bal.	4.2	0.2	0.6	1.25	3.0	<0.1	<0.08
Max		5.0	0.33	0.9	1.55	3.85		
ECKA (batch 1)	88.74	4.80	0.30	0.80	1.54	3.74	0.05	0.03
TLS (batch 2)	88.68	4.78	0.31	0.82	1.52	3.80	0.06	0.03

Table 3.7: Powder size distribution of the materials studied in this thesis.

Powder	Dv10 (µm)	Dv50 (µm)	Dv90 (µm)
AlSi10Mg	19.7	35.7	61.1
EN AW 2618	15.0	41.5	74.3
A20X Batch 1	14.9	33.4	51.4
A20X Batch 2	26.4	44.8	71.6

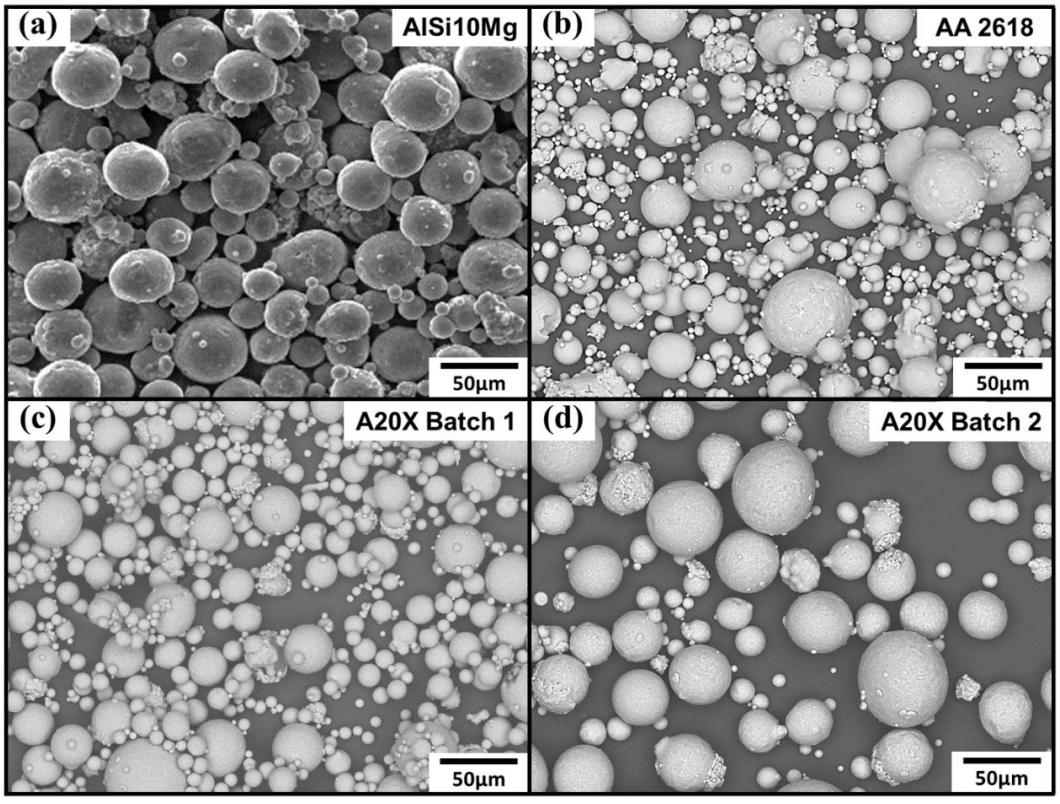


Figure 3.7: SE SEM images (×500) of the powder used in this thesis.

3.5 Parameter optimisation and process validation

3.5.1 Process parameter optimisation

LPBF process parameter optimisation of high-strength aluminium alloy was conducted in this thesis using a Renishaw "AM400" machine (see **section 3.3.3**). The best combination of parameters in terms of laser power, point distance, and exposure time and scan strategy, whilst keeping the layer thickness and hatch distance constant, was determined to achieve fully dense and crack-free material. To help the process parameter optimisation the linear energy density (E_L) was used to compare the amount of heat the powder bed received between the tested conditions and is defined as:

$$E_L = \frac{P}{s_v} \qquad \textbf{Equation 3.10}$$

where P and s_v are the laser power and scan speed which corresponds to the point distance divided by the exposure time. The aim of controlling energy density is to produce fully dense parts by exposing the powder to sufficient heat without overheating. High energy density can produce many types of defects such as vaporisation of low melting point elements, thermal stresses, trapped porosity. On the other hand, not enough energy creates porosity due to lack of fusion. Reducing the linear energy density can be achieved by lowering laser power, exposure time, increasing point distance. It must be mentioned that a range of laser powers and scanning speeds can produce the same energy density. Despite its drawbacks, this metric is widely used in the literature [156] and was used in this thesis owing to its simplicity.

3.5.2 Specimen preparation for microstructure and porosity

To characterise the porosity and microstructure of the different specimens produced by LPBF, 10 mm × 10 mm × 10 mm metallographic specimens were manufactured along with the test specimens. These cubes were used to measure the relative density, observe the microstructure, and measure the hardness, by sectioning the cubes in two and studying the inside surface. The cut was in different planes (*xy*, *xz*, or *yz*) to study the build orientation effect as illustrated in **Figure 3.8**.

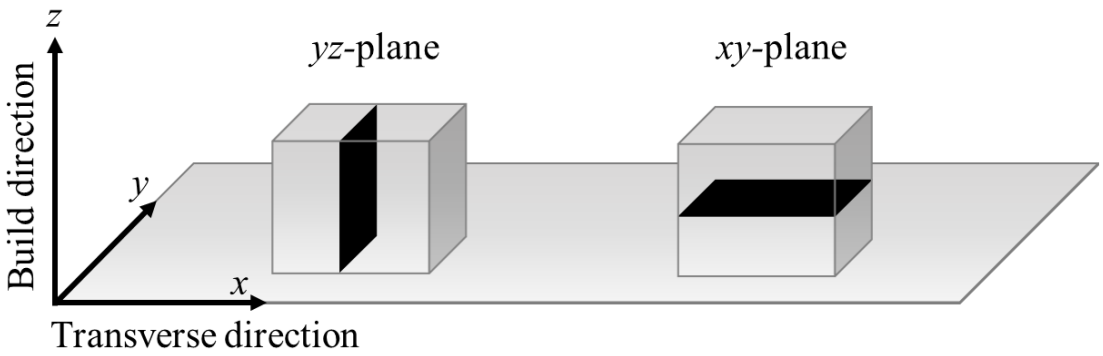


Figure 3.8: Build axis and orientation, represented in black the cross-sections examined for porosity and microstructure analysis.

The metallographic preparation was tailored for each material studied in this thesis (Ti6Al4V, AlSi10Mg, AA2618, and A20X). The Ti6Al4V specimens were prepared according to Struers application notes for Ti6Al4 [157]. The AlSi10Mg, AA2618, and A20X metallographic specimens were prepared as reported in **Table 3.8**, **Table 3.9**, and **Table 3.10**, respectively. To aid the reader, OP-S non-dry colloidal silica (0.25 μm) has been abbreviated to OP-S in the aforementioned tables. To reveal the microstructures of the aluminium alloys, specimens were etched in Keller's reagent for 5 – 10 seconds and rinsed before microscopy.

Table 3.8: Grinding and polishing procedure for LPBF AlSi10Mg.

Step	Media	Lubricant	Speed (rpm)	Time
1	SiC #240	Water	300	As desired
2	SiC #400	Water	300	Until plane
3	SiC #800	Water	300	60 s
4	SiC #1200	Water	300	60 s
5	MD-Mol	Dia Mol R3 3 µm diamond	150	120 s
6	MD-Chem	OP-S	150	<30 s

Table 3.9: Grinding and polishing procedure for LPBF EN AW AA2618.

Step	Media	Lubricant	Speed (rpm)	Time
1	SiC #240	Water	300	As desired
2	SiC #400	Water	300	Until plane
3	SiC #800	Water	300	60 s
4	SiC #1200	Water	300	60 s
5	MD-Mol	Dia Mol R3	150	120 s
6	MD-Chem	OP-S	150	<30 s

Table 3.10: Grinding and polishing procedure for LPBF A20X.

Step	Media	Lubricant	Speed (rpm)	Time
1	SiC #240	Water	300	As desired
2	SiC #400	Water	300	Until plane
3	SiC #800	Water	300	60 s
4	SiC #1200	Water	300	60 s
5	SiC #2500	Water	300	60 s
6	SiC #4000	Water	150	120 s
7	MD-Chem	OP-S	150	<30 s

The microstructure analysis and optical relative density measurements of the metallographic specimens were performed using a Nikon "Eclipse LV100ND" microscope with "TU Plan Fluor EPI" lenses and a 2560 × 1920 pixel colour sensor. Micrographs at minimum ×50 magnification covering a minimum of 340 mm^2 per section and a minimum of two sections per specimen were used to estimate the relative density. This was achieved using automated image thresholding and pore counting in the ImageJ image analysis software [158]. The images were imported into the software and converted to 8-bit grey-scale and a thresholding was performed on each image using the 'MaxEntropy' method. A threshold of 4 pixels was set as a minimum to detect a pore. The microstructures of AlSi10Mg, EN AW 2618, and A20X were also imaged and analysed using an "FEI Quanta 600" scanning electron microscope (SEM) with secondary and backscattered electron detection using an acceleration voltage of 20 kV and a Bruker electron dispersive x-ray spectrometer (EDS) was used for elemental composition analysis.

3.5.3 X-ray diffraction analysis

X-ray diffraction (XRD) analysis was performed using a Bruker AXS "D8 Advance" equipped with a "Da Vinci X-ray diffractometer" system and was used with Cu k-α monochromatic radiation source and DIFFRAC.WIZARD software. Copper X-ray radiation has a wavelength of 0.154 nm, close to the lattice spacings of many materials, including aluminium alloys, yielding a high count, thus a high signal to noise ratio. The diffractometer was used in Bragg-Brentano configuration with 2θ varying from 20° to 110° with a step value of 0.02° and a step time of 0.2 s. A constant rotation was applied to specimens, except to powder for safety reasons, during the scan to improve statistics. Bulk specimens were ground flat and polished up to P1200 SiC paper before they were mounted with plasticine onto the specimen holders. Powders were mounted into dedicated

specimen holders supplied by Bruker AXS. After the XRD scan, data was exported to DIFFRAC.EVA V4.2 software to be post-process. Post-processing steps include background subtraction and filtering k-α_2 using built-in software tools. Indexing peak was realised using the "Search/Match" function and the "PDF-2 release 2015 RDB" database from the International Centre for Diffraction Data (ICDD).

3.5.4 Hardness testing

Hardness testing was performed following the ASTM E92-17 [159] using an automated "Wilson VH3100 micro-hardness indenter" from Buehler Ltd. The machine was controlled with "Wilson DiatMet" software version 1.7.8010 provided by the machine manufacturer. The micro-hardness of AlSi10Mg and A20X was measured on mirror-polished surfaces (following the procedure described in **section 3.5.2**) using a Vickers indenter applying a load of 0.5 kg and averaging over a grid of a minimum of 20 points with at least 0.7 mm *xy*-spacing.

EN AW 2618 hardness was measured using a Buehler Ltd "1600-6400 micro-hardness tester" with a Vickers indenter with a load condition of 300 gf. A minimum of 15 points with at least 0.7 mm *xy*-spacing was averaged.

3.5.5 T7 Heat treatment investigation

A heat treatment investigation was performed to explore the effect of T7 heat treatment for A20X produced by LPBF. Cubes of 10 mm with 1.5 mm supports using the optimised process parameters developed in Chapter 7 were manufactured by LPBF. Firstly, specimens were only solution heat-treated (SHT) at 520 °C, soaking time was varied between 0.5, 1, 2 hours and was followed by water quenching to room temperature. The effectiveness of the SHT was determined by the dissolution of the Al_2Cu phase in the XRD pattern. One specimen remained in the as-built condition acting as reference point.

After the determination of the best soaking time for SHT, specimens were subjected to a full T7 heat treatment. It consists of a SHT at 520 °C followed by water quenching to room temperature then artificial ageing (AA) at 160 °C. The AA provokes the precipitation of secondary phases to provide increased strength and hardness. T7 temper is overaged and stabilised meaning that some degree of strength has been traded-off to improve other characteristics. In the case of A20X, it is intended to serve at elevated temperatures (up to 150 °C) requiring improved dimensional stability. T7 also increases ductility and resistance to stress corrosion cracking. The ageing durations employed were from 4 to 22 hours with 2 hours intervals. The heat treatments were conducted in an air furnace since the time interval between solution heat treatment and water quenching must be minimised and this would not be possible with a controlled atmosphere furnace.

The specimens were cross-sectioned, mounted, polished, and etched as previously reported in **section 3.5.2**. The influence of the different ageing durations on mechanical properties was evaluated by micro-hardness testing using the procedure reported in **section 3.5.4**.

3.5.6 Tensile testing

Tensile test specimens were designed based on ASTM E8/E8M [160] ‘Specimen 4 – test specimens with gauge length (20.0 mm) five times the diameter. LPBF regular hexagonal cross-section billets with an edge length of 6 mm and a total bar length of 58 mm were produced by LPBF in both build and transverse direction. After manufacture, the billets were cut by wire-EDM to release them from the build plate. Heat treatments were performed on the stock material after wire-EDM. As-built and heat-treated hexagonal bars were then machined to the dimensions prescribed in the ASTM E8/E8M and reported in **Figure 3.9(a)**.

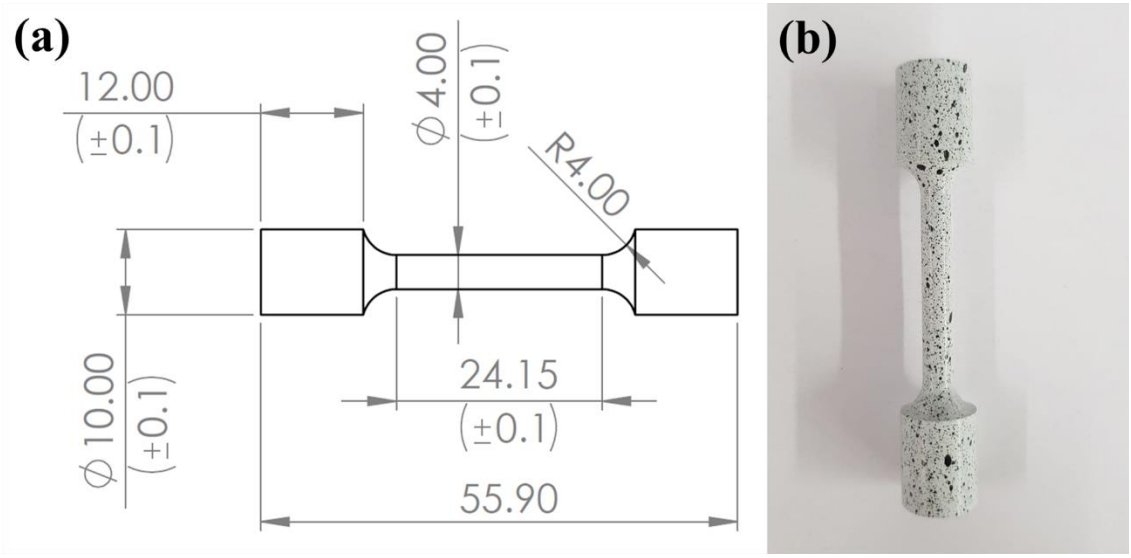


Figure 3.9: (a) Tensile test specimen dimensions (in mm); (b) Machined tensile bars spray-painted with a speckle pattern for strain measurement.

Monotonic uniaxial tension tests were carried out using an Instron 5969 universal testing machine with a load cell that has a maximum capacity of 50 kN. The load cell calibration/rating is UKAS class 0.5 down to 0.5 kN in tension. The tests were also conducted per ASTM E8/E8M. The cross-head speed was 0.1225 $mm \cdot min^{-1}$ employing a strain rate of 0.005 $mm \cdot mm^{-1} \cdot min^{-1}$. The tensile specimen surface was painted matt white with a matt black speckle pattern using spray paint (see **Figure 3.9(b**)) to collect strain data using an iMETRUM video extensometer equipped with a telecentric lens. This painted pattern was necessary to track the deformation of the test specimen via the camera of the video extensometer which is not possible when the surface is machined and devoid of recognisable features. The tensile properties were tested in each condition with 8 specimens in the transverse direction and 16 specimens in the build direction.

3.6 Summary

This research sets out to determine the capability of LPBF and lattice structures for thermal applications in aerospace. To explore this potential, the thermal conductivity of material and lattice structures that are manufactured by LPBF needs to be identified. Lightweight and aerospace alloys are the focus of this thesis: Ti6Al4V titanium alloy, EN AW 2618, A20X, and AlSi10Mg aluminium alloys. Despite its low thermal conductivity, Ti6Al4V is interesting due to its high-temperature performance and corrosion resistance and is widely used in aerospace. It also can be processed to high relative density using LPBF. AlSi10Mg is attractive due to its good specific thermal conductivity and is the go-to alloy with LPBF. Ti6Al4V and AlSi10Mg processing parameters were derived from previously published results [66,148]. High-strength aluminium alloys, EN AW 2618 and A20X are attractive due to their mechanical properties and pave the way for thermomechanical components but process parameters had to be developed and were based on AlSi10Mg. These materials were processed on a Realizer SLM50 for Ti6Al4V and a Renishaw AM250 for AlSi10Mg, and high-strength aluminium alloys 2618 and A20X on a Renishaw AM400 due to its higher laser power.

4 Original Method

4.1 Introduction

This chapter details the apparatus developed and used in this thesis as well as data analysis and performance metrics applied throughout the subsequent chapters.

4.2 Thermal conductivity of LPBF components

To achieve the objectives of this thesis, the design, and development of an in-house apparatus to measure thermal conductivity was undertaken. This was done in collaboration with Sam Catchpole-Smith (PhD student at the Centre for Additive Manufacturing, University of Nottingham). There are numerous reasons to develop an in-house apparatus and the major ones are listed below:

- Firstly, commercial measurement equipment exists but tends to be expensive and usually does not give full access to the user to all the control parameters. Furthermore, standard equipment is limited to a specific specimen geometry with no or minor possibility of changes that would not be suitable for LPBF specimens.
- Secondly, outsourcing the measurements would be expensive too considering the large number of specimens and the high manual labour required for the custom measurement technique.
- Thirdly, bespoke measurement techniques give more versatility and quick adjustments can be made to suit specific needs.

Before the design and development of the thermal conductivity apparatus, a review of thermal conductivity measurement methods for metallic material will be given.

4.2.1 Measurement methods for LPBF structures thermal conductivity

Thermal conductivity, λ, of metals is often estimated from their electrical conductivity, κ, through the empirically determined Wiedemann-Franz law (**Equation 4.1**) where T is the temperature and L_N is the Lorenz number which varies with temperature and material studied [161]. The Lorenz number is empirically determined based on electrical and thermal conductivity measurements. Consequently, this technique is unsuitable for asserting the thermal conductivity of lattice structures.

$$\frac{\lambda}{\kappa} = L_N T \qquad \textbf{Equation 4.1}$$

To measure the thermal conductivity of lattice structures, the measurement method needs to accommodate lattices' complex and wide variety of geometries. The complex 3D distribution of material can differ greatly between lattices and prevent precise and repeatable positioning and acquisition of temperature via measurement methods. Also, the conductivity apparatus must cover a wide range of thermal conductivities, given lattice structures can be fabricated with a wide range of volume fractions. Lattice volume fraction in this thesis was specified not to exceed 0.6, since most of the lightweight interest would be lost. Consequently, it is expected that aluminium lattice structure conductivity reaches up to 100 $W \cdot m^{-1} \cdot K^{-1}$ according to **Equation 2.6**. In addition, the base material of the lattice structures also needs to be thermally characterised due to the unique microstructure produced by LPBF and its possible effect on the conductivity. Conventionally cast AlSi10Mg can achieve thermal conductivities up to 170 $W \cdot m^{-1} \cdot K^{-1}$ according to DIN EN 1706:2010, while high-strength aluminium alloys are typically around $200 - 220\ W \cdot m^{-1} \cdot K^{-1}$. Conventionally manufactured Ti6Al4V has a thermal conductivity around 6.4 $W \cdot m^{-1} \cdot K^{-1}$. A lattice made of this Ti6Al4V would exhibit lower conductivity, the lowest targeted volume fraction is 0.15, which gives an estimated

thermal conductivity of approximately 0.4 $W \cdot m^{-1} \cdot K^{-1}$ using **Equation 2.6**. Consequently, the apparatus must cover a conductivity range of 0.4 – 220 $W \cdot m^{-1} \cdot K^{-1}$.

Many methods are used to measure the thermal conductivity of metals which can be separated into two categories: steady-state technique (absolute or comparative) and transient methods (hot wire, plane source, laser flash etc.). Each of these methods has its advantage and disadvantage: material, temperature range and conductivity range, specimen size, signal acquisition and analysis complexity, and cost.

In steady-state measurements, the thermal conductivity is measured based on Fourier's law (see **Equation 2.2**) by measuring the temperature difference along with the steady-state heat flow ($q_{conduction}$) across the specimen. This one-dimensional heat flow enables the characterisation of material anisotropy and measures the thermal conductivity of composites, which usually requires measurement of larger areas. However, steady-state methods require long-duration tests to reach thermal equilibrium and suffer from parasitic heat losses (i.e. heat lost to the environment).

Transient methods allow measuring several thermophysical properties simultaneously or cumulatively such as thermal diffusivity, α (i.e. the propagation rate of heat through the material), by pulsing the heat source. The short-duration test (typically a few minutes) reduces the chance to develop fluid convection around the test specimen. It also allows testing at high temperatures without suffering from great heat losses or requiring complex insulation to prevent losses to the environment. However, the transient techniques are limited to thin geometries and therefore not appropriate for the investigation of AM lattices.

A list of different methods to measure thermal conductivity for metals and lattice structure is reported in **Table 4.1** along with the applicable temperature and thermal conductivity range, and the specimen size. Techniques to measure the thermal conductivity such as

3ω [162] or photothermal [163] methods are often reported as a bulk measurement technique. However, they apply to specimens with thickness usually below 1 mm and therefore are not reported in **Table 4.1**. The heat-flow meter technique was also not reported in **Table 4.1** because this technique is reserved for insulating materials with thermal conductivities lower than 1 $W \cdot m^{-1} \cdot K^{-1}$. The guarded heat flow allows to measure thermal conductivities up to 30 $W \cdot m^{-1} \cdot K^{-1}$ or 60 $W \cdot m^{-1} \cdot K^{-1}$ with a reduced accuracy which could be suitable for lattice but not for bulk aluminium alloy specimens whose thermal conductivities are up to 200 $W \cdot m^{-1} \cdot K^{-1}$. The specimen surfaces must be flat and parallel and surface roughness must be below 10 μm [164]. The guarded hot plate technique only allows measuring thermal conductivity in a narrow range, which will be too small for aluminium lattice structures. Also, this technique requires larger specimens than the manufacturable size of commercial LPBF machines (approx. 250 × 250 × 250 mm) and would take days to manufacture a single specimen. The comparative guarded heat flow method offers a wider range of measured conductivities among steady-state methods. The uncertainty on the measurement with technique is higher than the two previously mentioned due to its comparative nature with the use of reference blocks that have precisely known thermal conductivity.

Among the transient methods for measuring solids reported in **Table 4.1**, the transient hot-wire measures a narrow range of thermal conductivity similar to the guarded hot plate conductivity range. Furthermore, this technique requires a drilled groove where the heating and sensing wire is inserted between two specimens or two specimen halves and is not compatible with lattice structures. The transient hot plane also requires a similar setup where a plane sensor is sandwiched in-between specimen halves which makes it not suitable for the measurement of lattice structure despite its wide range of measurable conductivity. However, the main limitation of the transient hot plane technique is the maximum thickness that can be measured and is function of the thermal conductivity of

the tested material. The laser flash method can measure a wide range of thermal conductivities over a wide range of temperatures that could potentially be used to measure lattice structures. It calculates the conductivity of the specimen from the thermal diffusivity and needs the density, ρ, and heat capacity, C_p, of the measured specimen (see **Equation 4.2**). Accurate measurement of those two properties is necessary to reduce uncertainty, which is usually lower than the other measurement methods discussed in this section [165].

$$\lambda = \alpha \rho C_p \qquad \textbf{Equation 4.2}$$

The use of a laser to quickly heat up the non-uniform bottom of the lattice and its open-cell nature may pose a problem to the measurement. Indeed, some lattices have a straight open path from the bottom to the top of the lattice and would likely need modification of the design by adding a top and bottom skin which would have to be accounted for in the thermal conductivity measurement.

The guarded comparative heat flow was selected as the conductivity measurement method over the laser flash method due to its high cost and the possible drawback of measuring lattice structures.

Table 4.1: Review of the main methods to measure the thermal conductivity of solids.

Measurement	Type	Material	Temperature range (K)	λ ($W \cdot m^{-1} \cdot K^{-1}$)	Typical specimen size	Applicable to lattice	References
Guarded hot plate	Steady-state	Transparent & opaque solids, porous	100 – 1500	Typically < 1 Practically < 16	0.2 – 1 m Thickness >10x bigger than smallest inhomogeneity	Yes	ASTM C177-19 [166]
Guarded heat flow	Steady-state	Opaque solids, homogeneous, multilayer, and composite	150 – 600	0.1 – 30 30 < λ < 60 (low accuracy)	< 25 mm	Yes	ASTM E1530-19 [164]
Guarded comparative heat flow	Steady-state	Opaque solids, homogeneous	90 –1300	0.2 – 200	Not reported	Yes	ASTM E1225-13 [167]
Transient plane source (Hot disc)	Transient	Solids, powders, pastes, fluids Homogeneous & isotropic, anisotropic with a uniaxial structure	50 – 1200	0.010 – 500	Dependent on material conductivity and thickness Thickness >20x bigger than smallest inhomogeneity	No	ASTM WK49591 ISO 22007-2 [168]
Transient hot wire	Transient	Refractory material, granules, powders, fluids, and gases anisotropic materials	230 – 1900	0.001 – 20 0.2 – 4	2 rectangular specimens $250 \times 125 \times 75$ mm^3 Minimum size >1mm diameter & 50 mm long	No	ASTM C1113/C1113M-09 [169] Assael *et al.* [170], [171]
Laser flash	Transient	homogeneous isotropic solids, metals, polymers, ceramics	175 – 3300	0.1 – 1500	Diameter 6 to 30 mm Thickness 1 to 6 mm	Potentially	ASTM E1461-13 [172]

4.2.2 Guarded-comparative-longitudinal heat flow technique

The guarded-comparative-longitudinal heat flow technique from the American standard test method (ASTM E1225-13) [173] was selected to measure the thermal conductivity of LPBF specimens. This measurement method allows measurement of thermal conductivity between 0.2 and 200 $W.m^{-1}.K^{-1}$ and an operational range between 90 and 1300 K. The method consists of a test specimen with unknown conductivity inserted under load between two reference blocks of known thermal properties. A thermal gradient is established by heating one side of the stack, whilst cooling the other side. When the system reaches steady-state, the thermal conductivity can be calculated from the measured temperature gradients across each specimen of the stack and the thermal conductivity of the reference blocks. The stack is under load to ensure good contact between each specimen. To minimise heat losses, the test stack is surrounded by insulating material and enclosed within a heated guard shell with a similar temperature gradient to the test stack.

4.2.3 Conductivity apparatus setup

In this work, the specimen size was limited by the LPBF capability (e.g. wall thickness and build envelope). A specimen length of 20 mm was found the most suitable to test various lattice cell sizes and volume fractions without wall thicknesses reaching manufacturing resolution. Also, no size effect is anticipated, therefore this size should be broadly representative. A cubic geometry reduces the number of manufactured specimens since both build and transverse directions could be tested on the same specimen. As a result, the thermal conductivity apparatus was designed for 20 mm cubic test specimens.

A positive temperature controller (PTC) heater, placed at the bottom of the stack, was used as a heat-source and regulated by a PID controller, while the top was water-cooled

with a copper heatsink to maintain a constant 293 K. The temperature of the bottom of the stack was chosen to be large enough so that the temperature gradient across the specimen and reference blocks was at least 30 K. This value led to minimal errors on temperature readings with T-type thermocouples which have an uncertainty of ± 0.5 K. The thermocouples were linked to a Pico 'TC-08' thermocouple data logger. Thermal equilibrium was reached for a temperature drift of less than 0.1 $K.min^{-1}$ at the specimen-reference block interfaces. Data recording started once the system was determined to have reached thermal equilibrium.

Insulation of the test stack was assured by a fibre blanket made from high-temperature insulation wool (calcium magnesium silicates, thermal conductivity of 0.04 $W.m^{-1}.K^{-1}$ at 473 K). Surrounding the insulating blanket, a guard tube is maintained to a temperature equal to the average temperature of the test stack. The top of the guard tube is closed with an insulating ceramic plate and a 5 kg deadweight was applied to the stack via a connecting rod.

After the first test iterations, modifications were made to the experimental set-up to ease the measurement, improve repeatability, and therefore reduce errors. First, loading and aligning the test stack was a difficult task. Two threaded nylon rods were added on the side of the stack to secure it before applying the dead weight. Since the secure mechanism is made of nylon66 (thermal conductivity, 0.24 $W.m^{-1}.K^{-1}$) and is not in direct contact with the stack, this addition is assumed not to affect the result. Second, the lattice complex geometries made it difficult to position thermocouples accurately and repeatedly. To solve this, thermocouples were soldered to thin silver sheets (thickness 0.08 mm) and sandwiched between each block. The conductivity of silver is 420 $W.m^{-1}.K^{-1}$ at 293 K, so its contribution to the total thermal resistance of the stack was assumed to be negligible. Furthermore, to ensure good thermal coupling silicone paste was applied at each interface. A schematic of the modified rig is presented in **Figure 4.1** and the thermal conductivity

of the specimen was calculated using **Equation 4.3** from the ASTM [173], where $\lambda_{specimen}$ and λ_M are the thermal conductivities of the measured specimen and the reference material.

$$\lambda_{specimen} = \frac{Z_4 - Z_3}{T_2 - T_3}\frac{\lambda_M}{2}\left(\frac{T_1 - T_2}{Z_2 - Z_1} + \frac{T_3 - T_4}{Z_6 - Z_5}\right) \qquad \textbf{Equation 4.3}$$

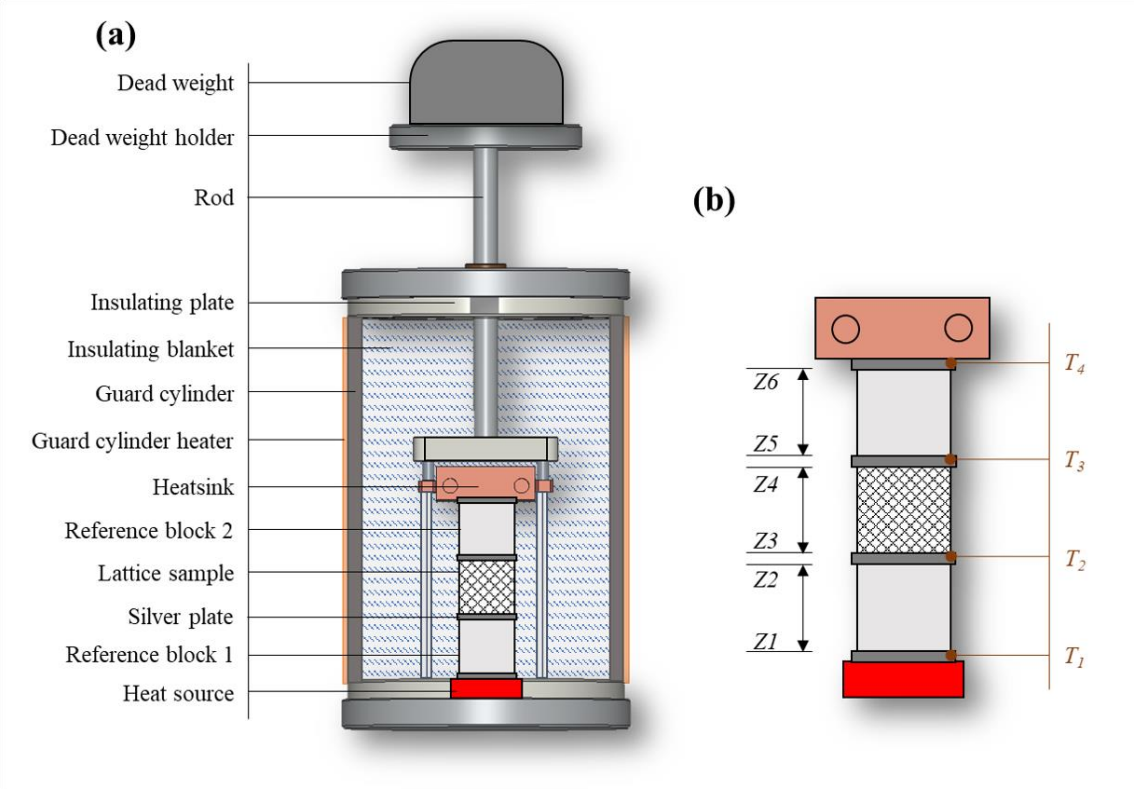


Figure 4.1: (a) Schematic of the apparatus used to measure the thermal conductivity of LPBF specimens. (b) Close view of the test stack with the position of the temperature measurements. Z_i and T_i denote the blocks' height (20 mm) and the position of the thermocouples.

4.2.4 Uncertainty analysis

Uncertainty in the thermal conductivity measurements was estimated following the ASTM E1225-13 standard with the following assumptions:

$$(T_2 - T_3) \sim (T_1 - T_2) \sim (T_3 - T_4) = 30\ K \quad \textbf{Equation 4.4}$$

$$\delta(T_2 - T_3) \sim \delta(T_1 - T_2) \sim \delta(T_3 - T_4) = 1\ K \quad \textbf{Equation 4.5}$$

$$(Z_2 - Z_1) \sim (Z_4 - Z_3) \sim (Z_6 - Z_5) = 20\ mm \quad \textbf{Equation 4.6}$$

$$\delta(Z_2 - Z_1) \sim \delta(Z_4 - Z_3) \sim \delta(Z_6 - Z_5) = 0.1\ mm \quad \textbf{Equation 4.7}$$

The temperature difference across each block was chosen to be around 30 K to achieve a large enough temperature gradient across the specimen and reference blocks to minimise measurement error and will be used for the uncertainty calculations as reported in **Equation 4.4**. The maximum absolute uncertainty of T-type thermocouples was taken to be 0.5 K, as indicated in **Equation 4.5**. The specimen and reference block heights are reflected in **Equation 4.6**, and the maximum measuring error with callipers was ± 0.1 mm, as reported in **Equation 4.7**. The uncertainty of the thermal conductivity of the reference block (λ_{M}) was given by the supplier to be 5 %. With these values, the percentage uncertainty in $\lambda_{specimen}$ is estimated to be ± 7.7 % by propagating these uncertainties through **Equation 4.3**. The uncertainty was calculated and reported for each measurement.

4.2.5 Rig validation: Measuring known material conductivity

Assessment of the conductivity measurement apparatus with its modifications was performed by testing a block made of brass alloy (UNS CW614N) with a known thermal conductivity of 123 $W.m^{-1}.K^{-1}$ at 293 K and using the same material as reference blocks. The results are shown in **Figure 4.2**. The average thermal conductivity out of five measurements is 127 $W.m^{-1}.K^{-1}$ with a standard deviation of 1 $W.m^{-1}.K^{-1}$. The measured

value was overestimated by 4 % compared to the nominal value but was within the uncertainty. The apparatus was therefore shown to provide accurate results for thermal conductivity.

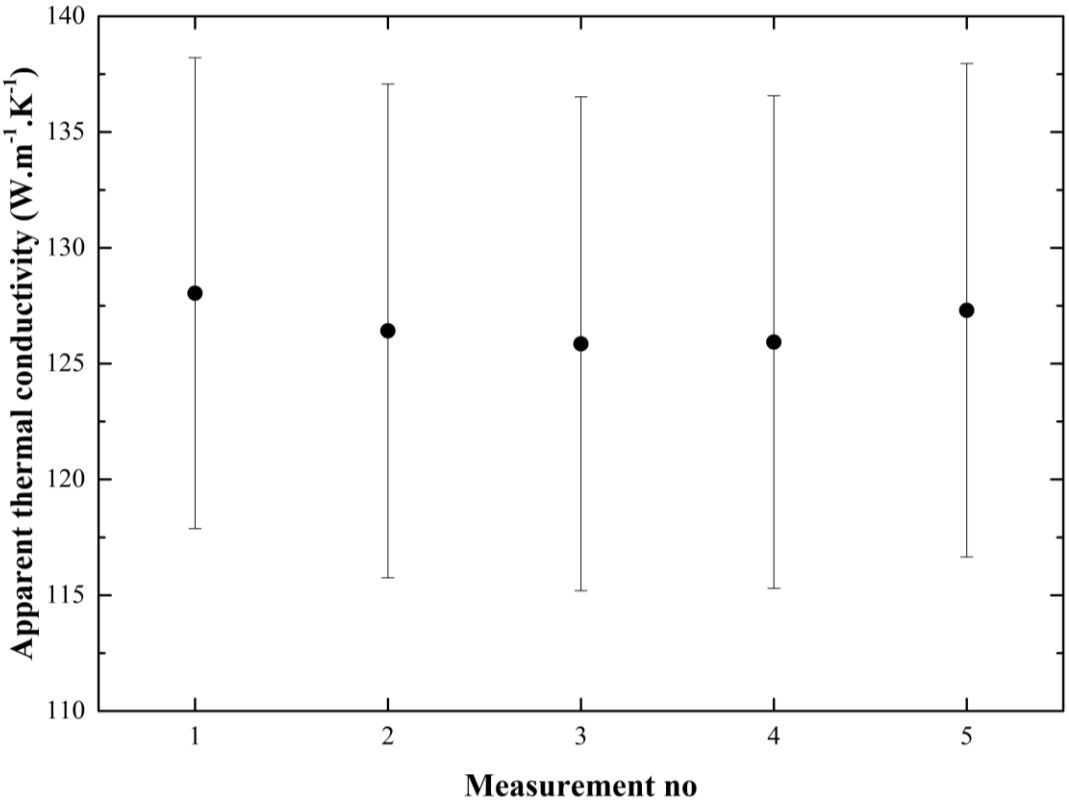


Figure 4.2: Thermal conductivity of brass reference block for apparatus validation. Error bars represent the measurement uncertainty according to 4.2.4.

4.2.6 Specimen manufacture and preparation

4.2.6.1 AlSi10Mg specimens

To determine the thermal conductivity of LPBF AlSi10Mg bulk and lattice structures, test specimens were designed to be 20 × 20 × 21 mm. After manufacture, they were removed from for the LPBF build plate by wire-EDM and ground to achieve dimensions of 20 × 20 × 20 mm within ± 0.1 mm with a final grinding step consisting of P2000 SiC paper. This final step provided a low surface roughness ensuring good thermal contact

during thermal conductivity measurements. Two specimens were tested in both build and transverse directions for each of the five conditions, which include the as-built state (i.e., directly following LPBF) and four heat treatments. Specimens were annealed by placing them in a preheated furnace set to 300 °C for 2 hours followed by air cooling. Two different solution heat treatments (SHT) were performed at 520 °C for one or two hours followed by water quenching to retain the high-temperature microstructure [76]. A T6-like heat treatment was carried out following the work of Aboulkhair *et al* [66] by applying a SHT for one hour at 520°C followed by water quenching, then artificially aged in a furnace at 160 °C for six hours followed by air cooling.

In addition to the solid specimens, gyroid matrix lattice structures were manufactured to study their response to an annealing heat treatment. The gyroid matrix lattice models were designed with dimensions of 20 × 20 × 20 mm within ± 0.1 mm with a final grinding step consisting of P2000 SiC paper; a unit cell size of 5 mm and volume fractions of 0.20 and 0.50 as illustrated in **Figure 4.3**. They were generated using in-house software and exported as STL files, prior to slicing and hatching for LPBF as described in **section 3.2**.

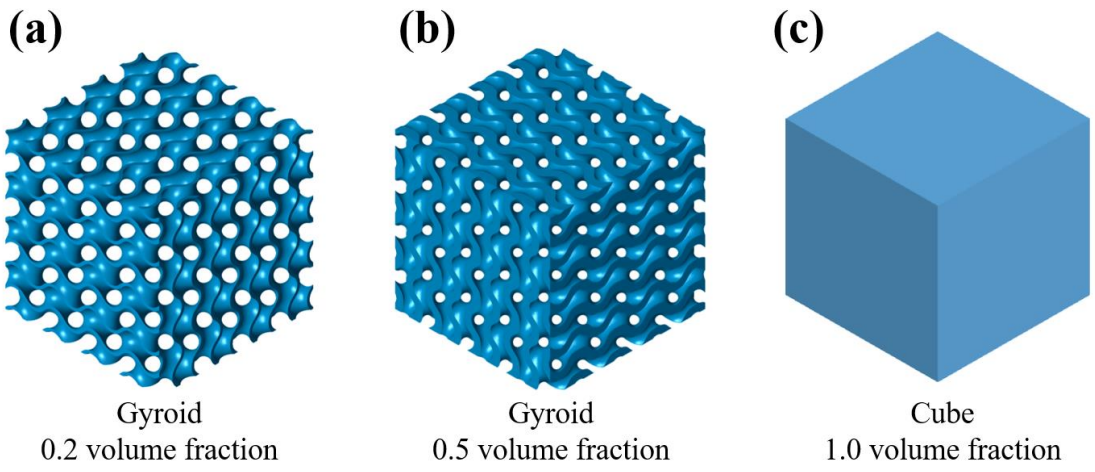


Figure 4.3: Cubic specimen used for thermal conduction tests; gyroid matrix 5 mm cell size (a) 0.20 volume fraction, (b) 0.50 volume fraction, (c) 1.0 volume fraction.

4.2.6.2 Ti6Al4V specimens

To determine lattice apparent thermal conductivity and the influence of the different lattice parameters, three unit cell designs (gyroid matrix, diamond matrix, and primitive matrix) with two volume fractions (0.2 and 0.5) and four different cell sizes (20, 10, 5 and 3.33 mm) were designed and are represented in **Figure 4.4**. Specimens were manufactured using a Realizer SLM50 desktop LPBF machine with Ti6Al4V as feedstock. Similar to AlSi10Mg lattice specimens, the lattice models were designed using FLatt Pack with dimensions of 20 × 20 × 20 mm within ± 0.1 mm with a final grinding step consisting of P2000 SiC paper. The volume fraction of each specimen was calculated by measuring the outside dimensions and dividing by its mass. These were then divided by the density of LPBF solid material (i.e. Ti6Al4V 4.42 $g.cm^{-3}$; AlSi10Mg 2.84 $g.cm^{-3}$) to obtain the actual volume fraction. The apparent thermal conductivity of each structure has been measured similarly to the AlSi10Mg solid specimens, with the difference that the reference blocks were changed from brass alloy (UNS CW614N) to AISI 304 stainless steel (thermal conductivity λ_M = 16.2 $W.m^{-1}.K^{-1}$ at 293 K) to match the lower conductivity of Ti6Al4V more closely.

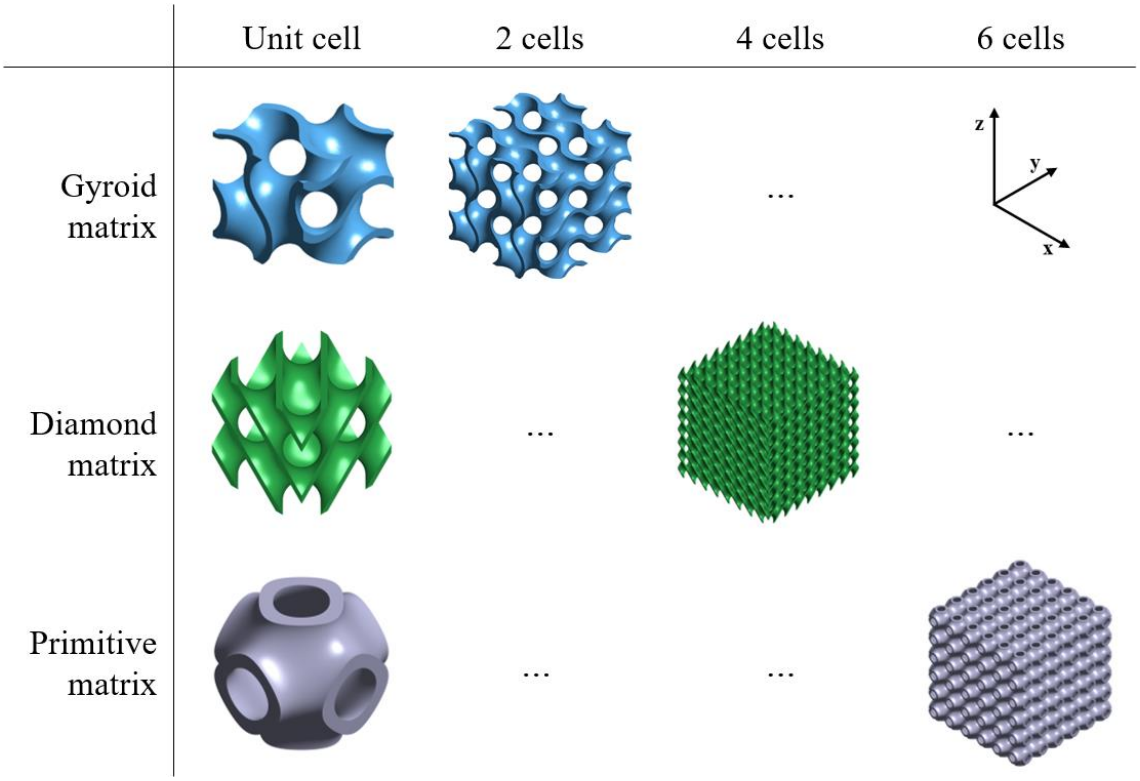


Figure 4.4: Unit cell designs and illustration of a variation of number cell at a constant 0.2 volume fraction.

4.3 Apparatus for forced convection heat transfer characterisation

As seen in the literature, there are no standard equipment nor methods to develop forced convection heat transfer apparatuses. Therefore, the development of a dedicated apparatus is required to measure the thermal performance of TPMS lattice structure in forced convection. This was accomplished in collaboration with Sam Catchpole-Smith (PhD student at the Centre for Additive Manufacturing, University of Nottingham). Sam Catchpole-Smith was responsible for: the design and manufacture of the convective heat transfer apparatus; performing ~50 % of the AlSi10Mg experiments. Richard Sélo was responsible for: the design and manufacture of AlSi10Mg specimens; performing ~50 % of the AlSi10Mg experiments, writing the MATLAB scripts for processing the experimental data and the error analysis of the experimental apparatus.

4.3.1 Description of the apparatus

Studies reported in the literature [174] use specimen sizes that closely match those of the target applications to limit discrepancies. Therefore, the forced convection heat transfer apparatus was developed after defining the specimen size. To best fit the target applications of LPBF lattice structures for compact heat exchangers, a specimen size of 50 × 50 × 12 mm was chosen. An illustration of the specimen geometry is shown in **Figure 4.5**. This size also allows testing several cell sizes without reaching LPBF machine restrictions. Lattice structures can have different inlet channel shapes depending on their orientation as seen in **Figure 4.5**. Consequently, a square-based cross-section was chosen to allow testing different lattice orientations within the same specimen, thus reducing the required number of manufactured specimens. A 1 mm skin was added to the top and bottom of the lattice structure to maximise and have a constant cross-sectional area for the contact surfaces. This specimen design geometry also allows testing more conventional geometries, such as pin-fins or corrugated walls.

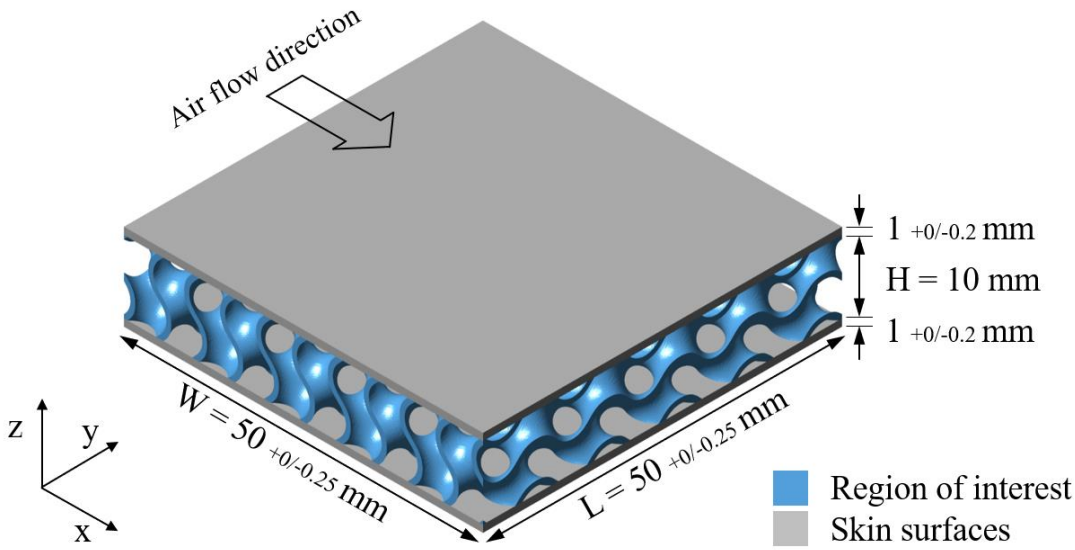


Figure 4.5: Specimen dimensions for forced convection heat transfer testing apparatus.

The primary components of the apparatus are presented in **Figure 4.6**, they include a high-pressure air supply line with a regulator valve, a test chamber, and a downstream exhaust line with a regulator valve and a muffler. The compressed air was supplied at 20 °C ± 2 °C with a pressure between 0 and 6.5 bar and acted as the coolant fluid for the forced convection testing. The flow rate was measured using in-line flow rate meters (SMC PFMC7202, 20 – 2000 $L \cdot min^{-1}$ range, and ± 1 % full-scale range accuracy). The main body of the testing apparatus was a machined aluminium section (see **Figure 4.6(b)**) that houses the specimen and sensors used to collect pressure and temperature readings. Six piezoresistive pressure transducers with integrated ASIC signal conditioning and amplification (Honeywell PX3 1–50 bar and ± 0.25 % full-scale range accuracy) provided real-time absolute pressure measurements along the length of the channel. A flow straightener was placed at the entrance of the primary channel to reduce swirl and lateral velocities and minimise turbulences. A honeycomb geometry with an open area of 0.795 was chosen due to its high effectiveness to reduce swirl and lateral velocity fluctuations as reported by Kulkarni *et al.* [175]. The pressure drop across the specimen was measured using a silicon differential pressure sensor with on-chip signal conditioning and temperature compensation (NXP MPX-series). To ensure maximum accuracy of the measurement, the differential pressure sensor model was chosen according to the expected pressure differential range for each specimen (MPX5010DP 0 – 10 kPa range, MPX5050DP 0 – 50 kPa range, and MPX5100DP 0 – 100 kPa range, all 2.5 % full-scale range accuracy). Four K-type thermocouples (± 0.5 K accuracy) are positioned in the coolant flow at the inlet and outlet of the specimen to determine the coolant temperature. A wire-wound mica 80 W heater placed at the bottom of the stack (see **Figure 4.6(c)**), was used as a heat source, and was regulated by a PID temperature controller. A 6 mm thick high drawn high conductivity (HDHC) copper heat spreading block (λ = 391 $W \cdot m^{-1} \cdot K^{-1}$ at 293 K) was placed between the heat source and the specimen base

to have a constant and uniformly distributed heat from the mica heater below due to the high thermal conductivity of copper. Four embedded thermocouples were positioned inside the copper block at regular intervals along the direction of coolant flow. The test stack was placed within a PTFE insulative block, which acts to minimise conduction losses into the aluminium test chamber. Above the test specimen was an acrylic viewing window which can be removed to change the specimen using eight screws. A controlled torque was applied to the screws to ensure that an equal clamping force is applied to each specimen under test and used to seal the test chamber by compressing a nitrile rubber gasket. This compressed the test stack and minimised thermal contact resistance between the various layers. Pressure and flow rate sensor data were recorded using a PicoLog 1216 data acquisition (DAQ) unit. The thermocouple data is recorded using a PicoLog TC-08 USB thermocouple data logger with integrated cold junction compensation. All data are recorded consecutively in real-time to a PC via USB using PicoLog 5.25.3 software and saved as a .txt file for further processing using MATLAB. The data processing includes the conversion from raw voltage data output from the data loggers into the correct units for the measurement to the calculations of mass flow rate, pressure drop and heat transfer coefficient.

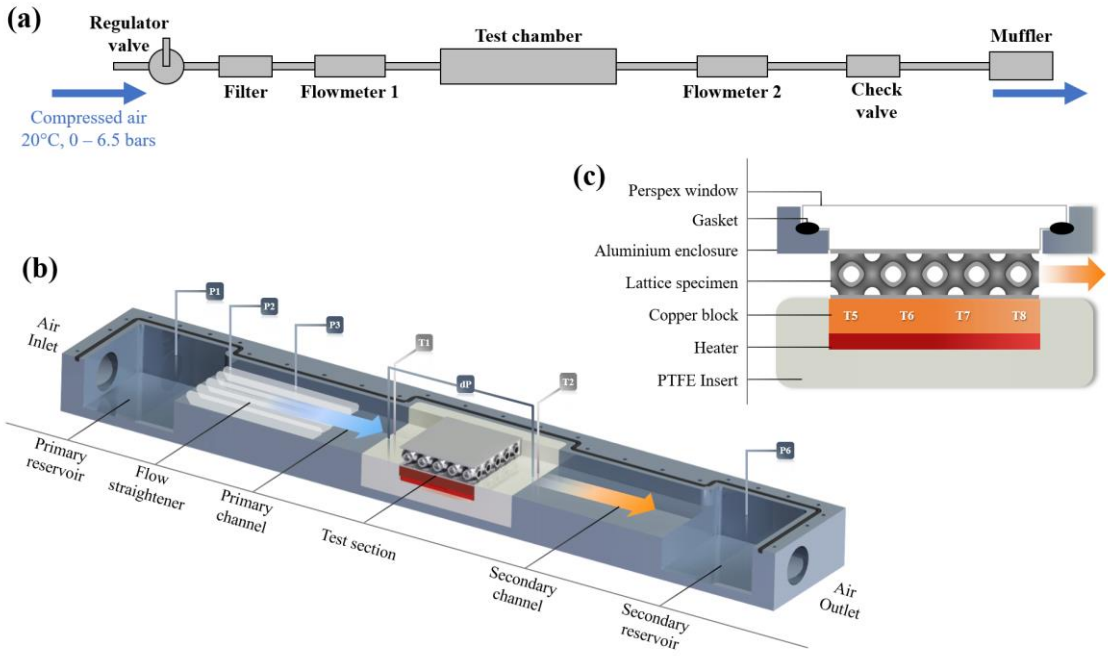


Figure 4.6: Schematic of the forced convection heat transfer apparatus (a) overall apparatus, (b) close view of the test chamber with the position of the pressure sensors P_i and thermocouples T_i, (c) Close view of the test stack with the position of the temperature measurements.

4.3.2 Pressure drop testing

Pressure drop testing was performed at ambient temperature (20 °C ± 2 °C), After each specimen was loaded in the test rig, the valve at the outlet of the main body was closed and the rig was pressurised to 1 bar to test for air leaks. If no leaks were found, the rig was de-pressurised by opening the outlet valve and the airflow was ramped down to zero. The DAQ software was then started, recording data from the different sensors. Before testing, a first record was made without any airflow for one minute to provide a baseline for each sensor at ambient conditions. Then, the airflow through the rig was increased from 200 $L \cdot min^{-1}$ to 700 $L \cdot min^{-1}$ in 100 $L \cdot min^{-1}$ increments using the flow regulator. A minimum of a three-minute hold at each measurement point was marked to allow the flow conditions to reach steady-state. Steady-state was further tested by calculating the

gradient of pressure drop against time. In theory, this gradient should be zero if the flow is at perfect steady-state condition. However in practice, if the gradient of the pressure drop was within one standard deviation of zero, the observed changes in pressure drop were considered to be solely due to experimental noise rather than a trend, consequently, the flow was considered at steady-state. If the stationary hypothesis was rejected, another three-minute wait period was marked to allow the system to reach steady-state. Once the system has reached steady-state, the experiment was started, and data were recorded for 1000 points at each flow rate. The DAQ was then stopped before the airflow rate was ramped down to zero to prevent anomalous data capture.

4.3.3 Convective heat transfer testing

The convective heat transfer testing procedure was similar to the previously described pressure drop testing method, with the addition of a heater. The flow rate was set to 200 $L.min^{-1}$ with the regulator before the heater was switched on to prevent damage to the acrylic window by excessive heating. The heater PID controller was set to 373 K (100 °C). Before the test recording was started, the test stack surrounded by the PTFE insulative insert was left to reach thermal equilibrium signified by a temperature drift below 0.1 $K \cdot min^{-1}$ at the specimen base. At steady-state, the DAQ was started and the recording of 1000 specimens. The flow rate was increased by increments of 100 $L \cdot min^{-1}$. At each increment, a waiting period is observed to allow the steady-state to be reached which can vary significantly depending on the specimen under investigation. At the end of the test sequence, the DAQ is stopped followed by the heater. The airflow is maintained for several minutes to allow the system to cool down.

4.3.4 Data processing and analysis method

The data processing started with the conversion from raw signal outputs from the data loggers into the correct units for the measurement. The experiments involved variation in air temperature and pressure as air passed through the specimen, consequently, air properties were not constant and needed to be calculated for each measurement point. This was achieved by using the mean air temperature and pressure across the specimen, $\bar{T}$ and $\bar{P}$and the following formulas.

To calculate air density, the ideal gas law can be used as follows, where *R* is the specific gas constant for dry air (287.058 $J \cdot Kg^{-1} \cdot K^{-1}$):

$$\rho_{air} = \frac{\bar{P}}{R \cdot \bar{T}} \qquad \textbf{Equation 4.8}$$

As the testing is at pressures well below 10 bar, air dynamic viscosity μ can be approximated by only considering the temperature variations [176]. Consequently, the air dynamic viscosity μ was calculated using the Sutherland formula:

$$\mu_{air} = \mu_0 \frac{T_0 + S}{\bar{T} + S}\left(\frac{\bar{T}}{T_0}\right)^{3/2} \qquad \textbf{Equation 4.9}$$

where *S* is an effective temperature called the Sutherland constant, which is characteristic of the gas, T_0 and μ_0 are reference values for the temperature and viscosity. White [176] reported the following values for air: $S = 110$ K, $\mu_0 = 1.716 \times 10^{-5}$ $Kg \cdot m^{-1} \cdot m^{-1}$, $T_0 = 273$ K.

Air kinematic viscosity ν can be directly calculated from air dynamic viscosity μ and air density ρ_{air}:

$$\nu = \frac{\mu}{\rho_{air}} \qquad \textbf{Equation 4.10}$$

Similarly to dynamic viscosity, the air thermal conductivity λ_{air} can also be calculated using the Sutherland formula in the form of:

$$\lambda_{air} = \lambda_0 \frac{T_0 + S}{\bar{T} + S} \left(\frac{\bar{T}}{T_0} \right)^n \qquad \textbf{Equation 4.11}$$

with the air conductivity λ_0 = 0.0241 W·m^{-1}·K^{-1} at the reference temperature T_0 = 273 K, and n = 0.81 [176].

Specific heat capacity c_p of air in the temperature range 273 – 573 K (0 – 300 °C) can be calculated using the empirical formula derived by Xiao *et al.* [177]:

$$c_p = 1.0026 + 5.1 \times 10^{-4} \cdot (\bar{T} - 273) \qquad \textbf{Equation 4.12}$$

After the air properties are calculated, the fluid flow and heat transfer properties can be determined. The heat transfer coefficient *h* is calculated by:

$$h = \frac{\dot{m} \cdot c_p \cdot (T_{out} - T_{in})}{A \cdot \left(T_{base} - \frac{T_{out} + T_{in}}{2} \right)} \qquad \textbf{Equation 4.13}$$

where $\dot{m}$ is the mass flow rate, c_p air specific heat capacity, A is heated area of the specimen, T_{in} and T_{out} are the temperature of the air before and after passing through the test specimen and T_{base} is the temperature at the base of the specimen. A modified heat transfer coefficient was used, the commonly used heat transfer surface area A is replaced by A_{base} the heated area at the base of the specimen. This was done to avoid to skew the heat transfer performance measured in favour of heat sinks with smaller surface areas.

$$h_{mod} = \frac{\dot{m} \cdot c_p \cdot (T_{out} - T_{in})}{A_{based} \cdot \left(T_{base} - \frac{T_{out} + T_{in}}{2} \right)} \qquad \textbf{Equation 4.14}$$

The overall thermal performance of each specimen was determined using a thermal performance metric consisting of the ratio between the modified heat transfer coefficient (as defined in the previous section) and the pressure drop in the form of $h_{mod}/\Delta P$.

This metric allows comparison of the heat transfer per unit of pumping power for each specimen by plotting it against the flow rate and was previously used in the literature to compare dissimilar geometries [24].

4.3.5 Uncertainty calculations for the convective apparatus

The measurement uncertainties for the force convective heat transfer measurements were quantified using the root sum of squares and were not constant across each flow condition. At the lowest flow rates, the pressure drop approached the lower limit of even the smallest differential pressure transducer and represent an absolute error of up to 50 % but quickly reduces as the flow rates increase to an average value of 10 %. Mass flow rate uncertainty ranges from 28 % (low flow rate) to 17 % (high flow rate) with an average of 20 %. Modified heat transfer coefficient uncertainty ranged from 30 % to 16 % for the lowest to the highest flow rate, respectively. The main contributor to uncertainty for the modified heat transfer coefficient at low flow rates was the ± 1 % full-scale range measurement error of the flow rate meter. The main contribution to uncertainties in the modified heat transfer coefficient was the low-temperature difference between the inlet and the outlet at higher flow rates.

4.3.6 Specimen manufacture and preparation

Lattice specimens were designed to be 50 × 12 × 51 mm with 1 mm solid extrusion acting as sacrificial supports and orientated on the LPBF build plate as illustrated in **Figure 4.7**. They were manufactured from AlSi10Mg powder with a Renishaw AM250 LPBF machine using process parameters reported in **Table 3.2**. After manufacture, specimens

were removed from the build plate by wire-EDM. The specimens were ground to achieve dimensions of 50 × 12 × 50 mm within +0 /-0.2 mm with a final grinding step comprising of P2000 SiC paper. This final step was to provide a low surface roughness ensuring good thermal coupling during the forced convection heat transfer test. All specimens were tested in the as-built state directly following LPBF.

In addition, a classic pin-fin geometry was designed and manufactured in AlSi10Mg with the Renishaw AM250 to establish a benchmark and compare the pressure drop and heat transfer performance of the lattice structures. The pin-fin spacing and geometry are illustrated in **Figure 4.8** and were chosen to achieve a volume fraction of 0.2, matching that of the lattice structures to ensure the thermal performance per unit volume can be compared.

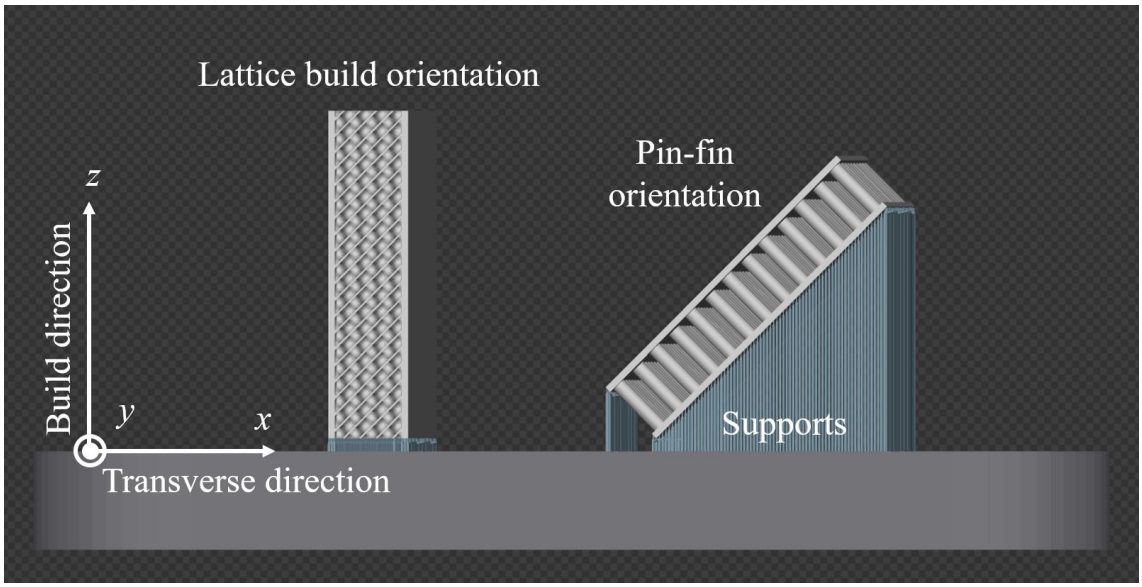


Figure 4.7: Part orientation and support structure for LPBF manufacture of (left) the lattice structures and (right) pin-fin specimens.

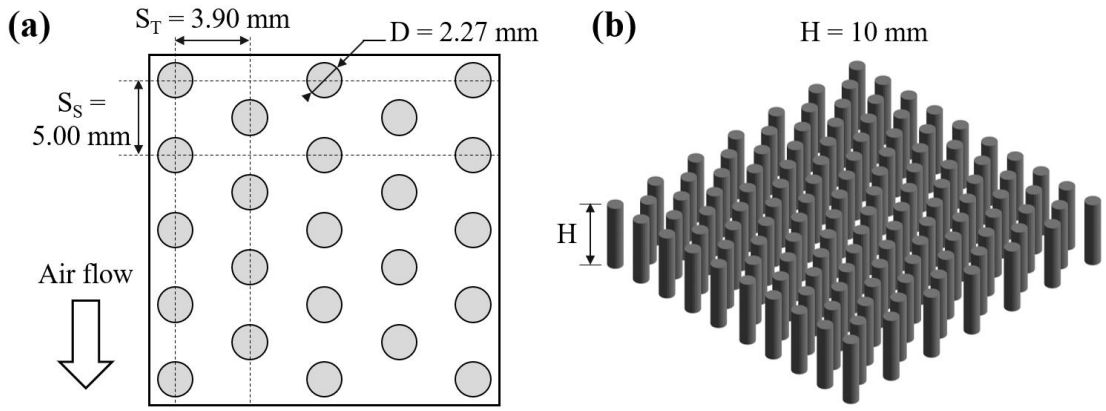


Figure 4.8: (a) CAD geometry for the pin-fin benchmark coupon with spanwise spacing S_S = 5.00 mm and streamwise spacing S_T = 3.90 mm, pin diameter D = 2.27 mm, and pin height H = 10 mm. (b) Pin-fin layout can be seen in isometric view (top and bottom skin removed for clarity).

4.4 Summary

The determination of thermal conductivity was achieved by the development of a dedicated apparatus based on the test standard ASTM E1225-13, “Thermal Conductivity of Solids Using the Guarded-Comparative-Longitudinal Heat Flow Technique”. This standard defines the equipment needed and the method to measure the thermal conductivity of material similar to those of the reference blocks. Standard procedures were established to ensure equal comparison and to give an accurate description of the relationship between the thermal conductivity and test cases as reported in chapter 5.

Forced convection heat transfer performance of lattice structures was measured using an in-house developed apparatus and are reported in chapter 6. The pressure drop and heat transfer coefficient are used to compare the different structures across a range of flow conditions and determine the thermal performance of the structures. Methods were established to ensure good reproducibility and determine an accurate description of the

relationship between lattice parameters (unit cell design, etc.) and heat transfer performances.

Different types of specimen were manufactured to determine properties of interest in this thesis. Cubes with 10 mm edge length were manufactured to measure the relative density, microstructure, and hardness. For thermal conductivity determination (see chapter 5), a cubic geometry was selected to test both build and transverse orientation on the same specimen, thus minimising the number of specimens to manufacture. A 20 mm cube geometry was selected to test various lattice cell sizes (20, 10, 5, and 3.33 mm) of three unit cell designs (gyroid, diamond, and Schwarz primitive) and two volume fractions (0.2 and 0.5). Heat treatments were performed to assess the effect on thermal conductivity and microstructure. For forced convection heat transfer performance determination (see chapter 6), a square cross-section was selected to test different lattice orientations by simply rotating the specimen, reducing the number of specimens to manufacture. A specimen geometry of 50 × 50 × 12 mm was selected to test several lattice cell sizes (10, 5, and 2.5 mm) of six unit cell designs so the minimum wall thickness does not reach manufacturing resolution and best fit targeted applications of compact heat exchangers.

5 Thermal conductivity of LPBF components

5.1 Introduction

The literature review (see chapter 2) indicated that the LPBF process creates a unique microstructure within the manufactured material. The presence of elongated grains in the build direction and a more equiaxed grain in the transverse direction and the possible presence of trapped porosity is well documented. However, how this manufacturing technique and its unique microstructure affects the thermal properties of the processed material has received little attention to date. The LPBF microstructure is sufficiently dissimilar that existing data from conventional material cannot be used. Furthermore, the thermal conductivity of LPBF parts must be studied they are to be used in a new family of high-performance AM components. This concern will be addressed in this chapter.

Lattice structures have been identified in the literature review as promising candidates for heat transfer applications due to their high surface area to volume ratio and easily controllable properties. Most studies have focussed on their mechanical properties and little to no thermal characterisation has been completed. This chapter also has the objective of measuring the apparent thermal conductivity which represents the conductivity in addition to other modes of heat transfer through lattice structures. How their parameters (volume fraction, cell size, unit cell design) affect the apparent thermal conductivity will be studied. Furthermore, their apparent thermal conductivity and response to heat treatment must be determined to maximise efficiency. From these, valuable guidelines can be designed to generate thermal components with prescribed variation in thermal conductivity, thus tailoring components to specific applications such as heatsinks. For the designer, these guideline models are summarised in **section 5.5**. These design rules will enable the emergence of new high-performance lightweight components by taking advantage of lattice structures to achieve specific thermal

conductivity. For instance, conductivity lower than the typical range of metals, to those of metallic foams while retaining control on the mechanical properties.

As seen in the method chapter (see **section 4.2.1**), several methods and standards exist to measure thermal conductivity depending on the material (refractory, metallic…), form and geometry (bulk, thin films, porous media), temperature range investigated, and measurement types (transient or steady-state). All methods have their advantages and disadvantages and must be selected according to specific requirements of the manufacturing process. The guarded comparative heat flow was selected and used as the conductivity measurement method (see **section 4.2.2**). It allows the thermal conductivity to be measured between 0.2 and 200 $W \cdot m^{-1} \cdot K^{-1}$ and a maximum temperature range within 90 and 1300 K.

5.2 Thermal conductivity and heat treatment of LPBF specimens

5.2.1 Introduction

To determine the thermal conductivity of LPBF AlSi10Mg, test specimens were created which were 20 × 20 × 20 mm within ± 0.1 mm using process parameters described in **section 3.3.2**. Two specimens of each test condition were created to reduce any manufacturing difference and measurement errors. These test conditions include as-built, as well as an annealing heat treatment typically used as a stress relief [178], as well as solution heat treated for one and two hours at 520 °C, as well as a T6-like heat treatment (SHT at 520 °C for 1 h, followed by water quenching, then artificial ageing at 160 °C for 6 h, followed by air cooling [66]) used to increase mechanical properties. Specimens were tested in both build and transverse directions. Relative density, microstructure, and hardness were reported to compare the effects of the various heat treatment on each of these properties. Subsequently, the thermal conductivity measurements are reported for

each condition and analysed. In addition, 20 × 20 × 20 mm gyroid matrix lattice structures with 5 mm cell size and two volume fractions (0.2 and 0.5) were created. These lattices were tested in both orientations for as-built and after the annealing heat treatment (300 °C for 2 h).

5.2.2 Microstructure and relative density

Specimens' relative densities were measured for each condition to ensure variation in thermal conductivity is only attributable to differences in the specimens' microstructure rather than a significant change in internal porosity. The measurement methods are detailed in **section 3.5.2** and are reported in **Table 5.1**. The average relative density of the solid specimens is 99.78% with a standard deviation of 0.06% and is in accordance with a previous study of the same material [179]. The observed porosity was mainly due to some lack of fusion with feature sizes below 100 μm and few trapped gas pores with a maximum size of 30 μm. The low variation in relative density between the specimens indicates that any significant differences in thermal conductivity are only attributable to changes in specimens' microstructure. As seen in the literature review (see section **2.2.3.2**) the main factor influencing the thermal conductivity is the Si content in solution, high Si content reduces the thermal conductivity of the alloy.

After manufacture, lattice structures were inspected for obvious geometrical distortions and broken cells; these were not observed in any of the manufactured specimens due to the relatively large cell size and the self-supporting geometry of the gyroid matrix structure. The volume fraction of each manufactured lattice structure was calculated by measuring the outside dimensions and dividing by its mass. These were then divided by the density of LPBF AlSi10Mg (2.67 $g.cm^{-3}$) to obtain the volume fraction. The lattice designed volume fractions were 0.20 and 0.50, and calculated volume fractions are 0.20 ± 0.03 and 0.49 ± 0.02, respectively, which are in good agreement.

Table 5.1: Relative densities of test specimens in various heat treatment conditions.

Heat Treatment	As-built	Annealed	SHT 1 hour	SHT 2hours	T6-like
Relative density (%)	99.71	99.81	99.80	99.68	99.92
Standard deviation (%)	0.19	0.08	0.15	0.22	0.030

Microstructures were observed after sectioning, polishing, and etching (described in **section 3.5.2**) under optical and scanning electron microscopes and are shown in **Figure 5.1**. Melt-pool boundaries from the laser scans are visible in the as-built specimen as indicated by the black arrows in **Figure 5.1(a)-(b)**. Each heat treatment modified the microstructure of the test specimen. Annealed specimens had much less distinct melt-pool boundaries but a similar fine microstructure to the as-built state. Solution heat treatment coarsened the microstructure with the coalescence of Si aggregates and the emergence and growth of needle-like Al_5FeSi precipitates, as also previously reported by Maamoun *et al* [180].

SEM observations reported in **Figure 5.1(k)-(t)** are similar to the optical micrographs with the difference that the ultrafine microstructures of as-built and annealed specimens can now be clearly seen. The as-built microstructure consists of elongated grains of a silicon-rich and aluminium-rich areas. The *xy*-plane shows more equiaxed grains compared to the *yz*-plane where grains are columnar in the direction of the thermal gradient. After annealing, the Si network has been broken down into circular aggregates, as shown in **Figure 5.1(n)**. Similar observations were made for the gyroid matrix lattice microstructure, as shown in **Figure 5.2**.

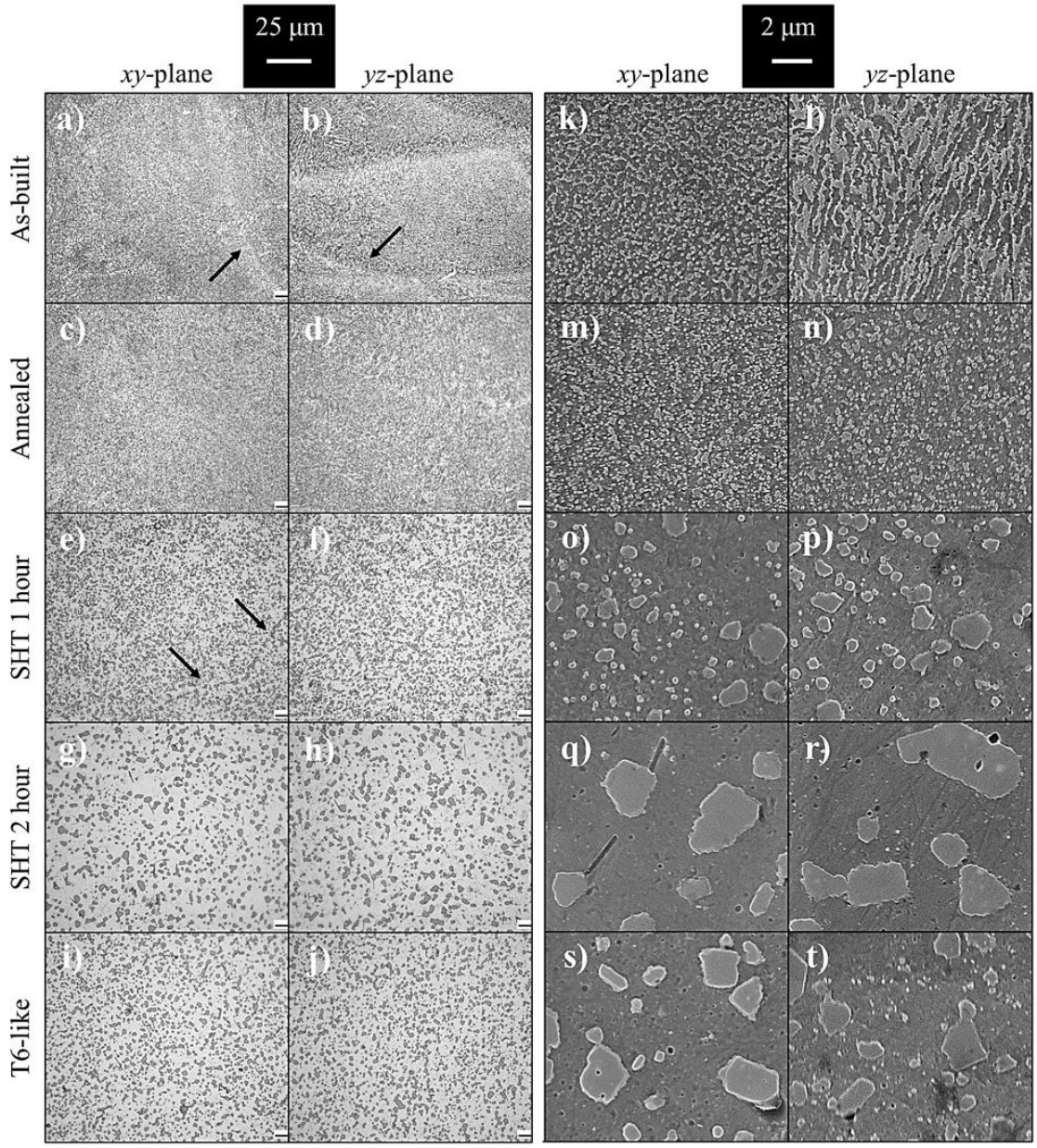


Figure 5.1: (a)-(j): Optical micrographs of polished specimens after etching. Al-rich areas have lighter contrast and Si-rich regions have dark contrast. Black arrows show LPBF melt pool boundaries; (k)-(t): SE SEM images showing the microstructure of LPBF AlSi10Mg after different heat treatments. Si-rich areas are light grey features and Al-rich regions are darker regions.

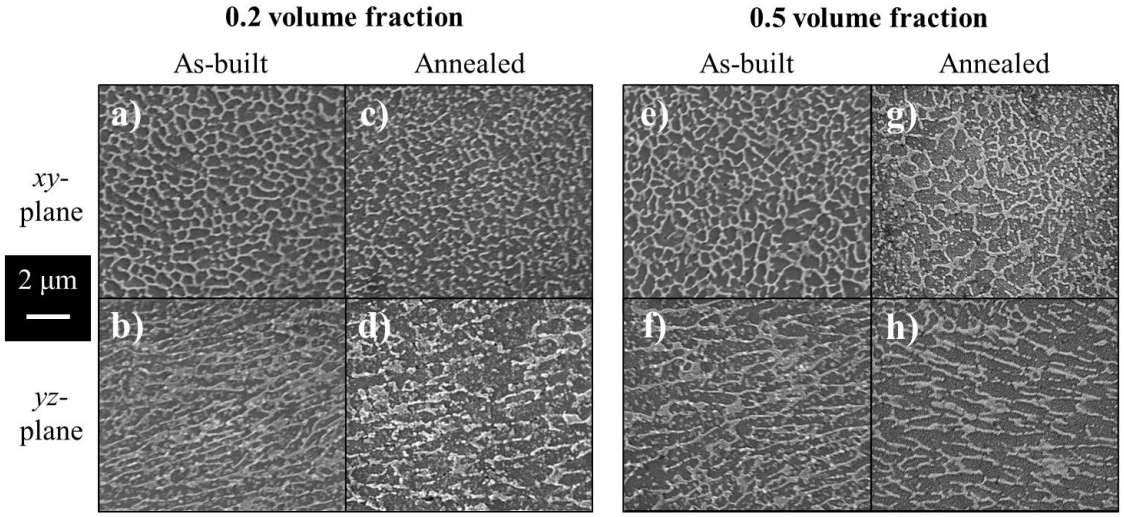


Figure 5.2: Microstructure of LPBF gyroid lattice structure in: as-built condition (a), (b), (e) and (f); annealed condition, (c), (d), (g) and (h). Si-rich regions are light grey features and Al-rich areas have darker contrast.

5.2.3 Micro-hardness and mechanical properties

The micro-hardness of the test specimen for each condition was measured following ASTM E92-17 using a micro-Vickers indenter with a load of 0.5 kg. A grid of 75 points was realised with 0.7 mm *xy*-spacing to map any variation in hardness across each specimen. Hardness measurements were also undertaken to verify the effectiveness of the heat treatment, especially the quench, and correlate this work to previously published mechanical studies on AlSi10Mg made by LPBF. The measured values after the different heat treatments are reported in **Figure 5.3**.

The average hardness of the as-built specimens is the highest among all tested conditions and was 126 $HV_{0.5}$. After annealing, the hardness dropped to an average of 88 $HV_{0.5}$.and further decreased after 1 h of solution heat treatment to an average of 78 $HV_{0.5}$. After 2 h of SHT, the hardness increased again to an average of 84 $HV_{0.5}$. After the T6-like HT, the hardness reached an average of 102 $HV_{0.5}$. These values and trends are in good agreement with previously reported values by Aboulkhair *et al.* [76]. It can be concluded that heat

treatments of LPBF AlSi10Mg are consistent and predictable. Mechanical tests of LPBF AlSi10Mg have been widely published in the literature [27,66,70] and were not performed as part of this work.

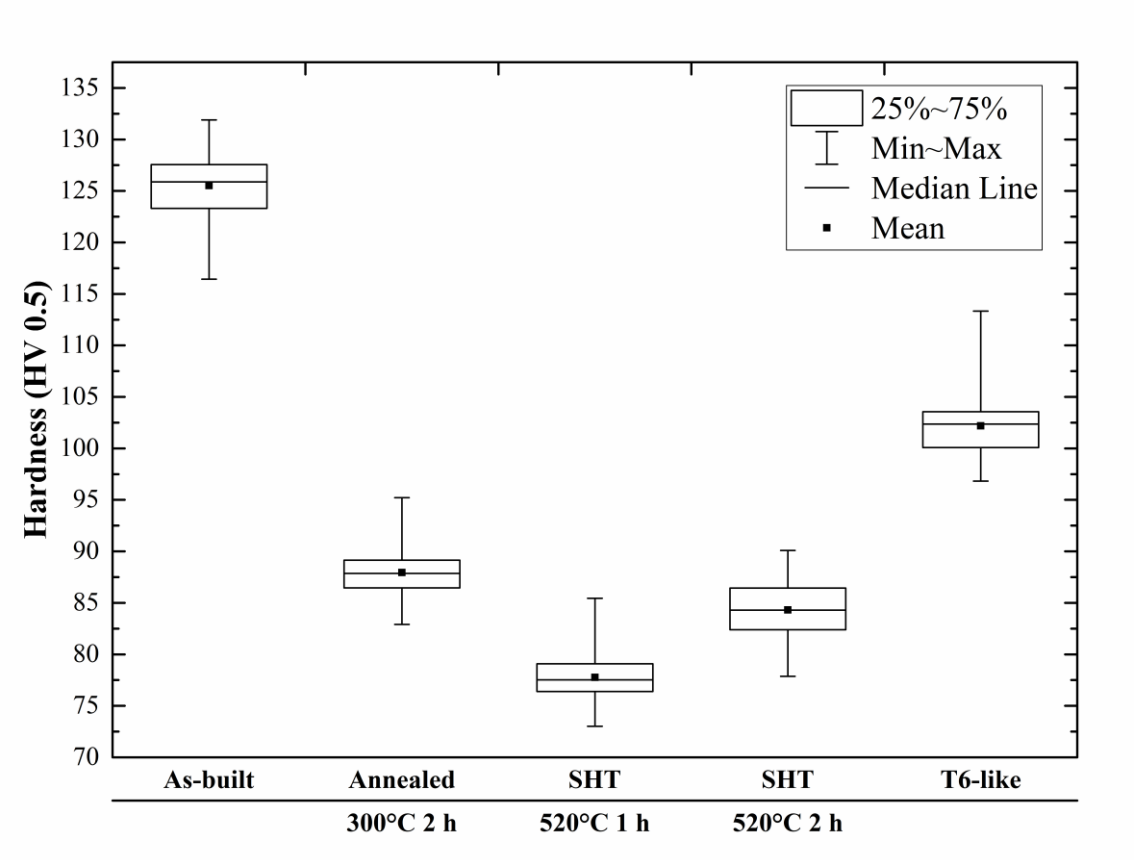


Figure 5.3: Evolution of micro-hardness of AlSi10Mg after different heat treatments.

5.2.4 Thermal conductivity measurements

Thermal conductivity results for AM AlSi10Mg coupons are shown in **Figure 5.4**. The lowest conductivity was measured for as-built specimens and the conductivity values were seen to vary greatly depending on the specimen orientation. The transverse direction exhibited lower conductivity than the build direction, with conductivity values of 115 ± 9 $W \cdot m^{-1} \cdot K^{-1}$ and 130 ± 10 $W \cdot m^{-1} \cdot K^{-1}$, respectively. After annealing, the thermal conductivity was significantly improved, by nearly (30 ± 20) %. Solution heat treated

specimens had similar values for both 1 h and 2 h duration tests. The highest thermal conductivity measured was for the T6-like heat treatment, with a value of 166 ± 13 $W \cdot m^{-1} \cdot K^{-1}$.

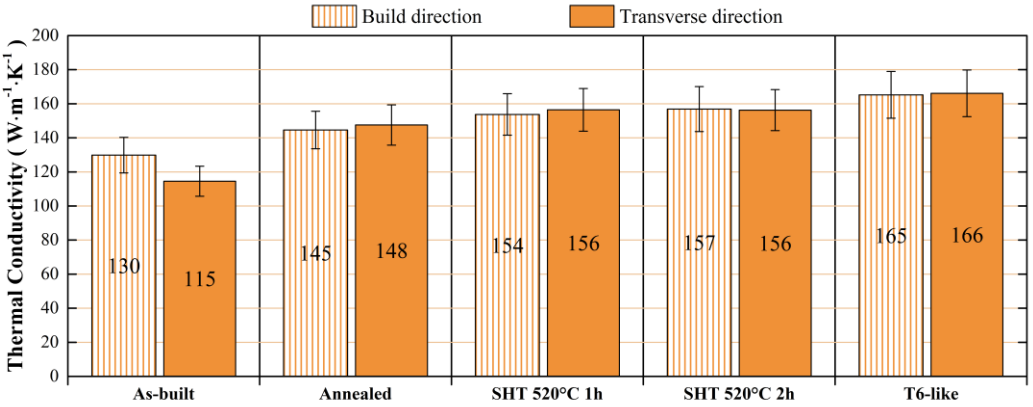


Figure 5.4: Thermal conductivity of AlSi10Mg after different heat treatments. Error bars represent measurement uncertainty as described in section 4.2.4.

The apparent thermal conductivities of the lattice structures in the as-built condition and after annealing heat treatment are reported in **Figure 5.5**. In the as-built condition, the gyroid lattices have similar apparent thermal conductivities in the build and transverse directions for both 0.2 and 0.5 volume fractions. They show similar trends to the bulk specimens, where the lowest apparent thermal conductivity is found in the as-built condition. Annealing heat treatments improved the apparent thermal conductivity of the 0.2 volume fraction lattice by (10 ± 20)% for both build and transverse directions. After annealing, the apparent thermal conductivity of the 0.5 volume fraction lattice increased by (30 ± 20) % for the build and transverse directions.

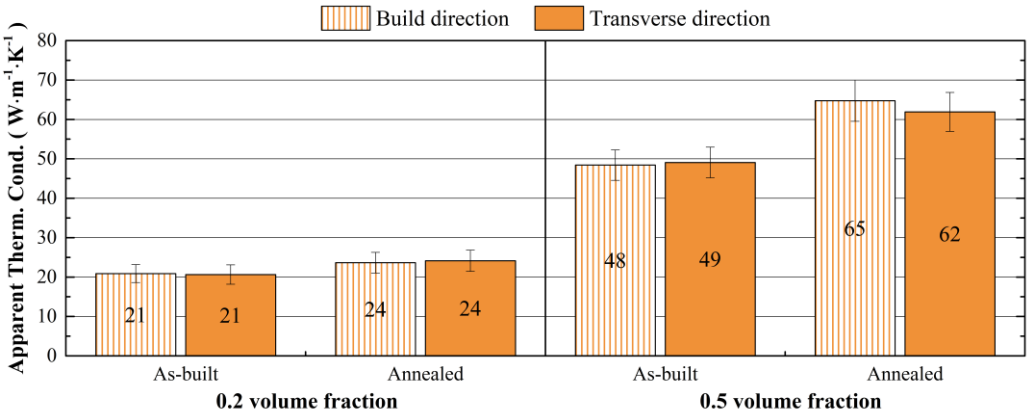


Figure 5.5: Apparent thermal conductivity of AlSi10Mg gyroid lattice structures before and after annealing heat treatment. Error bars represent the measurement uncertainty.

5.3 Thermal conductivity of lattice structures

Ti6Al4V was chosen due to its wide use in the aerospace industry and its good processability by LPBF, making it a good candidate to demonstrate the potential of lattice structures by LPBF for aerospace. Hastelloy-X measurements were performed by Sam Catchpole-Smith [181] and were added with his agreement to increase the statistical significance of this study. The volume fraction was calculated according to the method described in **section 4.2.6** with density for Hastelloy-X of 8.82 g.cm^{-3}.).

The apparatus and the calculation for the thermal conductivity are based on the testing standard for solid material [167] (ASTM E1225-13). However, a lattice structure can be considered a composite material, in our case made of metallic skeleton and air. The thermal conductivity of a lattice structure can be seen as the sum of contributions from four mechanisms as given in **Equation 2.4**; hence the name *apparent thermal conductivity* is preferred, as detailed in the standard [167].

Firstly, most of the measured conductivity is expected to arise from the metal conducting the heat flow (λ_s^*) due to the higher thermal conductivity of the metal, but heat flow is

also possible through conduction and convection in the air, (λ_g^*) and (λ_c^*) respectively, and from radiative heat transfer (λ_r^*). The radiative heat transfer is assumed to be negligible since the temperature stays well below 200 °C [182]. The contribution of conduction through the air was estimated based on Gibson and Ashby's work [95]. Conduction through the air is the product of the air thermal conductivity (0.03 $W \cdot m^{-1} \cdot K^{-1}$ at 20 °C) and the volume fraction of air in the lattice. For volume fractions of 0.2 and 0.5, the conduction through air is 0.02 $W \cdot m^{-1} \cdot K^{-1}$ and 0.01 $W \cdot m^{-1} \cdot K^{-1}$, respectively. This is more than forty-two times lower than the lowest measured conductivity in this thesis. Therefore, the contribution of conduction through the air to the apparent thermal conductivity of the lattice is considered negligible. The convective heat transfer contribution is difficult to estimate for lattice structure since they are open-cell structures, air within the cell can be exchanged with adjacent cells or within the whole structure, as opposed to closed-cell structures (i.e. foams). Convective heat transfer provided therefore, an inseparable contribution to the apparent thermal conductivity measurement. Finally, the lattice geometry affects the heat flow path in the metal due to their inherent morphological differences. For these reasons, the measurement represented an apparent thermal conductivity from both the material and geometry, rather than a pure material property.

5.3.1 Volume fraction vs. apparent thermal conductivity

The main parameter describing a lattice structure after the unit cell design is the volume fraction. To understand the relationship between the lattice thermal conductivity and the volume fraction, the apparent thermal conductivity was measured for a gyroid matrix lattice structure with dimensions of 20 × 20 × 20 mm and a unit cell size of 5 mm, made of AlSi10Mg, Ti6Al4V. For statistical purpose Hastelloy-X. The designed volume fractions ranged from 0.15 to 1 (solid specimen) and the conductivities were divided by

the solid thermal conductivity λ_s to remove the material effect. It can be observed in **Figure 5.6** that the relative apparent thermal conductivity (λ^*/λ_s) decreases with the volume fraction of the specimen, as expected. The intention here is to develop a simple analytical tool for designers to predict the thermal conductivity for a certain application. These design for additive manufacturing (DfAM) guidelines are a necessary first step to allow the development of the first generation of LPBF high-performance components and promote the adoption of lattice structures.

Models to correlate the volume fraction to material properties of cellular solids have previously been developed [129,130,183–187]. However, the main emphasis was on predicting the mechanical properties, and thermal properties have been the subject of fewer investigations. This could be partly due to the difficulty of developing a simple and precise model including multiple thermal transport mechanisms occurring in cellular solids. Furthermore, before the development of AM, most cellular solids consisted of closed-cell structures, hence, modelling was focused on these, assuming ideal pore shapes with low volume fractions. Attempts have been made to apply these models to a wider range of geometries and volume fractions with little success. Gibson and Ashby in 'Cellular Solids' [95] considered a simple power-law for estimating the mechanical properties based on the volume fraction (ρ^*/ρ_s) and previous data of similar cellular structures independently of the material studied. They also proposed a power-law for estimating the electrical resistivity. **Equation 5.1** adapts this power relationship for thermal conductivity,

$$\frac{\lambda^*}{\lambda_s} = C_1\left(\frac{\rho^*}{\rho_s}\right)^n + C_0 \qquad \textbf{Equation 5.1}$$

where λ^*/λ_s is the relative apparent thermal conductivity, C_1, C_0 and n are the fitting coefficients. A linear model has also been applied to the dataset following **Equation 5.1** (fixing $n = 1$). For both models, each data point was weighted by $w_i = 1/\Delta(\lambda^*/\lambda_s)_i^2$ to

incorporate measurement uncertainty into the fittings. Both models along with the dataset have been plotted in **Figure 5.6**. Fitting parameters and goodness of fit indicators for both fittings are reported in **Table 5.2**.

Figure 5.6 shows that both models fit the dataset well. To decide which model provides a better description of the data with regards to the degree of freedom (i.e. the number of parameters used in the model) the χ^2 statistic was examined. For the power-law model χ^2_{min} = 0.194 with a number of degrees of freedom υ = 4 yields a reduced-χ^2 of 0.049. For the linear model, χ^2_{min} = 0.293 with the number of degrees of freedom υ = 5. The reduced-χ^2 is therefore 0.059. The probability of obtaining an observed value of χ^2_{min} or higher for a given number of degrees of freedom is given by the cumulative probability function $P(\chi^2_{min}\ ;\ \upsilon)$, accessible with lookup tables. This cumulative probability function has a much weaker dependence on ν than χ^2_{min} and is used here due to the low number of degrees of freedom [188]. For the power-law model, $P(0.194;\ 4)$ = 0.996 and for the linear model, $P(0.293;\ 5)$ = 0.998. Based on the χ^2 statistic alone, we cannot distinguish between the quality of the fit for the power-law and the linear model. A greater measurement precision would be helpful to differentiate between the two models. A linear model would show that only the volume fraction influences the thermal conductivity. On the other hand, a power-law could reveal, for instance, a dependence on the lattice geometry. From the uncertainty analysis performed in **section 4.2.4**, the uncertainty mainly comes from the precision of the temperature measurement. A reduction of 50 % in the temperature uncertainty would reduce the thermal conductivity uncertainty by 24 %. For the same uncertainty reduction in the thermal conductivity of the reference block, the overall uncertainty would decrease by 17 %. Finally, a 50 % decrease in the uncertainty of the specimen height would reduce the overall uncertainty by 0.5 %. Consequently, the uncertainty is expected to be greatly reduced with higher precision

temperature measurement techniques or the use of reference material with a more precisely known thermal conductivity. This would allow differentiation between the two models and inform on the thermal mechanisms.

As shown in **Figure 5.6**, the linear model is fully capable of describing the data, consequently, it can be used to engineer the thermal conductivity of a component using a gyroid matrix lattice.

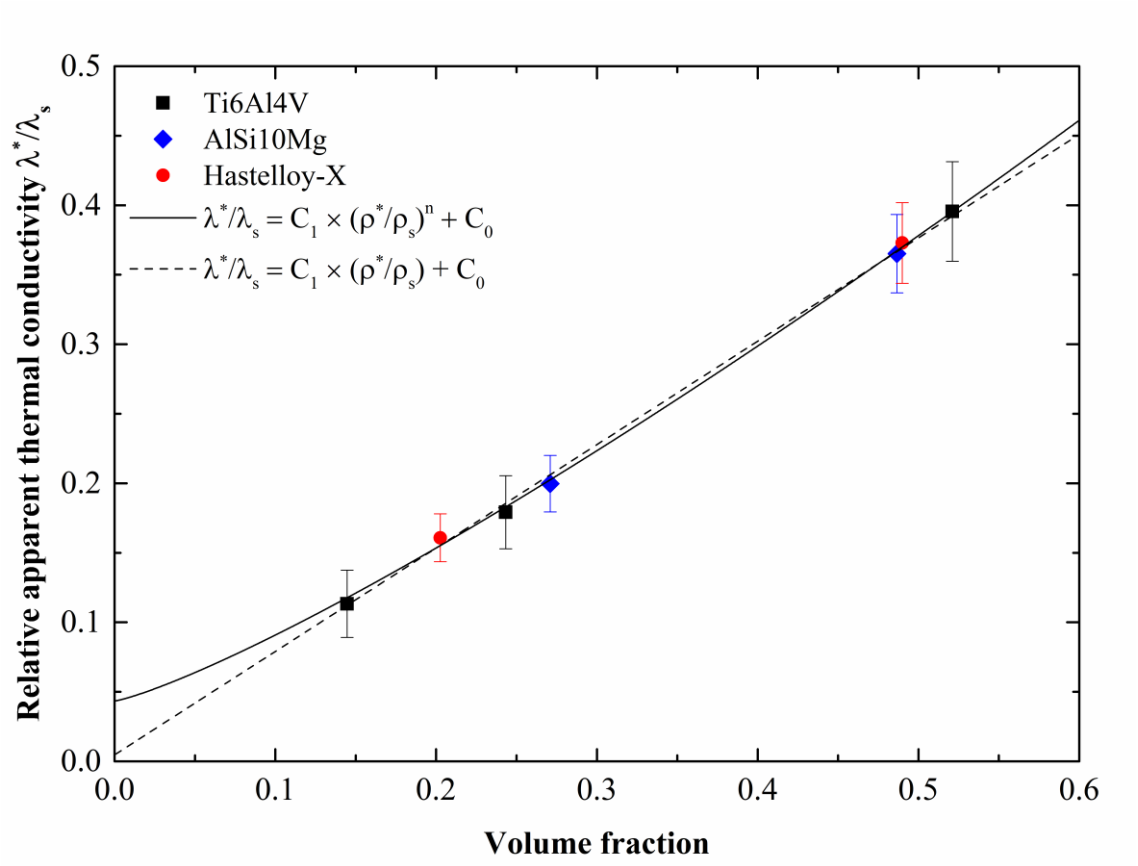


Figure 5.6: Influence of the volume fraction of a gyroid matrix lattice structure on the apparent thermal conductivity normalised from bulk material properties.

Table 5.2: Curve fitting parameters for the linear and power-law fits relating apparent thermal conductivity to the actual volume fraction with degree of freedom ν, and goodness of fit indicators: χ_{min}^2 and reduced-χ^2. Fitting parameters are given within one standard deviation.

	Power-law	**Linear fit**
n	1.21 ± 0.15	1.00
C_1	0.78 ± 0.04	0.74 ± 0.02
C_0	0.04 ± 0.02	0.01 ± 0.01
ν	4	5
χ_{min}^2	0.19	0.29
Reduced-χ^2	0.05	0.06

5.3.2 Cell size vs. apparent thermal conductivity

Prior to investigating the effect of the cell size on the apparent thermal conductivity, the apparent thermal conductivity was normalised to the actual specimen volume fraction. This was necessary to accommodate variations of volume fraction in the manufactured lattice specimens. The data were then plotted in **Figure 5.7** and **Figure 5.8** according to their designed volume fractions, 0.2 and 0.5 respectively, to improve readability. A linear fit was applied to both designed volume fractions using fitting weights $w_i = 1/\Delta(\lambda^*/\lambda_s)_i^2$ where $\Delta(\lambda^*/\lambda_s)_i$ are the measurement uncertainty. Gradient coefficients with their standard errors are reported in **Figure 5.7** and **Figure 5.8**. In both figures, the primitive matrix lattice systematically shows higher normalised apparent thermal conductivity than the gyroid and diamond matrix based on the same cell size and volume fraction. A similar trend has been observed for Hastelloy-X [181]. This higher normalised

apparent thermal conductivity for the primitive seems to indicate the unit cell design influences the thermal conductivity and this is investigated further in section **5.3.3**.

For the 0.2 designed volume fraction (**Figure 5.7**) there is a clear non-linear increase trend between the normalised apparent thermal conductivity and cell size. This indicates the cell size influences the conductivity of the lattice, with lower cell size having lower thermal conductivity. The maximum effect of the cell size for the 0.2 designed volume fraction represents a variation between 20 % ± 32 % and 26% ± 33 % on the normalised apparent thermal conductivity for the different lattice types over the examined range of cell size. For 0.5 designed volume fraction (**Figure 5.8**), the increase is questionable. To determine if the upward trend is significant a linear fit was performed including weights based on the experimental uncertainties. The gradient of the linear fit was compared to its standard error; if the gradient and its standard error were within zero, the normalised apparent thermal conductivity was considered constant, thus the cell size did not affect the normalised apparent thermal conductivity. For all three unit cells at the 0.5 designed volume fraction, the gradient is distinguishable from its standard error, thus they all have a statistically significant upward trend. However, the effect of the cell size at the 0.5 designed volume fraction represents a variation below 7 % ± 18 % on the normalised apparent thermal conductivity for the tested cell size. From the comparison of the linear fits between **Figure 5.7** and **Figure 5.8**, it can be concluded that the cell size influences the normalised apparent thermal conductivity of lattice structures at low volume fraction. On the other hand, the cell size effect becomes less significant at high volume fraction. Although the cell size influences the normalised apparent thermal conductivity, it only translates to less than 5 % ± 25 % in apparent thermal conductivity for both 0.2 and 0.5 volume fractions. The effect of the cell size on the apparent thermal conductivity for both designed volume fraction (0.2 and 0.5) cannot be distinguished from the effect of the volume fraction due to the large uncertainty of the measurement. Consequently, based on

the evidence here, the effect of the cell size on the apparent thermal conductivity may be considered of secondary importance compared to the dominant effect of the volume fraction.

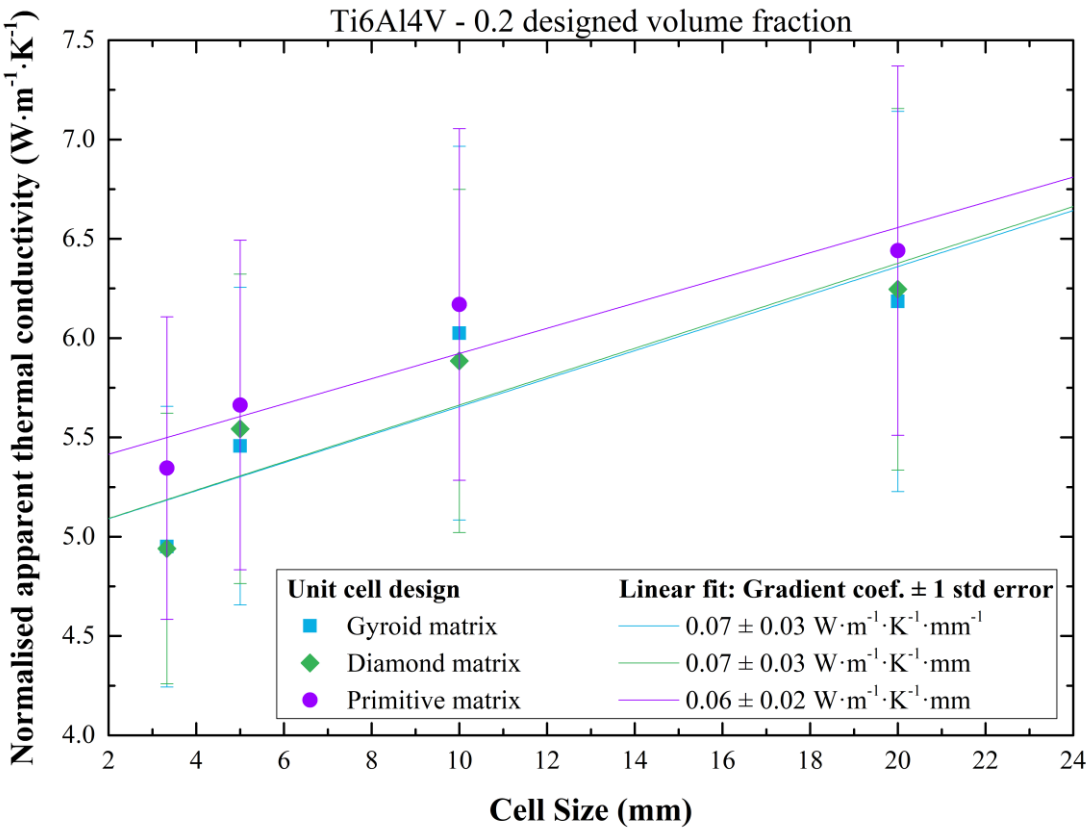


Figure 5.7: Normalised apparent thermal conductivity against lattice cell size at 0.2 designed volume fraction for Ti6Al4V lattice specimens. Error bars are calculated from the measurements as described in 4.2.4.

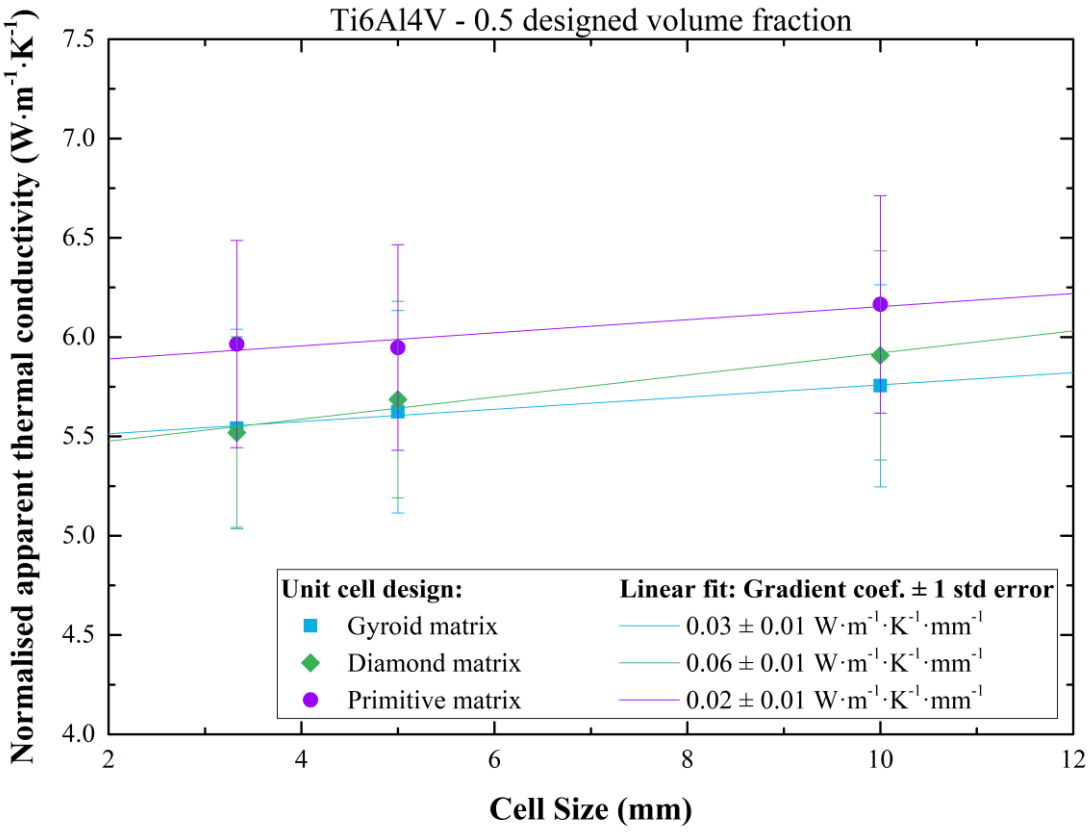


Figure 5.8: Normalised apparent thermal conductivity against lattice cell size at 0.5 designed volume fraction for Ti6Al4V lattice specimens. Error bars are calculated from the measurements as described in 4.2.4.

5.3.3 Unit cell design vs. apparent thermal conductivity

The relative apparent thermal conductivity (λ^*/λ_s) of the gyroid, diamond, and primitive matrices was plotted against the actual volume fraction for different cell sizes (20, 10, 5, and 3.33 mm), as shown in **Figure 5.9**. At low volume fractions (i.e. <0.35), three different unit cell designs have a similar apparent thermal conductivity. However, at higher volume fractions (i.e. >0.35), the apparent thermal conductivity of the primitive matrix is higher than diamond matrix and gyroid matrix, for the three cell sizes, as seen in **Figure 5.7** and **Figure 5.8**. As seen in section **5.3.1** the relative apparent thermal conductivity can be described by a linear relationship with the volume fraction of the

lattice. Also in **section 5.3.2**, the effect of the cell size was seen to be negligible compared with the volume fraction. A linear relationship seems to be observed between the volume fraction and the relative apparent thermal conductivity for all lattices of the same unit cell design regardless of the cell size. To test this hypothesis, a fit in the form reported in **Equation 5.1** where $n = 1$ was applied to each unit cell design and the whole dataset, using fitting weights: $w_i = 1/\Delta(\lambda^*/\lambda_s)_i^2$ where $\Delta(\lambda^*/\lambda_s)_i$ are the measurement uncertainty. Their fitting parameters and goodness of fit were then compared; if the fitting parameters are within one standard deviation it could be concluded that the diamond, gyroid, and primitive matrix relative apparent thermal conductivity and volume fraction can be appropriately described by a single relationship. The linear fit parameters for each unit cell design are reported in **Table 5.3**. The fitting parameters of the gyroid and diamond matrix unit cell type (0.75 ± 0.02 and 0.76 ± 0.03, respectively) are similar within one standard deviation. This shows the diamond and gyroid matrix apparent thermal conductivities share a similar relationship to the volume fraction. However, the linear gradient of the primitive matrix is significantly greater than the gyroid and diamond matrices (0.82 ± 0.02 vs 0.75 ± 0.02 and 0.76 ± 0.03, respectively). This indicates the primitive matrix relative apparent thermal conductivity has a higher proportionality to the volume fraction than the gyroid and diamond matrix, therefore, cannot be described by the same relationship.

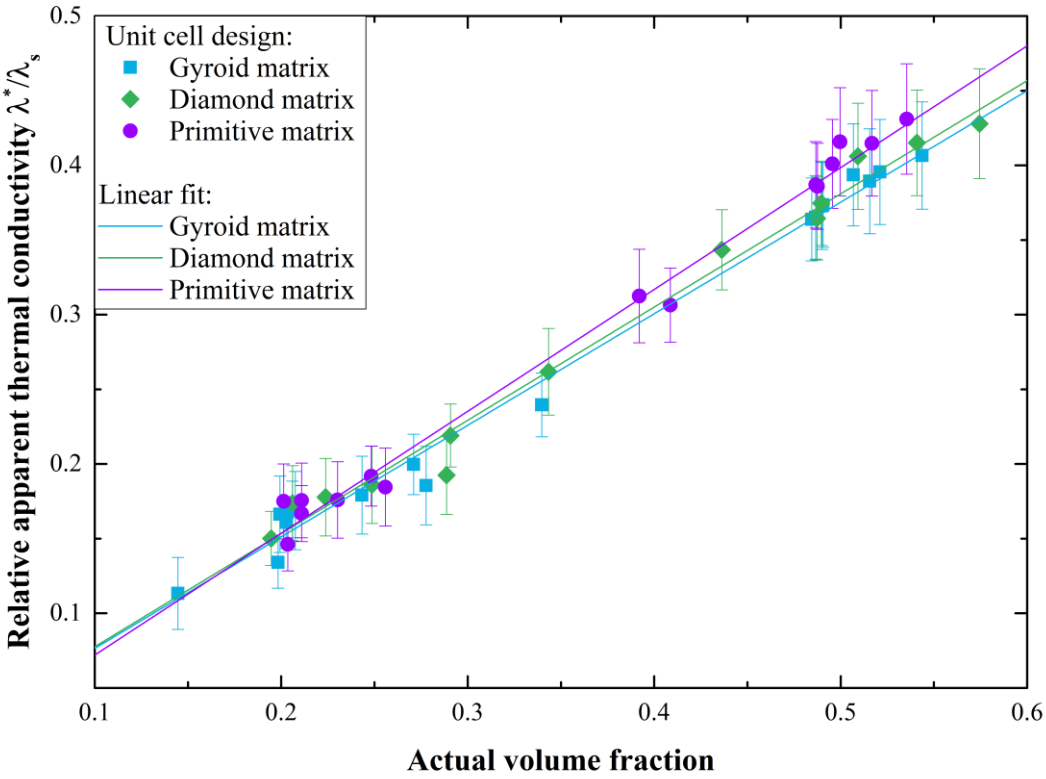


Figure 5.9: Relative apparent thermal conductivity against actual volume fraction of lattice structures. Error bars are calculated from the measurements as described in section 4.2.4.

Table 5.3: Fitting parameters with one standard deviation for a linear model linking apparent thermal conductivity to actual volume fraction for each of the tested unit cell designs. Fitting parameters are given within one standard deviation.

	C_1	C_0	v	χ^2	Reduced-χ^2
Gyroid matrix	0.75 ± 0.02	0.00 ± 0.01	15	3.86	0.26
Diamond matrix	0.76 ± 0.03	0.00 ± 0.01	10	2.21	0.22
Primitive matrix	0.82 ± 0.02	-0.01 ± 0.01	12	2.44	0.20
Gyroid + Diamond	0.75 ± 0.00	0.02 ± 0.01	29	6.24	0.23

To corroborate further the linear approximation, lattice specimens with different unit cell designs and cell sizes in which volume fractions were calculated from **Equation 5.1** with n = 1 and fitting parameters from **Table 5.3** to achieve specific relative apparent thermal conductivities. Specimens were manufactured, measured, and tested in the same conditions as previously described, and details of specimen design and measurements are provided in **Table 5.4**. Firstly, all manufactured lattice structures had a higher volume fraction than designed (between 5.4 % and 10.5 %). This results in 10.9 % to 16 % higher measured apparent thermal conductivity. However, by calculating the expected thermal conductivity from the measured volume fraction ρ^*/ρ_s from the manufactured specimen, the difference is reduced to less than 1 %. This shows that lattice apparent thermal conductivity can be predicted and achieved using **Equation 5.1** and fitting constants from **Table 5.4** for gyroid, diamond and primitive matrix structures, regardless of the cell size.

Table 5.4: Design parameters and experimental data for the Ti6Al4V target thermal conductivity lattice specimens.

	Gyroid matrix	**Diamond matrix**	**Primitive matrix**
Cell size (mm)	3.33	10	5
Target λ^*/λ_s	0.337	0.236	0.270
CAD ρ^*/ρ_s	0.467	0.325	0.372
Measured ρ^*/ρ_s	0.516	0.343	0.392
Measured λ^*/λ_s	0.390	0.262	0.313
λ^*/λ_s from measured ρ^*/ρ_s	0.390	0.260	0.310
ρ^*/ρ_s %diff	10.6	5.7	5.4
λ^*/λ_s %diff	15.7	11.0	15.9
λ^*/λ_s %diff from measured ρ^*/ρ_s	0.1	0.9	0.9
Surface area (mm^2)	14385	6470	7702
Vol. (mm^3)	3749	2608	2983
SA : vol (mm^{-1})	3.8	2.5	2.6

5.4 Discussion

5.4.1 AlSi10Mg thermal conductivity and heat treatments

The laser powder bed fusion manufacturing process creates a characteristic microstructure with elongated grains in the *yz*-plane and a more equiaxed microstructure in the *xy*-plane as seen in **Figure 5.1**. The high cooling rates, up to 10^6 °C.s^{-1} [56] result in an ultrafine microstructure compared to the cast version of AlSi10Mg alloy, as previously reported [189]. When solidification starts, α-Al solidifies first, rejecting Si into the melt pool and creating needle-like α-Al grains oriented toward the heat source (parallel to the build direction). As the material cools further, Si-rich liquid solidifies around the aluminium rich grains creating a cellular microstructure shown in **Figure 5.1(k)-(l)**. Within the microstructure, three distinctive regions are present: a fine microstructure in the melt pool core transitioning to a coarser microstructure around the melt pool and finishing in a disordered microstructure due to successive reheating during the manufacturing process [60].

Solution heat treatments break down the cellular microstructure by allowing Si to diffuse within the aluminium matrix and precipitates into larger Si nodules as seen in **Figure 5.1**. A controlled size precipitation of the Si nodules was achieved with artificial ageing after SHT, resulting in higher hardness. However, in **Figure 5.3** the as-built condition exhibits the highest hardness and the T6-like heat treatment does not outperform it, even though T6 is designed to optimise mechanical properties. As-built specimens benefit from grain boundary strengthening; the smaller the grain size, the more grain boundaries. These act as insurmountable obstacles for dislocations to propagate. Any heat treatment coarsens the ultrafine microstructure of the as-built specimen, which decreases the grain boundary strengthening effect [76].

The difference in thermal conductivity between the as-built and the heat-treated specimens indicates that microstructure was the cause of the differences in thermal properties. All specimens were manufactured in the same conditions from the same feedstock with the same parameters and exhibited similar very low levels of porosity (e.g. porosity variation <0.2 %, see **Table 5.1**). For the as-built condition, the Si particle morphological differences, observed in **Figure 5.1,** translate to disparities in conductivity, since Si has a lower conductivity than Al; 156 $W \cdot m^{-1} \cdot K^{-1}$ for Si compared to 237 $W \cdot m^{-1} \cdot K^{-1}$ for Al [155]. Heat is transferred less efficiently in the transverse direction because the connectivity of the α-Al matrix is hampered by the finely dispersed Si cellular structure (see **Figure 5.1**). Whereas, in the build direction, the heat can travel mostly through the elongated α-Al areas. It is also worth noting that the thermal conductivity of the as-built specimen may be further diminished due to the high solubility of Si in the α-Al matrix [190].

The breakdown of the Si cellular structure into spheroids under heat treatment was the key mechanism to enhance thermal conductivity. Heat was more effectively transferred through the highly conductive α-Al matrix and with fewer Si barriers, thermal anisotropy disappeared. The annealing treatment used here is typically used to relieve thermal stresses of AlSi10Mg parts made by LPBF and reduced distortions and enhance ductility. It has been shown here to also remove thermal anisotropy. The enhancement of the thermal conductivity of the heat-treated specimens is a result of several mechanisms such as the coarsening of the grain structure and the diffusion of the different solute elements such as Si from the α-Al matrix. The measured thermal conductivities for heat-treated LPBF AlSi10Mg are within the range given by the DIN EN 1706:2010 standard for cast aluminium. This specifies λ = 140 – 170 $W \cdot m^{-1} \cdot K^{-1}$ depending on the condition.

The apparent thermal conductivity of gyroid lattice structures was measured before and after annealing. As-built lattices do not exhibit thermal anisotropy, which differs from

solid specimens discussed before despite having the same observed microstructure. The isotropic apparent thermal conductivity is believed to be due to the anisotropic microstructure combined with the lattice complex shape. Tortuous thin walls prevent the heat from being preferentially transported through the more conductive Al-matrix columnar grains. Instead, the heat must flow across successive Si barriers. The as-built lattice microstructure in **Figure 5.2(a)-(b)** shows the same anisotropy as the solid specimens despite exhibiting isotropic thermal conductivity. After annealing heat treatment, the microstructure follows the same trend as for solid specimens with the breakdown of the Si network. An increase in thermal conductivity compared to the as-built condition is also observed. The effectiveness of the heat treatment was tested by examining two different volume fractions (0.2 and 0.5). For the 0.2 volume fraction, the increase in thermal conductivity is smaller compared to the effect on the 0.5 volume fraction, despite having the same microstructure evolution with the breaking down of the Si network (**Figure 5.2**). This is caused by the preponderant effect of the volume fraction and will be discussed next.

5.4.2 Thermal conductivity of lattice structures

As detailed at the beginning of **section 5.3**, the main heat transport mechanism considered was the conduction through the solid phase. **Figure 5.6** showed that the apparent thermal conductivity of the material can be described by a power-law or linear relationship with volume fraction. However, the uncertainty of the measurements does not allow differentiation between the two models. Furthermore, the variation of volume fraction also influences the wall thickness, surface area, and free interval volume of the lattice structures. A better description of the relationship between the apparent thermal conductivity and those parameters could be achieved with a higher measurement precision. However, their relationships to the volume fraction and inter-relationships are

not fully understood yet and require a large amount of data from lattice structures with dissimilar geometries. The aim here is to develop a more practical model that designers can use and facilitates the widespread adoption of lattice structures for heat management applications.

The effect of lattice cell size on thermal conductivity was isolated from volume fraction by normalising the apparent thermal conductivity across the lattice specimens and is shown in **Figure 5.7** and **Figure 5.8**. It was observed that the normalised conductivity increases with the cell size, with a greater impact on the 0.2 volume fraction. Two phenomena can explain this trend. Firstly, at small cell sizes, the wall thicknesses are notably lower compared to larger cell sizes at constant volume fraction (**Table 5.5**). This is illustrated in **Figure 5.10** where lattice structures have their cell size variation, whilst their volume fraction was kept constant at 0.2. A reduced wall thickness diminishes the heat transfer efficiency and reduces thermal coupling between the lattice specimen and the reference blocks. Also, potential defects (i.e. porosity) in thinner walls can further reduce the thermal conductivity. Moreover, LPBF surfaces generally exhibit high roughness due to attached particles, which represents a greater proportion of the total wall thickness than for thicker walls. These attached particles are usually partially fused which limits thermal conductivity due to imperfect metallurgical bonds. Secondly, the contribution of natural convection to the overall thermal conductivity was assumed to be negligible. This is true for smaller cell sizes where air is constrained to tightly spaced cells and cannot travel large distances in the direction of the thermal gradient. With larger cell size the air currents can travel larger distances, thus increasing the apparent thermal conductivity of the specimens through convection. This effect has been reported by Griffin and Skochdopole in closed-cell foams [191]. The convection through air was assumed to be constant and a negligible contribution to the measurement. Convection within the cell is inherent to the lattice geometry but could be controlled with the lattice

cell size as shown in **Figure 5.7** and **Figure 5.8**, where larger cell size would maximise natural convection for passive cooling or insulation can be maximised by reducing the cell size. The increase in apparent thermal conductivity from the cell size was observed to be greater for lower volume fraction. However, this effect only represents a small percentage of the apparent thermal conductivity for the tested volume fraction. The effect of convection within the lattice structure could be exposed not only by having more precise temperature measurements, but also by encapsulating the test apparatus and replacing its atmosphere with a gas similar to air but with a significantly different thermal conductivity and repeating the measurements. If the apparent thermal conductivities in both gas atmosphere are similar, this would confirm the convection contribution is negligible. If not, differences in conductivity would reveal the size of the effect of convection within the lattice structure.

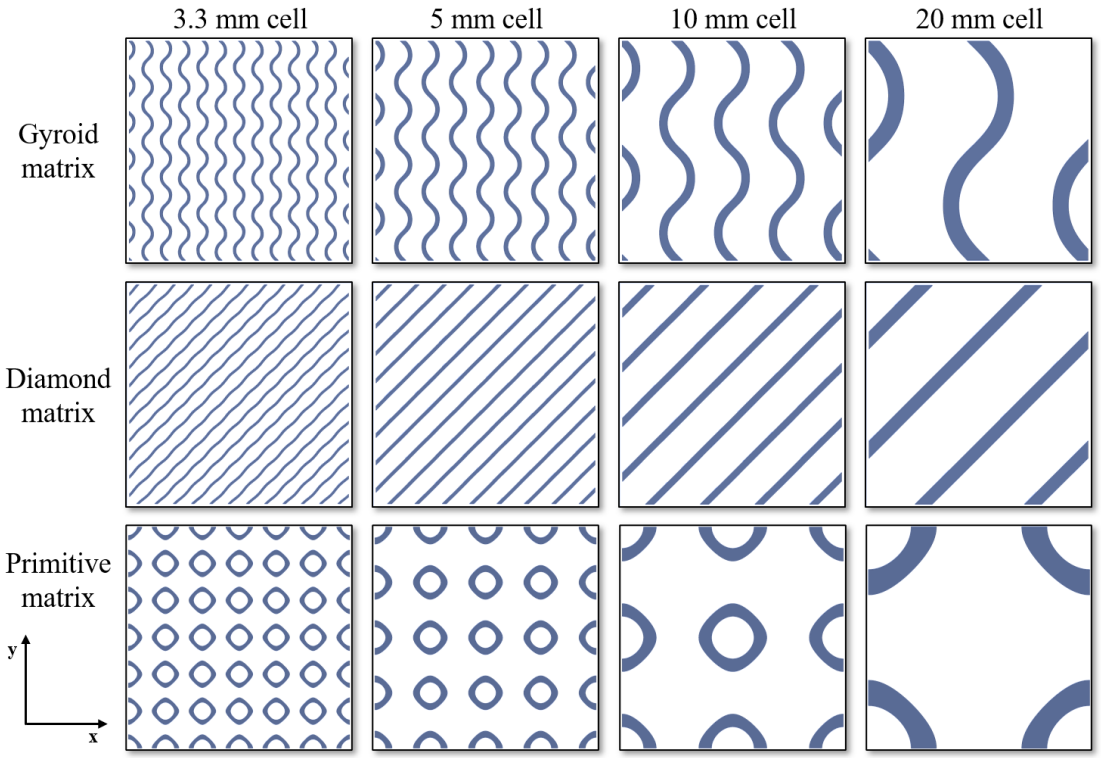


Figure 5.10: Cross-sectional representation of changes in wall thicknesses and internal free space across different unit cell sizes at a constant 0.2 volume fraction for the gyroid, diamond, and primitive matrix lattices.

Table 5.5: Surface area, volume, and the minimum wall thickness of each lattice structure CAD model.

Unit cell	ρ^*/ρ_s	Cell size (mm)	Surface area (mm^2)	Volume (mm^3)	SA : vol	Minimum wall thickness (µm)
Gyroid matrix	0.2	3.33	14960	1572	9.5	230
		5	10127	1579	6.4	355
		10	5252	1584	3.3	725
		20	2825	1601	1.8	1410
	0.5	3.33	14109	3994	3.5	610
		5	9772	4003	2.4	910
		10	5429	4008	1.4	1820
Diamond matrix	0.2	3.33	18583	1509	12.3	190
		5	12485	1584	7.9	275
		10	6412	1584	4.0	555
		20	3384	1602	2.1	1110
	0.5	3.33	17131	4004	4.3	490
		5	11793	3995	3.0	730
		10	6379	4006	1.6	1480
Primitive matrix	0.2	3.33	11399	1595	7.1	265
		5	7744	1590	4.9	400
		10	4050	1590	2.5	795
		20	2211	1600	1.4	1850
	0.5	3.33	10584	4005	2.6	685
		5	7406	3999	1.9	1030
		10	4210	4000	1.1	2070

The effect of the unit cell design and volume fraction on the apparent thermal conductivity was explored and reported in **Figure 5.9**. It was observed that lattices with primitive unit cells have the highest apparent thermal conductivity among all tested unit cell designs. In addition, the primitive unit cell has the highest gradient (see **Table 5.3**), thus it is better

at conducting heat at higher volume fractions than gyroid and diamond unit cells. These indicate that the primitive unit cell has different heat transport mechanisms contributing to the measured apparent thermal conductivity. This is believed to be caused by the larger wall thicknesses and smaller internal free volume at higher volume fraction. The primitive unit cell benefits from fewer walls but greater wall thicknesses (see **Figure 5.10** and **Table 5.3**) and possible convective heat transfer due to its large internal sphere-like void. Furthermore, the geometry of the primitive unit cell allows air to travel directly from the bottom to the top with very little restrictions, which promote convection currents, whereas the gyroid and diamond unit cells have a similar and more tortuous flow path. These could explain why the primitive unit cell had the highest apparent thermal conductivity among all tested unit cell designs (**Figure 5.9**) and why gyroid and diamond lattices have similar apparent thermal conductivities.

The apparent thermal conductivity of a lattice structure manufactured by LPBF can be easily controlled by changing the volume fraction. To demonstrate this, lattices were manufactured with volume fractions calculated from the fitting equation and parameters (**Equation 5.1** and **Table 5.3**) to achieve a chosen thermal conductivity. The measurements show good agreement with the previous data (**Figure 5.9**), despite discrepancies between the designed and actual volume fractions of the target specimens. This highlights the effect of geometry and process parameters on the designed and actual volume fraction. The higher the surface area to volume ratio, the more sintered particles are attached, which results in higher volume fraction as can be seen in **Table 5.4**. Among the target specimens, the gyroid has the highest surface area to volume and shows the highest volume fraction difference. This emphasizes that lattice structures require further optimisation from bulk material parameters due to differences in thermal mass and special attention to border parameters is needed for thin sections to limit the amount of sintered particles. The target specimens showed that by solely controlling the lattice volume

fraction, specimens with specific apparent thermal conductivity could be manufactured. This enables the creation of graded-lattice structures with spatially-controlled thermal properties to respond optimally to thermal loading; thermal pathways consisting of high volume fraction lattices can be used to conduct heat away, while low volume fraction areas protect temperature-sensitive regions. Furthermore, a component can be designed to achieve a specific thermal conductivity by choosing its volume fraction and the cell size can be selected to fulfil a mechanical criterion such as stiffness or energy absorption [122,192]. This paves the way for the development of multifunctional components.

5.5 Design models for thermal conductivity of lattices

In this chapter, several models have been explored to link the relative apparent thermal conductivity (λ^*/λ_s) of lattice structures to lattice parameters such as volume fraction (ρ^*/ρ_s) cell size and unit cell design. It has been shown that the volume fraction has a preponderant effect on the thermal conductivity. This section summarises the models that can best be used to design lattice structures with specific thermal conductivity to help designers in their task.

Model $\frac{\lambda^*}{\lambda_s} = f\left(\frac{\rho^*}{\rho_s}\right)$ for gyroid matrix for ρ^*/ρ_s ranging from 0.15 to 0.55.

$$\frac{\lambda^*}{\lambda_s} = 0.74 \times \frac{\rho^*}{\rho_s} + 0.01 \qquad \textbf{Equation 5.2}$$

Model $\frac{\lambda^*}{\lambda_s} = f\left(\frac{\rho^*}{\rho_s}\right)$ for gyroid, diamond matrix for ρ^*/ρ_s ranging from 0.20 to 0.55.

$$\frac{\lambda^*}{\lambda_s} = 0.75 \times \frac{\rho^*}{\rho_s} + 0.02 \qquad \textbf{Equation 5.3}$$

Model $\frac{\lambda^*}{\lambda_s} = f\left(\frac{\rho^*}{\rho_s}\right)$ for primitive matrix for ρ^*/ρ_s ranging from 0.20 to 0.55.

$$\frac{\lambda^*}{\lambda_s} = 0.82 \times \frac{\rho^*}{\rho_s} + 0.02 \qquad \textbf{Equation 5.4}$$

5.6 Summary

In this chapter, the thermal conductivity of AlSi10Mg coupons and lattice test specimens were measured and reported in the as-built condition and after several post-heat treatments using a custom-build test apparatus. The specimens were on average (99.78 ± 0.06) % dense. This high relative density indicates that any significant variation in thermal conductivity is attributable to differences in the specimen microstructure. As-built specimens have anisotropic microstructures with elongated aluminium grains along with segregated silicon-rich areas in the build direction. In the transverse direction, a cellular network of aluminium-rich nodules surrounded by silicon-rich regions was observed. This anisotropy was also observed in the thermal conductivity with a higher value in the build direction than in the transverse direction. This was understood to be caused by the higher thermal conductivity of aluminium over silicon, thus the Si network hampers the overall thermal conductivity. The key mechanism to improve the thermal conductivity was the breakdown of the Si network through heat treatment, allowing heat to flow more effectively through the α-Al phase. All the tested heat treatments increased the thermal conductivity of LPBF AlSi10Mg compared to the as-built condition and brought it in alignment with the DIN EN 1706:2010 standard, which stipulates conductivity values between 140 – 170 $W \cdot m^{-1} \cdot K^{-1}$. Annealing heat treatment, which is mostly used as a stress relief treatment post-manufacture, eliminated the as-built thermal conductivity anisotropy and enhanced the conductivity by nearly 30 % in the transverse direction. Solution heat treatments enhanced further the conductivity (36 % compared to as-built). The greatest enhancement was found with the T6-like heat treatment (44 % compared to as-built), which is usually used to improve the mechanical properties of LPBF AlSi10Mg. Therefore, T6-like heat treatment must be not only considered as a mechanical, but as thermo-mechanical heat treatment.

The thermal conductivity of gyroid matrix lattice structures in as-built condition was shown to be almost isotropic, despite observing the same anisotropic microstructure of the as-built coupons. This is believed to be due to the tortuous geometry of the gyroid geometry forcing the heat to flow across successive Si barriers rather than shortcutting through the α-Al phase in the build direction. Annealing heat treatments increased thermal conductivity proportionally to the lattice volume fraction, i.e. lower volume fractions showing smaller improvements. This indicates that lattice structure could be used to minimise, or potentially control, the degree of thermal anisotropy in LPBF components. From these results, we can surmise graded-density lattice structures may have not only spatially-varying mechanical and thermal properties, but also a spatially-varying response to any post-manufacture heat treatment. This opposes the conventional design views that assume heat treatments have a homogeneous effect on the material properties. The effect of graded structures can be further reinforced by heat treatments, reducing further the amount of material needed leading to even lighter components, making such structures even more attractive to designers.

The volume fraction, unit cell design, and cell size were correlated to the apparent thermal conductivity of lattice structures. It was shown that the thermal conductivity can be described by a linear relationship with the volume fraction. It was also observed that the volume fraction has a preponderant effect on the apparent thermal conductivity of the specimen. The unit cell design and cell size play a secondary role, increasing the apparent thermal conductivity possibly through thicker walls. The unit cell design and cell size can also increase the apparent thermal conductivity via promoting convective heat transfer when large internal free volumes are available. This is believed to explain the higher thermal conductivity of the primitive compared to the gyroid and diamond matrix. An estimation of the convection contribution by the test apparatus would require the replacement of air by another gas having a significantly different thermal conductivity

and repeating the measurements with higher precision temperature measurements. It also was demonstrated that lattice structures with a pre-defined apparent thermal conductivity can be manufactured by LPBF from the linear model developed in this chapter.

High volume fraction lattice structures should be applied in additively manufactured parts in areas where heat must be transferred effectively. On the other hand, low volume fraction may be used to insulate temperature-sensitive areas from high heat flux. These can be easily achieved by the parameterisation of lattice structures which gives total control over the material's distribution via volume fraction but also to a lesser extent through lattice unit cell design and cell size. This is of importance, in particular for multifunctional applications, a component can be designed to achieve a specific thermal conductivity by solely choosing its volume fraction whilst a second property such as its mechanical behaviour or pressure drop can be adjusted by tweaking the cell topology. The latter will be investigated in the next chapter.

The findings and the models summarised in **section 5.5** in this chapter are particularly useful in designing lattice structures for thermal application and better predict LPBF component response to thermal loads and will enable the development of high-performance AM components in thermal management as well as multifunctional components.

6 Forced Convection Heat Transfer

6.1 Introduction

The literature review in **section 2.3.4** indicates that the thermal performance of lattice structures has mainly been investigated for non-additively manufactured strut-based lattices. TPMS lattice structures have been identified as a promising candidate for heat transfer applications due to their high surface-to-volume ratio, complex flow paths which maximise fluid-surface contact time, and easily controllable geometrical features. However, few investigations have been conducted for TPMS lattice structures.

The literature reported two main factors for the characterisation of structures in forced convection heat transfer: the pressure drop, which indicates the pumping power required to circulate a flow across the considered structure, and heat transfer coefficient, which reports the amount of heat energy the system can dissipate. These two numbers are functions of the flow condition. Generally, dimensionless numbers are preferred to facilitate comparison across different systems, with the pressure drop expressed by the friction factor (see **Equation 2.10**), the heat transfer coefficient by the Nusselt number (see **Equation 2.8**) and the flow condition represented by the Reynolds number (see **Equation 2.9**). However, this chapter compares the thermal performance of geometrically dissimilar shapes, which precludes the use of dimensionless numbers to avoid the introduction of bias, therefore the data is presented in dimensional form.

This chapter has the objective of investigating the thermal performance of lattice structures by experimentally measuring the pressure drop and heat transfer of several AlSi10Mg TPMS lattice structures manufactured by LPBF in forced convection heat transfer over a range of flow conditions using dry air as the heat transfer fluid. It also has the objective of understanding how lattice parameters (cell size and unit cell design) affect pressure losses and heat transfer coefficients. The performance of AlSi10Mg TPMS

lattice structures is reported in terms of pressure drop and heat transfer coefficient across a range of mass flow rates. These allow deriving a set of design rules for the use of TPMS lattice structures for heat exchange and their implementation in high-performance components across a range of materials and use cases.

6.2 Pin fin benchmark

6.2.1 Benchmark geometry

The experimental apparatus described in section **4.3.1** was benchmarked using a pin-fin geometry reported in **Figure 4.8** manufactured in AlSi10Mg by LPBF using the parameters reported in section **3.3.2** and the preparation method described in section **4.3.6**. The geometry dimensions are reported in **Figure 4.8** and **Table 6.1**.

Table 6.1: Pin-fin benchmark dimensions.

	Vol. frac.	***S*** **(mm)**	***T*** **(mm)**	***H*** **(mm)**	***D*** **(mm)**	S_v **(mm2)**	**Number of pin**	A_{min} **(mm2)**
CAD	0.20	3.90	5	10	2.27	9790	124	335
Measured	0.20	3.88	4.98	9.87	2.27	-	124	-

6.2.2 Pressure drop validation

The pressure drop across the pin-fin benchmark coupon was measured and its friction factor is reported in **Figure 6.1** along with results that are available in the literature for similar geometries. For ease of comparison, the Reynolds number and friction factor are based on the pin diameter, D, and maximum fluid velocity, U_{max}, and are defined as follows:

$$Re_{D,U_{max}} = \frac{U_{max} \cdot D}{\nu_{air}} \qquad \textbf{Equation 6.1}$$

$$f_D = \frac{\Delta P \cdot D}{L} \cdot \frac{2}{\rho_{air} \cdot {U_{max}}^2} \qquad \textbf{Equation 6.2}$$

$$U_{max} = \frac{S_T}{S_T - D} \cdot \overline{U} \qquad \textbf{Equation 6.3}$$

where $\overline{U}$ is the mean air velocity calculated from the cross-sectional area of the apparatus (10 mm × 50 mm) and the volumetric flow rate, ρ_{air} and ν_{air} are the air density and kinematic viscosity, S_T is the pin spanwise spacing, and D is the pin diameter (see **Figure 4.8**).

Short's empirical correlation [193] allows determination of the friction factor of smooth pin-fins based on the streamwise spacing ratio *S/D*, transverse spacing ratio *T/D*, and pin height to diameter ratio *H/D* for Reynolds number from 10^2 to 10^4 with a maximum error between ± 16 % and ± 46 %. Gaddis *et al.* [194] also provided an analytical model to predict the friction factor of a given smooth pin-fin based on its geometry over Reynolds numbers ranging from 10^1 to 3×10^5 with a maximum error of ± 35 %. In addition, additively manufactured pin-fins from Wong *et al.* [24] and Kirsch *et al.* [138] were also reported in **Figure 6.1**. The pin-fin benchmark tested in this thesis has a lower friction factor than predicted by Short and Gaddis correlations with a steeper dependence on Reynolds number for $Re_d > 3\cdot10^3$. The differences with Wong and Kirsch measurements are mainly believed to be due to the different specimen geometries with significantly different *T/D* (i.e. pin spanwise spacing to pin diameter ratio). Differences in surface roughness could also explain some of the discrepancies with Wong and Kirsch data. This work differs between (10 ± 52) % and (56 ± 50) % with Gaddis empirical model and between (36 ± 31) % and (69 ± 34) % with Short empirical model. Both models were intended for smooth surface pin-fins while AM surfaces exhibit high levels of roughness. For laminar flow ($Re_d < 2\times10^3$), the friction is independent of the surface roughness

whereas for turbulence flow ($Re_d > 2\times10^3$) the friction tends to become only dependent on the surface roughness of the flow channels [195]. This explains the larger discrepancy observed for $Re_d > 2\times10^3$. Therefore, the measured pressure drop of the LPBF pin-fins meets the theoretical behaviour.

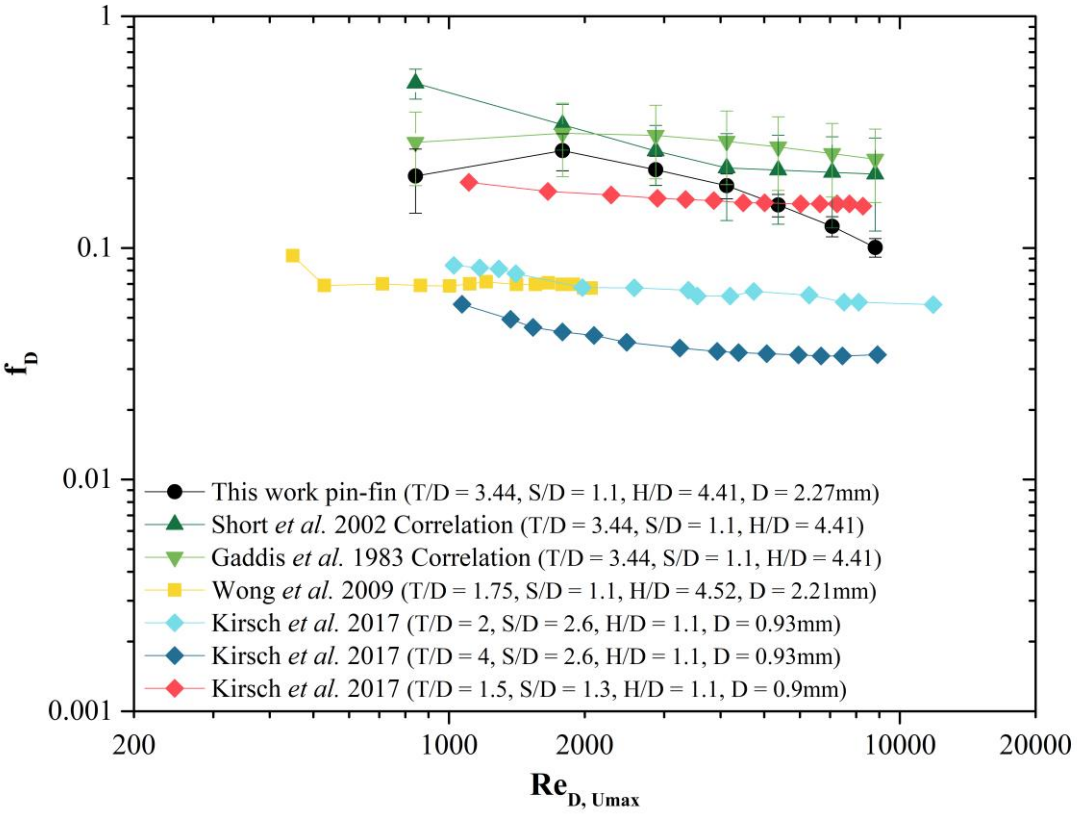


Figure 6.1: Friction factor of pin-fin benchmark coupon against Reynolds number based on the pin diameter *D* and U_{max} compared to the existing literature for similar geometries. Error bars represent the measurement uncertainty.

6.2.3 Heat transfer validation

Nusselt numbers based on the pin diameter of the pin-fin benchmark coupon along with Gnielinski's correlation [196] and Wong *et al.* [24], and Kirsch *et al.* [138] AM pin-fins are reported in **Figure 6.2**. The Nusselt number of the pin-fin benchmark tested in this thesis is significantly lower than predicted by Gnielinski's correlation. This is due to the

absence of thermal paste between the copper block and the lattice skin creating high thermal resistance. However, this setup is sufficient to examine the relative difference in thermal transport in a range of AM lattices, which is the main aim of this chapter.

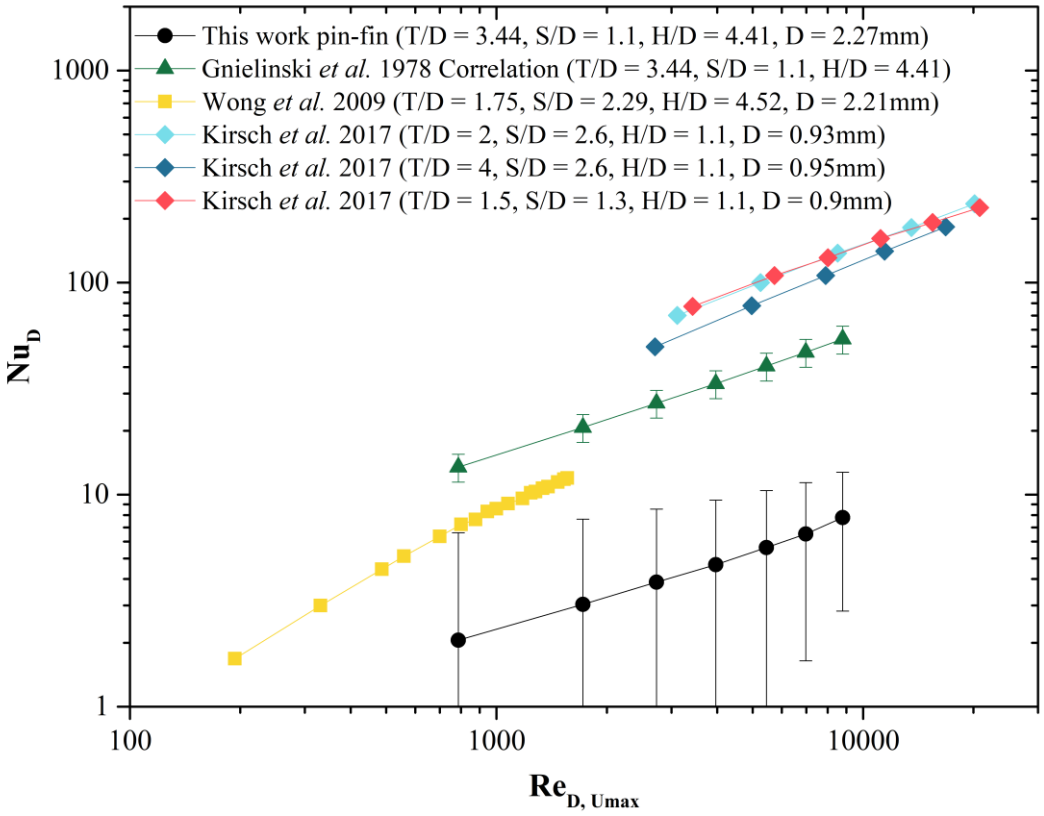


Figure 6.2: Nusselt number of pin-fin benchmark coupon against Reynolds number based on the pin diameter and U_{max} along with existing literature for similar geometries. Error bars represent the measurement uncertainty.

6.3 TPMS lattice structures

6.3.1 Lattice geometries

Isometric views of the lattice unit cells are displayed in the top row in **Figure 6.3** to illustrate the variation seen in the unit cells in 3D. The bottom row shows the frontal area contacted by the flow, where the flow direction is into the page. This can aid the understanding of some of the geometric features that result in a large variation in both the

pressure drop and heat transfer performance across the specimen set. These lattice structures have been chosen due to their distinct shapes allowing different flow paths. **Figure 6.3** provides geometrical data for the lattice structure specimens under investigation, such as specific surface area per unit volume and the minimal cross-sectional area of the flow domain (A_{min}). (Note: The specific surface area per unit volume relates to the volume of solid material within each cell, not the volume of the specimen bounding box). As cell size decreases, the S_v increases following a multiplicative inverse relationship. It is worth noting that the minimal cross-sectional area of the flow domain does not change with the cell size and the small differences observed are due to change in file resolution and represent a variation well below 1 %.

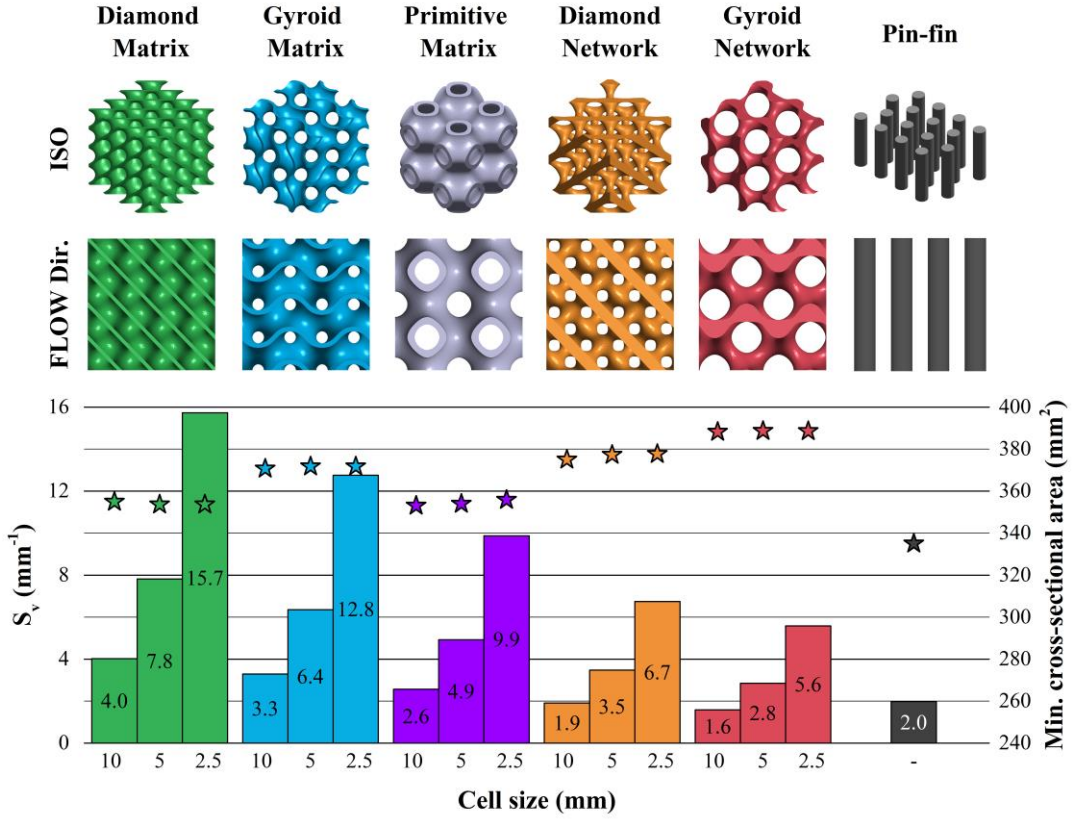


Figure 6.3: View of 10 × 10 × 10 mm section with 5 mm unit cell size cut of unit cell under investigation in this chapter in ISOmetric and in FLOW Direction. Lattice specific surface area per unit volume S_v are reported along with the minimal cross-sectional area of the fluid domain in the flow direction for each lattice.

Table 6.2 reports the designed and measured volume fractions of the AlSi10Mg tested lattice structures manufactured by LPBF. The measured volume fraction increases as the lattice cell size decreases. This is believed to be due to the manufacturing process. LPBF induced surface roughness constituted by sintered particles that will remain constant across feature size scales, i.e. the surface roughness will be similar for a 5 mm thick wall as it will be for a 500 μm thick wall. Consequently, as the surface area to volume ratio of the lattice increases, the amount of sintered particles increases, leading to extra mass therefore a large volume fraction. This is expected to affect negatively the pressure drop and positively the heat transfer performance of the lattices as previously observed by Kirsch *et al.* [138] for pin-fins manufactured by LPBF. However, the effect of the surface roughness on the thermal performances of lattice structures is complex and would require its own investigation, which is not the subject of this thesis. The 2.5 mm cell size diamond and gyroid matrix lattices exhibit large differences between the CAD and measured volume fractions. This would affect the thermal measurements of these lattices; therefore, these two specimens have been disregarded.

Table 6.2: Lattice structures CAD vs. measured volume fractions.

Cell type	Unit cell	Cell size	CAD vol. frac.	Measured vol. frac.	%diff.
Matrix	DIA	10	0.2	0.19	-4.3
		5		0.21	5.8
		2.5		0.32	49.0
	GYR	10		0.19	-1.1
		5		0.20	1.5
		2.5		0.29	44.5
	PRI	10		0.18	-7.1
		5		0.19	-1.2
		2.5		0.22	8.7
Network	DIA	10	0.2	0.19	-4.2
		5		0.19	-2.7
		2.5		0.19	-1.7
	GYR	10		0.19	-1.3
		5		0.19	-0.6
		2.5		0.19	0.3

6.3.2 Pressure drop results

The pressure drop measurements for all lattice structures are shown alongside the pin-fin benchmark coupon results in **Figure 6.4**. First, the matrix phase lattices exhibit a higher pressure drop than network phase lattices and the benchmarked pin-fin geometry. At low mass flow rates ($<5\times10^{3}$ kg·s^{-1}), the different lattice specimens of the same phase exhibit similar pressure drops. Among the matrix phase, the gyroid has the lowest pressure drop for each tested cell type. The primitive has the highest pressure drop for both 10 mm and 5 mm cell size. Among the network phase lattices, the gyroid has a lower pressure drop than the diamond across all cell sizes and the pressure drop difference between these two

unit cell designs are greater in the network phase than for the matrix phase. The difference in pressure drop between the 2.5 mm cell size diamond and gyroid network is greater than for the larger cell sizes. This is thought to be caused by the increasing influence of the smallest channel acting as bottleneck as the cell size decreases. It is worth noting that the larger cell size of network phase lattices has a similar pressure drop to the pin-fin benchmark. This indicates these lattice structures could be a replacement for traditional pin-fin geometry.

The reduction of the cell size increases the pressure drop owing to the increase in the amount of surface exposed to the fluid, increasing the frictional resistance. Consequently, smaller cell size specimens have higher pressure drops, shown for both matrix and network phases in **Figure 6.5** where the pressure drop of the lattice specimens against the mass flow rate and specific surface area per unit volume is reported. A correlation between the specific surface area per unit volume S_v and the pressure drop seems to be observed. When the cell size is halved, the specific surface area per unit volume, S_v, doubles and so does the pressure drop, regardless of the unit cell design (see **Figure 6.3** and **Figure 6.4**). This is particularly true for 10 mm to 5 mm cell size. The diamond network pressure drop triples from 5 mm to 2.5 mm, despite having a volume fraction 1.7 % lower than CAD. This is believed to be caused by the increasing influence of the smallest channel acting as bottleneck that greatly increases flow resistance, thus pressure drop. A two-variable second order polynomial in the form of:

$$\Delta P(x,y) = p_{00} + p_{10}\,x + p_{01}\,y + p_{20}\,x^2 + p_{11}\,xy \qquad \textbf{Equation 6.4}$$

where x is the mass flow rate and y is S_v, was applied and plotted in **Figure 6.5**, and a second order polynomial was applied using the uncertainty as weights for each data point ($w_i = 1/\Delta(\Delta P)_i^2$). The fitting coefficient with their standard error and a 95 % confidence band interval along with the R^2 statistic are also reported in **Figure 6.5**. This second order

polynomial fits the data relatively well for S_v < 4 mm^{-1} and diverges at higher S_v with the exception of the primitive matrix. This unit cell design exhibits the highest pressure drop amongst matrix phase lattices despite having the lowest specific surface area per unit volume S_v : in average 58 % and 29 % lower than diamond and gyroid matrix respectively, regardless of the cell size. This highlights the importance of unit cell design over the surface area and results directly in a higher pressure drop for the primitive compared to the diamond and gyroid matrix. It also demonstrates that unit cell design has a significant effect on the pressure drop and it is not S_v alone that dictates the pressure drop of lattice structures.

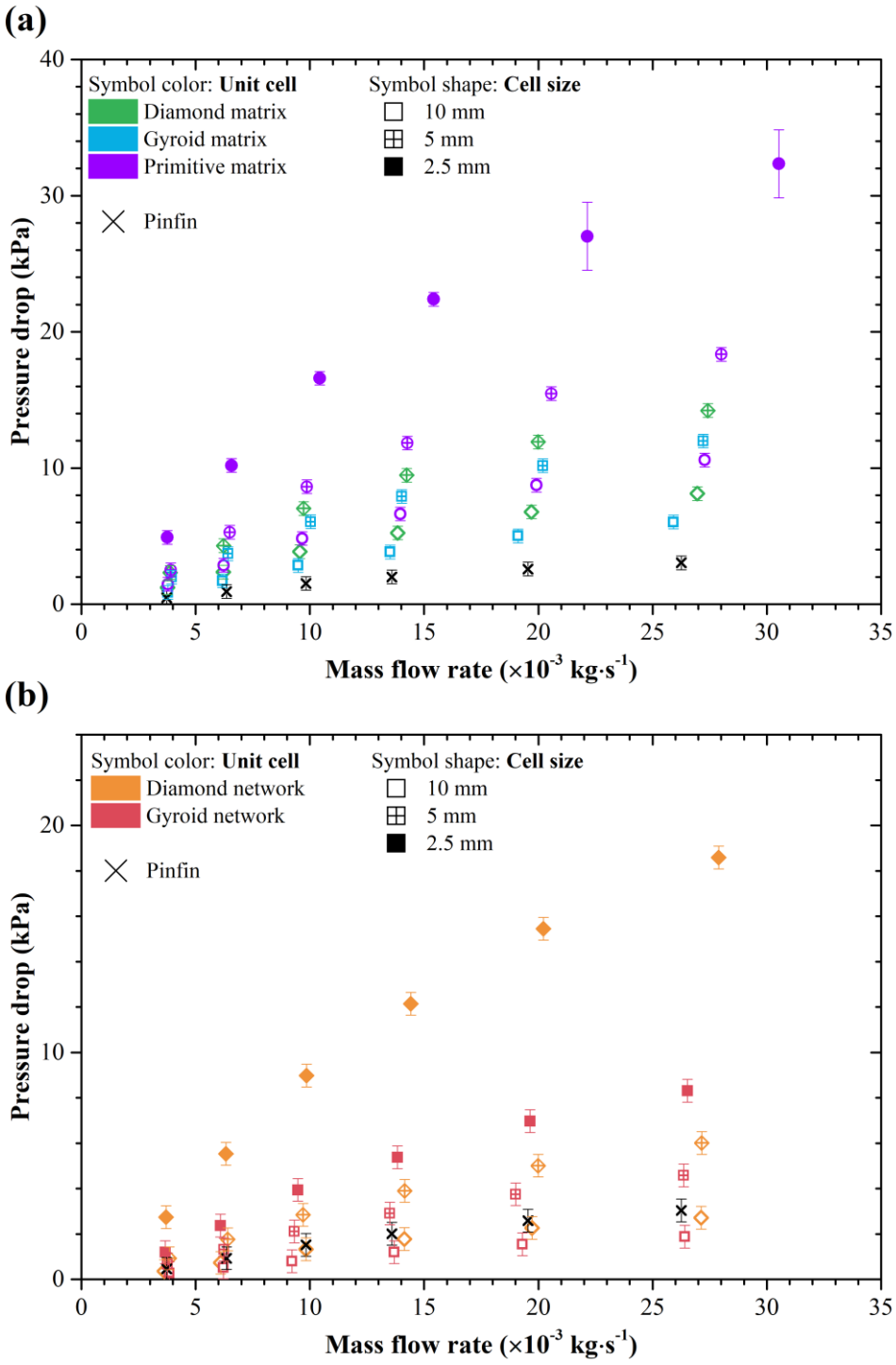


Figure 6.4: Pressure drop against mass flow rate (a) matrix and (b) network TPMS lattice structures along with the pin-fin benchmark coupon. Error bars represent the measurement uncertainty. Note the larger error bars for matrix 2.5 mm cell size for mass flow rate > 0.03 kg·s^{-1} are due to the use of a higher pressure sensor than for the rest of the measurements.

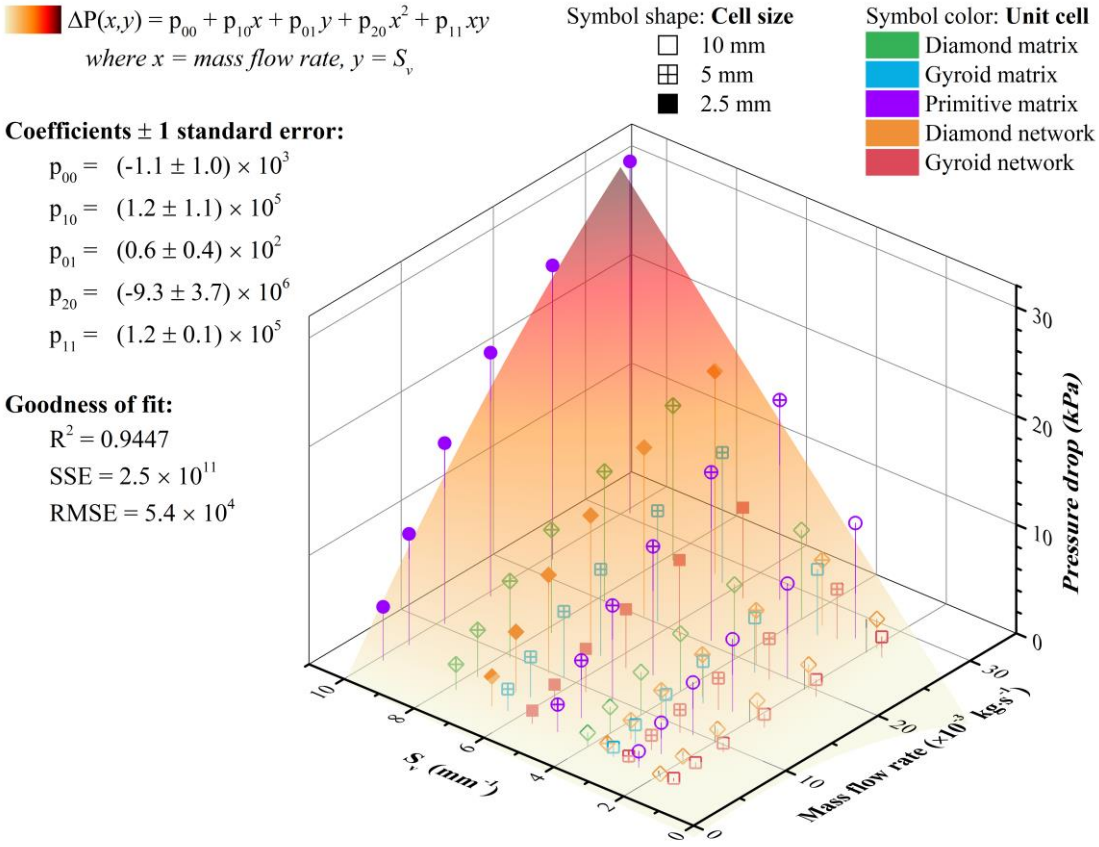


Figure 6.5: Pressure drop of TPMS lattice structures against mass flow rate and S_v.

To gain insights on how the structure topology affects the pressure drop, thus find a good geometrical descriptor for lattice pressure drop, the evolution of the cross-sectional area of the 10 mm cell size lattice specimens was plotted and reported in **Figure 6.6**. A correlation between the pressure drop of the unit cell design and A_{range} (the difference between the minimal and maximal cross-sectional area, respectively A_{min} and A_{max}) seems to be observed: unit cell design with lower A_{range} have lower pressure drop. A_{range}/C_s helps to consider narrow channels that act as bottlenecks, thus increase the pressure losses. To test this hypothesis, the pressure drop is compared against the A_{range} divided by the cell size (C_s) of the specimen to reflect the topology of each specimen using a two variable second order polynomial in the form of **Equation 6.4** where x is the mass flow rate and y is A_{range}/C_s and using the aforementioned weighting. The results are presented in **Figure 6.7** along with the fitting coefficients with their standard errors,

a 95 % confidence band interval and the R^2 statistic. The model has some discrepancies with the data such as the 2.5 mm cell size diamond network. Also, several lattices (e.g. diamond and primitive matrix) have similar A_{range}/C_s with pressure drop that can differs by 2.5 kPa. This can be explained by the differences well below 1 % in A_{min} and A_{max} (minimal and maximal cross-sectional area) between diamond and primitive. However, the internal geometry of the lattice specimens is very different between the diamond and gyroid, and the primitive matrix as shown in **Figure 6.6(a)**. The primitive matrix may visually appear to provide an easy path for fluid through the holes in the geometry (see **Figure 6.6**). However, this entrance region is highly restrictive as the fluid is mainly forced through these holes and is then rapidly expanded inside the primitive cell to be forced again through holes upon exit. It is believed that as the flow expands, separation of the internal flow boundary layer occurs, creating recirculating flow and resulting in an increased pressure drop. On the other hand, gyroid and diamond matrix unit cell design have a more meandering path that benefits from less rapid expanding channels (see **Figure 6.6**). A major limitation of using a single number is that it does not capture the details of the lattice complex geometry. Although A_{range}/C_s correlates better the pressure drop than the S_v, it is not a complete metric since it cannot predict the pressure drop in the complete space of all possible lattice structure topology. Nevertheless, it could be used by designers as a quick estimator of the pressure drop for the lattices and mass flow rate tested here without the need to do experimental testing or CFD, both of which are time and resource hungry.

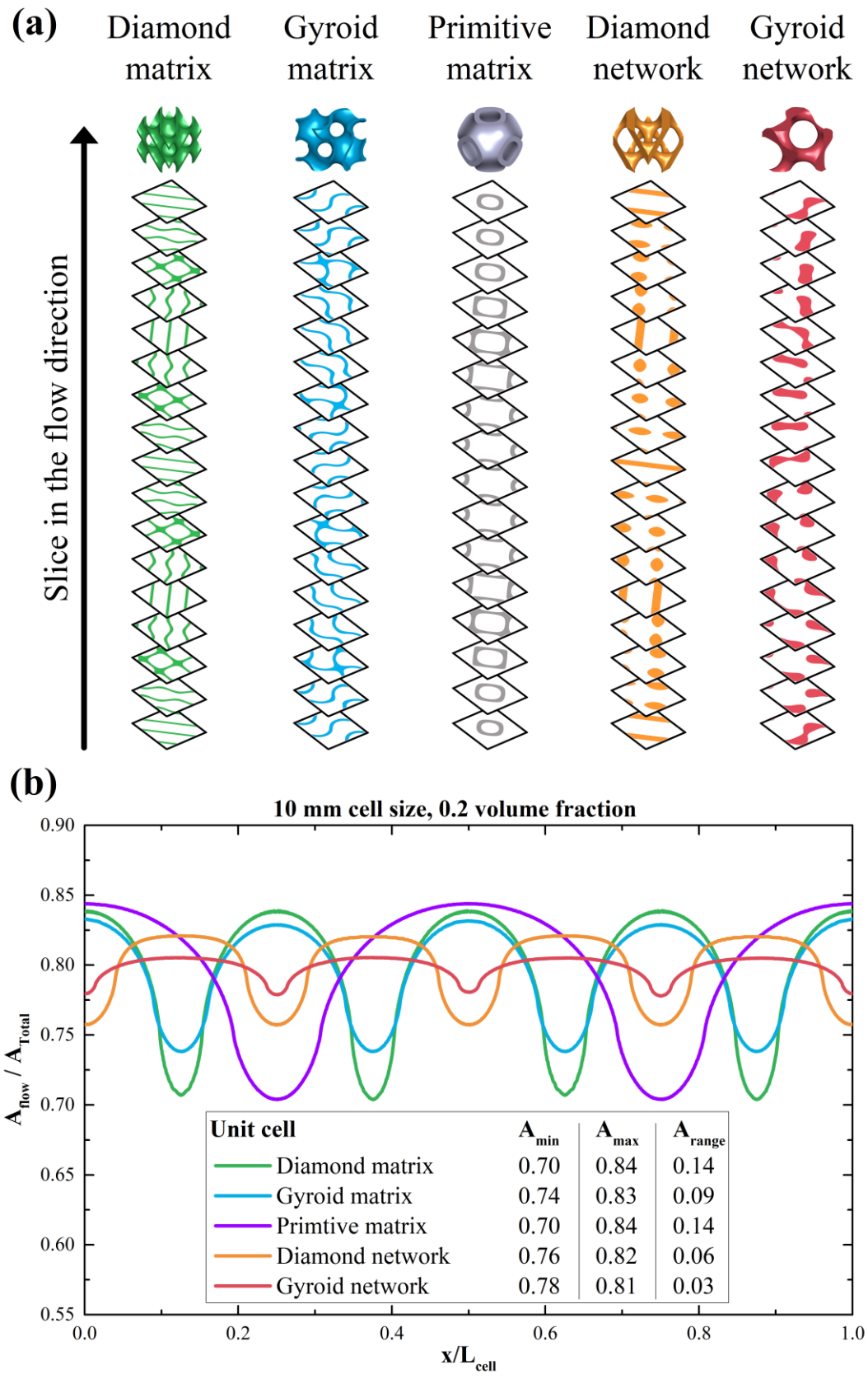


Figure 6.6: (a) Cross-sectional slices of the tested lattices for one unit cell, (b) change in flow area through the flow direction for one unit cell.

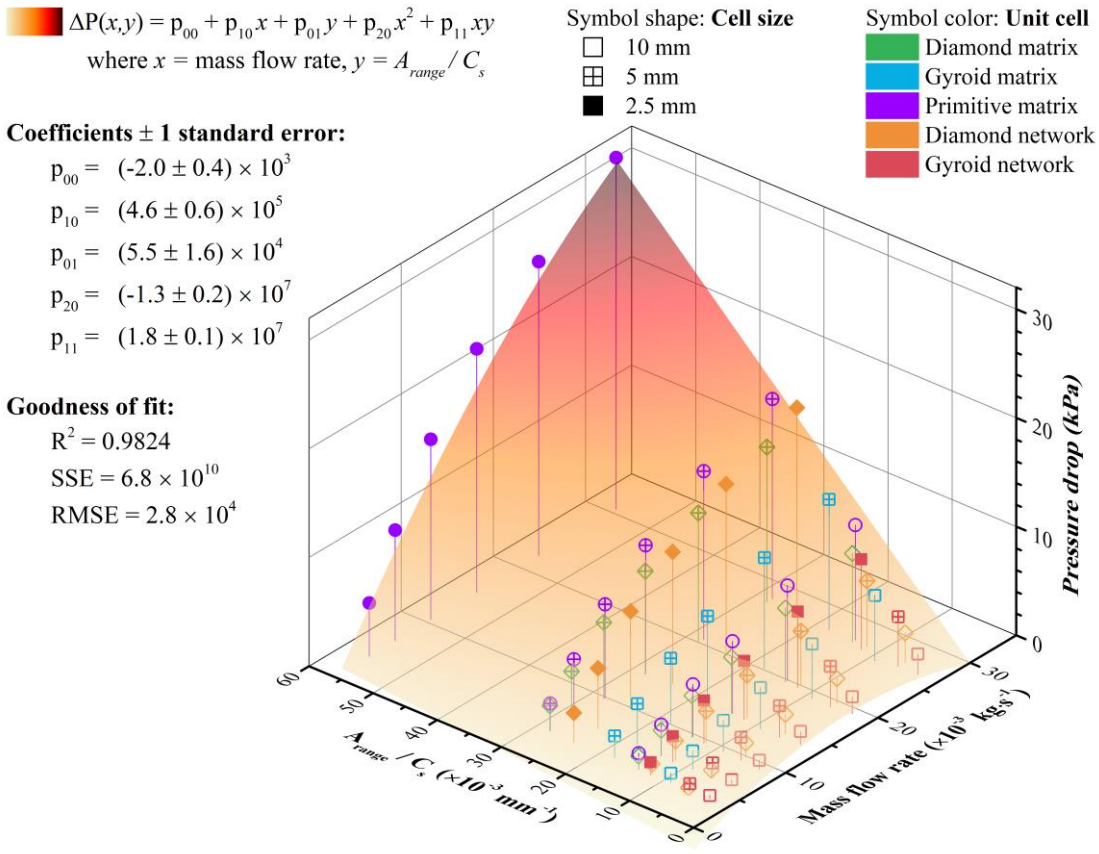


Figure 6.7: Pressure drop of TPMS lattice structures against the mass flow rate and A_{range}/C_s.

6.3.3 Heat transfer results

Heat exchangers are generally selected based on the amount of heat they can dissipate from a surface; a modified heat transfer coefficient is used to represent the heat transfer performance where the heated area, A_{base}, replaces the commonly used heat transfer surface area A. This prevents the skewing of the heat transfer performance in favour of specimens with a smaller surface area. **Figure 6.8** shows the modified heat transfer coefficient for the matrix and network phase lattices along with the pin-fin geometry. It illustrates the wide range of performance possible using lattices, where a minimum of 5 times increase in heat transfer compared to the benchmarked pin-fin geometry was seen. This indicates that the lattice geometries dictate a flow path that develops significant

mixing. Therefore, they are highly effective at inducing heat transfer from the structure to the coolant flow. For both matrix and network specimens, the heat transfer coefficient increased with smaller cell size. The highest heat transfer coefficient was achieved with the 2.5 mm cell size specimens. For the matrix phase, the highest heat transfer is achieved by the gyroid closely followed by the diamond and primitive. The primitive matrix with 10 mm cell size had the lower heat transfer coefficient among all matrix phase lattices. Comparable to the pressure drop, the gap in performance of the primitive with the diamond and gyroid is closing with the smaller cell size. For the network phase lattices, the 2.5 mm and 5 mm cell size of network phase lattices heat transfer coefficients converged as the mass flow rate increases. Comparing the network to the matrix phase, the latter has higher heat transfer coefficients at equal cell size. The 2.5 mm cell size network lattices have similar performance to the 10 mm and 5 mm cell size matrix phase lattices. The gyroid and diamond network are composed of channels aligned with the flow for the length of the specimen (see **Figure 6.3**), which allow air to travel through without much interaction with the structure, thus not improving the heat transfer coefficient. Furthermore, the upstream unit cell prevents fluid flow from impinging on the downstream cell, thus reducing heat transfer, whereas the wavy walls of the matrix phase force the fluid to interact with the structure, thus increasing heat transfer.

The modified heat transfer coefficient was plotted against the specific surface area per unit volume and the mass flow rate in **Figure 6.9**. It can be seen that the heat transfer coefficient increases with smaller cell size, but is clearly different for each unit cell design. Furthermore, heat transfer gains are not proportional to the specific surface area per unit volume as further demonstrated by the two variable second order polynomial in the form of:

$$h_{mod}(x, y) = p_{00} + p_{10}\,x + p_{01}\,y + p_{20}\,x^2 + p_{11}\,xy \qquad \textbf{Equation 6.5}$$

where x is the mass flow rate and y is S_v. Measurement uncertainty was used as weight for each data point ($w_i = 1/\Delta(h_{mod})_i^2$). For the network phase specimens, an initial increase is observed in heat transfer between (41 ± 6) % and (48 ± 16) % when reducing the cell size from 10 mm to 5 mm. This showed that decreasing cell size results in enhanced interaction between the fluid flow and the surface of the lattice geometry. However, no additional gain in heat transfer was seen by further reducing cell size to 2.5 mm. This suggests that there is a fundamental limit to the improvement of heat transfer performance achievable via the reduction of feature size (or increase in S_v), beyond which the proportion of boundary layer to free flow area becomes too large. For the matrix phase specimens, heat transfer coefficient increased with smaller cell size without reaching the limit observed by the network phase lattices. While cell size reduction results in an increasingly more tortuous flow path, thus increasing the flow length and surface area, the wavy nature of the matrix phase (see **Figure 6.3**) benefits the heat transfer and would explain their differences in heat transfer gains compared to network phase specimens. As for the pressure drop results, the heat transfer coefficient h_{mod} against A_{range}/C_s was plotted, however, no correlation was observed. A_{range}/C_s tends to describe the constriction of the flow area, whereas heat transfer is dependent on how the structure promotes flow mixing and interaction with its surface. Therefore, a simple geometric descriptor will not suffice to predict the heat transfer of a particular lattice structure. Empirical models such as that developed by Short *et al.* [197] for pin-fin cold walls rely on a substantial amount of specimens with a wide range of geometric configurations tested over a large set of flow conditions.

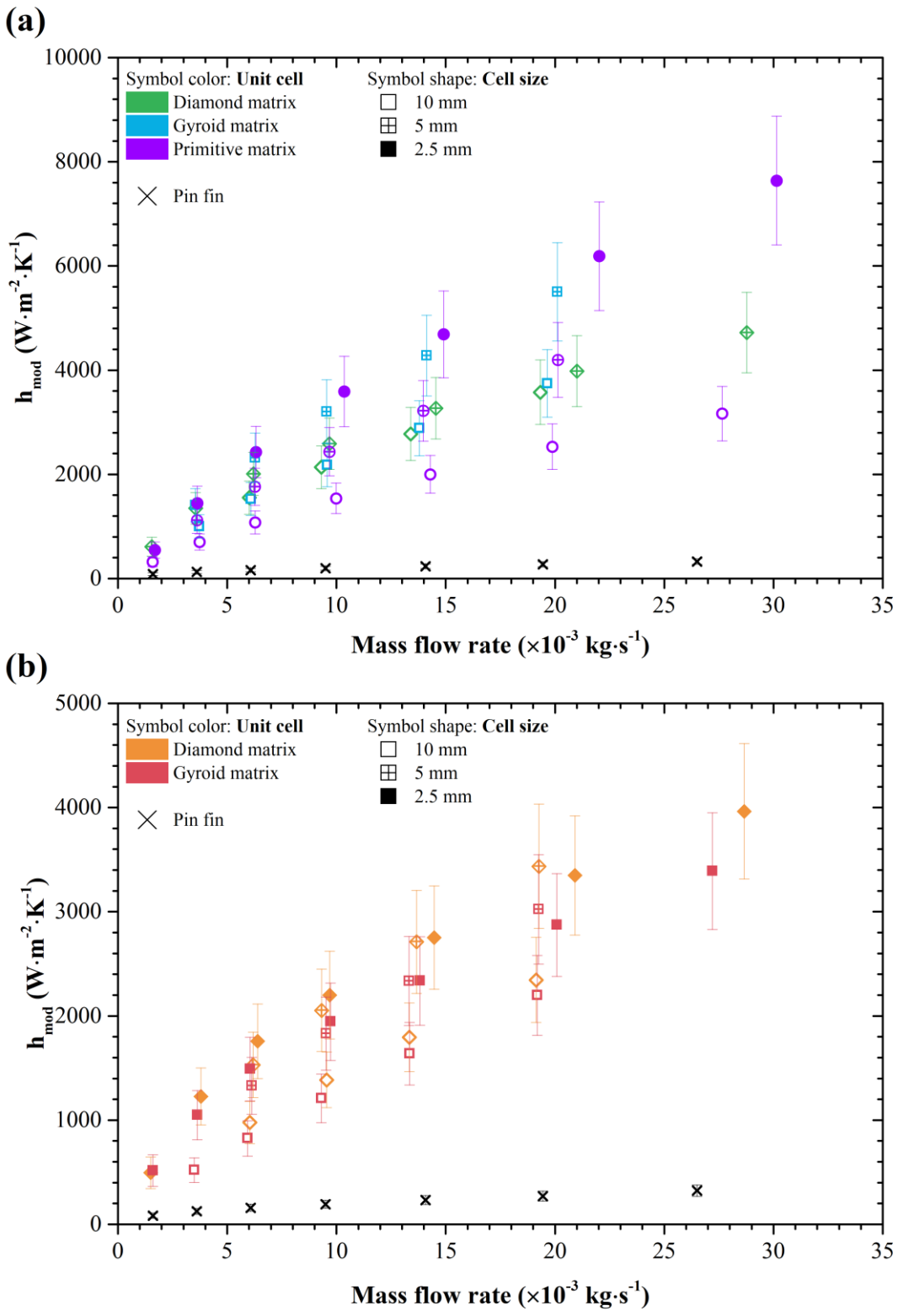


Figure 6.8: Modified heat transfer coefficient against mass flow rate at minimal cross-sectional area for (a) matrix and (b) network TPMS lattices along with the pin-fin benchmark coupon. Error bars represent measurement uncertainty.

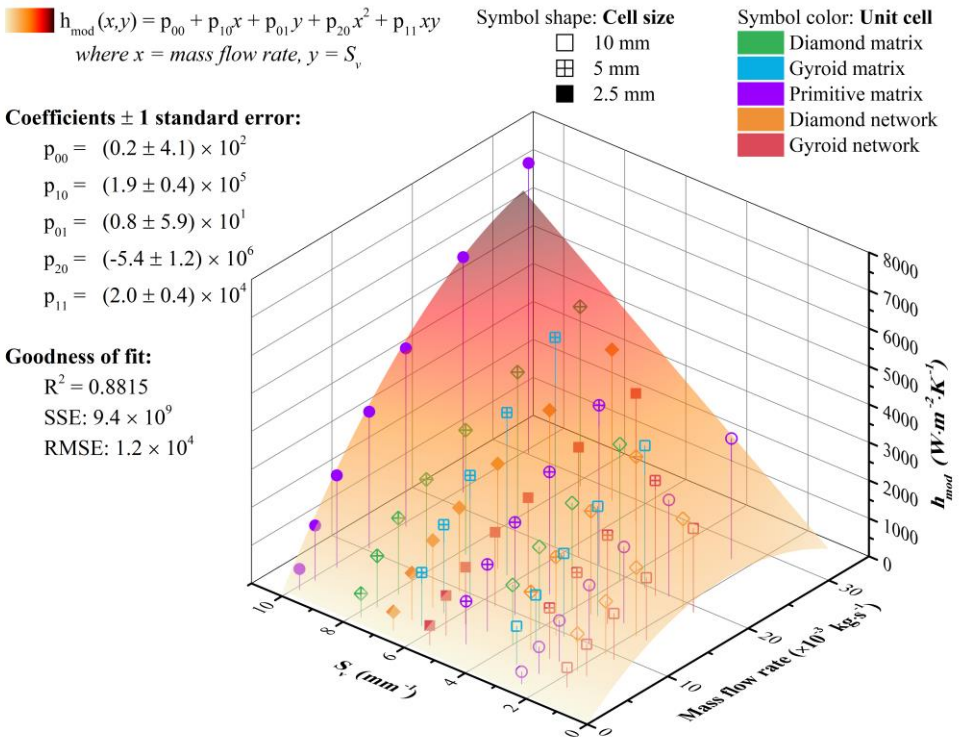


Figure 6.9: Modified heat transfer coefficient of TPMS lattice structures against mass flow rate and S_v.

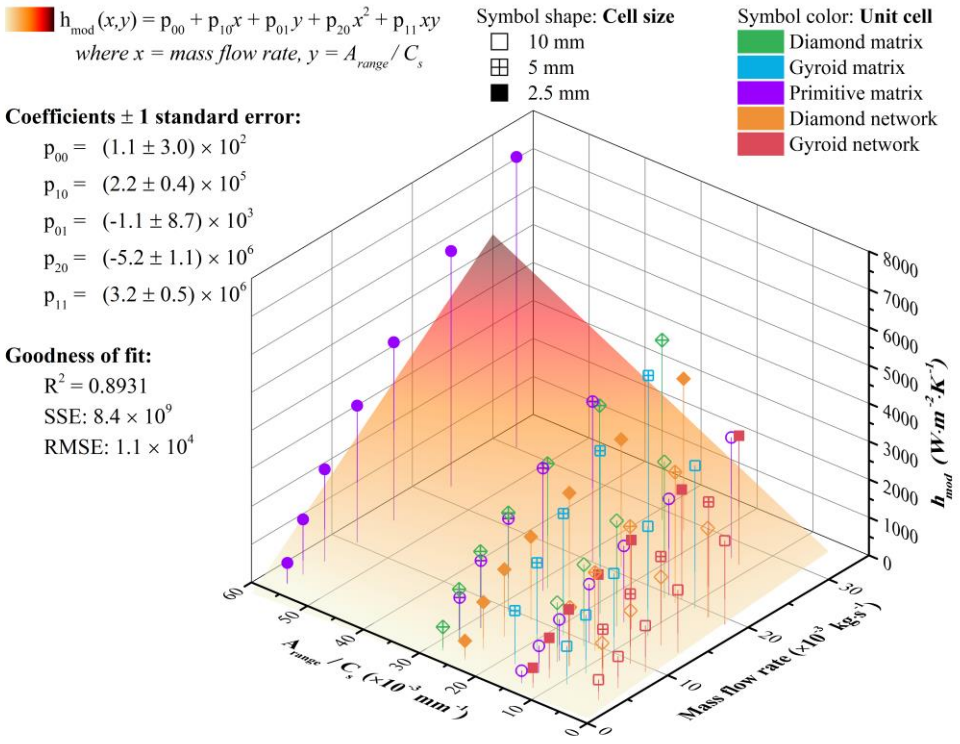


Figure 6.10: Modified heat transfer coefficient of TPMS lattice structures against mass flow rate and A_{range}/C_s.

6.3.4 Thermal performance of lattice structures

The thermal performance rating of a heat exchange geometry can be represented in multiple ways, but often relies on the ratio of energy transfer to momentum transfer. A thermal performance metric that considers the pressure drop and the heat transfer characteristics equally, previously reported in the literature [24], was applied and reported in **Figure 6.11**. It consists of the ratio between the modified heat transfer coefficient (as defined in the previous section) and the pressure drop in the form of $h_{mod}/\Delta P$, which represents the heat exchanger per unit of pumping power. To improve the readability, the graphs have been divided according to their phase (e.g. matrix or network) and their thermal performance behaviour. The highest $h_{mod}/\Delta P$ performance is achieved by the 2.5 mm cell size gyroid network for mass flow rates below 8×10^{-3} kg·s^{-1}. For higher flow rates, the 5 mm cell size gyroid matrix has the best $h_{mod}/\Delta P$ performance.

All matrix phase lattice specimens provide a thermal performance enhancement over the pin-fin benchmark for mass flow rates > 6×10^{-3} kg·s^{-1}. For lower mass flow rates, most lattices have a similar or outperformed the benchmark pin-fin geometry to the exception of 2.5 mm cell size lattices for flow rates < 2×10^{-3} kg·s^{-1}. The latter has the lowest performance across the tested range of flow rates. Similar to the matrix specimens, network phase lattices provide a thermal performance enhancement over the pin-fin benchmark for mass flow rates > 6×10^{-3} kg·s^{-1}. For lower mass flow rates, the diamond 10 mm cell size has a similar performance as the pin fin geometry while the gyroid network 10 mm underperformed the pin-fin.

Two behaviours can be observed in the thermal performance of the lattices (see **Figure 6.11**). The first, affecting all 2.5 mm cell size matrix and network along with diamond 5 mm and primitive 10 mm cell size, and the pin-fin, shows that lattice thermal performance decreases with higher flow rates (**Figure 6.11(a) and (c)**. This reveals that

the increase in pressure losses begins to dominate the gains in heat transfer coefficient as mass flow rates increases. The second behaviour (see **Figure 6.11(b) and (d)**), affecting 10 mm and 5 mm cell size network lattices along with 10 mm cell size diamond and gyroid and 5 mm cell size gyroid and primitive matrix phase, reveals an increase in the heat transfer performance with the flow rates. This reveals that the gains in heat transfer overweigh the increase of pressure drop as the flow rates increases. These two behaviours originate from the cell size with larger cell sizes increasing heat transfer at a greater rate than the pressure drop except for the 10 mm cell size primitive matrix. As mentioned in **section 6.3.2**, primitive cell design is believed to promote flow separation owing to the rapid expansion and contraction of the internal cross-sectional area (see **Figure 6.6**). It is also dependent on the cell type, both gyroid matrix 10 and 5 mm cell sizes have a positive correlation with the mass flow rate while only the diamond matrix 10 mm shows this behaviour. This is due to the significantly lower heat transfer coefficient of the diamond over the gyroid. **Figure 6.11** also shows that the thermal performance of several lattices is equivalent, such as the 5 mm cell size gyroid and diamond networks. It allows the selection of a particular lattice not only based on thermal performance but also according to other properties such as elastic modulus. In this particular example, if the elastic modulus needs to be maximised, the diamond matrix 5 mm would be selected over the primitive 10 mm based on the work reported by Chen *et al.* [198]. This is of particular interest for multifunctional components, where several properties need to be maximised simultaneously.

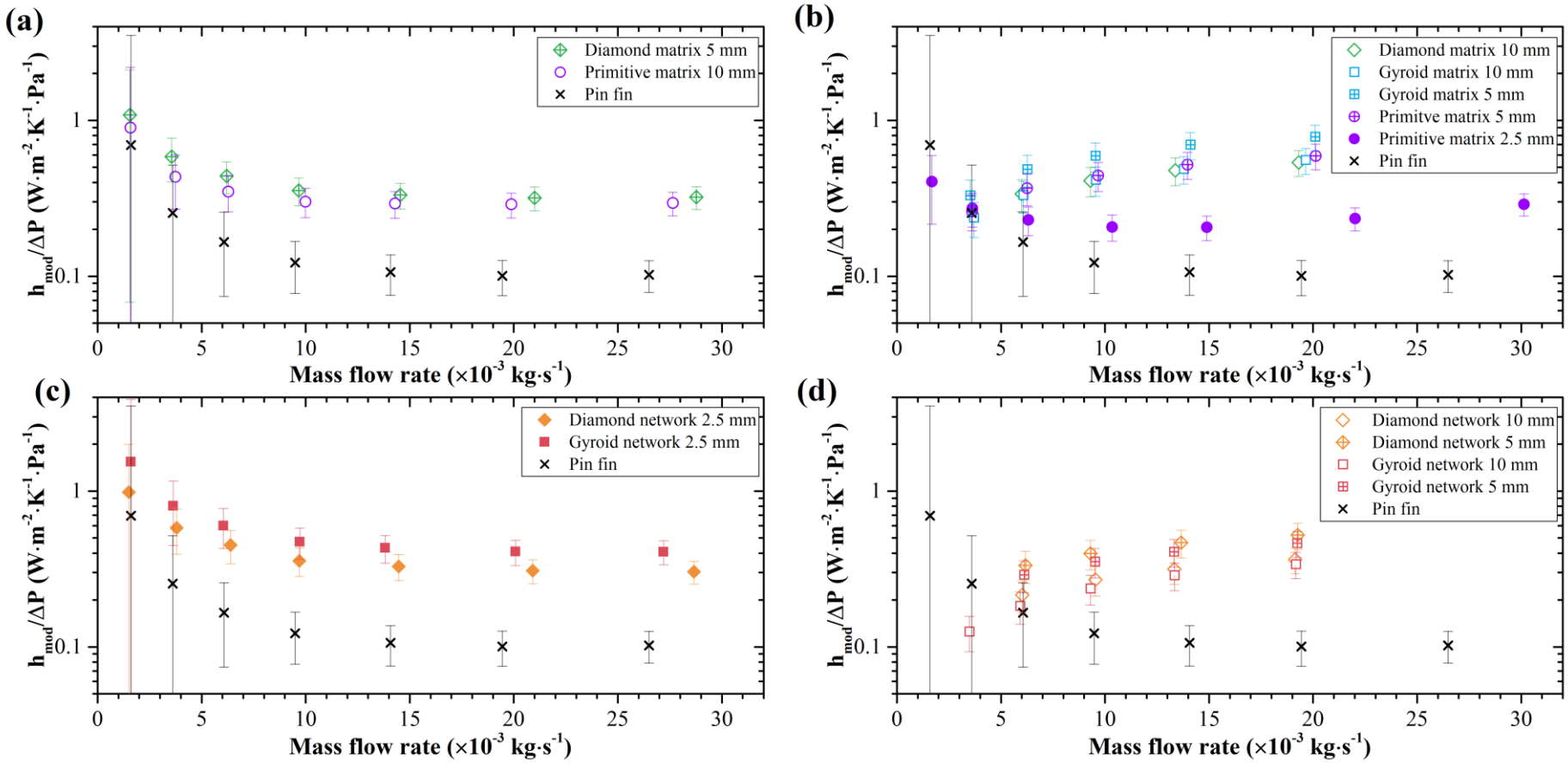


Figure 6.11:Thermal performance of (a)-(b) matrix and (c)-(d) network phase lattice structures along with the pin-fin benchmark coupon. Error bars correspond to the measurement uncertainty.

6.4 Summary

In this chapter, the pressure drop and heat transfer coefficient were experimentally evaluated for fifteen TPMS lattice structure specimens across five unit cell designs: diamond matrix, gyroid matrix, primitive matrix, diamond network, and gyroid network; and three cell sizes: 10 mm, 5 mm, and 2.5 mm. This experiment was designed to identify the heat transfer properties of lattice structures subjected to forced convection (mass flow rates < 3.5×10^{-3} kg·s^{-1}) with dry air as the heat transfer medium. It was shown that the tested lattice structures outperformed the heat transfer properties of a benchmarked pin-fin geometry with a similar volume fraction. However, all lattice specimens had a pressure drop higher than the pin-fin benchmark except for the 10 mm cell size diamond and gyroid network. This means more energy is required to push air flow through the lattice compared to the pin-fin benchmark. It was observed that the pressure drop increases inversely to the cell size. The specific surface area per unit volume of the lattice increases with smaller cell sizes. However, it was demonstrated that the specific surface area per unit volume does not alone dictate the pressure drop of lattice structures. The topology of the unit cell design was seen to play an important role in the pressure drop with the matrix TPMS lattice structures having higher pressure losses compared to network counterparts. This is thought to be due to the differences between the phase flow paths: the wavy-channels of the gyroid and diamond matrix allows a more meandering path increasing the flow length, thus increasing surface interaction, whereas their network counterparts have channels aligned with the flow preventing fluid interaction with the structure. A metric based on variation in cross-sectional area of the studied lattice structures was proposed to quickly estimate the pressure drop for the tested flow rates.

Lattice topology also strongly affected the heat transfer and resulted in varied thermal performance. For the matrix phase specimens, a reduction in cell size results in higher

heat transfer coefficients. On the other hand, for network specimens, cell size reduction improves the heat transfer until it reaches a plateau, beyond which the proportion of boundary layer to free flow area becomes too large preventing further improvement in heat transfer performance. Matrix phase heat transfer coefficients exceed those of the network phase. This can be attributed to the topology of the network phase with channels aligned with the flow preventing fluid flow from impinging on the downstream structure, thus reducing their heat transfer coefficient. On the other hand, the matrix phase allows further enhancement of the heat transfer coefficient with its wavy channel forcing the flow to interact with the structure.

The heat transfer performance characterised by $h_{mod}/\Delta P$ was calculated for each lattice specimen and pin-fin benchmark. It was shown that lattice structures provided significantly improved performance over the pin-fin benchmarked, especially for higher mass flow rates. For flow rates above 8×10^{-3} kg·s^{-1}, the highest thermal performance was achieved with the 5 mm cell size gyroid matrix. For lower flow rates, the 2.5 mm cell gyroid network for mass has the best thermal performance. This is of importance, showing that the best lattice thermal properties are dependent on the fluid flow considered for the application.

Based on the results of this chapter, it can be concluded that lattice structures are excellent candidates for thermal applications and can outperform pin-fin geometry with a similar amount of material, thus with no weight penalty. The findings in this chapter are particularly useful for the design of heat exchangers using TPMS lattice structures to achieve specific pressure drop and heat transfer properties. Furthermore, lattice structures can also provide additional mechanical performance over convectional heat exchange geometries [20,21], further enhancing component value for thermomechanical loading. This is of particular interest in the aerospace industry where the mass of components and therefore specific properties are important. Consequently, a lattice structure that provided

equivalent thermal performance to pin-fin but uses less material is of particular interest. On the other hand, component efficiency may be increased by improving cooling performance and adding strength or stiffness without increasing weight. However, these aspects must be balanced and optimised for the effective implementation of lattice structures for thermomechanical applications.

7 High-strength aluminium alloy for LPBF

7.1 Introduction

AlSi10Mg is the go-to aluminium alloy for LPBF, it has good thermal properties as seen in chapters 5 and 6. However, AlSi10Mg suffers from low mechanical properties limiting its applications. Therefore, aluminium alloys with good mechanical and thermal properties are needed and will be the subject of this chapter. These alloys are key materials for many industries, especially in the aerospace sector. Their development is of major importance to broaden the adoption of LPBF for thermomechanical applications. Not only would it allow LPBF materials to benefit from greater mechanical properties that can compete against conventional materials, but it is necessary for the adoption of designs that supersede conventional solutions. The literature review (see **section 2.2.4**) showed that high-strength aluminium alloys are difficult to manufacture with LPBF process as they suffer from solidification cracking [35]. This cracking issue arises during the solidification melt pool owing to the large solidification range of high-strength aluminium alloys (see example in **Figure 2.8**), the high solidification shrinkage and the poor fluidity of the molten phase [67]. Furthermore, the high-thermal gradients arising from the rastering of the LPBF laser source results in high residual stresses, which when combined with columnar grains, can exacerbate cracking leading to cracks spanning several millimetres as reported by Kaufmann *et al.* [69]. For these reasons, high-strength aluminium alloys have not been as widely researched for LPBF as AlSi10Mg. The first part of this thesis chapter explores the processability and characterisation of the conventional EN AW 2618 high-strength aluminium alloy by altering the scan strategy to reduce the thermal gradient, thus the solidification rate, therefore avoiding solidification cracking. The second part of this chapter explores the processability and

characterisation of A20X, a high-strength aluminium alloy specifically developed for LPBF.

The optimal combination of parameters in terms of laser power, point distance, exposure time and scan strategy, whilst keeping the layer thickness constant, is determined to achieve fully dense and crack-free material. Heat treatments are carried out to maximise mechanical properties by measuring material hardness and phase transformations. Then, the thermal conductivity and tensile mechanical properties under monotonic uniaxial tension are measured in as-built condition in both build and transverse directions and for the determined optimum post heat treatment. The microstructure is also investigated in terms of phases, anisotropy, and changes after heat treatment. The results are then discussed and summarised at the end of this chapter. This enables the emergence of new high-performance lightweight components by developing a high-strength aluminium alloy that supersedes AlSi10Mg, the most processed LPBF aluminium alloy. Owing to the higher mechanical properties of the base material, mechanical properties achievable with lattice structures should also be improved.

Part of the work achieved in this chapter was for Innovate UK Functional Lattices for Automotive Components (FLAC) running from June 2016 to May 2019. This project aimed to use LPBF and lattice structures to create lightweight automotive components with high mechanical properties, thus improving performance and fuel efficiency, thus reducing CO_2 emissions. To achieve this aim, the FLAC project tackled several areas such as the development of high-strength aluminium alloys for LPBF, which Richard Sélo joined in October 2017. Before he joined the project, preliminary work to assess the suitability of EN AW 2618 for LPBF was performed by Dr. Nesma Aboulkhair and Dr. Ian Maskery. They realised the manufacture and analysis of thin walls and the design,

manufacture, and porosity measurement of the inverse pyramid for process parameter optimisation. They also designed and manufactured a following build with different scan strategies. Richard Sélo lead the porosity analysis and realised the entirety of the work after this.

7.2 EN AW 2618 LPBF parameter optimisation

EN AW 2618 or AlCu2Mg1.5Ni is a heat-treatable high-strength aluminium alloy and well suited to parts requiring high strength-to-weight ratios. Heat-treated EN AW 2618-T61 has an ultimate tensile strength (UTS) of 440 MPa with an elongation at break of 10 % [42] compared to a UTS of 292 MPa and 3.9 % elongation at break for T6-like AlSi10Mg [66]. Furthermore, EN AW 2618 retains its mechanical properties at temperatures up to 150 °C and has a thermal conductivity of 146 $W \cdot m^{-1} \cdot K^{-1}$, making it an excellent candidate for thermomechanical applications such as aircraft engine parts [42]. Thus, it is also ideal for multifunctional heat exchangers that combine loading bearing and heat transfer.

7.2.1 Thin walls

The preliminary work included the manufacture of thin walls to investigate processability and eliminate regions of processing space based on a pass/fail test (i.e. did the thin wall build satisfactorily?). The process parameters of AlSi10Mg supplied by Renishaw for its AM400 LPBF machine were used as a starting point. Thin wall specimens were consisting of 30 mm long and 10 mm stacked single laser tracks and are illustrated in **Figure 7.1**. They were divided into three batches: (1) the point distance and exposure time was kept constant while the laser power was varied; (2) the laser power was kept constant and the speed was varied by varying the point distance; (3) the laser power and point distance was varied simultaneously to achieve a constant linear energy density.

Parameter values tested are listed in **Table 7.1**. All thin wall specimens were manufactured without any part failure (i.e. no broken wall). The wall thicknesses were measured using Vernier callipers and reported in **Figure 7.2**. A variation of 0.08 mm in wall thickness can be observed using the default AlSi10Mg parameters for the AM400 LPBF machine. Also, the thickest wall sections in batch 3 (constant linear energy density) does not correspond to the slowest speed or the highest power which is traditionally observed. This could be due to the accuracy of the measurement method. The successful manufacture of all the thin walls suggested that the selected process parameters could be used to manufacture parts made from the juxtaposition of several lines, i.e., 3D structures.

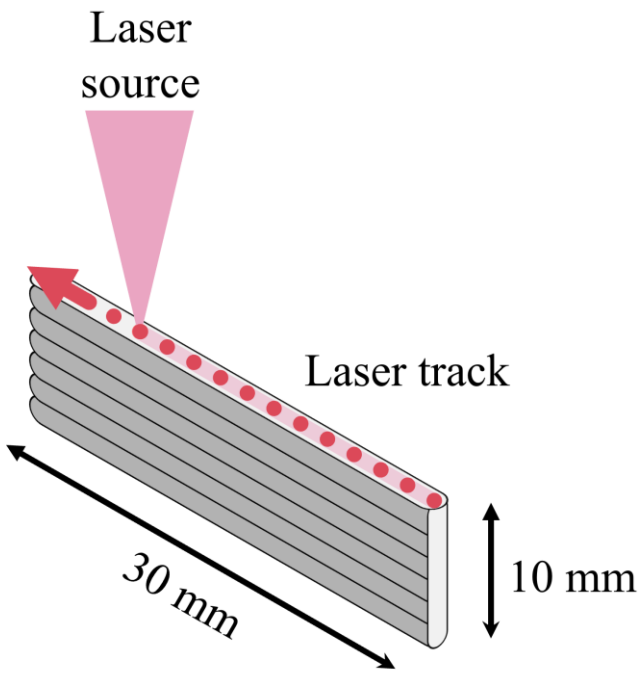


Figure 7.1: Thin wall specimen schematic

Table 7.1: EN AW 2618 LPBF variables for initial parameter optimisation.

Parameter	Batch 1	Batch 2	Batch 3
Laser power (W)	200 – 400	275	200 – 400
Point distance (µm)	80	50 – 110	58.2 – 116.4
Exposure time (µs)	40	40	40

Speed ($m \cdot s^{-1}$)	2	1.25 – 2.75	1.5 – 2.9
Linear energy density ($J \cdot m^{-1}$)	100 – 200	100 – 220	137.5
Hatch distance (mm)		0.08	
Layer thickness (µm)		25	

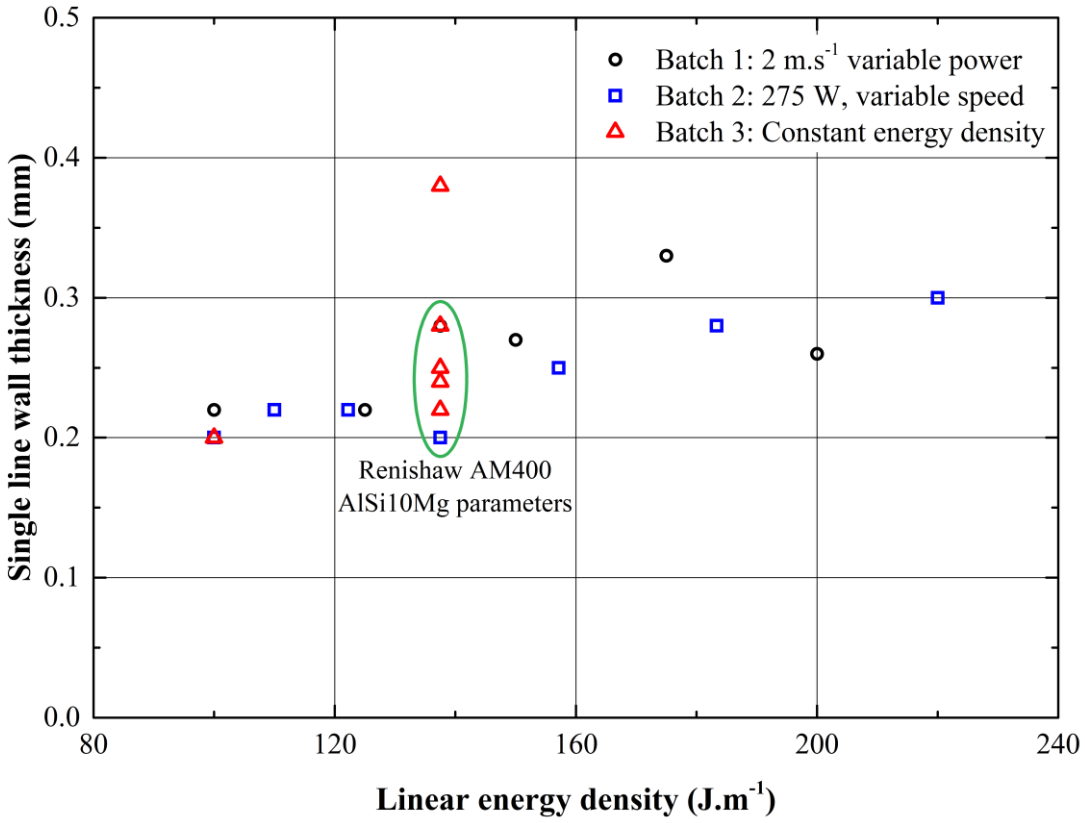


Figure 7.2: Wall thicknesses for the tested process parameters.

7.2.2 3D structures

A build consisting of a 15 mm inverted pyramid with a square top section and a 10 mm edge length using the same process parameters as the thin walls (see **Table 7.1**) was manufactured and analysed by Dr. Ian Maskery. An inverted pyramid shape was used to ease the separation of the test specimen from the build plate since parameters optimisation requires printing large number of test specimens. All specimens were manufactured without failure, the relative density was measured as described in **section 3.5.2** and reported in **Figure 7.3**. All specimens had little visible external differentiation. Cross-

sectional observations by optical microscopy revealed that all specimens exhibited a high level of cracks and pores which diminished with increasing laser power and speed. Due to the solidification cracking sensitivity of EN AW 2618, cracks were expected and have been previously reported in the literature using a meander scan strategy [49]. Micrographs show cracks could propagate through pores and do not follow melt pool boundaries but are parallel to the build direction. However, crack initiation was not clearly distinguishable. **Figure 7.3** suggests a low porosity processing regime with power above 300 W and speed below 2.5 $m \cdot s^{-1}$. High laser power and slower laser scan speed increase linear energy density which creates a deeper and more stable melt pool [199]. However, effort must be focused on the elimination of cracks.

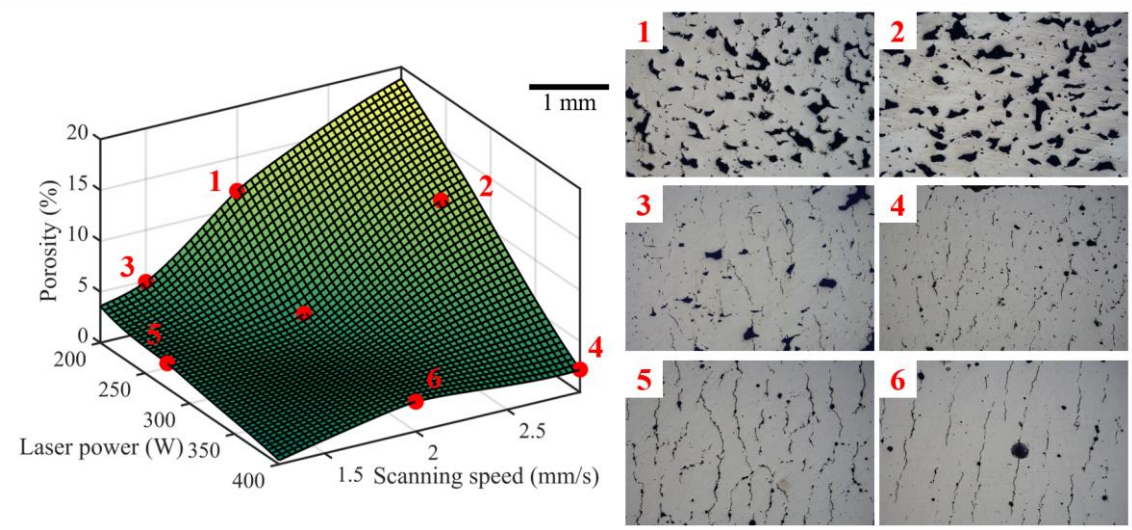


Figure 7.3: Porosity of EN AW 2618 initial build based on AlSi10Mg parameters.

7.2.3 Scan strategy investigation

As seen in the literature review (**section 2.2.4**), cracking can be reduced and possibly eliminated by altering the scan strategy. For this purpose, several scan strategies, shown in **Figure 7.4**, were tested as follow:

- Fractal consisting of a second-order Hilbert curve.
- Checkerboard with island sizes of 5 mm.
- Multiple scan n°1 consisting of a first pass at 1x speed 0.5x power and a second pass at 1x speed and 1x power.
- Multiple scans n°2 consisting of a first pass at 2x speed at 1x power and a second pass at 1x speed and 1x power.
- Meander scans strategy acting as the reference point.

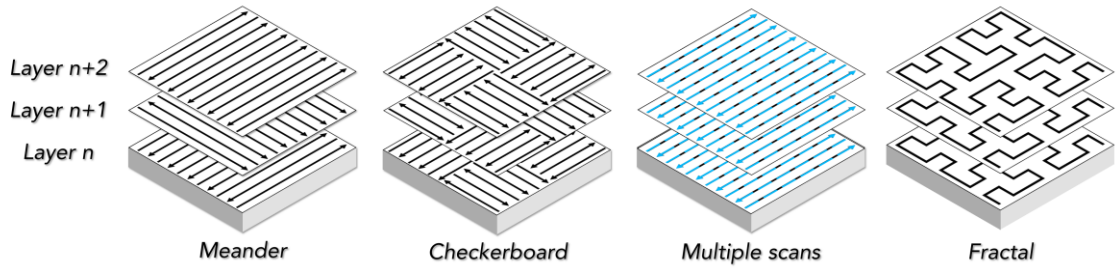


Figure 7.4: Illustration of the tested scan strategies.

The meander strategy is the most used strategy used for hatching. The laser path vectors are scanned with a constant hatching distance in the opposite direction of the neighbouring scan vector. Large areas scanned with a meander strategy could induce high residual stresses due to the high temperature gradient in the opposite ends of the scanning vectors. Dividing the scanned area into numerous sub-areas where each sub-area is scanned with the meander strategy combined with a semi-random scanning order is considered beneficial to reduce stresses and overheating of small areas. This approach is known as checkerboard strategy or island scanning. In **Figure 7.4**, the hatching angle

between each island is 90° for ease of representation but was set to 67° in the process parameters. Scanning each layer multiple times can be used to eliminate residual stress and porosity. This approach is known as remelting or pre-sintering depending on the energy used in the first exposure. The first exposure uses a lower laser power or higher scan speed to preheat the layer while maintaining a uniform powder height. It has been shown that it could be beneficial for the melting during the second exposure with the full power due to lower temperature gradients, and energy absorption could be higher while maintaining the same scanning speed [49].

A first build was manufactured comprising of 15 mm inverted pyramids with a square top section and a 10 mm edge length with the parameters deduced from the preliminary work and listed in **Table 7.2** and the five aforementioned scan strategies. This build was designed and manufactured by Dr. Ian Maskery and cross-sectioning, polishing and porosity measurements were performed by Richard Sélo. After analysing the manufactured pyramids, it was found that all produced specimens with linear energy density below 200 $J \cdot m^{-1}$ exhibited large cracks spanning up to several millimetres, regardless of the laser power or scan strategy employed, as shown in **Figure 7.5(a)**. Etching revealed cracks originated from the bottom of the melt pool and were not following melt pool boundaries but were aligned in the build direction. Large cracks occurred with low linear energy density regardless of the scan strategy, suggesting that fast cooling promotes crack development. Micro-cracks spanning few grains (<200 μm) appeared at both 300 W and 350 W laser powers with scan speed lower than 1.5 $m \cdot s^{-1}$ regardless of the scan strategy, except for the fractal scan and are illustrated in **Figure 7.5(b)**. Porosity level ranged widely as reported in **Table 7.3**; the highest porosity level was observed for the fractal scan with 13.7 % with a standard deviation of 1.5 % while the lowest porosity was measured for the checkerboard scan with 0.1 % with a

standard deviation of 0.1 %. It was found that the lower scan speed achieved the lowest porosity levels except for the fractal scan.

Table 7.2: 1st parameter set tested to produce crack-free EN AW 2618 by LPBF.

Parameter	Values
Laser power (W)	300; 350
Point distance (µm)	60; 10
Exposure time (µs)	40
Speed ($m \cdot s^{-1}$)	1.5 - 2.5
Linear energy density ($J \cdot m^{-1}$)	120 - 233
Scan strategy	2nd order Hilbert fractal, Multiple scans n°1, Multiple scan n°2, Checkerboard, Meander
Rotation angle between layer (°)	67
Layer thickness (µm)	25

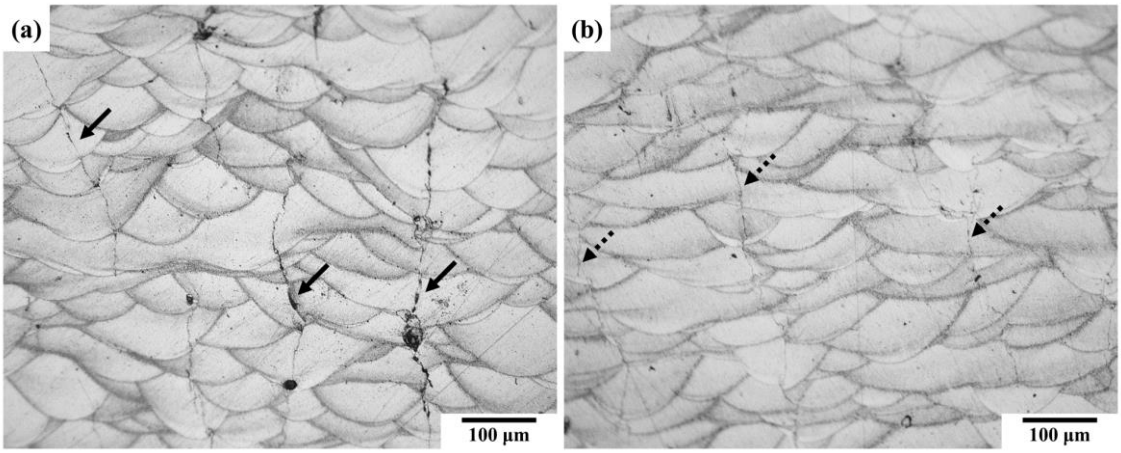


Figure 7.5: Example of (a) macro-cracks indicated with solid black arrows for specimen with 2.5 $m \cdot s^{-1}$ laser scan speed, (b) micro-cracks indicated with dashed black arrows for 1.5 $m \cdot s^{-1}$ laser scan speed.

Table 7.3: Porosity range for the tested scan parameters.

Scan strategy	Porosity range (%)
Checkerboard	0.1 – 2.3
Fractal	0.6 – 13.7
Meander	0.1 – 1.5
Multiple scans n°1	0.3 – 6.4
Multiple scans n°2	0.4 – 6.0

A second build was manufactured comprising of cubes with a 10 mm edge length and 2 mm supports with the process parameters that have produced specimens with only micro-cracks and reported in **Table 7.4**. Cubes were chosen over inverted pyramids to give a more even thermal distribution. Furthermore, downskin (i.e. a surface area facing down without any volume in the previous layer) is a stress raiser and prone to crack initiation due to high surface roughness [200]. The addition of supports has been shown by Ahuja *et al.* [201] and Karg *et al.* [202] to increase the relative density of the produced specimens compared to those that were built directly onto the build plate.

All specimens processed with a laser power of 350 W showed macro-cracks regardless of the scan strategy. Specimens processed with a laser power of 300 W showed micro-cracks varying in sizes. Reducing the checker length size did not change significantly the number of cracks observed in the specimen, but an increase in porosity was observed. A similar trend was observed by Lu *et al.* [203] for Inconel 718. They reported that the increase in porosity with smaller checker size is due to the higher number of overlaps between islands where unmelted powders remain. However, this increase in porosity with smaller checker size could also be due to other factors such as the concentration of energy in the reduced area leading to a change in welding mode to keyholing, vaporisation of elements and the inclusion of vapour pocket. Another explanation could be powder

denudation owing to the recoil pressure of the laser, which may push away the powder and create a powder deficit in the subsequent zones to be scanned. This was shown by Matthews *et al.* [204] for steel and Ti powder. However, only single scan tracks were tested, and further investigation is still required. Reduction in the checker length size adversely affected the porosity, even more for 350 W laser power compared to 300 W. This suggests the concentration of energy in a reduced area as the main cause for the observed increase porosity with smaller island size. For the meander scan strategy, both variations, reduction and increase of laser scan speed by altering the point distance showed an increase in micro-cracking. The same trend was observed for the multiple scan strategy tested.

Table 7.4: 2nd set of parameters tested to produce crack-free EN AW 2618 by LPBF.

Parameter	Checkerboard	Meander	Multi scans n°1
Laser power (W)	300; 350	300; 350	300
Point distance (µm)	60	50, 60, 70	50, 60, 70
Exposure time (µs)	40	40	40
Speed ($m \cdot s^{-1}$)	1.5	1.25, 1.5, 1.75	1.25, 1.5, 1.75
Linear energy density ($J \cdot m^{-1}$)	200; 233	171 – 240	171 – 240
Checker size (mm)	2.5, 3.5, 5	-	-
Rotation between layer (°)	67		
Layer thickness (µm)	25		

This build was repeated, where specimens were left on the build plate and heat treated for 2 hours at 300 °C and furnaced cooled. This annealing heat treatment was performed to prevent the crack formation due to residual stresses within the specimens before separation from the build plate. Specimens were removed from the build and prepared for microscopy following the same method used previously. The heat-treated specimens

revealed higher levels of cracks as shown in **Figure 7.6**. The cracks started from the bottom of the specimens spanning across the specimens.

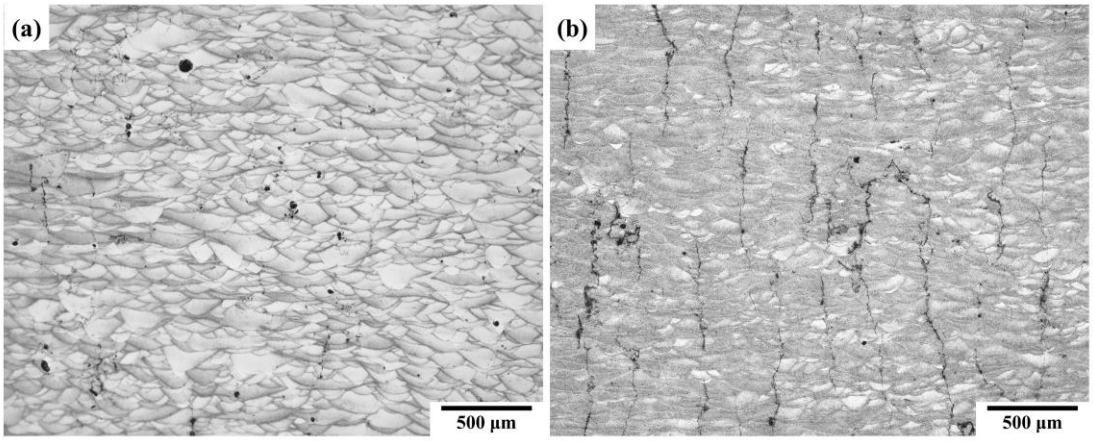


Figure 7.6: EN AW 2618 microstructure in (a) as-built condition, (b) after stress-relief heat treatment.

Despite the wide range of tested scan strategies, micro-cracks were still present within the material. It was found that macro-cracks appeared with high laser power regardless of the scan strategy. A reduction of the laser power from 350 W to 300 W results in a large reduction of cracks. Reductions in porosity from 6 % to <1 %were observed for linear energy density between 171 – 240 $J \cdot m^{-1}$ and near-fully dense specimens with relative densities reaching 99.9 % ± 0.1 % of EN AW 2618 was shown possible. To eliminate potential micro-cracks due to high residual stresses, a stress-relief heat treatment was tested with the metallographic specimens still attached to the build plate to reduce stress level before specimen removal by wire-EDM. However, cracks were exacerbated and spanned over several millimetres. Cracks are deemed unacceptable since they reduce mechanical properties and increase the risk of failure during component operation. Furthermore, EN AW 2618 is used for applications where high strength and low density are required, the presence of cracks is therefore unacceptable. A new approach was chosen by using newly developed high-strength aluminium alloy, A20X, specifically developed for LPBF process conditions.

7.3 A20X LPBF parameter optimisation

The high-strength 2xxx series alloy Al-Cu-Ag-Mg-Ti-TiB_2, A20X, was chosen due to its promising mechanical properties (see **Table 7.5**) and its compatibility with LPBF process according to the manufacturer. A20X is a version of A201 casting alloy with modified composition (through the addition of Ti and TiB_2) to reduce hot cracking developed by Aeromet International Ltd using an in-situ process [93,205]. A20X can be hardened by precipitation strengthening.

Table 7.5: Tensile properties of heated aluminium alloys: LPBF AlSi10Mg, conventional EN AW 2618, and A20X.

	AlSi10Mg T6-like [66]	**EN AW 2618 T61** [42]	**A20X T7**
Young modulus (GPa)	73	74	79
Yield strength (MPa)	239	370	390 – 440
UTS (MPa)	292	440	450 – 511
Elongation (%)	3.9	10	10 – 13

7.3.1 Process parameter optimisation

Similar to EN AW 2618, process parameter development was started by manufacturing thin walls (see **Figure 7.1**) using the reduced build volume (RBV) (see **section 3.3.3**) to investigate processability and eliminate regions of processing space based on the same pass/fail test. The process parameters were divided into the same three batches: (1) the point distance and exposure time was kept constant while the laser power was varied; (2) the laser power was kept constant and the speed was varied by varying the point distance; (3) the laser power and point distance was varied simultaneously to achieve a constant linear energy density. Parameter values tested are based on the EN AW 2618 development

and parameters recommended by Renishaw and listed in **Figure 7.7** using a meander scan strategy. Three build repeats were performed with randomisation of the specimen positions. However, the pass/fail test was not conclusive caused by the RBV recoater blade detaching the thin walls from the build plate. Consequently, it was decided to continue the parameters optimisation by manufacturing 10 mm cubes using a meander scan strategy and parameters reported in **Figure 7.7**. Three build repeats were performed with randomisation of the specimen positions. This was performed to ensure the RBV setup had no adverse effect on the relative density, thus improve the reproducibility of the porosity measurements.

The relative densities of the manufactured specimens are reported in **Figure 7.7**. The relative density ranged between 95 % and 99.8 % with an average of 99.1 %. The lowest laser power (270 W, specimen 'P1'), achieved the highest density with 99.77 ± 0.16 %. Among all manufactured specimens, no signs of cracks or micro-cracks have been observed as seen in **Figure 7.8**.

ID	Laser power (W)	Point Distance (µm)	Exposure point (µs)	Speed (m·s^{-1})
D1	330	60	50	1.20
D2	330	65	50	1.30
D3	330	70	50	1.40
D4	330	75	50	1.50
D5	330	80	50	1.60
E1	330	70	30	2.33
E2	330	70	40	1.75
E3	330	70	50	1.40
E4	330	70	60	1.17
E5	330	70	70	1.00
P1	270	70	50	1.40
P2	300	70	50	1.40
P3	330	70	50	1.40
P4	360	70	50	1.40
P5	390	70	50	1.40

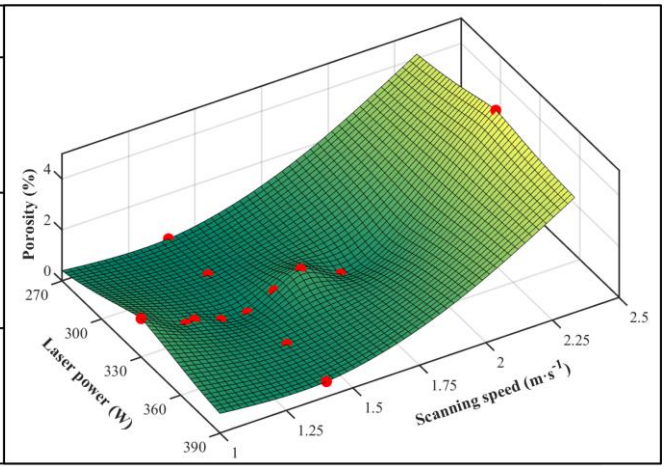


Figure 7.7: A20X LPBF parameters and relative densities achieved for initial parameter optimisation.

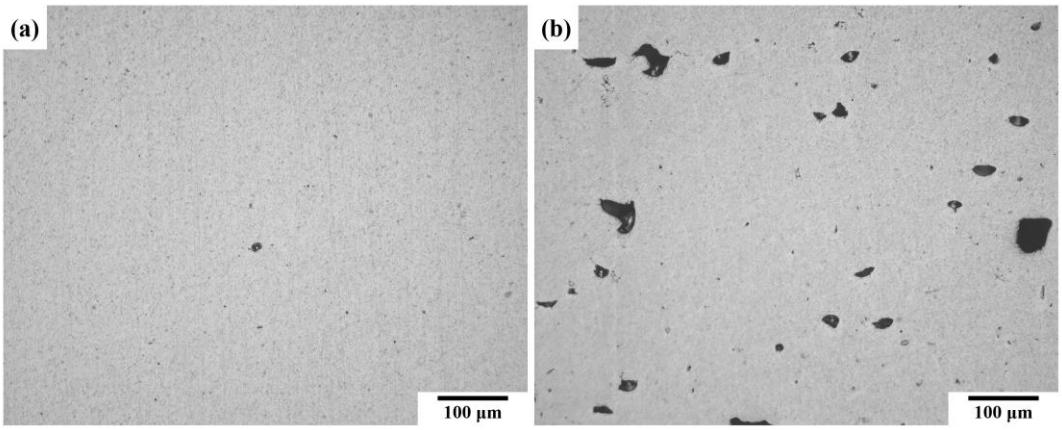


Figure 7.8: Optical micrograph of A20X porosity in initial parameter optimisation (a) P1, (b) E1.

With these promising initial results, absence of cracks and high relative density, the RBV was removed from the Renishaw AM400 and the parameter optimisation was continued using the standard LPBF machine configuration. The best set of parameters ('P1') determined using the RBV returned similar relative density values, with 99.75 ± 0.23 % in the standard machine configuration and 99.77 ± 0.16 with the RBV. In addition to the tested parameters, a similar parameter set recommended by Renishaw (reported in **Table 7.6**) using a meander scan strategy to achieve near fully dense material was tested. This parameter set achieved a relative density of 99.86 ± 0.11 % and was used for manufacturing all subsequent A20X specimens.

Table 7.6: A20X LPBF process parameters for Renishaw AM400 using a meander scan strategy.

Laser Power (W)	Point distance (µm)	Exposure time (µs)	Hatch distance (mm)	Layer rotation (°)	Layer thickness (µm)
250	60	50	0.1	67	25

7.3.2 As-built microstructure and properties

XRD was performed on the powder and as-built LPBF A20X bulk specimens and patterns are reported in **Figure 7.9** where the diffraction peaks of the α-Al matrix are represented with the Miller indices (*hkl*). Firstly, no peak shift nor peak broadening between the powder feedstock and the as-built specimen was observed. Also, the normalised peak intensities of the α-Al matrix are identical for the powder feedstock and the as-built manufactured specimen. The XRD peaks of TiB_2 have been detected in both specimens, indicating that the TiB_2, with its high melting point (3225 °C [206]) and strong chemical stability, have not been affected by the extreme temperatures and cooling rates reached in the melt pool during the LPBF process [56]. $\theta - Al_2Cu$ diffraction peaks were also detected in both specimens, with a higher intensity for the powder feedstock. $\theta - Al_2Cu$ is an intermetallic phase that forms at the last stage of the solidification [207]. Although no other intermetallic peaks were detected, their very low intensities could have made them indistinguishable from the background noise.

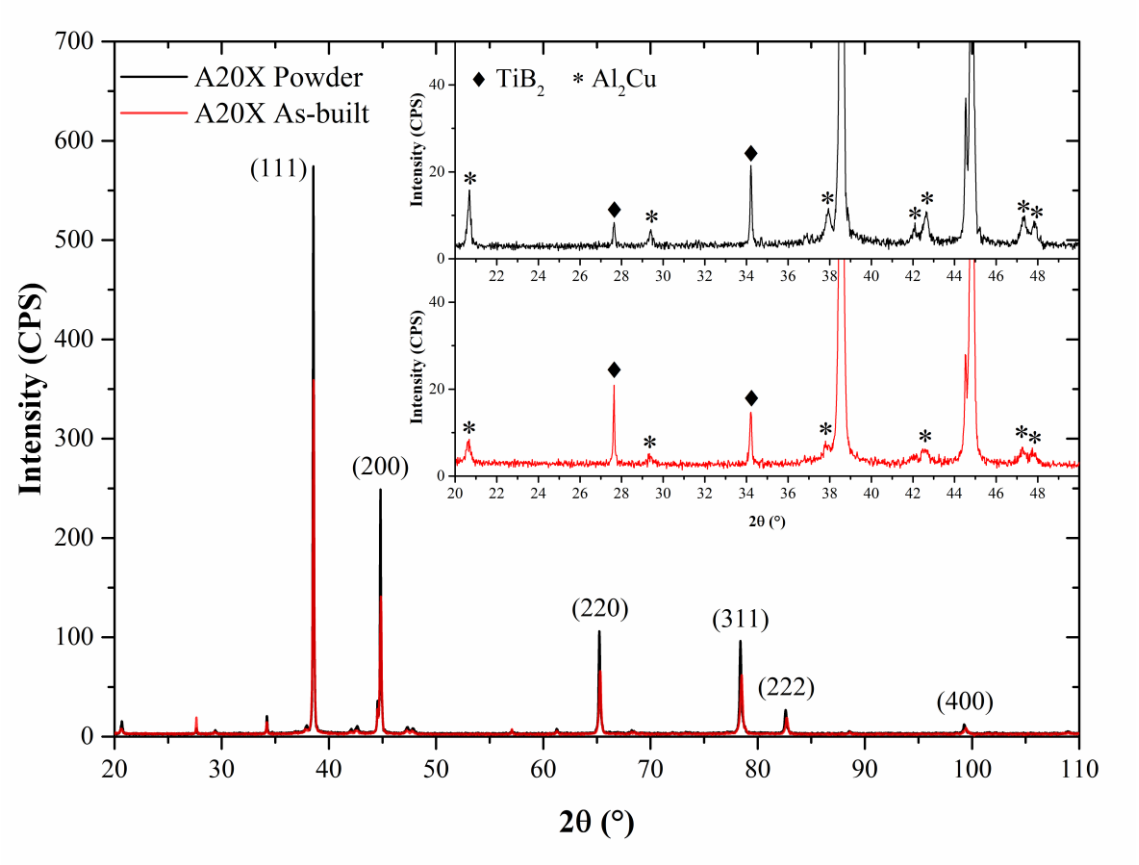


Figure 7.9: XRD patterns of A20X powder feedstock and as-built LPBF specimen. The Miller indices represent α-Al.

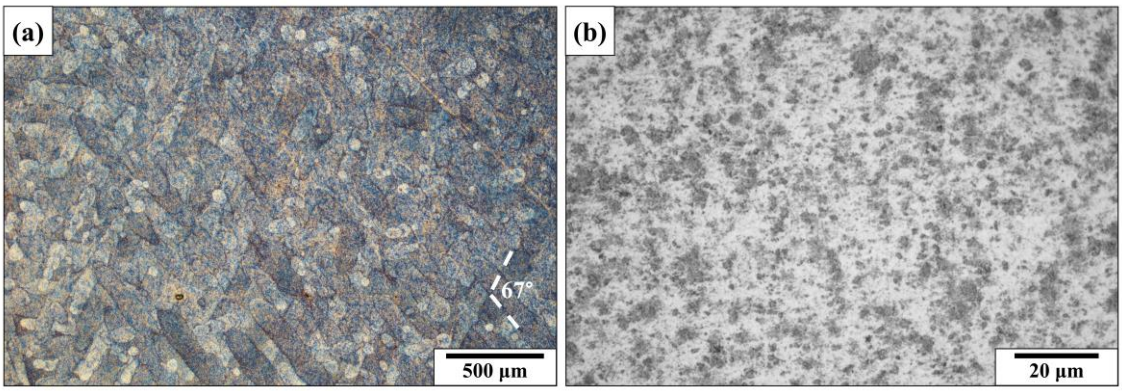


Figure 7.10: Optical micrographs of A20X cross-sections in the *xy*-plane showing (a) the scan tracks, (b) the ultrafine microstructure at high magnification.

Figure 7.10 shows the optical micrograph of an etched cross-sectional area of the as-built A20X manufactured by LPBF in the transverse direction. In **Figure 7.10(a)**, the scan tracks of several layers can be observed and the 67° rotation between them. In **Figure 7.10(b)** a very fine equiaxed morphology can be distinguished in the *xy*-plane which could be due to both LPBF high cooling rates and high amounts of Ti and TiB_2 (grain refiners) in the A20X alloy [205].

A20X ultrafine microstructure can be appreciated in the SEM observations reported in **Figure 7.11** for both build and transverse directions. The as-built specimens do not exhibit the LPBF anisotropic microstructure, with elongated grains in the *yz*-plane very fine and more equiaxed in the *xy*-plane. This isotropic microstructure suggests that the mechanical properties of as-built specimens should be isotropic. The small white needles that can be observed in **Figure 7.11** correspond to TiB_2 particles as confirmed by EDS elemental mapping displayed in **Figure 7.12**. They range in size between 0.7 and 2.5 µm with an average size of 1.5 µm. The dark grey regions are the aluminium matrix with an average grain size of 0.4 µm. The lighter grey areas seen in **Figure 7.11** are the grain boundaries and are Cu-rich as seen by the elemental mapping (see **Figure 7.12**). Studies have been recently published investigating the microstructure of this alloy [208–210]. They reported similar findings with needle-shaped TiB_2 and Cu-rich grain boundaries.

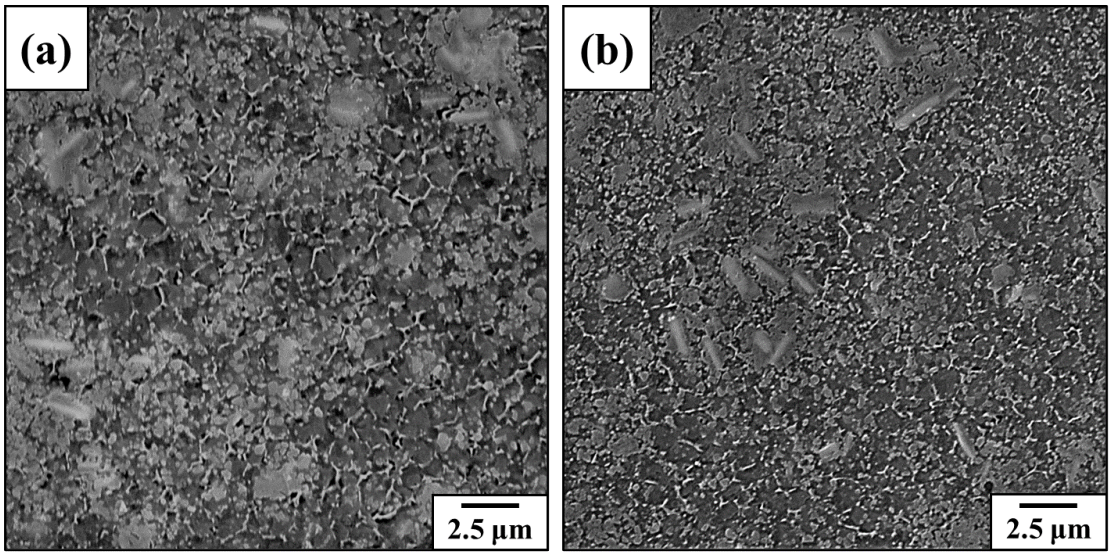


Figure 7.11: SE SEM images of etched A20X in as-built condition for (a) *xy*-plane and (b) *yz*-plane.

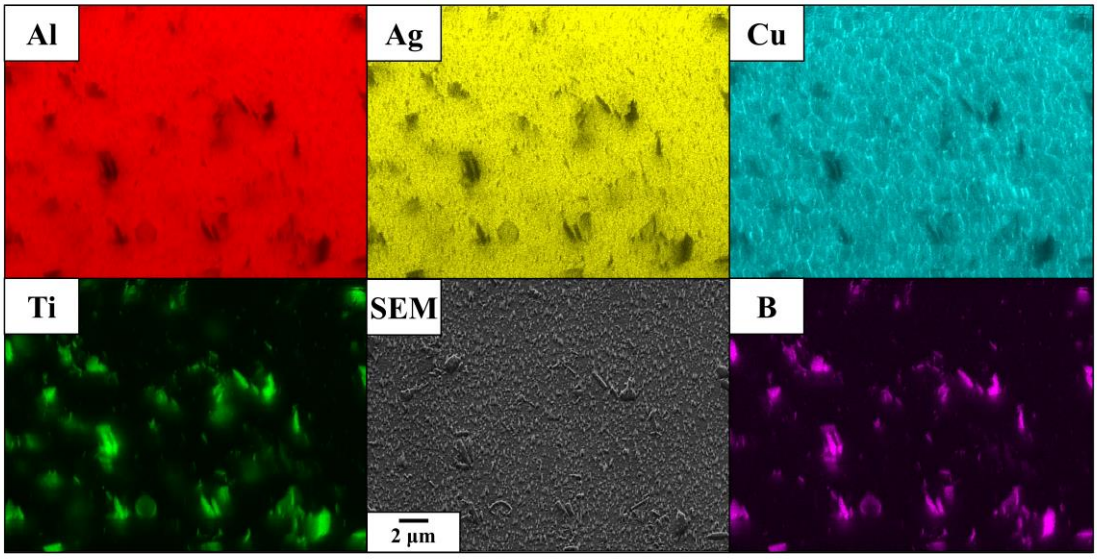


Figure 7.12: SE SEM image with EDS elemental mapping

7.3.3 Heat treatment investigation

A20X is a heat treatable alloy and T7 heat-treated specimen was studied along with the effect of the heat treatment on the tensile properties. The first step of the T7 treatment consists of the full homogenisation of the material by a solution heat treatment (SHT).

This involves maintaining the material at elevated temperature (520 °C), close to the melting point of the alloy, for a certain duration (typically several hours) to obtain a homogenous supersaturated solid solution with the maximum practical amount of hardening solutes (such as Cu, Mg, Si, Ag) after quenching. Too short duration of the SHT leads to incomplete dissolution of all the alloying elements present in the material. On the other hand, too long duration means adding more energy than necessary [211], thus less efficient economically. The supersaturated structure is retained by rapid cooling down to room temperature and was achieved by water quenching the specimens. The effectiveness of the SHT was determined by the dissolution of the Al_2Cu phase in XRD patterns and compared with the as-built condition. The XRD patterns are reported in **Figure 7.13**. No changes were observed in the TiB_2 peaks or with the aluminium peaks regardless of the SHT soaking time. The only change was for the Al_2Cu peaks which decreases as the soaking time increased and disappeared after 2 hours of SHT.

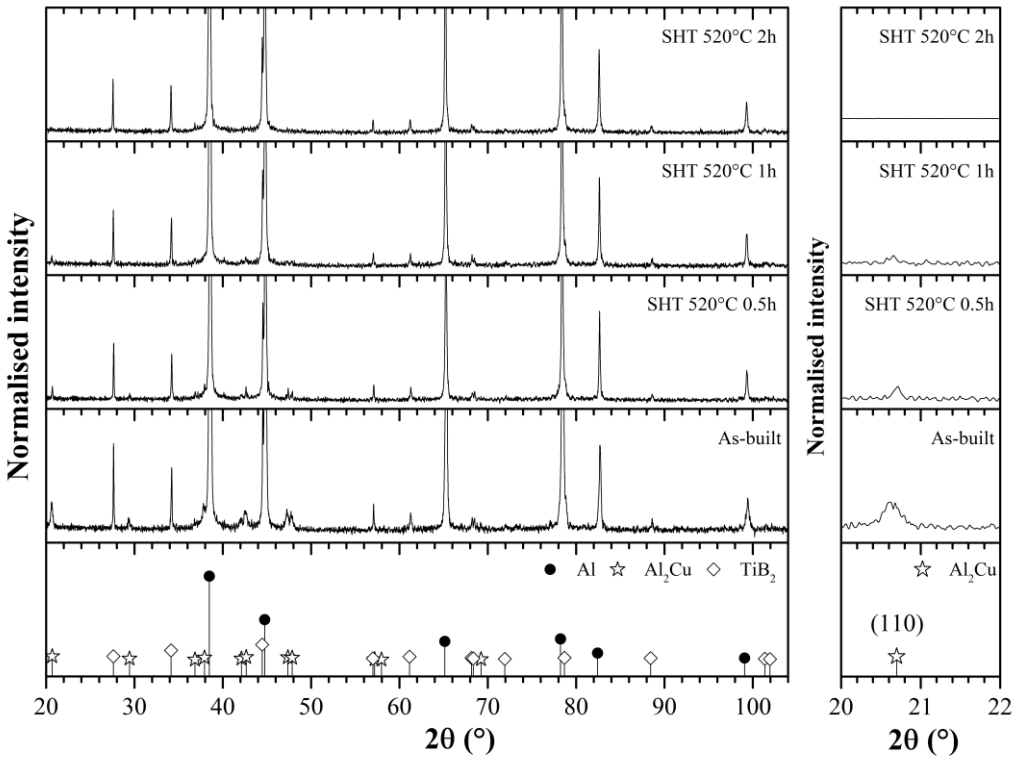


Figure 7.13: XRD patterns of A20X after SHT at 520 °C for various soaking time.

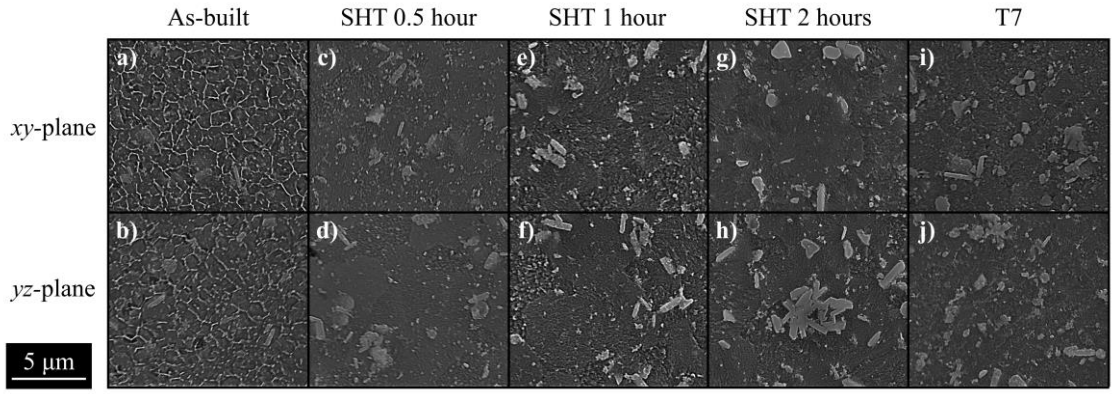


Figure 7.14: SE SEM images of LPBF A20X microstructure in the *xy*-plane: (a) as-built condition, after SHT at 520 °Cfor (c) 0.5 h, (e) 1 h, (g) 2 h, and (i) after T7 treatment; and in the *yz*-plane (b) as-built condition, after SHT for (d) 0.5 h, (f) 1 h, (h) 2 h, and (j) after T7 heat treatment.

The effect of the SHT duration is shown in **Figure 7.14**. After 0.5 hour of SHT, most of the as-built cellular microstructure is erased with the diffusion of alloying elements into the α-Al matrix from the grain boundary. Diffusion in materials occurs to decrease the Gibbs free energy [212]. Heat treatments provide the activation energy required for diffusion with higher diffusion rates for higher temperatures. A material with a fine grain structure has a high amount of grain boundaries which promotes diffusion, thus high diffusion rates. High amount of grain boundaries favour diffusion due to their higher energy states owing to higher density of lattice defects (e.g. atomic vacancies and dislocations) [213]. Increasing SHT duration further promotes diffusion and the dissolution of Al_2Cu as confirmed by the intensity reduction of the Al_2Cu peak in the XRD patterns in **Figure 7.13**. After 2 hours, the Al_2Cu phase and the scan tracks are fully dissolved, yielding a more homogeneous microstructure before artificial ageing. The hardness of the different SHT duration is reported in **Figure 7.15** along with the porosity measurements. A small positive hardness trend can be observed with the SHT duration and will be discussed in section **7.4**.

Specimens were subjected to heat treatment consisting first of a solutionising step (SHT) at 520 °C for 2 hours followed by water quenching to room temperature and finishing by an artificial ageing step (AA) at 160 °C. The duration for the ageing was varied from 4 to 22 hours with a 2-hour interval to determine the optimum time for a T7 temper (i.e. just after the hardness peak). The hardness for each treatment was measured and reported in **Figure 7.15** along with the measured relative density from cross-sectioning. For small ageing durations (< 8 hours) the hardness does not change. After 10 hours of ageing, the hardness increased by 12 % and maintained a value around 148 $HV_{0.5}$ for longer ageing durations. The hardness peak was reached for 10 hours of ageing at 160 °C. T7 is a slightly overaged temper, consequently, the optimum ageing duration at 160 °C was selected to be just after the hardness peak, 12 hours. The T7 heat treatment for A20X proposed in this thesis consists of a 2-hour SHT at 520 °C followed by a water quench, artificial ageing of 12 hours at 160 °C and air-cooled to room temperature. The microstructure resulting from the T7 heat treatment is reported in **Figure 7.14**. No microstructural variation between the 2 hours SHT step and T7 was observed. This specific T7 will be used in the following section for the determination of A20X mechanical properties.

Comparing post-heat treatment hardness of A20X, AlSi10Mg (reported in **section 5.2.4**), and EN AW 2618 [42]: A20X shows the highest value with 148 $HV_{0.5}$ where ENAW 2618 is 120 HV and AlSi10Mg is 102 $HV_{0.5}$. This indicates that A20X have higher mechanical properties which are measured in the next section.

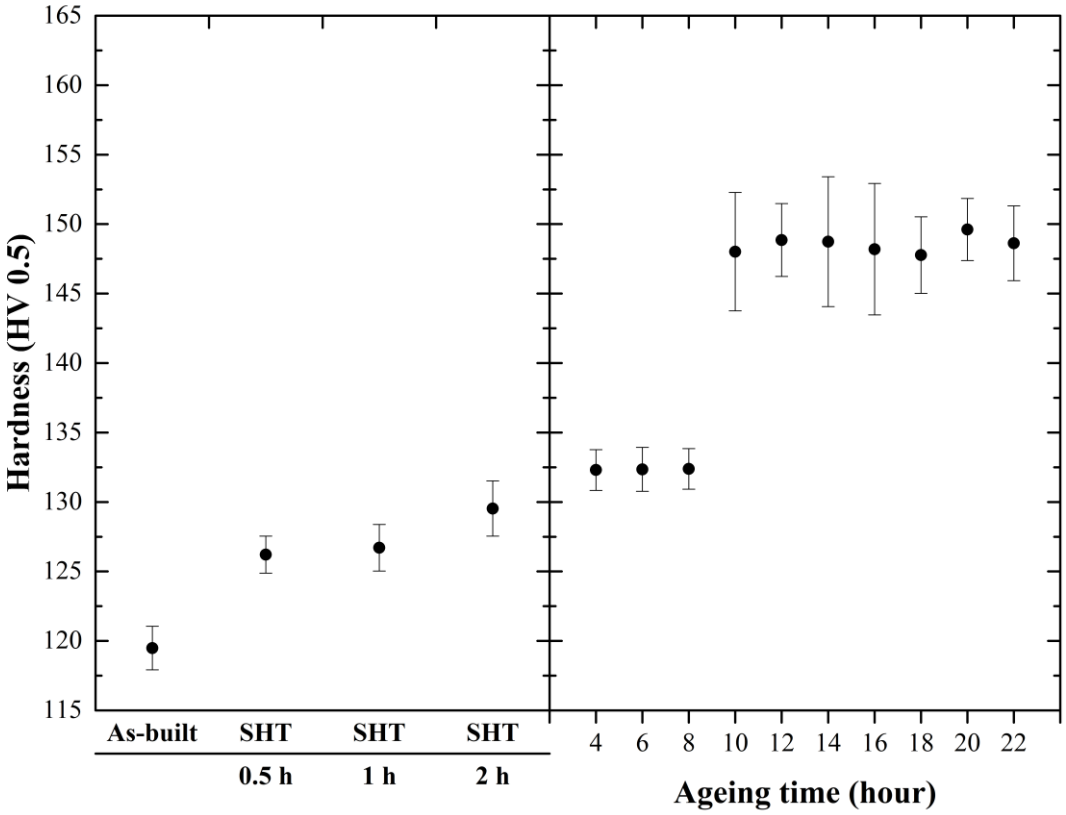


Figure 7.15: Hardness and relative density of LPBFed A20X in as-built, annealed at 300 °C for 2 h, solutionised at 520 °C with varying soaking time and after a 2 h SHT followed by varying ageing duration. The error bars represent the standard deviation.

7.3.4 Tensile properties

The tensile properties for as-built and T7 heat-treated A20X in both build and transverse direction are reported in **Table 7.7** and an example of the typical stress-strain curves is shown in **Figure 7.16**. The tensile properties have good consistency across the tested specimens in each condition. In both as-built and heat-treated conditions, similar tensile properties can be observed in build direction and transverse direction respectively, therefore the material was isotropic.

For the as-built condition, the material had an elastic modulus of 74 ± 4 GPa and achieved an ultimate tensile strength (UTS) of 420 ± 5 MPa with an elongation at break of

14.6 ± 0.8 %. The material exhibited a 0.2 % offset yield strength ($R_{P0.2\%}$) of 357 ± 7 MPa. A yield-drop phenomenon was observed at the beginning of the plastic deformation followed by a yield plateau elongation, or yield-point elongation (YPE). The YPE corresponds to the difference between the elongation of the specimen at the start and at the end of discontinuous yielding (i.e. an increase of strain occurs without an increase in stress). The maximum and minimum tensile yield strength and yield elongation are reported in **Table 7.8**. An inhomogeneous straining with serrations was observed during the plastic deformation. After the inhomogeneous plastic deformation, the specimen had a homogeneous deformation with a gradual work hardening until the UTS is reached. Little stress reduction happened after the UTS and is in accord with little to no necking observed in the gauge section of the test specimens. For the T7 temper, the material had an elastic modulus of 83 ± 4 GPa and achieved an ultimate tensile strength (UTS) of 480 ± 13 MPa with an elongation at break of 11.6 ± 1.0 and 13.7 ± 0.8 in the build and transverse direction, respectively. The material exhibited a 0.2 % offset yield strength ($R_{P0.2\%}$) of 378 ± 14 MPa. The plastic deformation was homogeneous with no yield-drop phenomenon, no yield elongation, nor inhomogeneous straining. Similar to the as-built specimens, little to no necking was observed in the gauge section of the test specimens.

Table 7.7: Averaged tensile properties of LPBF A20X in as-built and after a T7 heat treatment developed in this thesis.

Condition	**As-built**		**T7 temper**	
	Build dir.	**Trans. Dir.**	**Build dir.**	**Trans. dir.**
E (GPa)	75 ± 3	73 ± 3	85 ± 4	81 ± 2
$R_{P0.2\%}$ (MPa)	347 ± 6	366 ± 3	378 ± 10	379 ± 10
UTS (MPa)	418 ± 5	422 ± 2	478 ± 10	481 ± 9
Elongation (%)	14.4 ± 0.7	14.7 ± 0.4	11.6 ± 1.0	13.7 ± 0.8

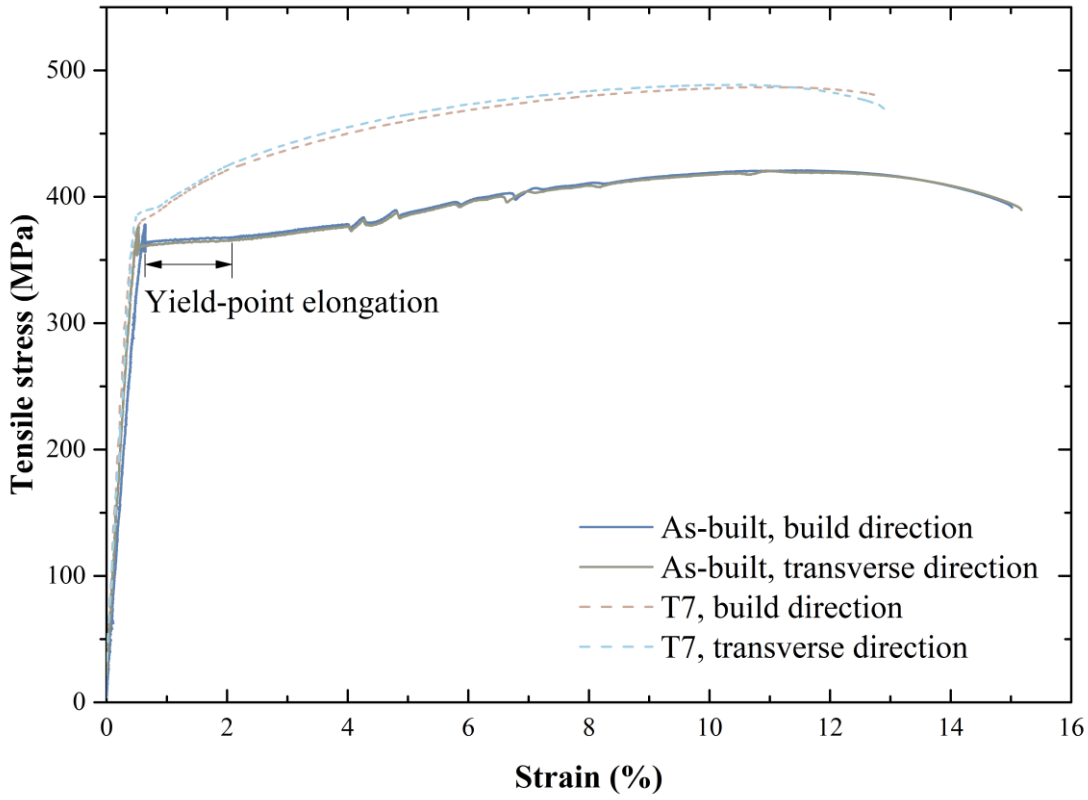


Figure 7.16: Example of A20X tensile behaviour of as-built and T7 states in build and transverse directions.

Table 7.8: Minimum and maximum yield strength and yield elongation of as-built A20X.

Orientation	Build direction	Transverse direction
Minimum yield strength (MPa)	339 ± 5	358 ± 4
Maximum yield strength(MPa)	354 ± 5	381 ± 3
Yield elongation (%)	2.1 ± 0.4	2.5 ± 0.3

7.3.5 Thermal conductivity

The thermal conductivity of as-built and heat-treated A20X was measured across three different specimens using the same procedure as AlSi10Mg described in **section 4.2.3** and was reported in **Table 7.9**. The thermal conductivity of as-built A20X is similar in build (159 ± 13 $W \cdot m^{-1} \cdot K^{-1}$) and transverse ($156 \pm 13$ $W \cdot m^{-1} \cdot K^{-1}$) directions and reflects the isotropic microstructure and mechanical properties reported previously. After T7 heat treatment, the specimens' thermal conductivity decreased in the build (149 ± 12 $W \cdot m^{-1} \cdot K^{-1}$) and transverse direction (150 ± 12 $W \cdot m^{-1} \cdot K^{-1}$), i.e. a decrease between (4 ± 15) % and (6 ± 15) %. However, this decrease is not significant enough to be measured by the thermal conductivity apparatus owing to the large experimental uncertainty. The thermal conductivity of AlSi10Mg measured in **section 5.2.4** was also reported in **Table 7.9** for comparison. As-built A20X exhibits a thermal conductivity up to (40 ± 20) % higher, almost achieving the conductivity of T6-like AlSi10Mg. A20X in T7 condition has a thermal conductivity $(10 \% \pm 20)$ % lower than T6-like AlSi10Mg, which is again not significant owing to the large experimental uncertainty.

Table 7.9: Thermal conductivity of LPBF A20X and AlSi10Mg in as-built and heat-treated state measured in this thesis.

Conductivity ($W \cdot m^{-1} \cdot K^{-1}$)	**Build direction**	**Transverse direction**
A20X as-built	159 ± 13	156 ± 13
A20X T7	149 ± 12	150 ± 12
AlSi10Mg as-built	130 ± 10	115 ± 9
AlSi10Mg T6-like	165 ± 14	166 ± 14

7.4 Discussion

Near fully dense EN AW 2618 specimens (99.9 % ± 0.1 %) were produced using LPBF in this study. However, micro-cracking remained present within the material. This is due to the nature of the LPBF process and the EN AW 2618 alloy. The high cooling rates of LPBF promote hot tearing owing to dendritic solidification. During solidification, the primary equilibrium phase solidifies first at a different composition from the bulk liquid, resulting in solute enrichment in the liquid near the solidifying interface [214]. The locally changing temperature of equilibrium liquidus produces an unstable and undercooled condition [214]. Consequently, there is a breakdown of the solid-liquid interface leading to a dendritic grain growth with long channels of interdendritic liquid trapped between solidified regions, conventionally called a 'mushy zone'. As the solidification continues, the solidifying material is exposed to shear or tensile stresses [215] due to volumetric solidification shrinkage and thermal contraction in these channels which produces cavities and hot tearing cracks that can span the entire length of the columnar grain and propagate through intergranular regions [216]. Ahuja *et al.* [201] investigated the processing of EN AW 2618 by LPBF. They reported the manufacture of crack-free LPBF EN AW 2618 specimens with a relative density of 99.96 %. According to the author, this is mainly due to the reduction of heat transfer between the specimens and the build plate when the supports' cross-sectional area of the supports is small compared to that of the specimens. Reducing the thermal gradient, thus the solidification rate, was studied by altering the scan strategy in conjunction with the use of support structures in this thesis. It was shown that they can reduce drastically the crack size but were unsuccessful in fully eliminating cracks. This was also observed by Koutny *et al.* [49]. Ahuja *et al.* [201] specimen size was limited to cubes with 5 mm edge length. As indicated by Koutny *et al.* [49], for a given set of parameters, the level of porosity in EN AW 2618 increases with the specimen size, therefore, having a significant

impact on cracking. This could explain the crack-free specimens produced by Ahuja *et al.,* while Koutny *et al.* and this thesis produced specimens suffering from cracks. Using high baseplate temperature could be beneficial to reduce the thermal gradient, which could reduce cracking. Uddin *et al.* [217] showed the removal of cracks for another unweldable high-strength aluminium alloy, EN AW 6061, using an induction heating system to maintain the build environment at 500°C during manufacturing. They reported mechanical properties similar to that of the wrought alloy with a reduction in ductility. High chamber temperatures keep the powder bed temperature closer to the alloy melting point, which would prevent the breakdown of the solid-liquid interface in the mushy zone [214]. Furthermore, reducing the thermal gradient reduces volumetric solidification shrinkage and thermal contractions, thus limiting residual stress and preventing the initiation and propagation of cracks [38]. However, it was shown by Koutny *et al* [49] that increasing the baseplate temperature to 400°C did not result in a significant reduction in cracks. Most commercial LPBF systems only allow temperatures up to 200 °C but a new generation of machines are being developed with increased baseplate temperature capability (from 500 °C [78] to 1200 °C[218]). The results presented in this chapter continue to confirm that crack-free EN AW 2618 is difficult if not impossible to manufacture by LPBF, for large components (e.g. >10 mm).

Studies have been conducted to alter the chemical composition of Al-Cu alloys [81,83,219] and most recently ceramic phases such as TiB_2 [209,210]. As previously discussed in the literature review, additions of Sc tends to be uneconomic but confers to the final product higher mechanical strength and crack-free parts. Additions of ceramic phases tend to be more cost-effective, but have specific challenges such as inhomogeneous distribution and poor ceramic to matrix bonding [91,220]. Altering the chemical composition offers the possibility to design bespoke alloys that benefit most of the particularities of the LPBF process. Furthermore, changing the alloy composition

allows controlling the solidification microstructure to that of the preferred fine equiaxed grains [51]. However, in this thesis, the commercially available high-strength A20X aluminium alloy was investigated.

A20X has a wide LPBF process window as seen in the initial process parameter investigation where specimens exhibit high relative density (e.g. >95 %). The absence of cracks can be explained by the high content of grain refiner. From the chemical composition given by Aeromet (see **Table 3.6**), the alloy is 4.95 wt.% TiB_2 with the approximately 0.33 wt.% remaining Ti is present in solution. The ceramic phase TiB_2 and solute Ti alters the solidification mechanism of A201 (on which A20X is based) and significantly improves the castability of the alloy, which was previously where A201 suffers from poor castability owing to its broad freezing range [221] resulting in hot-tearing. The XRD patterns of the A20X powder feedstock and the as-built specimen in **Figure 7.9** revealed that the TiB_2 particles have not been altered by the LPBF process and retained their grain refinement ability as observed on micrographs in **Figure 7.11**. The efficacity of TiB_2 grain refiners to produce uniform microstructures with ultrafine equiaxed grain can also be observed in **Figure 7.11**. Although the precise mechanism of grain refinement in Al alloys remains unclear [222], despite intensive research [223–228], the ultrafine microstructure of A20X could be due to three different grain refinement mechanisms. Firstly, the peritectic Ti of 0.33 wt.% acts via constitutional supercooling (i.e. activating nearby particles for nucleation which is essential in the nucleation of an equiaxed grain) for grain refinement due to the high segregating ability of Ti to restrict the growth of the solid-liquid interface in Al [222,229]. In addition, Wang *et al.* [228] reported that Ti refines the grain size through the introduction of potent nuclei (i.e. strongly favour nucleation in the melt pool) formed through the reaction of Ti with impurities. The constitutional supercooling is also enhanced due to the high cooling and solidification rates resulting in a higher amount of solute accumulating at the

solidification interface [230]. The second mechanism of grain refinement comes from large amounts of TiB_2 (4.95 wt.%), acting as heterogeneous nucleation sites, having a good grain-refining effect. They become much more effective when in combination with solute Ti owing to the potential formation of a monolayer of Al_3Ti two-dimensional compounds (2DC) on TiB_2 particles' surfaces as reported by Fan *et al.* [231]. Finally, the last refinement mechanism is by grain pinning with the impingement of grain boundaries by TiB_2 particles. This is of particular importance for the LPBF process where a laser melts and reheats the subsequent layer leading to grain coarsening as typically observed in the heat-affected zone of welds. These three mechanisms, constitutional supercooling, heterogeneous nucleation, and grain pinning produce the ultrafine equiaxed microstructure of as-built A20X and imprint on the material properties.

The as-built isotropic microstructure directly translates into the isotropic mechanical behaviour as seen in **Figure 7.16**. The highly refined microstructure provides grain boundary strengthening (Hall-Petch relationship) resulting in high strength with an average UTS of 420 MPa and 14.6 % elongation at break. These isotropic mechanical properties could eliminate the need for heat treatments, which are generally required due to LPBF anisotropic microstructures. However, the presence of yield-point elongation (YPE) and serration during the plastic deformation are often considered detrimental [232,233]. YPE has mostly been studied for low carbon steels and only a few investigations have been reported for Al-Mg alloys [232,234]. YPE often occurs after a yield drop, as observed here: the stress first drops sharply to a lower value before remaining through the yield elongation, also referred to as yield plateau. This occurs in alloys with low initial mobile dislocation densities and is generally attributed to three factors: (i) rapid multiplication of dislocations during yielding, (ii) the associated increase in mobile dislocation density leading to lower dislocation velocities, and (iii) slower moving dislocations under lower stresses [235]. Inagaki *et al.* [232] reported the effect of

grain size, Mg content, temperature and strain rates on the YPE of Al-Mg alloys. They reported the YPE increases linearly with the strain rate and Mg content. They also reported that the grain size strongly affects the YPE and disappears above a critical grain size. The serration observed on the stress-strain curve of the as-built specimens corresponds to the Portevin-Le Chatelier (PLC) effect. The constitutional supercooling and high cooling rates during LPBF reject more solute to the solidification interface, finishing at the grain boundaries. The solute atoms located at the grain boundaries impede the dislocation motion. Consequently, the dislocations require more energy (i.e. higher stress) to overcome the solute atoms. Once the dislocations are released from the solute pinning points, a yield drop occurs until the dislocation encounters another pinning point resulting in the observed YPE and serrated stress-strain curve. In addition, TiB_2 also acts as dislocation pinning points. It is acknowledged that the differences between the coefficient of expansion for TiB_2 and Al results in a higher density of dislocations at Al/TiB_2 interface and brings a higher diffusion rate of the solute atoms to the dislocations' core [89,236,237]. Therefore, the solute atoms combined with TiB_2 is the most probable cause of the YPE and serrated plastic deformation.

Although A20X has good mechanical properties in as-built condition, these can be enhanced using heat treatments. The SHT leads to the dissolution of Al_2Cu as depicted by the micrographs in **Figure 7.14** and confirmed by the XRD patterns in **Figure 7.13**. The hardness of A20X increases slightly with SHT duration (see **Figure 7.15**). This opposes the conventionally observed behaviour, where hardness decreases with SHT duration due to grain growth. However, no significant changes in the grain size were observed owing to the large presence of TiB_2 particles impeding grain growth. A possible explanation is the relaxation of residual stresses within the specimen after the first SHT. However, the continuous increase in hardness with SHT duration suggests otherwise. A preferred explanation is the enrichment of α-Al matrix in alloying elements by the

dissolution of phases such as Al_2Cu, as observed in the XRD patterns (see **Figure 7.13**), leading to solid solution strengthening. As-built specimens exhibit large quantities of θ-Al_2Cu phase due to the LPBF process; the specimen is maintained at elevated temperature (>150 °C) during the whole manufacturing process acting as in-situ ageing leading to the large precipitation of Al_2Cu. The SHT treatment of A20X results in a supersaturated solution while retaining the ultrafine microstructure, leading to increased hardness.

The influence of artificial ageing duration on hardness was investigated after 2 h solution SHT at 520 °C. The ageing peak was reached after 10 hours at 160 °C. Liu *et al.* [238] reported that high ratios of Cu:Mg in Al–Cu–Mg alloys result in the precipitation of precursors of θ – Al_2Cu over S – (Al_2CuMg) precursors. The presence of Ag in A20X (0.8wt.%) improves the corrosion resistance of the alloy [42] and thermal stability above 100 °C. Also, the addition of Ag leads to the formation of the Ω phase which improves the response of the alloy to precipitation strengthening [239,240]. Ringer *et al.* [241] studied the role of Ag in Al-Cu-Mg-Al alloys for a similar Cu:Mg ratio (6.33) as A20X (6.12). They followed the evolution of microstructure during the early stage of ageing at 180 °C using high-resolution transmission electron microscopy (TEM) and selected area electron diffraction (SAED). The precipitation sequence from the supersaturated solid solution (SSSS) was reported as follows:

$$SSSS \rightarrow GP + \Omega \rightarrow GP + \theta^{"} + \Omega \rightarrow \theta' + \Omega \rightarrow \theta(Al_2Cu)$$

where GP correspond to Guinier-Preston zones. Intermetallics such as AgAlMg and $Ag_5Mg_3Al_2$ have been observed by Zhou and Froyen [242] in Al-Cu-Ag-Mg alloying system. These phases are concurrently formed with α-Al and θ-Al_2Cu phases through a quaternary eutectic reaction. However, the concentration of such intermetallics remained low enough to not be detected by XRD (see **Figure 7.13**). The chemical composition of

A20X offers a wide variety of precipitates and competing precipitation mechanisms and would benefit from further investigations [205].

Results of tensile tests of A20X after the T7 heat treatment determined in this thesis show no yield drop, nor serrated plastic deformation This tends to confirm the constitutional supercooling and high cooling and solidification rates of LPBF was the cause of the serrated plastic deformation. The heat treatment allowed the dissolution of a high amount of solute accumulating at the grain boundaries back in the α-Al matrix.

A significant increase in yield strength ($R_{P0.2\%}$) and UTS with a slight decrease in ductility was observed which proves the effectiveness of the heat treatment. An increase in Young's modulus was also observed. This indicates that the material stiffened after heat treatment and could be possibly explained by the formation of nano-size precipitates that interacts with the elastic deformation.

7.5 Summary

In this chapter, the development of high-strength aluminium alloy for LPBF was undertaken. The parameter optimisation process used cubes and relative density as a measure to compare results. Firstly, EN AW 2618 was trialled, multiple scan parameters were used to increase relative density and remove cracks. However, cracks were observed within the manufactured specimens. Multiple scan strategies and parameters were tested, which reduced the crack dimensions but were not able to successfully remove them. Despite the presence of cracks, a relative density of 99.9 ± 0.1 % was achieved. The presence of cracks is unacceptable since they increase the risk of failure during component operation. Consequently, it was decided to change the material of study and test a newly developed high-strength aluminium alloy, A20X, designed for LPBF process conditions.

The parameter optimisation of A20X aluminium alloy showed its good processability. No cracks were observed in the manufactured specimens. The absence of cracks is due to the high content of grain refiner that changes the solidification mechanism limiting the formation of dendritic structure, thus removing hot cracking. A relative density of 99.9 ± 0.1% was achieved with optimum parameters. As-built specimens' microstructure was seen to be isotropic with an ultrafine grain structure. This is believed to be due to three mechanisms: (1) peritectic Ti (0.33 wt.%) acting as constitutional supercooling further enhanced by fast cooling and solidification rates of LPBF, (2) large amount of grain refiner TiB_2 (4.95 wt.%) acting as heterogeneous nucleation sites, (3) pinning of grain boundaries by TiB_2 particles. Although the presence of numerous alloying elements in A20X offers the possibility of the formation of numerous precipitates and intermetallics, the XRD patterns did not reveal any compounds other than Al, TiB_2, and Al_2Cu. Further investigation to characterise the material microstructure is necessary using advanced characterisation techniques such as high-resolution transmission electron microscopy and electron backscattered diffraction.

A20X isotropic microstructure could allow the use of as-built A20X without heat treatments. However, the tensile test of as-built specimens revealed a serrated plastic deformation which is believed to be due to the accumulation of solute atoms at the grain boundaries. A T7 heat treatment was successfully developed for A20X to enhance mechanical properties. However, a better understanding of the precipitation phases and formation mechanisms during ageing would allow taking full advantage of the A20X alloy.

A summary table of the thermo-mechanical properties of A20X is reported in **Table 7.10** along with EN AW 2618, and the go-to aluminium alloy for LPBF, AlSi10Mg. T7 A20X produced in this work is within the specifications recently reported by 3T [243]. Also, the measured mechanical properties measured in this thesis supersede AlSi10Mg and EN AW

2618. Only the thermal conductivity of AlSi10Mg (measured in this thesis) is higher than A20X with a 10 % margin.

Table 7.10: Comparative of A20X, EN AW 2618, and AlSi10Mg thermo-mechanical properties.

	AlSi10Mg T6-like [66]	**EN AW 2618 T61** [42]	**A20X T7** [243]	**A20X T7 here**
Young modulus (GPa)	73	74	75 ± 5	83
Yield strength (MPa)	239	370	370 – 430	379
UTS (MPa)	292	440	460 – 510	480
Elongation (%)	3.9	10	>10	12.7
λ ($W \cdot m^{-1} \cdot K^{-1}$)	165 (here)	146	-	150

Based on the results of this chapter, it can be concluded that A20X is an excellent candidate for high-strength applications, and its good thermal conductivity combined with its thermal stability indicated by the manufacturer makes it ideal for thermo-mechanical loading. The findings in this chapter could be particularly useful for the manufacture of high-performance components, where high-strength and good thermal conductivity are required. Furthermore, the development of high-performance material for LPBF directly allows to further improve the capability of lattice structure owing to higher properties of the based material.

8 Conclusion and future work

The thermal properties of bulk and lattice structures manufactured by LPBF have been investigated through the development of two apparatus. Information about

Influences of

In addition, high-strength aluminium alloy

AM offers unique design freedom compared to conventional techniques and is actively researched to enhance existing components or develop new and more efficient heat transfer components.

It has been shown in this thesis that a newly developed high-strength aluminium alloy for LPBF was able to compete with conventional high-strength aluminium alloys by taking advantage of the unique solidification rates of LPBF process.

This work has developed two apparatus for the thermal characterisation of lattice structures to broaden their adoption for heat exchangers and thermal management. This work has shown how the lattice structure parameters influence the thermal conductivity of the component. It has also been shown that topology plays a major role in the lattice heat transfer properties under forced air convection. This thesis has demonstrated the potential of TPMS lattice structures for thermal management beyond only weight-reducing and stiffening. This enables the development of numerous applications depending on the unit cell design, volume fraction, cell size, material choice and post-treatments. The cost penalty of additive manufacturing could be rapidly overcome by the benefits offered by lattice structure, especially in high-value component industries such as aerospace. The cost of flying is a huge motivator for even modest weight and efficiency savings, in which this industry heavily invests.

8.1 Conclusions

8.1.1 Thermal conductivity of LPBF components

AlSi10Mg coupons were manufactured with a high relative density and their thermal conductivity were measured using an in-house developed guarded-comparative longitudinal heat flow apparatus. The findings showed:

- As-built specimens exhibited anisotropic thermal conductivity owing to the anisotropic microstructure induced by LPBF process.
- Highest thermal conductivity was measured in the build direction.
- Heat treatment restored both microstructure and thermal conductivity to that of conventional processes.
- T6-like heat treatment was not only effective for enhancing the mechanical properties of AlSi10Mg, but also improving the thermal conductivity of the alloy.

TPMS lattice structures have been manufactured by LPBF from a variety of aerospace materials (AlSi10Mg, Ti6Al4V, Hastelloy-X) and their apparent thermal conductivity was experimentally measured and correlated to their unit cell design, volume fraction, and cell size. The findings here showed:

- Volume fraction had a preponderant effect on the apparent thermal conductivity.
- Apparent thermal conductivity can be predicted from the volume fraction of the lattice structure using a linear or power-law model.
- Cell size had a small effect on the apparent thermal conductivity but was not quantified due to the large measurement uncertainty.
- Lattice with pre-defined thermal conductivity was successfully manufactured and tested.

- Heat treatment response of lattice structures was dependent on lattice's volume fraction

8.1.2 Forced convection heat transfer of TPMS lattice structures

Matrix and network phase TPMS lattice structures were manufactured by LPBF in AlSi10Mg. Their thermal performance under forced air convection heat transfer was measured and compared to a pin-fin geometry (also manufactured by LPBF in AlSi10Mg) using a bespoke in-house apparatus. The findings here showed:

- Most of the examined lattices had a higher pressure drop than the pin-fin geometry.
- Lattice unit cell's topology played an important role in the pressure drop:
    - Matrix phase TPMS lattice had higher pressure drop and heat transfer than their network counterpart with the same amount of material.
    - Pressure drop increased inversely to the cell size of the lattice and correlated with the increase in the specific surface area to unit volume for most lattices.
    - Specific surface area per unit volume did not alone dictate the pressure drop of lattice structures.
    - Lattices' pressure drop for the tested flow rates could be quickly estimated using the variation of the cross-sectional area of the lattice.
- Lattices were highly effective at inducing heat transfer from the structure to the coolant flow:
    - Heat transfer of lattices exceeded that of the pin-fin with a minimum of 5 times increase for a similar volume fraction.
    - Matrix phase modified heat transfer coefficient increased with smaller cell size without reaching a plateau.

  - Network phase modified heat transfer coefficient increased with smaller cell size but reached a plateau for cell size lower than 5 mm.
  - No correlation was found between the increase in specific surface area to unit volume and the modified heat transfer coefficient.
- Lattices provided significantly improved thermal performance over the benchmarked pin-fin geometry.

8.1.3 Development of high-strength aluminium alloy for LPBF

The process optimisation and characterisation of high-strength aluminium alloys were undertaken:

- For EN AW 2618, previously published data indicated processing difficulties with LPBF owing to its high crack sensitivity. The findings here showed:
  - Relative density of 99.9 % was achieved by lowering cooling rates via specific scan strategies.
  - Lowering cooling rates by altering the scan strategy did not fully eliminate cracks.
  - For this reason, EN AW 2618 has been proven incompatible with LPBF process, which is in agreement with a previous study by Koutny *et al.* [49].
- For A20X, a commercial high-strength aluminium alloy developed for AM processes, the findings here showed:
  - A20X had good processability and achieved a relative density of 99.9 % with no cracks.
  - As-built specimens revealed an ultrafine isotropic microstructure.
  - As-built ultrafine isotropic microstructure resulted in isotropic thermo-mechanical properties.
  - As-built specimens show an ultimate tensile strength of 420 MPa.

- Stress-strain curves of as-built specimens revealed yield-point elongation and serrated plastic deformation.
- T7 heat treatment increased ultimate tensile strength to 480 MPa and removed the serrated plastic deformation and yield-point elongation.
- A20X-T7 exceeds the mechanical properties of EN AW 2618-T61
- Measured thermal conductivity was similar to that of EN AW 2618.

8.2 Future work

There is much potential for interesting research avenues within the manufacture and design of heat exchangers using lattice structures and materials processed by LPBF. Through the work presented in this thesis, there have been several areas identified that require further investigation and must be tackled by a multi-disciplinary team.

8.2.1 On the conductivity of lattice structures

In chapter 5, the conductivity of material produced by LPBF and lattice structures have been measured. Greater measurement precision in the measurement would enable distinguishing between the two theoretical models, thus more accurate predictions. The main source of uncertainty has been identified as being the T-type thermocouples that could be replaced by a more accurate sensor such as a PT-100 sensor (a platinum resistance thermometer) or determining the temperature calibration curve for each T-type thermocouples. Furthermore, the contribution of convective heat transfer within the lattice cells to the overall apparent thermal conductivity has not been quantified. A proposed method to determine convective contribution, would be by encapsulating the apparatus in a gas having dissimilar thermal conductivity than air but with similar other physical properties (i.e. viscosity, heat capacity…). The true conductivity of the structure can then be extrapolated by comparing the measured apparent conductivity of the

structure between both gas medium and determine the convective contribution. A more precise temperature measurement would also be beneficial for that purpose.

One of the advantages of lattice structure is the possibility to create graded structures according to a user-defined mathematical equation. The determination of the thermal conductivity of these graded structures is necessary. This would allow even further weight reduction by only using material where essential. Furthermore, it will allow to create structures with a very specific heat distribution without requiring a custom resistive element or filament to be manufactured, which is of interest for space missions to protect components from freezing. This can also be of interest in other areas, such as printed circuit boards, regions of high conduction can be defined while keeping other regions insulated from the heat.

8.2.2 On the forced convection heat transfer of lattice structures

In chapter 6, the forced convection transfer of lattice structures has been experimentally determined. Lattice structures are intricate structures and forced convective heat transfer involves complex phenomena, therefore it would benefit from more investigation. From this thesis, several axes of improvement have been identified.

Firstly, the lattice orientation has been seen to affect the thermal performance of lattice but has not been fully investigated and was not reported in this thesis. Secondly, the influence of the volume fraction on the lattice thermal performance has not been studied but is expected to play a significant role. The volume fraction defines the amount of material, thus the conductivity of the structure as demonstrated in chapter 5, but it also affects the flow area, with lower volume fraction resulting in bigger flow area and thinner walls whilst higher volume fraction reduces the flow area thicker walls. From those two antagonistic effects, it is expected that for a specific flow condition an optimum volume

fraction exists dependent on the maximisation of flow area for heat dissipation while allowing sufficient conduction through the lattice walls. Therefore, it is necessary to develop a generic model that could help to predict the thermal performance of the lattice structure and find this optimum point. This would allow designers to quickly select a lattice structure that fits their needs, thus facilitating the wider adoption of lattice structures to thermal applications.

This thesis has not covered the effect of surface roughness on lattice thermal performance. Current class LPBF generates surfaces rougher to those conventionally machined. Whilst it has been seen in the literature that it increases the pressure drop and heat transfer, designers must strike a balance to maximise the heat transfer while keeping the pressure drop low for each application. Surface finishing processes are necessary to reach the machined standard and are actively researched for LPBF components. However, lattice complex internal geometry limits the use of finishing processes. This area of study would benefit from more development. Alternatively, surface roughness is dependent on the LPBF process parameters. Therefore, it could be controlled directly from the manufacture to achieve specific roughness levels, thus limiting the need for surface finishing. However, this would need significant development on the process parameters comprehension and optimisation but could be alleviated by the use of artificial intelligence such as machine learning or deep learning algorithms in the coming years.

8.2.3 On the high-strength aluminium alloy for LPBF

A20X is a recently developed alloy that presents numerous alloying elements and offers the possibility of the formation of numerous precipitates and intermetallics. The XRD results did not reveal any compounds other than Al, TiB_2, and Al_2Cu in as-built and heat-treated. Further investigation into the material microstructure immediately following this thesis should be performed to understand how these alloying elements influence the

microstructure behaviour in the as-built and heat-treated conditions. This should be conducted with advanced characterisation techniques such as high-resolution transmission electron microscopy and electron backscattered diffraction. This would confirm the origin of the yield-drop phenomenon and serrated plastic deformation. Furthermore, advanced microstructural characterisation would also allow to better design heat treatment and enhance the mechanical properties of the alloy.

Monotonous uniaxial tensile testing was carried out to determine the mechanical properties of the alloy and to compare it to EN AW 2618. It was found that the elongation at break between the build and transverse direction after heat treatment are dissimilar despite having comparable elongation values in as-built condition. Combined with the aforementioned advanced microstructural analysis, the study of the fracture profiles of the specimens would help to understand this phenomenon.

The mechanical characterisation in this thesis aimed to show the potential for the A20X as high-strength aluminium alloy that could compete against conventional alloy such as EN AW 2618. Some characterisation work, therefore, remains before wider adoption. The presence of TiB_2 particles could adversely promote crack initiation by TiB_2/Al interface debonding, thus reducing fatigue resistance. Therefore, fatigue testing of the alloy should also be investigated. Also, the high strength and good thermal conductivity of A20X could make it ideal for thermo-mechanical loading. However, the thermal stability of its mechanical properties must be characterised.

9 References

[1] W.M. Kays, A.L. London, Compact heat exchangers, (1984).

[2] J.J. Murray, A. Guha, A. Bond, Overview of the development of heat exchangers for use in air-breathing propulsion pre-coolers, Acta Astronaut. 41 (1997) 723–729. https://doi.org/10.1016/S0094-5765(97)00199-9.

[3] R. Varvill, Heat exchanger development at Reaction Engines Ltd., Acta Astronaut. (2010). https://doi.org/10.1016/j.actaastro.2009.11.010.

[4] T.D. Ngo, A. Kashani, G. Imbalzano, K.T.Q. Nguyen, D. Hui, Additive manufacturing (3D printing): A review of materials, methods, applications and challenges, Compos. Part B Eng. 143 (2018) 172–196. https://doi.org/10.1016/j.compositesb.2018.02.012.

[5] EOS GmbH - Electro Optical Systems, Material Data Sheet: EOS Aluminium AlSi10Mg, (2014) 1–5. http://gpiprototype.com/images/PDF/EOS_Aluminium_AlSi10Mg_en.pdf.

[6] D. Jafari, W.W. Wits, The utilization of selective laser melting technology on heat transfer devices for thermal energy conversion applications: A review, Renew. Sustain. Energy Rev. 91 (2018) 420–442. https://doi.org/10.1016/j.rser.2018.03.109.

[7] nTopology's partnership with Betatype yields 28% reduction in build time for rocket nozzle part, proving intelligent design and complex functionality can go hand in hand with increased productivity with Metal AM., (2019). https://www.betaty.pe/case-studies/rocket-nozzle/ (accessed June 1, 2020).

[8] Stratasys introduces new PEKK thermoplastic material for FDM 3D printing technology, (2018). https://www.tctmagazine.com/additive-manufacturing-3d-printing-news/stratasys-introduces-new-pekk-thermoplastic-material-for-fdm/ (accessed June 1, 2020).

[9] Formlabs releases ceramic 3D printing resin, (2018). https://www.tctmagazine.com/additive-manufacturing-3d-printing-news/formlabs-ceramic-3d-printing-resin/.

[10] Binder Jet metal Additive Manufacturing: Process chain considerations when moving towards series production, (2018). https://www.metal-am.com/articles/binder-jet-metal-3d-printing-process-chain-considerations/ (accessed March 3, 2019).

[11] ASTM International, ISO/ASTM 52900:2015(E) - Standard Terminology for Additive Manufacturing Technologies, Rapid Manuf. Assoc. i (2013) 10–12. https://doi.org/10.1520/F2792-12A.2.

[12] J.P. Kruth, J. Deckers, E. Yasa, R. Wauthlé, Assessing and comparing influencing factors of residual stresses in selective laser melting using a novel analysis method, Proc. Inst. Mech. Eng. Part B J. Eng. Manuf. 226 (2012) 980–991. https://doi.org/10.1177/0954405412437085.

[13] P. Mercelis, J. Kruth, Residual stresses in selective laser sintering and selective laser melting, Rapid Prototyp. J. 12 (2006) 254–265. https://doi.org/10.1108/13552540610707013.

[14] A. Patterson, S. Messimer, P. Farrington, C. Carmen, J. Kendrick, Practical DOE-Based Approach for Predicting Impact of Stress and Deformation in SLM Overhanging Features During Product Design, (2018) 1–16.

[15] A. Kirchheim, H. Dennig, L. Zumofen, Industrializing Additive Manufacturing - Proceedings of Additive Manufacturing in Products and Applications - AMPA2017, Ind. Addit. Manuf. - Proc. Addit. Manuf. Prod. Appl. - AMPA2017. (2018). https://doi.org/10.1007/978-3-319-66866-6.

[16] C. Emmelmann, P. Sander, J. Kranz, E. Wycisk, Laser additive manufacturing and bionics: Redefining lightweight design, Phys. Procedia. 12 (2011) 364–368. https://doi.org/10.1016/j.phpro.2011.03.046.

[17] N. Chantarapanich, A. Laohaprapanon, S. Wisutmethangoon, P. Jiamwatthanachai, P. Chalermkarnnon, S. Sucharitpwatskul, P. Puttawibul, K. Sitthiseripratip, Fabrication of three-dimensional honeycomb structure for aeronautical applications using selective laser melting: A preliminary investigation, Rapid Prototyp. J. 20 (2014) 551–558. https://doi.org/10.1108/RPJ-08-2011-0086.

[18] A. Rindi, E. Meli, E. Boccini, G. Iurisci, S. Corbo, S. Falomi, Static and Modal Topology Optimization of Turbomachinery Components, J. Eng. Gas Turbines Power. 138 (2016) 1–9. https://doi.org/10.1115/1.4033512.

[19] L. Yang, O.L.A. Harrysson, D. Cormier, H. West, S. Zhang, H. Gong, B. Stucker, Design for additively manufactured lightweight structure: A perspective, Solid Free. Fabr. 2016 Proc. 27th Annu. Int. Solid Free. Fabr. Symp. - An Addit. Manuf. Conf. SFF 2016. (2016) 2165–2180.

[20] T. Maconachie, M. Leary, B. Lozanovski, X. Zhang, M. Qian, O. Faruque, M. Brandt, SLM lattice structures: Properties, performance, applications and challenges, Mater. Des. 183 (2019) 108137. https://doi.org/10.1016/j.matdes.2019.108137.

[21] K.J. Maloney, K.D. Fink, T.A. Schaedler, J.A. Kolodziejska, A.J. Jacobsen, C.S. Roper, Multifunctional heat exchangers derived from three-dimensional micro-lattice structures, Int. J. Heat Mass Transf. 55 (2012) 2486–2493. https://doi.org/10.1016/j.ijheatmasstransfer.2012.01.011.

[22] Large scale metal lattice structure for complex satellite part, (n.d.). https://www.metal-am.com/large-scale-metal-lattice-structure-complex-satellite-part/ (accessed January 10, 2017).

[23] B. Jackson, Monash additive manufacturing postdoc reimagines rocket engine design with BetatypeNo Title, (2017). https://3dprintingindustry.com/news/monash-additive-manufacturing-postdoc-reimagines-rocket-engine-design-betatype-118049/ (accessed July 15, 2017).

[24] M. Wong, I. Owen, C.J. Sutcliffe, Pressure loss and heat transfer through heat sinks produced by selective laser melting, Heat Transf. Eng. 30 (2009) 1068–1076. https://doi.org/10.1080/01457630902922228.

[25] E.O. Olakanmi, R.F. Cochrane, K.W. Dalgarno, A review on selective laser sintering/melting (SLS/SLM) of aluminium alloy powders: Processing, microstructure, and properties, Prog. Mater. Sci. 74 (2015) 401–477. https://doi.org/10.1016/j.pmatsci.2015.03.002.

[26] K.N. Amato, S.M. Gaytan, L.E. Murr, E. Martinez, P.W. Shindo, J. Hernandez, S.

Collins, F. Medina, Microstructures and mechanical behavior of Inconel 718 fabricated by selective laser melting, Acta Mater. 60 (2012) 2229–2239. https://doi.org/10.1016/j.actamat.2011.12.032.

[27] K. Kempen, L. Thijs, J. Van Humbeeck, J.P. Kruth, Mechanical Properties of AlSi10Mg Produced by Selective Laser Melting, Phys. Procedia. 39 (2012) 439–446. https://doi.org/10.1016/j.phpro.2012.10.059.

[28] B. Ahuja, A. Schaub, M. Karg, M. Lechner, M. Merklein, M. Schmidt, Developing LBM process parameters for Ti-6Al-4V thin wall structures and determining the corresponding mechanical characteristics, Phys. Procedia. 56 (2014) 90–98. https://doi.org/10.1016/j.phpro.2014.08.102.

[29] L.E. Murr, E. Martinez, K.N. Amato, S.M. Gaytan, J. Hernandez, D.A. Ramirez, P.W. Shindo, F. Medina, R.B. Wicker, Fabrication of metal and alloy components by additive manufacturing: Examples of 3D materials science, J. Mater. Res. Technol. 1 (2012) 42–54. https://doi.org/10.1016/S2238-7854(12)70009-1.

[30] S. Tsopanos, R.A.W. Mines, S. McKown, Y. Shen, W.J. Cantwell, W. Brooks, C.J. Sutcliffe, The Influence of Processing Parameters on the Mechanical Properties of Selectively Laser Melted Stainless Steel Microlattice Structures, J. Manuf. Sci. Eng. 132 (2010) 041011. https://doi.org/10.1115/1.4001743.

[31] N.T. Aboulkhair, N.M. Everitt, I. Ashcroft, C. Tuck, Reducing porosity in AlSi10Mg parts processed by selective laser melting, Addit. Manuf. 1 (2014) 77–86. https://doi.org/10.1016/j.addma.2014.08.001.

[32] S.A. Khairallah, A.T. Anderson, A. Rubenchik, W.E. King, Laser powder-bed fusion additive manufacturing: Physics of complex melt flow and formation mechanisms of pores, spatter, and denudation zones, Acta Mater. 108 (2016) 36–45. https://doi.org/10.1016/j.actamat.2016.02.014.

[33] N.T. Aboulkhair, I. Maskery, C. Tuck, I. Ashcroft, N. Everitt, Nano-hardness and microstructure of selective laser melted AlSi10Mg scan tracks, in: Ind. Laser Appl. Symp., 2015: p. 965702. https://doi.org/10.1117/12.2190015.

[34] G.K.L. Ng, A.E.W. Jarfors, G. Bi, H.Y. Zheng, Porosity formation and gas bubble retention in laser metal deposition, Appl. Phys. A Mater. Sci. Process. 97 (2009) 641–649. https://doi.org/10.1007/s00339-009-5266-3.

[35] A. Mauduit, S. Pillot, H. Gransac, Study of the suitability of aluminum alloys for additive manufacturing by laser powder-bed fusion, UPB Sci. Bull. Ser. B Chem. Mater. Sci. 79 (2017) 219–238.

[36] B. Liu, R. Wildman, C. Tuck, I. Ashcroft, R. Hague, Investigation the effect of particle size distribution on processing parameters optimisation in selective laser melting process, 22nd Annu. Int. Solid Free. Fabr. Symp. - An Addit. Manuf. Conf. SFF 2011. (2011) 227–238.

[37] L. Thijs, K. Kempen, J.P. Kruth, J. Van Humbeeck, Fine-structured aluminium products with controllable texture by selective laser melting of pre-alloyed AlSi10Mg powder, Acta Mater. 61 (2013) 1809–1819. https://doi.org/10.1016/j.actamat.2012.11.052.

[38] M. Balbaa, S. Mekhiel, M. Elbestawi, J. McIsaac, On selective laser melting of Inconel 718: Densification, surface roughness, and residual stresses, Mater. Des. 193 (2020) 108818. https://doi.org/10.1016/j.matdes.2020.108818.

[39] C. Silbernagel, L. Gargalis, I. Ashcroft, R. Hague, M. Galea, P. Dickens, Electrical

resistivity of pure copper processed by medium-powered laser powder bed fusion additive manufacturing for use in electromagnetic applications, Addit. Manuf. 29 (2019) 100831. https://doi.org/10.1016/j.addma.2019.100831.

[40] W.F. Gale, T.C. Totemeier, Smithells metals reference book, 2003.

[41] DIN EN 1706:2013-12, (2013).

[42] ASM International, ASM Handbook Volume 2: Properties and Selection: Nonferrous Alloys and Special-Purpose Materials, ASM International, 1990. https://www.asminternational.org/home/-/journal_content/56/10192/06182G/PUBLICATION/.

[43] Thyssenkrupp Materials (UK) Ltd, Stainless Steel 1.4404 Data Sheet, Mater. Data Sheet. (2018) 1–4.

[44] J. Trapp, A.M. Rubenchik, G. Guss, M.J. Matthews, In situ absorptivity measurements of metallic powders during laser powder-bed fusion additive manufacturing, Appl. Mater. Today. 9 (2017) 341–349. https://doi.org/10.1016/j.apmt.2017.08.006.

[45] T. Kimura, T. Nakamoto, Thermal and mechanical properties of commercial-purity aluminum fabricated using selective laser melting, Mater. Trans. 58 (2017) 799–805. https://doi.org/10.2320/matertrans.L-M2017809.

[46] E. Louvis, P. Fox, C.J. Sutcliffe, Selective laser melting of aluminium components, J. Mater. Process. Technol. 211 (2011) 275–284. https://doi.org/10.1016/j.jmatprotec.2010.09.019.

[47] A. Gloria, R. Montanari, M. Richetta, A. Varone, Alloys for aeronautic applications: State of the art and perspectives, Metals (Basel). 9 (2019) 1–26. https://doi.org/10.3390/met9060662.

[48] F.M. Ghaini, M. Sheikhi, M.J. Torkamany, J. Sabbaghzadeh, The relation between liquation and solidification cracks in pulsed laser welding of 2024 aluminium alloy, Mater. Sci. Eng. A. 519 (2009) 167–171. https://doi.org/10.1016/j.msea.2009.04.056.

[49] D. Koutny, D. Palousek, L. Pantelejev, C. Hoeller, R. Pichler, L. Tesicky, J. Kaiser, Influence of scanning strategies on processing of aluminum alloy EN AW 2618 using selective laser melting, Materials (Basel). 11 (2018). https://doi.org/10.3390/ma11020298.

[50] Y. Otani, S. Sasaki, Effects of the addition of silicon to 7075 aluminum alloy on microstructure, mechanical properties, and selective laser melting processability, Mater. Sci. Eng. A. 777 (2020) 139079. https://doi.org/10.1016/j.msea.2020.139079.

[51] J.H. Martin, B.D. Yahata, J.M. Hundley, J.A. Mayer, T.A. Schaedler, T.M. Pollock, 3D printing of high-strength aluminium alloys, Nature. 549 (2017) 365–369. https://doi.org/10.1038/nature23894.

[52] R. González, D.I. Martínez, J.A. González, J. Talamantes, S. Valtierra, R. Colás, Experimental investigation for fatigue strength of a cast aluminium alloy, Int. J. Fatigue. 33 (2011) 273–278. https://doi.org/10.1016/j.ijfatigue.2010.09.002.

[53] T. Kimura, T. Nakamoto, M. Mizuno, H. Araki, Effect of silicon content on densification, mechanical and thermal properties of Al-xSi binary alloys fabricated using selective laser melting, Mater. Sci. Eng. A. 682 (2017) 593–602.

https://doi.org/10.1016/j.msea.2016.11.059.

[54] V. Kumar, H. Mehdi, A. Kumar, Effect of Silicon content on the Mechanical Properties of Aluminum Alloy, Int. Res. J. Eng. Technol. 2 (2015) 1326–1330.

[55] G.A. Edwards, K. Stiller, G.L. Dunlop, M.J. Couper, The precipitation sequence in Al-Mg-Si alloys, Acta Mater. 46 (1998) 3893–3904. https://doi.org/10.1016/S1359-6454(98)00059-7.

[56] P.A. Hooper, Melt pool temperature and cooling rates in laser powder bed fusion, Addit. Manuf. 22 (2018) 548–559. https://doi.org/10.1016/j.addma.2018.05.032.

[57] Z. Luo, Y. Zhao, Efficient thermal finite element modeling of selective laser melting of Inconel 718, Comput. Mech. 65 (2020) 763–787. https://doi.org/10.1007/s00466-019-01794-0.

[58] A. Aversa, M. Lorusso, F. Trevisan, E. Ambrosio, F. Calignano, D. Manfredi, S. Biamino, P. Fino, M. Lombardi, M. Pavese, Effect of Process and Post-Process Conditions on the Mechanical Properties of an A357 Alloy Produced via Laser Powder Bed Fusion, Metals (Basel). 7 (2017) 68. https://doi.org/10.3390/met7020068.

[59] Y. Li, D. Gu, Parametric analysis of thermal behavior during selective laser melting additive manufacturing of aluminum alloy powder, Mater. Des. 63 (2014) 856–867. https://doi.org/10.1016/j.matdes.2014.07.006.

[60] W. Li, S. Li, J. Liu, A. Zhang, Y. Zhou, Q. Wei, C. Yan, Y. Shi, Effect of heat treatment on AlSi10Mg alloy fabricated by selective laser melting: Microstructure evolution, mechanical properties and fracture mechanism, Mater. Sci. Eng. A. 663 (2016) 116–125. https://doi.org/10.1016/j.msea.2016.03.088.

[61] E.J. Lavernia, J.D. Ayers, T.S. Srivatsan, Rapid solidification processing with specific application to aluminium alloys, Int. Mater. Rev. 37 (1992) 1–44. https://doi.org/10.1179/imr.1992.37.1.1.

[62] N.E. Uzan, S. Ramati, R. Shneck, N. Frage, O. Yeheskel, On the effect of shot-peening on fatigue resistance of AlSi10Mg specimens fabricated by additive manufacturing using selective laser melting (AM-SLM), Addit. Manuf. 21 (2018) 458–464. https://doi.org/10.1016/j.addma.2018.03.030.

[63] K.G. Prashanth, S. Scudino, H.J. Klauss, K.B. Surreddi, L. Löber, Z. Wang, A.K. Chaubey, U. Kühn, J. Eckert, Microstructure and mechanical properties of Al-12Si produced by selective laser melting: Effect of heat treatment, Mater. Sci. Eng. A. 590 (2014) 153–160. https://doi.org/10.1016/j.msea.2013.10.023.

[64] X.P. Li, X.J. Wang, M. Saunders, A. Suvorova, L.C. Zhang, Y.J. Liu, M.H. Fang, Z.H. Huang, T.B. Sercombe, A selective laser melting and solution heat treatment refined Al-12Si alloy with a controllable ultrafine eutectic microstructure and 25% tensile ductility, Acta Mater. 95 (2015) 74–82. https://doi.org/10.1016/j.actamat.2015.05.017.

[65] N. Takata, H. Kodaira, A. Suzuki, M. Kobashi, Size dependence of microstructure of AlSi10Mg alloy fabricated by selective laser melting, Mater. Charact. 143 (2018) 18–26. https://doi.org/10.1016/j.matchar.2017.11.052.

[66] N.T. Aboulkhair, I. Maskery, C. Tuck, I. Ashcroft, N.M. Everitt, The microstructure and mechanical properties of selectively laser melted AlSi10Mg: The effect of a conventional T6-like heat treatment, Mater. Sci. Eng. A. 667 (2016) 139–146. https://doi.org/10.1016/j.msea.2016.04.092.

[67] H. Zhang, H. Zhu, T. Qi, Z. Hu, X. Zeng, Selective laser melting of high strength Al-Cu-Mg alloys: Processing, microstructure and mechanical properties, Mater. Sci. Eng. A. 656 (2016) 47–54. https://doi.org/10.1016/j.msea.2015.12.101.

[68] S. Zia Uddin, D. Espalin, J. Mireles, P. Morton, C. Terrazas, S. Collins, L.E. Murr, R. Wicker, Laser powder bed fusion fabrication and characterization of crack- free aluminum alloy 6061 using in-process powder bed induction heating, Solid Free. Fabr. Symp. (2016) 214–227.

[69] N. Kaufmann, M. Imran, T.M. Wischeropp, C. Emmelmann, S. Siddique, F. Walther, Influence of process parameters on the quality of aluminium alloy en AW 7075 using Selective Laser Melting (SLM), Phys. Procedia. 83 (2016) 918–926. https://doi.org/10.1016/j.phpro.2016.08.096.

[70] I. Rosenthal, A. Stern, N. Frage, Microstructure and Mechanical Properties of AlSi10Mg Parts Produced by the Laser Beam Additive Manufacturing (AM) Technology, Metallogr. Microstruct. Anal. 3 (2014) 448–453. https://doi.org/10.1007/s13632-014-0168-y.

[71] N.T. Aboulkhair, I. Maskery, C. Tuck, I. Ashcroft, N.M. Everitt, Improving the fatigue behaviour of a selectively laser melted aluminium alloy: Influence of heat treatment and surface quality, Mater. Des. 104 (2016) 174–182. https://doi.org/10.1016/j.matdes.2016.05.041.

[72] L. Cheng, X. Liang, J. Bai, Q. Chen, J. Lemon, A. To, On utilizing topology optimization to design support structure to prevent residual stress induced build failure in laser powder bed metal additive manufacturing, Addit. Manuf. 27 (2019) 290–304. https://doi.org/10.1016/j.addma.2019.03.001.

[73] W. Shifeng, L. Shuai, W. Qingsong, C. Yan, Z. Sheng, S. Yusheng, Effect of molten pool boundaries on the mechanical properties of selective laser melting parts, J. Mater. Process. Technol. 214 (2014) 2660–2667. https://doi.org/10.1016/j.jmatprotec.2014.06.002.

[74] C. Cingi, V. Rauta, E. Suikkanen, J. Orkas, Effect of heat treatment on thermal conductivity of aluminum die casting alloys, Adv. Mater. Res. 538–541 (2012) 2047–2052. https://doi.org/10.4028/www.scientific.net/AMR.538-541.2047.

[75] N. Takata, H. Kodaira, K. Sekizawa, A. Suzuki, M. Kobashi, Change in microstructure of selectively laser melted AlSi10Mg alloy with heat treatments, Mater. Sci. Eng. A. 704 (2017) 218–228. https://doi.org/10.1016/j.msea.2017.08.029.

[76] N.T. Aboulkhair, C. Tuck, I. Ashcroft, I. Maskery, N.M. Everitt, On the Precipitation Hardening of Selective Laser Melted AlSi10Mg, Metall. Mater. Trans. A Phys. Metall. Mater. Sci. 46 (2015) 3337–3341. https://doi.org/10.1007/s11661-015-2980-7.

[77] S. Catchpole-Smith, N. Aboulkhair, L. Parry, C. Tuck, I.A. Ashcroft, A. Clare, Fractal scan strategies for selective laser melting of ‘unweldable’ nickel superalloys, Addit. Manuf. 15 (2017) 113–122. https://doi.org/10.1016/j.addma.2017.02.002.

[78] Trumpf, TruPrint 5000 highly productive 3D printing for industrial serial production, (n.d.). https://www.trumpf.com/en_US/products/machines-systems/additive-production-systems/truprint-5000/.

[79] C.E. Roberts, D. Bourell, T. Watt, J. Cohen, A novel processing approach for

additive manufacturing of commercial aluminum alloys, Phys. Procedia. 83 (2016) 909–917. https://doi.org/10.1016/j.phpro.2016.08.095.

[80] M.L. Montero Sistiaga, R. Mertens, B. Vrancken, X. Wang, B. Van Hooreweder, J.P. Kruth, J. Van Humbeeck, Changing the alloy composition of Al7075 for better processability by selective laser melting, J. Mater. Process. Technol. 238 (2016) 437–445. https://doi.org/10.1016/j.jmatprotec.2016.08.003.

[81] H. Zhang, H. Zhu, X. Nie, J. Yin, Z. Hu, X. Zeng, Effect of Zirconium addition on crack, microstructure and mechanical behavior of selective laser melted Al-Cu-Mg alloy, Scr. Mater. 134 (2017) 6–10. https://doi.org/10.1016/j.scriptamat.2017.02.036.

[82] S. Toschi, E. Balducci, L. Ceschini, E.A. Mørtsell, A. Morri, M. Di Sabatino, Effect of Zr addition on overaging and tensile behavior of 2618 aluminum alloy, Metals (Basel). 9 (2019) 3–12. https://doi.org/10.3390/met9020130.

[83] K. Schmidtke, F. Palm, A. Hawkins, C. Emmelmann, Process and mechanical properties: Applicability of a scandium modified Al-alloy for laser additive manufacturing, Phys. Procedia. 12 (2011) 369–374. https://doi.org/10.1016/j.phpro.2011.03.047.

[84] U.S. Geological Survey, Mineral Commodity Summaries 2020, 2020. https://doi.org/https://doi.org/10.3133/ mcs2020.

[85] S. Griffiths, J.R. Croteau, M.D. Rossell, R. Erni, A. De Luca, N.Q. Vo, D.C. Dunand, C. Leinenbach, Coarsening- and creep resistance of precipitation-strengthened Al–Mg–Zr alloys processed by selective laser melting, Acta Mater. 188 (2020) 192–202. https://doi.org/10.1016/j.actamat.2020.02.008.

[86] Y. Zhou, S. Wen, C. Wang, L. Duan, Q. Wei, Y. Shi, Effect of TiC content on the Al-15Si alloy processed by selective laser melting: Microstructure and mechanical properties, Opt. Laser Technol. 120 (2019). https://doi.org/10.1016/j.optlastec.2019.105719.

[87] M. Opprecht, J.P. Garandet, G. Roux, C. Flament, M. Soulier, A solution to the hot cracking problem for aluminium alloys manufactured by laser beam melting, Acta Mater. 197 (2020) 40–53. https://doi.org/10.1016/j.actamat.2020.07.015.

[88] J. Geng, G. Liu, T. Hong, M. Wang, D. Chen, N. Ma, H. Wang, Tuning the microstructure features of in-situ nano TiB2/Al-Cu-Mg composites to enhance mechanical properties, J. Alloys Compd. 775 (2019) 193–201. https://doi.org/10.1016/j.jallcom.2018.10.078.

[89] Y. Shen, X. Li, T. Hong, J. Geng, H. Wang, Effects of TiB2 particles on microstructure and mechanical properties of an in-situ TiB2-Al-Cu-Li matrix composite, Mater. Sci. Eng. A. 655 (2016) 265–268. https://doi.org/10.1016/j.msea.2015.12.104.

[90] L. Zhang, Q. Zheng, H. Jiang, J. Zhao, Interfacial energy between Al melt and TiB2 particles and efficiency of TiB2 particles to nucleate α-Al, Scr. Mater. 160 (2019) 25–28. https://doi.org/10.1016/j.scriptamat.2018.09.042.

[91] S. Suresh, N.S.V. Moorthi, Aluminium- Titanium diboride (Al-TiB2) metal matrix composites: Challenges and opportunities, Procedia Eng. 38 (2012) 89–97. https://doi.org/10.1016/j.proeng.2012.06.013.

[92] J.S. Nuechterlein, J.J. ITEN, Additive manufacturing of metal alloys and metal alloy matrix composites, US20180161874A1, 2018.

https://patents.google.com/patent/US20180161874A1/.

[93] P. Bale, Feeding Properties of the Highly Grain Refined A20X Alloy, 2011.

[94] T. Tanaka, Y. Kamitakahara, Highly heat-resistant aluminum alloy “KS2000,” Res. Dev. Kobe Steel Eng. Reports. 66 (2016) 79–83.

[95] L.J. Gibson, M.F. Ashby, Cellular Solids, 2nd ed., Cambridge University Press, Cambridge, 1997. https://doi.org/10.1017/CBO9781139878326.

[96] T. Tashiro, A. Ishida, M. Hori, M. Igisu, M. Koike, P. Méjean, N. Takahata, Y. Sano, T. Komiya, Early trace of life from 3.95 Ga sedimentary rocks in Labrador, Canada, Nature. 549 (2017) 516–518. https://doi.org/10.1038/nature24019.

[97] G. Ryan, A. Pandit, D.P. Apatsidis, Fabrication methods of porous metals for use in orthopaedic applications, Biomaterials. 27 (2006) 2651–2670. https://doi.org/10.1016/j.biomaterials.2005.12.002.

[98] J. Tian, T. Kim, T.J. Lu, H.P. Hodson, D.T. Queheillalt, D.J. Sypeck, H.N.G. Wadley, The effects of topology upon fluid-flow and heat-transfer within cellular copper structures, Int. J. Heat Mass Transf. 47 (2004) 3171–3186. https://doi.org/10.1016/j.ijheatmasstransfer.2004.02.010.

[99] C.S. Roper, Multiobjective optimization for design of multifunctional sandwich panel heat pipes with micro-architected truss cores, Int. J. Heat Fluid Flow. 32 (2011) 239–248. https://doi.org/10.1016/j.ijheatfluidflow.2010.07.002.

[100] L. Chuan, X.D. Wang, T.H. Wang, W.M. Yan, Fluid flow and heat transfer in microchannel heat sink based on porous fin design concept, Int. Commun. Heat Mass Transf. 65 (2015) 52–57. https://doi.org/10.1016/j.icheatmasstransfer.2015.04.005.

[101] J. Banhart, Manufacture, characterisation and application of cellular metals and metal foams, Prog. Mater. Sci. 46 (2001) 559–632. https://doi.org/10.1016/S0079-6425(00)00002-5.

[102] M. Smith, Z. Guan, W.J. Cantwell, Finite element modelling of the compressive response of lattice structures manufactured using the selective laser melting technique, Int. J. Mech. Sci. 67 (2013) 28–41. https://doi.org/10.1016/j.ijmecsci.2012.12.004.

[103] C.Y. Yap, C.K. Chua, Z.L. Dong, Z.H. Liu, D.Q. Zhang, L.E. Loh, S.L. Sing, Review of selective laser melting: Materials and applications, Appl. Phys. Rev. 2 (2015). https://doi.org/10.1063/1.4935926.

[104] S. Amin Yavari, S.M. Ahmadi, R. Wauthle, B. Pouran, J. Schrooten, H. Weinans, A.A. Zadpoor, Relationship between unit cell type and porosity and the fatigue behavior of selective laser melted meta-biomaterials, J. Mech. Behav. Biomed. Mater. 43 (2015) 91–100. https://doi.org/10.1016/j.jmbbm.2014.12.015.

[105] A.G. Evans, M.Y. He, V.S. Deshpande, J.W. Hutchinson, A.J. Jacobsen, W.B. Carter, Concepts for enhanced energy absorption using hollow micro-lattices, Int. J. Impact Eng. 37 (2010) 947–959. https://doi.org/10.1016/j.ijimpeng.2010.03.007.

[106] T. Tancogne-Dejean, A.B. Spierings, D. Mohr, Additively-manufactured metallic micro-lattice materials for high specific energy absorption under static and dynamic loading, Acta Mater. 116 (2016) 14–28. https://doi.org/10.1016/j.actamat.2016.05.054.

[107] M. Leary, M. Mazur, J. Elambasseril, M. McMillan, T. Chirent, Y. Sun, M. Qian, M. Easton, M. Brandt, Selective laser melting (SLM) of AlSi12Mg lattice structures, Mater. Des. 98 (2016) 344–357. https://doi.org/10.1016/j.matdes.2016.02.127.

[108] M. Mazur, M. Leary, S. Sun, M. Vcelka, D. Shidid, M. Brandt, Deformation and failure behaviour of Ti-6Al-4V lattice structures manufactured by selective laser melting (SLM), Int. J. Adv. Manuf. Technol. 84 (2016) 1391–1411. https://doi.org/10.1007/s00170-015-7655-4.

[109] M.G. Rashed, M. Ashraf, R.A.W. Mines, P.J. Hazell, Metallic microlattice materials: A current state of the art on manufacturing, mechanical properties and applications, Mater. Des. 95 (2016) 518–533. https://doi.org/10.1016/j.matdes.2016.01.146.

[110] H.A. Schwarz, Gesammelte Mathematische Abhandlungen, Springer Berlin Heidelberg, 1890. https://doi.org/10.1007/978-3-642-50665-9.

[111] E.R. Neovius, Bestimmung zweier speciellen periodischen Minimalflächen, auf welchen unendlich viele gerade Linien und unendlich viele ebene geodätische Linien liegen, (1883).

[112] A.H. Schoen, Infinite periodic minimal surfaces without self-intersections, Nasa Tech. Note D-5541. (1970) 92. http://ntrs.nasa.gov/search.jsp?R=19700020472.

[113] I. Maskery, N.T. Aboulkhair, A.O. Aremu, C.J. Tuck, I.A. Ashcroft, Compressive failure modes and energy absorption in additively manufactured double gyroid lattices, Addit. Manuf. 16 (2017) 24–29. https://doi.org/10.1016/j.addma.2017.04.003.

[114] A.A. Zadpoor, Bone tissue regeneration: The role of scaffold geometry, Biomater. Sci. 3 (2015) 231–245. https://doi.org/10.1039/c4bm00291a.

[115] I. Maskery, L. Sturm, A.O. Aremu, A. Panesar, C.B. Williams, C.J. Tuck, R.D. Wildman, I.A. Ashcroft, R.J.M. Hague, Insights into the mechanical properties of several triply periodic minimal surface lattice structures made by polymer additive manufacturing, Polymer (Guildf). 152 (2018) 62–71. https://doi.org/10.1016/j.polymer.2017.11.049.

[116] V. Rauta, C. Cingi, J. Orkas, Effect of annealing and metallurgical treatments on thermal conductivity of aluminium alloys, Int. J. Met. 10 (2016) 157–171. https://doi.org/10.1007/s40962-015-0017-z.

[117] H. Dong, B. Wen, R. Melnik, Relative importance of grain boundaries and size effects in thermal conductivity of nanocrystalline materials, Sci. Rep. 4 (2014) 7037. https://doi.org/10.1038/srep07037.

[118] E. Bianchi, T. Heidig, C.G. Visconti, G. Groppi, H. Freund, E. Tronconi, An appraisal of the heat transfer properties of metallic open-cell foams for strongly exo-/endo-thermic catalytic processes in tubular reactors, Chem. Eng. J. 198–199 (2012) 512–528. https://doi.org/10.1016/j.cej.2012.05.045.

[119] C.Y. Zhao, Review on thermal transport in high porosity cellular metal foams with open cells, Int. J. Heat Mass Transf. 55 (2012) 3618–3632. https://doi.org/10.1016/j.ijheatmasstransfer.2012.03.017.

[120] P. Ranut, On the effective thermal conductivity of aluminum metal foams: Review and improvement of the available empirical and analytical models, Appl. Therm. Eng. 101 (2016) 496–524. https://doi.org/10.1016/j.applthermaleng.2015.09.094.

[121] C. Yan, L. Hao, A. Hussein, S.L. Bubb, P. Young, D. Raymont, Evaluation of light-weight AlSi10Mg periodic cellular lattice structures fabricated via direct metal laser sintering, J. Mater. Process. Technol. 214 (2014) 856–864. https://doi.org/10.1016/j.jmatprotec.2013.12.004.

[122] I. Maskery, A.O. Aremu, M. Simonelli, C. Tuck, R.D. Wildman, I.A. Ashcroft, R.J.M. Hague, Mechanical Properties of Ti-6Al-4V Selectively Laser Melted Parts with Body-Centred-Cubic Lattices of Varying cell size, Exp. Mech. 55 (2015) 1261–1272. https://doi.org/10.1007/s11340-015-0021-5.

[123] J.C. Wallach, L.J. Gibson, Mechanical behavior of a three-dimensional truss material, Int. J. Solids Struct. 38 (2001) 7181–7196. https://doi.org/10.1016/S0020-7683(00)00400-5.

[124] T. Kim, C.Y. Zhao, T.J. Lu, H.P. Hodson, Convective heat dissipation with lattice-frame materials, Mech. Mater. 36 (2004) 767–780. https://doi.org/10.1016/j.mechmat.2003.07.001.

[125] T. Kim, H.P. Hodson, T.J. Lu, Contribution of vortex structures and flow separation to local and overall pressure and heat transfer characteristics in an ultralightweight lattice material, Int. J. Heat Mass Transf. 48 (2005) 4243–4264. https://doi.org/10.1016/j.ijheatmasstransfer.2005.04.026.

[126] T.J. Lu, L. Valdevit, A.G. Evans, Active cooling by metallic sandwich structures with periodic cores, Prog. Mater. Sci. 50 (2005) 789–815. https://doi.org/10.1016/j.pmatsci.2005.03.001.

[127] E. Bianchi, W. Schwieger, H. Freund, Assessment of Periodic Open Cellular Structures for Enhanced Heat Conduction in Catalytic Fixed-Bed Reactors, Adv. Eng. Mater. 18 (2016) 608–614. https://doi.org/10.1002/adem.201500356.

[128] J.C. Maxwell, A treatise on electricity and magnetism / by James Clerk Maxwell., 2nd. ed., Clarendon Press, Oxford, 1881.

[129] R.K. Abu Al-Rub, D.W. Abueidda, A.S. Dalaq, Thermo-electro-mechanical properties of interpenetrating phase composites with periodic architectured reinforcements, Adv. Struct. Mater. 64 (2015) 1–18. https://doi.org/10.1007/978-3-319-19440-0_1.

[130] Z. Hashin, S. Shtrikman, A variational approach to the theory of the elastic behaviour of multiphase materials, J. Mech. Phys. Solids. 11 (1963) 127–140. https://doi.org/10.1016/0022-5096(63)90060-7.

[131] J. Kuehndel, B. Kerler, C. Karcher, Air side thermal performance of wavy fin heat exchangers produced by selective laser melting, 7th Eur. Therm. Conf. Eurotherm 2016. 745 (2016). https://doi.org/10.1088/1742-6596/745/3/032057.

[132] J. Dewatwal, Design of Compact Plate Fin Heat Exchanger, Natl. Inst. Technol. Rourkela. (2009) 1–61.

[133] T.L. Bergman, F.P. Incropera, D.P. DeWitt, A.S. Lavine, Fundamentals of Heat and Mass Transfer, 7th ed., John Wiley & Sons, 2011.

[134] N.C. De Jong, L.W. Zhang, A.M. Jacobi, S. Balachandar, D.K. Tafti, A complementary experimental and numerical study of the flow and heat transfer in offset strip-fin heat exchangers, J. Heat Transfer. 120 (1998) 690–698. https://doi.org/10.1115/1.2824338.

[135] M. Iyengar, A. Bar-Cohen, Design for manufacturability of SISE parallel plate

forced convection heat sinks, IEEE Trans. Components Packag. Technol. 24 (2001) 150–158. https://doi.org/10.1109/6144.926377.

[136] N. Sahiti, F. Durst, A. Dewan, Heat transfer enhancement by pin elements, Int. J. Heat Mass Transf. 48 (2005) 4738–4747. https://doi.org/10.1016/j.ijheatmasstransfer.2005.07.001.

[137] R.S. Matos, J.V.C. Vargas, T.A. Laursen, F.E.M. Saboya, Optimization study and heat transfer comparison of staggered circular and elliptic tubes in forced convection, Int. J. Heat Mass Transf. 44 (2001) 3953–3961. https://doi.org/10.1016/S0017-9310(01)00006-0.

[138] K.L. Kirsch, K.A. Thole, Pressure loss and heat transfer performance for additively and conventionally manufactured pin fin arrays, Int. J. Heat Mass Transf. 108 (2017) 2502–2513. https://doi.org/10.1016/j.ijheatmasstransfer.2017.01.095.

[139] T.-M. Jeng, S.-C. Tzeng, Numerical Simulation of Laminar Forced Convection of Pin-Fin Heat-Sink Array in a Channel by Using Porous Approach, Appl. Sci. 5 (2015) 1846–1868. https://doi.org/10.3390/app5041846.

[140] R. Mertens, S. Clijsters, K. Kempen, J.P. Kruth, Optimization of Scan Strategies in Selective Laser Melting of Aluminum Parts with Downfacing Areas, J. Manuf. Sci. Eng. Trans. ASME. 136 (2014). https://doi.org/10.1115/1.4028620.

[141] M. Wong, I. Owen, C.J. Sutcliffe, A. Puri, Convective heat transfer and pressure losses across novel heat sinks fabricated by Selective Laser Melting, Int. J. Heat Mass Transf. 52 (2009) 281–288. https://doi.org/10.1016/j.ijheatmasstransfer.2008.06.002.

[142] A. Leon, E. Aghion, Effect of surface roughness on corrosion fatigue performance of AlSi10Mg alloy produced by Selective Laser Melting (SLM), Mater. Charact. 131 (2017) 188–194. https://doi.org/10.1016/j.matchar.2017.06.029.

[143] C.K. Stimpson, J.C. Snyder, K.A. Thole, D. Mongillo, Roughness Effects on Flow and Heat Transfer for Additively Manufactured Channels, J. Turbomach. 138 (2016) 051008. https://doi.org/10.1115/1.4032167.

[144] L. Gao, Y.G. Sun, Fluid Flow and Heat Transfer Characteristics of Composite Lattice Core Sandwich Structures, J. Thermophys. Heat Transf. 28 (2014) 258–269. https://doi.org/10.2514/1.T4264.

[145] D. Yoo, New paradigms in internal architecture design and freeform fabrication of tissue engineering porous scaffolds, Med. Eng. Phys. 34 (2012) 762–776. https://doi.org/10.1016/j.medengphy.2012.05.008.

[146] I. Maskery, A.O. Aremu, L. Parry, R.D. Wildman, C.J. Tuck, I.A. Ashcroft, Effective design and simulation of surface-based lattice structures featuring volume fraction and cell type grading, Mater. Des. 155 (2018) 220–232. https://doi.org/10.1016/j.matdes.2018.05.058.

[147] A. Panesar, M. Abdi, D. Hickman, I. Ashcroft, Strategies for functionally graded lattice structures derived using topology optimisation for Additive Manufacturing, Addit. Manuf. 19 (2018) 81–94. https://doi.org/10.1016/j.addma.2017.11.008.

[148] M. Simonelli, C. Tuck, N.T. Aboulkhair, I. Maskery, I. Ashcroft, R.D. Wildman, R. Hague, A Study on the Laser Spatter and the Oxidation Reactions During Selective Laser Melting of 316L Stainless Steel, Al-Si10-Mg, and Ti-6Al-4V, Metall. Mater. Trans. A Phys. Metall. Mater. Sci. 46 (2015) 3842–3851. https://doi.org/10.1007/s11661-015-2882-8.

[149] S. Vock, B. Klöden, A. Kirchner, T. Weißgärber, B. Kieback, Powders for powder bed fusion: a review, Prog. Addit. Manuf. 4 (2019) 383–397. https://doi.org/10.1007/s40964-019-00078-6.

[150] N.T. Aboulkhair, Additive manufacture of an aluminium alloy: processing, microstructure, and mechanical properties, University of Nottingham, 2015.

[151] Q.B. Nguyen, M.L.S. Nai, Z. Zhu, C.N. Sun, J. Wei, W. Zhou, Characteristics of Inconel Powders for Powder-Bed Additive Manufacturing, Engineering. 3 (2017) 695–700. https://doi.org/10.1016/J.ENG.2017.05.012.

[152] C. Pleass, S. Jothi, Influence of powder characteristics and additive manufacturing process parameters on the microstructure and mechanical behaviour of Inconel 625 fabricated by Selective Laser Melting, Addit. Manuf. 24 (2018) 419–431. https://doi.org/10.1016/j.addma.2018.09.023.

[153] ISO - ISO 13320:2009 - Particle size analysis — Laser diffraction methods, 2009. https://www.iso.org/standard/44929.html (accessed August 24, 2020).

[154] L.C. Ardila, F. Garciandia, J.B. González-Díaz, P. Álvarez, A. Echeverria, M.M. Petite, R. Deffley, J. Ochoa, Effect of IN718 recycled powder reuse on properties of parts manufactured by means of Selective Laser Melting, Phys. Procedia. 56 (2014) 99–107. https://doi.org/10.1016/j.phpro.2014.08.152.

[155] D. Taarea, S.I. Bakhtiyarov, 14 - General physical properties, Smithells Met. Ref. B. (Eighth Ed. 7 (2004) 1–45. https://doi.org/http://dx.doi.org/10.1016/B978-075067509-3/50017-8.

[156] Z. Xiang, M. Yin, G. Dong, X. Mei, G. Yin, Modeling of the thermal physical process and study on the reliability of linear energy density for selective laser melting, Results Phys. 9 (2018) 939–946. https://doi.org/10.1016/j.rinp.2018.03.047.

[157] B. Taylor, E. Weidmann, Metallographic preparation of titanium, Struers Appl. Notes, Http//Www. Struers. Com, As. 8 (2007) 3–4. https://doi.org/10.2014 / 62140202.

[158] C.A. Schneider, W.S. Rasband, K.W. Eliceiri, NIH Image to ImageJ: 25 years of image analysis, Nat. Methods. 9 (2012) 671–675. https://doi.org/10.1038/nmeth.2089.

[159] ASTM-E92, Standard Test Method for Vickers Hardness of Metallic Materials, ASTM Int. 82 (1997) 1–10. https://doi.org/10.1520/E0092-82R03E02.2.

[160] ASTM E8, ASTM E8/E8M standard test methods for tension testing of metallic materials 1, Annu. B. ASTM Stand. 4. (2010) 1–27. https://doi.org/10.1520/E0008.

[161] C. Kittel, Introduction to solid state physics, 8th ed., I, Wiley, Hoboken, N.J., 2005.

[162] D. Zhao, X. Qian, X. Gu, S.A. Jajja, R. Yang, Measurement techniques for thermal conductivity and interfacial thermal conductance of bulk and thin film materials, J. Electron. Packag. Trans. ASME. 138 (2016) 1–64. https://doi.org/10.1115/1.4034605.

[163] J. Bodzenta, A. Kaźmierczak-Bałata, J. Mazur, Photothermal methods for determination of thermal properties of bulk materials and thin films, Cent. Eur. J. Phys. 8 (2010) 207–220. https://doi.org/10.2478/s11534-009-0133-6.

[164] A.S. for T. Materials, E1530 - Standard Test Method for Evaluating the Resistance

to Thermal Transmission of Materials by the Guarded Heat Flow Meter Technique, (2006) 9. https://doi.org/10.1520/E1530-19.2.

[165] S. Min, J. Blumm, A. Lindemann, A new laser flash system for measurement of the thermophysical properties, Thermochim. Acta. 455 (2007) 46–49. https://doi.org/10.1016/j.tca.2006.11.026.

[166] American Society for Testing and Materials (ASTM), ASTM C177-19: Standard test method for steady-state heat flux measurements and thermal transmission properties by means of guarded-hot-plate apparatus, Am. Soc. Test. Mater. (2013) 1–13. https://doi.org/10.1520/C0177-19.2.

[167] ASTM E1225-04, Standard test method for thermal conductivity of solids by means of the guarded-comparative-longitudinal heat flow technique, 2004. https://doi.org/10.1520/E1225-13.2.

[168] International Organization for Standardization, ISO 22007-2: Plastics — Determination of thermal conductivity and thermal diffusivity — Part 2: Transient plane heat source (hot disc) method, Iso. 2008 (2008) 17.

[169] A.S. for T. Materials, Standard Test Method for Thermal Conductivity of Refractories by Hot Wire (Platinum Resistance Thermometer Technique), Astm. 09 (2015) 1–6. https://doi.org/10.1520/C1113.

[170] M.J. Assael, K.D. Antoniadis, I.N. Metaxa, S.K. Mylona, J.A.M. Assael, J. Wu, M. Hu, A Novel Portable Absolute Transient Hot-Wire Instrument for the Measurement of the Thermal Conductivity of Solids, Int. J. Thermophys. 36 (2015) 3083–3105. https://doi.org/10.1007/s10765-015-1964-6.

[171] evitherm, Virtual Institute for Thermal Metrology, (n.d.). http://www.evitherm.org/default.asp?ID=308 (accessed September 1, 2020).

[172] A.S. for T. Materials, Standard Test Method for Thermal Diffusivity by the Flash Method 1, i (2012) 1–13. https://doi.org/10.1520/E1461-07.10.1520/E1461-11.2.

[173] ASTM, E1225-13: Standard Test Method for Thermal Conductivity of Solids Using the Guarded-Comparative-Longitudinal Heat Flow Technique, ASTM Int. i (2015) 1–10. https://doi.org/10.1520/E1225-13.2.

[174] C.K. Stimpson, Cooling Performance of Additively Manufactured Microchannels and Film Cooling Holes, (2017) 1–164.

[175] V. Kulkarni, N. Sahoo, S.D. Chavan, Simulation of honeycomb-screen combinations for turbulence management in a subsonic wind tunnel, J. Wind Eng. Ind. Aerodyn. 99 (2011) 37–45. https://doi.org/10.1016/j.jweia.2010.10.006.

[176] F.M. White, Viscous fluid flow, 2nd ed., McGraw-Hill, New York, 1991.

[177] H. Xiao, H. Liu, An Empirical Formula of Mean Specific Heat Capacity of Ideal Gases, Int. Conf. Educ. Manag. Inf. Med. (2015) 1083–1086. https://doi.org/10.2991/emim-15.2015.206.

[178] Renishaw, AlSi10Mg-0403 powder for additive manufacturing, 2015. http://resources.renishaw.com/en/details/data-sheet-alsi10mg-0403-200-w-powder-for-additive-manufacturing--73121.

[179] C. Silbernagel, I. Ashcroft, P. Dickens, M. Galea, Electrical resistivity of additively manufactured AlSi10Mg for use in electric motors, Addit. Manuf. 21 (2018) 395–403. https://doi.org/10.1016/j.addma.2018.03.027.

[180] A.H. Maamoun, M. Elbestawi, G.K. Dosbaeva, S.C. Veldhuis, Thermal post-processing of AlSi10Mg parts produced by Selective Laser Melting using recycled powder, Addit. Manuf. 21 (2018) 234–247. https://doi.org/10.1016/j.addma.2018.03.014.

[181] S. Catchpole-Smith, R.R.J. Sélo, A.W. Davis, I.A. Ashcroft, C.J. Tuck, A. Clare, Thermal Conductivity of TPMS Lattice Structures Manufactured via Laser Powder Bed Fusion, Addit. Manuf. 30 (2019) 100846. https://doi.org/10.1016/j.addma.2019.100846.

[182] C.Y. Zhao, T.J. Lu, H.P. Hodson, J.D. Jackson, The temperature dependence of effective thermal conductivity of open-celled steel alloy foams, Mater. Sci. Eng. A. 367 (2004) 123–131. https://doi.org/10.1016/j.msea.2003.10.241.

[183] A.N. Abramenko, A.S. Kalinichenko, Y. Burtser, V.A. Kalinichenko, S.A. Tanaeva, I.P. Vasilenko, Determination of the thermal conductivity of foam aluminium, J. Eng. Phys. Thermophys. 72 (1999) 369–373.

[184] R.L. Coble, W.D. Kingery, Effect of Porosity on Physical Properties of Sintered Alumina, J. Am. Ceram. Soc. 39 (1956) 377–385. https://doi.org/10.1111/j.1151-2916.1956.tb15608.x.

[185] B. Dietrich, G. Schell, E.C. Bucharsky, R. Oberacker, M.J. Hoffmann, W. Schabel, M. Kind, H. Martin, Determination of the thermal properties of ceramic sponges, Int. J. Heat Mass Transf. 53 (2010) 198–205. https://doi.org/10.1016/j.ijheatmasstransfer.2009.09.041.

[186] G. Tichá, W. Pabst, D.S. Smith, Predictive model for the thermal conductivity of porous materials with matrix-inclusion type microstructure, J. Mater. Sci. 40 (2005) 5045–5047. https://doi.org/10.1007/s10853-005-1818-x.

[187] M. Kandula, On the Effective Thermal Conductivity of Porous Packed Beds with Uniform Spherical Particles, J. Porous Media. 14 (2011) 919–926. https://doi.org/10.1615/JPorMedia.v14.i10.70.

[188] I. Hughes, T. Hase, Measurements and Their Uncertainties: A Practical Guide to Modern Error Analysis, Oxford: Oxford University Press, Incorporated, Oxford, 2010.

[189] F. Trevisan, F. Calignano, M. Lorusso, J. Pakkanen, A. Aversa, E.P. Ambrosio, M. Lombardi, P. Fino, D. Manfredi, On the selective laser melting (SLM) of the AlSi10Mg alloy: Process, microstructure, and mechanical properties, Materials (Basel). 10 (2017). https://doi.org/10.3390/ma10010076.

[190] S.K. Bose, R. Kumar, Structure of rapidly solidified aluminium-silicon alloys, J. Mater. Sci. 8 (1973) 1795–1799. https://doi.org/10.1007/BF02403532.

[191] J.D. Griffin, R.E. Skochdopole, Engineering design for plastics, E. Baer. V, Rheinhold New York, 1964.

[192] C. Yan, L. Hao, A. Hussein, D. Raymont, Evaluations of cellular lattice structures manufactured using selective laser melting, Int. J. Mach. Tools Manuf. 62 (2012) 32–38. https://doi.org/10.1016/j.ijmachtools.2012.06.002.

[193] B.E. Short, P.E. Raad, D.C. Price, Performance of pin fin cast aluminum coldwalls, Part 1: Friction factor correlations, J. Thermophys. Heat Transf. 16 (2002) 389–396. https://doi.org/10.2514/2.6692.

[194] E.S. Gaddis, V. Gnielinski, Druckverlust in querdurchströmten Rohrbündeln,

Verfahrenstechik 17, Nr. 7. 17 (1983) 410–418.

[195] F.M. White, Fluid mechanics, 7th ed., McGraw-Hill, New York, NY, 2010.

[196] V. Gnielinski, Gleichungen zur Berechnung des Wärmeübergangs in querdurchströmten einzelnen Rohrreihen und Rohrbündeln, Forsch. Im Ingenieurwes. 44 (1978) 15–25. https://doi.org/10.1007/BF02560750.

[197] B.E. Short, P.E. Raad, D.C. Price, Performance of pin fin cast aluminum coldwalls, Part 2: Colburn j-factor correlations, J. Thermophys. Heat Transf. 16 (2002) 397–403. https://doi.org/10.2514/2.6693.

[198] Z. Chen, Y.M. Xie, X. Wu, Z. Wang, Q. Li, S. Zhou, On hybrid cellular materials based on triply periodic minimal surfaces with extreme mechanical properties, Mater. Des. 183 (2019) 108109. https://doi.org/10.1016/j.matdes.2019.108109.

[199] W.E. King, H.D. Barth, V.M. Castillo, G.F. Gallegos, J.W. Gibbs, D.E. Hahn, C. Kamath, A.M. Rubenchik, Observation of keyhole-mode laser melting in laser powder-bed fusion additive manufacturing, J. Mater. Process. Technol. 214 (2014) 2915–2925. https://doi.org/10.1016/j.jmatprotec.2014.06.005.

[200] A. Riemer, S. Leuders, M. Thöne, H.A. Richard, T. Tröster, T. Niendorf, On the fatigue crack growth behavior in 316L stainless steel manufactured by selective laser melting, Eng. Fract. Mech. 120 (2014) 15–25. https://doi.org/10.1016/j.engfracmech.2014.03.008.

[201] B. Ahuja, M. Karg, K.Y. Nagulin, M. Schmidt, Fabrication and characterization of high strength Al-Cu alloys processed using Laser Beam Melting in metal powder bed, Phys. Procedia. 56 (2014) 135–146. https://doi.org/10.1016/j.phpro.2014.08.156.

[202] M. Karg, B. Ahuja, S. Kuryntsev, A. Gorunov, M. Schmidt, Processability of high strength aluminium-copper alloys AW-2022 and 2024 by laser beam melting in powder bed, 25th Annu. Int. Solid Free. Fabr. Symp. An Addit. Manuf. Conf. SFF 2014. (2014) 420–436.

[203] Y. Lu, S. Wu, Y. Gan, T. Huang, C. Yang, L. Junjie, J. Lin, Study on the microstructure, mechanical property and residual stress of SLM Inconel-718 alloy manufactured by differing island scanning strategy, Opt. Laser Technol. 75 (2015) 197–206. https://doi.org/10.1016/j.optlastec.2015.07.009.

[204] M.J. Matthews, G. Guss, S.A. Khairallah, A.M. Rubenchik, P.J. Depond, W.E. King, Denudation of metal powder layers in laser powder bed fusion processes, Acta Mater. 114 (2016) 33–42. https://doi.org/10.1016/j.actamat.2016.05.017.

[205] M. Indriyati, Effect of TiB2 addition on the microstructure and mechanical properties of Al-Cu-Mg-Ag alloy, PhD Dissertation, 2016.

[206] R.G. Munro, Material Properties of Titanium Diboride, J. Res. Natl. Inst. Stand. Technol. 105 (2000) 709. https://doi.org/10.6028/jres.105.057.

[207] M.H. Ghoncheh, S.G. Shabestari, A. Asgari, M. Karimzadeh, Nonmechanical criteria proposed for prediction of hot tearing sensitivity in 2024 aluminum alloy, Trans. Nonferrous Met. Soc. China (English Ed. 28 (2018) 848–857. https://doi.org/10.1016/S1003-6326(18)64718-1.

[208] M.N. Patel, D. Qiu, G. Wang, M.A. Gibson, A. Prasad, D.H. StJohn, M.A. Easton, Understanding the refinement of grains in laser surface remelted Al–Cu alloys, Scr. Mater. 178 (2020) 447–451. https://doi.org/10.1016/j.scriptamat.2019.12.020.

[209] M.H. Ghoncheh, M. Sanjari, A.S. Zoeram, E. Cyr, B.S. Amirkhiz, A. Lloyd, M. Haghshenas, M. Mohammadi, On the microstructure and solidification behavior of new generation additively manufactured Al-Cu-Mg-Ag-Ti-B alloys, Addit. Manuf. 37 (2021) 101724. https://doi.org/10.1016/j.addma.2020.101724.

[210] P. Mair, L. Kaserer, J. Braun, N. Weinberger, I. Letofsky-Papst, G. Leichtfried, Microstructure and mechanical properties of a TiB2-modified Al–Cu alloy processed by laser powder-bed fusion, Mater. Sci. Eng. A. 799 (2021) 140209. https://doi.org/10.1016/j.msea.2020.140209.

[211] A.M.A. Mohamed, F.H. Samuel, A Review on the Heat Treatment of Al-Si-Cu/Mg Casting Alloys, in: Intech, IntechOpen, 2012: pp. 55–70. https://doi.org/http://dx.doi.org/10.5772/79832.

[212] D.A. Porter, Phase transformations in metals and alloys / D.A. Porter, K.E. Easterling., 2nd ed., Chapman & Hall, London, 1992.

[213] W.F. Hosford, Physical metallurgy / William F. Hosford., 2nd ed., CRC Press, Boca Raton, Fla. ; London, 2010.

[214] W. Kurz, Fundamentals of solidification / W. Kurz, D.J. Fisher., 4th rev. e, Trans Tech Publications, Uetikon-Zuerich, Switzerland, 1998.

[215] D.G. Eskin, Suyitno, L. Katgerman, Mechanical properties in the semi-solid state and hot tearing of aluminium alloys, Prog. Mater. Sci. 49 (2004) 629–711. https://doi.org/10.1016/S0079-6425(03)00037-9.

[216] N. Coniglio, C.E. Cross, Initiation and growth mechanisms for weld solidification cracking, Int. Mater. Rev. 58 (2013) 375–397. https://doi.org/10.1179/1743280413Y.0000000020.

[217] S.Z. Uddin, L.E. Murr, C.A. Terrazas, P. Morton, D.A. Roberson, R.B. Wicker, Processing and characterization of crack-free aluminum 6061 using high-temperature heating in laser powder bed fusion additive manufacturing, Addit. Manuf. 22 (2018) 405–415. https://doi.org/10.1016/j.addma.2018.05.047.

[218] Aconity 3D, (2020). https://aconity3d.com/products/aconitymidi/ (accessed August 30, 2020).

[219] Q. Tan, J. Zhang, Q. Sun, Z. Fan, G. Li, Y. Yin, Y. Liu, M.X. Zhang, Inoculation treatment of an additively manufactured 2024 aluminium alloy with titanium nanoparticles, Acta Mater. 196 (2020) 1–16. https://doi.org/10.1016/j.actamat.2020.06.026.

[220] G.S. Pradeep Kumar, R. Keshavamurthy, C.S. Ramesh, T.P. Bharathesh, Mechanical properties of Hot forged Al6061-TiB2 In-situ Metal Matrix Composites, Mater. Today Proc. 2 (2015) 3107–3115. https://doi.org/10.1016/j.matpr.2015.07.270.

[221] Y.S. Kuo, Mechanical properties and porosity content of A201 aluminum alloy castings in different cooling rate sand molds, Adv. Mater. Res. 154–155 (2011) 787–793. https://doi.org/10.4028/www.scientific.net/AMR.154-155.787.

[222] M. Easton, D. Stjohn, Grain refinement of aluminum alloys: Part I. The nucleant and solute paradigms - a review of the literature, Metall. Mater. Trans. A Phys. Metall. Mater. Sci. 30 (1999) 1613–1623. https://doi.org/10.1007/s11661-999-0098-5.

[223] A. Cibula, The mechanism of grain refinement of sand castings in aluminium

alloys, J. Inst. Met. 76 (1949) 321.

[224] J.A.M. Antonio, L.F.M. Lfo, Grain refinement in aluminum alloyed with titanium and boron, Metall. Trans. 2 (1971) 465–471. https://doi.org/10.1007/BF02663335.

[225] L. Backerud, S. Yidong, Grain refining mechanisms in aluminium as a result of additions of titanium and boron. I, Aluminium. 67 (1991) 780–785.

[226] B.S. Murty, S.A. Kori, M. Chakraborty, Grain refinement of aluminium and its alloys by heterogeneous nucleation and alloying, Int. Mater. Rev. 47 (2002) 3–29. https://doi.org/10.1179/095066001225001049.

[227] P.S. Mohanty, J.E. Gruzleski, Mechanism of grain refinement in aluminium, Acta Metall. Mater. 43 (1995) 2001–2012. https://doi.org/10.1016/0956-7151(94)00405-7.

[228] F. Wang, Z. Liu, D. Qiu, J.A. Taylor, M.A. Easton, M.X. Zhang, Revisiting the role of peritectics in grain refinement of Al alloys, Acta Mater. 61 (2013) 360–370. https://doi.org/10.1016/j.actamat.2012.09.075.

[229] J.H. Li, B. Oberdorfer, S. Wurster, P. Schumacher, Impurity effects on the nucleation and growth of primary Al 3(Sc,Zr) phase in Al alloys, J. Mater. Sci. 49 (2014) 5961–5977. https://doi.org/10.1007/s10853-014-8315-z.

[230] M. Bermingham, D. StJohn, M. Easton, L. Yuan, M. Dargusch, Revealing the Mechanisms of Grain Nucleation and Formation During Additive Manufacturing, in: Jom, Springer US, 2020: pp. 1065–1073. https://doi.org/10.1007/s11837-020-04019-5.

[231] Z. Fan, Y. Wang, Y. Zhang, T. Qin, X.R. Zhou, G.E. Thompson, T. Pennycook, T. Hashimoto, Grain refining mechanism in the Al/Al-Ti-B system, Acta Mater. 84 (2015) 292–304. https://doi.org/10.1016/j.actamat.2014.10.055.

[232] H. Inagaki, T. Komatsubara, Yield point elongation in Al-Mg alloys, Mater. Sci. Forum. 331 (2000). https://doi.org/10.4028/www.scientific.net/msf.331-337.1303.

[233] A. Yilmaz, The Portevin-Le Chatelier effect: A review of experimental findings, Sci. Technol. Adv. Mater. 12 (2011). https://doi.org/10.1088/1468-6996/12/6/063001.

[234] O. Nijs, B. Holmedal, J. Friis, E. Nes, Sub-structure strengthening and work hardening of an ultra-fine grained aluminium-magnesium alloy, Mater. Sci. Eng. A. 483–484 (2008) 51–53. https://doi.org/10.1016/j.msea.2006.11.166.

[235] E.O. Hall, Yield Point Phenomena in Metals and Alloys, US Edition, Springer Science \& Business Media, New York, USA, 1970. https://doi.org/10.1007/978-1-4684-1860-6.

[236] R. Asthana, Reinforced cast metals: Part II Evolution of the interface, J. Mater. Sci. 33 (1998) 1959–1980. https://doi.org/10.1023/A:1004334228105.

[237] R.J. Arsenault, N. Shi, Dislocation generation due to differences between the coefficients of thermal expansion, Mater. Sci. Eng. 81 (1986) 175–187. https://doi.org/10.1016/0025-5416(86)90261-2.

[238] J.Z. Liu, S.S. Yang, S.B. Wang, J.H. Chen, C.L. Wu, The influence of Cu/Mg atomic ratios on precipitation scenarios and mechanical properties of Al-Cu-Mg alloys, J. Alloys Compd. 613 (2014) 139–142. https://doi.org/10.1016/j.jallcom.2014.06.045.

[239] M. Tiryakioğlu, J. Campbell, Ductility, structural quality, and fracture toughness of Al-Cu-Mg-Ag (A201) alloy castings, Mater. Sci. Technol. 25 (2009) 784–789. https://doi.org/10.1179/174328408X378645.

[240] X. Zhou, Z. Liu, S. Bai, M. Liu, P. Ying, The influence of various Ag additions on the nucleation and thermal stability of Ω phase in Al-Cu-Mg alloys, Mater. Sci. Eng. A. 564 (2013) 186–191. https://doi.org/10.1016/j.msea.2012.11.081.

[241] S.P. Ringer, K. Hono, I.J. Polmear, T. Sakurai, Nucleation of precipitates in aged Al-Cu-Mg-(Ag) alloys with high Cu:Mg ratios, Acta Mater. 44 (1996) 1883–1898. https://doi.org/10.1016/1359-6454(95)00314-2.

[242] B. Zhou, L. Froyen, Combined Two- and Three-Dimensional (2D and 3D) Characterization of Directionally Solidified Al-Cu-Ag-Mg Quaternary Eutectic, Metallogr. Microstruct. Anal. 3 (2014) 164–173. https://doi.org/10.1007/s13632-014-0129-5.

[243] Aluminium A20X ™ (AM205) Data Sheet, n.d. https://www.3t-am.com/sites/threeT/files/Aluminium A20X_Datasheet.pdf.